5-2018

Polymer Materials Via Melt Based 3D Printing: Fabrication and Characterization

Pu Zhu
Clemson University, pzhu@g.clemson.edu

POLYMER MATERIALS VIA MELT BASED 3D PRINTING: FABRICATION AND CHARACTERIZATION

A Thesis

Presented to

the Graduate School of

Clemson University

In Partial Fulfillment

of the Requirements for the Degree

Master of Science

Materials Science and Engineering

by

Pu Zhu

May 2018

Accepted by:

Dr. Igor Luzinov, Committee Chair

Dr. Philip Brown

Dr. Peng Fei

ABSTRACT

Additive manufacturing, commonly known as 3D printing, first emerged in the 1980s. Currently, the application of 3D printing has been expanded to various areas, such as automotive, aerospace and bio-engineering to mention a few. However, a number of serious challenges with the 3D printing fabrication have been found such as lower mechanical characteristics, relatively high surface roughness and anisotropy in mechanical and physical properties. To expand 3D printing technology into practical final products manufacturing, the improvement of the mechanical properties for the 3D printed parts should be addressed. To this end, the work reported in this thesis is focusing on searching for feasible approaches to improve the mechanical behavior of the 3D printed mono-component and bi-component polymer objects. Specifically, the heat treatment was conducted to improve properties of mono-component samples fabricated from poly (lactic acid) (PLA) and polyethylene terephthalate glycol modified (PETG) filaments. Then, PLA/PETG bi-component hybrid structures were fabricated and heat treated to improve their mechanical characteristics. Further improvement of the mechanical properties for the printed bi-component structures was achieved by utilizing PLA/PETG blend filament. At each step, the morphology, structure, and properties of the materials used and printed samples were characterized using optical microscopy, rheometry, atomic force microscopy, thermal gravimetric analysis, differential scanning calorimetry, Fourier transform infrared spectroscopy, tensile tests and dynamic mechanical analysis (DMA).

DEDICATION

This thesis is dedicate to my parents, Liang Zhu and Baozhen Chang, and my little brother, Zishang Zhu for their support and love.

ACKNOWLEDGEMENTS

I would like to pass my sincere gratitude to my advisor Dr. Luzinov for providing an opportunity to do research under his supervising. His erudition, patience, dynamic and humor made this thesis come into the world and supported my stay in Clemson University. It is the time I spent in his group that helped me decide to pursue a PhD. degree in the future and devote myself into polymer study. I'll always remember his suggestions on both the research and my career development.

I would also like to show my gratitude to my committee members, Dr. Philip Brown and Dr. Peng Fei for their time and advice for this research. I had a great time talking with Dr. Brown about everything. And Dr. Peng helped me to realize my shortcomings and gave me lots of suggestions on how to improve myself. I will always be grateful for their selfless contributions.

My special thanks goes to Kim Ivey for her always giving me a hand while I was doing the experiments and answering my numerous questions. She is as patient as a mother. Her laughter made me feel energetic every day and her hard working motivated me a lot.

Finally I really appreciate all the staffs in MS&E department. They made my life at Clemson University great.

TABLE OF CONTENTS

PAGE

LIST OF FIGURES

FIGURE PAGE

LIST OF TABLES

TABLE PAGE

CHAPTER 1

INTRODUCTION

Additive manufacturing, commonly known as 3D printing, first emerged in the 1980s[1]. Ever since, the application of 3D printing has been expanded to various areas, such as automotive, aerospace and bio-engineering to mention a few[2-4]. The rapid growth of 3D printing originates from its advantages in comparison with the traditional manufacturing techniques, such as the fabrication of complex structures, decrease in materials waste, and affordability of the equippment[5-7]. However, a number of serious challenges with the 3D printing fabrication have been found and reported as well, such as lower mechanical characteristics, relatively high surface roughness and anisotropy in mechanical and physical properties[8-11]. To expand 3D printing technique into practical final products manufacturing, the improvement of the mechanical properties for the 3D printed parts should be addressed. Several methods for the improvement of the properties have been proposed and studied by researchers, such as introducing cross-links and embedding fillers[12-14].

To this end, the work reported in this thesis is mainly focusing on searching for feasible approaches to improve the mechanical performances of the 3D printed simple and bi-component objects significantly. The heat treatment was conducted to improve properties of samples fabricated from poly (lactic acid) (PLA) and polyethylene terephthalate glycol modified (PETG) filaments. Then, PLA/PETG bi-component hybrid structures were fabricated and heat treated to improve their mechanical characteristics.

Further improvement of the mechanical properties for the printed bi-component structures was achieved by utilizing PLA/PETG blend filament.

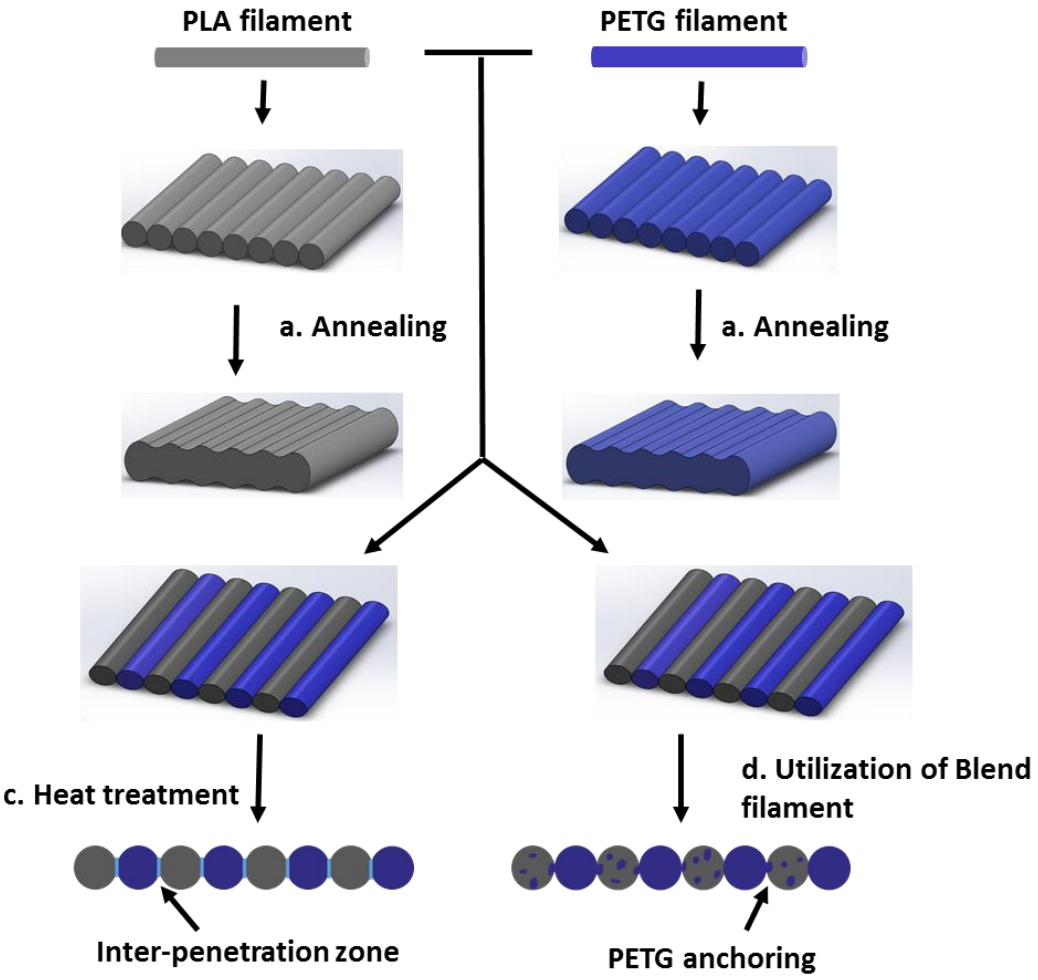

Figure 1.1: Schematic representation of the work flow in this work: (a) represent the heat treatment performed on samples printed from pure PLA and PETG polymers; (b) is the fabrication of PLA/PETG bi-component hybrid structures; (c) shows the heat treatment conducted on bi-component structures; (d) presents the utilization of PLA/PETG blend filament.

Figure 1.1 illustrates the flow of our work. **Figure 1.1 (a)** represents the heat treatment performed on samples printed from pure PLA and PETG filaments. The increase of mechanical properties of the printed samples results from the polymer chains inter diffusion at the layers interface. **Figure 1.1 (b)** shows the fabrication of PLA and PETG bi-component samples through the dual-feed 3D printer. **Figure 1.1 (c)** depicts the heat treatment performed on the hybrid structures, forming an inter-penetration zone at PLA/PETG interface. **Figure 1.1 (d)** depicts the utilization of PLA/PETG blend filament to enhance bonding strength between PLA/PETG interface via PETG phase in the PLA/PETG blend filament.

At each step, the morphology, structure, and properties of the materials and printed samples were characterized using optical microscopy, rheometery, atomic force microscopy (AFM), thermal gravimetric analysis (TGA), differential scanning calorimetry (DSC), Fourier transform infrared spectroscopy (FTIR), tensile tests and dynamic mechanical analysis (DMA).

This thesis is structured as follows:

- **Chapter 2** is a literature review of additive manufacturing with a specific focus 3D printing via fused deposition modeling (FDM). Challenges of the FDM technique and methods to address them are briefly introduced. Fabrication of multi-component materials using 3D printing technology is also discussed;

- **Chapter 3** introduces all characterization techniques and the details of fabrication procedures for fabrication of the 3D printed polymer samples.
- **Chapter 4** describes the fabrication of PLA structures and influence of heat treatment on their mechanical performances. Two different PLA materials were used in the study. The mechanical properties of 3D printed structures made from the materials were discussed and contrasted.
- **Chapter 5** is devoted to the fabrication of PETG samples. Comparison of physical properties between two different PETG materials is reported in order to investigate their feasibility in 3D printing. Annealing was also performed on the printed PETG samples and its effects on the improvement of mechanical properties is reported.
- **Chapter 6** focuses on the manufacturing of PLA/PETG bi-component objects. Heat treatment was conducted on the hybrid structures to improve the bonding strength between PLA and PETG materials in the structures. Blend filament insertion was also explored to integrate these two highly immiscible parts together.
- **Chapter 7** concludes the present work by summarizing the key findings;

References

1. Terry Wohlers, T. G., History of additive manufacturing.pdf. **2012**.
2. https://www.grandviewresearch.com/industry-analysis/3d-printing-industry-analysis. (accessed 02/05/2018).
3. Gross, B. C.; Erkal, J. L.; Lockwood, S. Y.; Chen, C. P.; Spence, D. M., Evaluation of 3D Printing and Its Potential Impact on Biotechnology and the Chemical Sciences. *Analytical Chemistry* **2014,** *86* (7), 3240-3253.

4. Lipson, H.; Kurman, M., *Fabricated : the new world of 3D printing*. John Wiley & Sons: Indianapolis, Indiana, 2013; p xiv, 302 pages, 12 pages of plates.
5. Isakov, D. V.; Lei, Q.; Castles, F.; Stevens, C. J.; Grovenor, C. R. M.; Grant, P. S., 3D printed anisotropic dielectric composite with meta-material features. *Mater Design* **2016,** *93*, 423-430.
6. Ning, F.; Cong, W.; Qiu, J.; Wei, J.; Wang, S., Additive manufacturing of carbon fiber reinforced thermoplastic composites using fused deposition modeling. *Composites Part B: Engineering* **2015,** *80*, 369-378.
7. Carneiro, O. S.; Silva, A. F.; Gomes, R., Fused deposition modeling with polypropylene. *Mater Design* **2015,** *83*, 768-776.
8. Kalsoom, U.; Nesterenko, P. N.; Paull, B., Recent developments in 3D printable composite materials. *Rsc Adv* **2016,** *6* (65), 60355-60371.
9. Christ, J. F.; Aliheidari, N.; Ameli, A.; Potschke, P., 3D printed highly elastic strain sensors of multiwalled carbon nanotube/thermoplastic polyurethane nanocomposites. *Mater Design* **2017,** *131*, 394-401.
10. Ahn, S. H.; Montero, M.; Odell, D.; Roundy, S.; Wright, P. K., Anisotropic material properties of fused deposition modeling ABS. *Rapid Prototyping J* **2002,** *8* (4), 248-257.
11. Lalehpour, A.; Barari, A., Post processing for Fused Deposition Modeling Parts with Acetone Vapour Bath. *Ifac Papersonline* **2016,** *49* (31), 42-48.
12. Hwang, S.; Reyes, E. I.; Moon, K.-s.; Rumpf, R. C.; Kim, N. S., Thermo-mechanical Characterization of Metal/Polymer Composite Filaments and Printing Parameter Study for Fused Deposition Modeling in the 3D Printing Process. *Journal of Electronic Materials* **2014,** *44* (3), 771-777.
13. Appuhamillage, G. A.; Reagan, J. C.; Khorsandi, S.; Davidson, J. R.; Voit, W.; Smaldone, R. A., 3D printed remendable polylactic acid blends with uniform mechanical strength enabled by a dynamic Diels-Alder reaction. *Polym Chem-Uk* **2017,** *8* (13), 2087-2092.
14. Davidson, J. R.; Appuhamillage, G. A.; Thompson, C. M.; Voit, W.; Smaldone, R. A., Design Paradigm Utilizing Reversible Diels-Alder Reactions to Enhance the Mechanical Properties of 3D Printed Materials. *Acs Appl Mater Inter* **2016,** *8* (26), 16961-16966.

CHAPTER 2

LITERATURE REVIEW

This thesis is focusing on the improvement of mechanical properties of 3D printed objects with a particular interest in fabrication of multi-component structures. Therefore, a brief overview of studies addressing the challenges of 3D printing and the fabrication of multi-component objects via 3D printing is presented.

2.1: Additive Manufacturing Technology

Additive manufacturing, commonly referred as 3D printing, keeps drawing both educational and industrial attention. The rapid expansion of 3D printing market is resulting from its efficiency in fabricating complex structures, significant decrease in material waste and high cost efficiency[1-3]. The method compensates for the shortages of traditional manufacturing techniques. There is a wide range of 3D printing methods, including stereo lithography (SLA), selective laser melting (SLM)[4], fused deposition modeling (FDM) and inkjet printing. In general, the 3D printing, which was first introduced in 1980s, has been revolutionizing the art of manufacturing[5].

Stereo lithography

Stereo lithography (SLA) was the first 3D printing technique that was introduced. This technology involves solidifying liquid photosensitive resin through the exposure to ultra-violate (UV) or visible light[6]. **Figure 2.1** shows the schematic of a SLA 3D printer.

The main parts include x-y scanning mirror which directs the laser beam in the x-y plane, the blade which sweeps photosensitive resin over the cross-section of already cured objects and the platform that moves downwards after each layer is cured. The distance that the platform moves downward depends on the laser cure height and the objects' resolution.

One of the disadvantages of this technique is its discontinuity. Tumbleston et al. proposed to solve this problem by taking advantage of oxygen inhibition during the photo-polymerization[7]. During the polymer synthesis, the free radicals would combine with oxygen forming peroxide and quench the process. By making an oxygen dead zone, the photosensitive resin can flow on the surface of already cured surface automatically, making the whole process continuous without the use of blade.

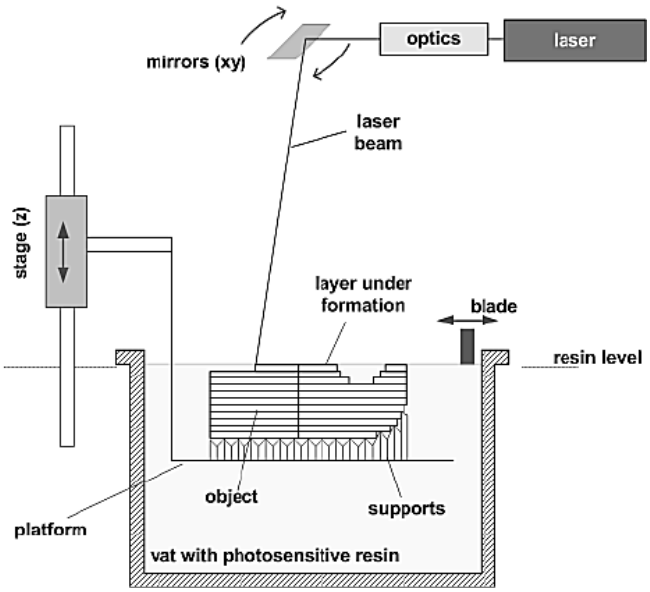

Figure 2.1: Schematic of stereo lithography technology. (Image reproduced with permission from reference 6)

Selective laser melting

Selective laser melting (SLM) enables the ceramic and metal powder fabricated into complex geometries layer-by-layer[8]. **Figure 2.2** shows a schematic of SLM technique. Very similar to SLA, selective laser melting apparatus uses a laser beam, a support platform, and a wiper or roller. However, rather than using photo-polymerization, a high power laser beam is utilized in SLM to melt ceramic and metal powder. The powder solidifies as the laser beam moves away and forms an object with a density close to 100%. Unlike SLA technology, the printed objects are not immersed in a liquid raw material. The wiper or roller sweeps powder from a separate container onto the top of the solidified sample. The whole process is conducted under inert atmosphere to avoid oxidization.

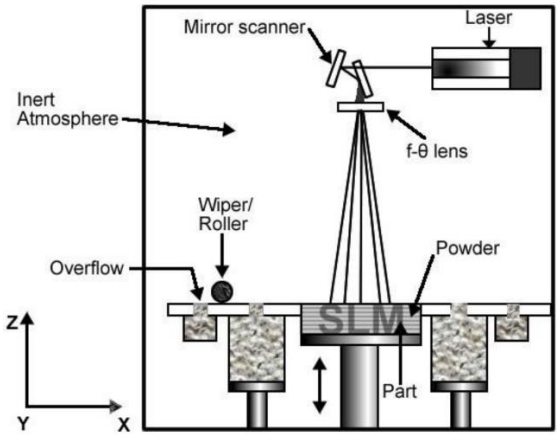

Figure 2.2: Schematic of SLM technology. (Image reproduced with permission from reference 8)

Inkjet printing

The most commonly used inkjet printing technology is the digital inkjet printer which can be seen in every office. Inkjet printing has been used to print two-dimensional

images. The materials or ink used in inkjet printing are a solute dissolved or dispersed in a solvent[9-10]. As shown in **Figure 2.3**, the critical step in inkjet printing is to eject a certain amount of ink through the nozzle by a sudden, quasi-adiabatic reduction of the chamber volume via piezoelectric action. When a pulse voltage is applied, the piezoelectric transducer changes its shape, causing pressure on the liquid ink and forcing a droplet of ink from the nozzle. The droplet is then dried as solvent evaporates. Unlike other techniques, the platform of inkjet printing can move in the x-y plane. Viscosity and surface tension are essential in inkjet printing. One of the greatest advantages of inkjet printing is that no heating band is needed, making the method quite cost effective.

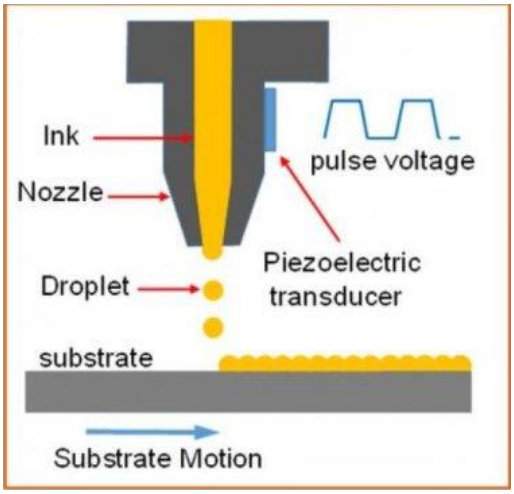

Figure 2.3: Schematic of inkjet printing technology. (Image reproduced with permission from reference 9)

Fuse deposition modeling

Fuse deposition modeling (FDM), although introduced after SLA, is the most commonly used technique in industries and academics[11]. Easy operation, cost efficiency and low material waste makes it increasingly popular. **Figure 2.4** presents the schematic representation of FDM technique[12]. A polymer filament is fed by a roller and heated into the melted state by a heater band. Melted materials is then extruded out of the nozzle and is deposited onto the platform in the form of solid layer. For polymer materials, which are unlikely to adhere to the platform, a heated platform is often necessary. The list of polymer materials that can be used in FDM is quite limited due to the specific requirements such as glass transition temperature (Tg), melting temperature (Tm) and low shrinkage upon cooling[13]. To expand the materials, polymer composites and blends are currently actively explored[14-17].

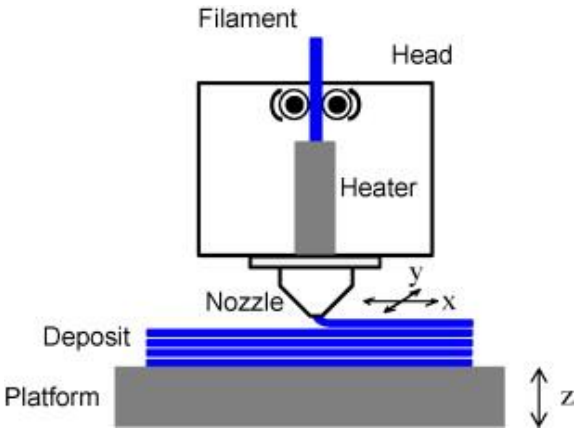

Figure 2.4: Schematic representation of fused deposition modeling technology. (Image reproduced with permission from reference 12)

2.2: Fused Deposition Modeling Technology

As already mentioned above, FDM is the most widely used additive manufacturing technique. Since the 1980s, when the idea of FDM appeared, this technique has significantly evolved and already spread to numerous manufacturing areas, such as aerospace, automatic and biomedical engineering[18-19]. Printing of multi-component objects is the latest development of FDM. For this purpose, more than one nozzle can be used[20-21]. Also, two or more filaments are fed into nozzle simultaneously. Interfaces between different materials can be bonded by adhesives[22]. 4D printing is a new intriguing invention which can be used to fabricate electronic devices[23]. The new added time dimension involves utilizing shape memory polymer (SMP) as a feedstock. It can return to its original shape upon temperature or optical stimulation. Most extensive usage of FDM technology is in fabrication of biological scaffolds having complicated 3D geometries which is difficult to fabricate by traditional manufacturing techniques. However, there is still a number of challenges of FDM that needed to be addressed.

Processing parameters

The properties of 3D printed objects are heavily dependent on the printing parameters. For example, Dawoud et al. pointed the influence of raster angle and air gap on the mechanical behaviors of obtained 3D printed structures[24]. It is concluded that samples printed at 45° raster angle show the highest tensile and impact strength while the ones printed at 90° raster angle have the maximum flexural strength. Gordon et al.

suggested the optimum settings for maximizing the yield stress and ultimate tensile stress for the printed PLA samples after investigating parameters such as layer orientation, infill percentage, nozzle temperature and traveling speed[25]. The best mechanical performance is demonstrated by samples printed at 215°C with a 100% infill percentage, 60 mm/s nozzle travels speed and 0°/90° raster angle. Wu et al. researched the influence of layer thickness and raster angle on the mechanical properties of PEEK 3D printed objects[26]. Tensile, compressive and bending strengths were tested and it was found out that the optimum mechanical properties were achieved when samples printed at 0° raster angle with a 300μm layer thickness.

The significant problem in all studies mentioned above is that their conclusions are not generally applicable. The printing results are heavily dependent on the particular printers used and the characteristics of printing materials. However, a general tendencies can be summarized that the best mechanical properties are observed for the objects printed at 0°/90° raster angle.

Anisotropic nature of 3D printed objects

Objects fabricated using 3D printers have directionally dependent properties. This anisotropic behavior is observed in the mechanical properties difference in z-axis versus x-y plane[27-28]. Anisotropic nature of physical properties for the 3D printed objects is caused by the dissimilar bonding mechanisms for the different directions. Materials lines in the x-y plane are connected by covalent bonds. Thus the mechanical properties in this plane are

mainly determined by the material intrinsic properties. While mechanical properties along z-axis depend on the bonding strength between the solidified layers deposited, which in the most cases are weaker. Therefore, the only way to reduce the anisotropic effect is to increase an adhesion between the layers. The ideal goal is to obtain the adhesion between layers that is comparable to the covalent bonding.

In fact, efforts have been made to reduce this physical properties anisotropy by increasing the adhesion between the deposited layers. Torrado et al. attempted to mitigate the anisotropy of FDM parts by mixing six other components with the ABS copolymer[17]. Results indicate that a ternary blend of ABS combined with styrene ethylene butadiene styrene (SEBS) and ultra- high molecular weight polyethylene (UHMWPE) can lower this anisotropy in mechanical properties from 48% to 22%. Utilization of ionic irradiation to induce cross-links between layers results in the decline of anisotropy as well[29]. This after-processing method took advantage of blending thermoplastics with radiation sensitizer like triallyisocyanurate (TAIC). Shaffer et al. was utilizing gamma rays to irradiate PLA material, showing that both the ultimate stress and strain difference in the horizontal and vertical directions decreased after irradiating PLA at 60°C with a gamma radiation power of 50kGy[29].

Mechanical properties

Due to the weak interlayers' adhesion, FDM printed objects have lower mechanical performances in comparison with molded objects. Parts of the efforts were made to

improve the mechanical properties of the printed materials themselves via addition of reinforcing phases. The main focus here is to enhance the bonding strength between layers, which reduce the anisotropy in mechanical properties as well. Ravi et al. have used a near IR-laser beam to locally re-melt the already solidified layers, creating better bonding during the deposition of the next layer[30]. This pre-deposition heating method not only increased by 50% interlayer bonding strength but also reduces anisotropy of FDM parts. A post-processing approach which is utilizing the thermally reversible Diels-Alder reaction was also proposed[3,31]. It improves both the strength and toughness by 25% for X and Y print directions. While there is about 100% improvement in two print directions for samples with 25wt% mending agent. **Figure 2.5** shows the mechanism of Diels-Alder Reaction. **Figure 2.6** presents the tensile tests results for the printed samples after relizing this reaction.

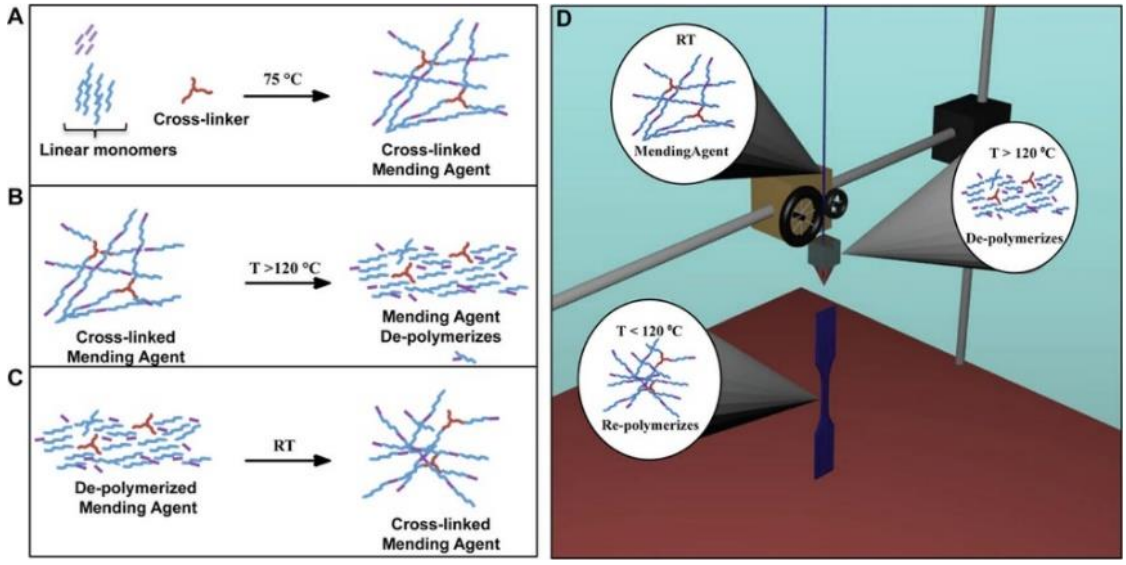

Figure 2.5: Mechanism of Diels-Alder Reaction. (Image reproduced with permission from reference 31)

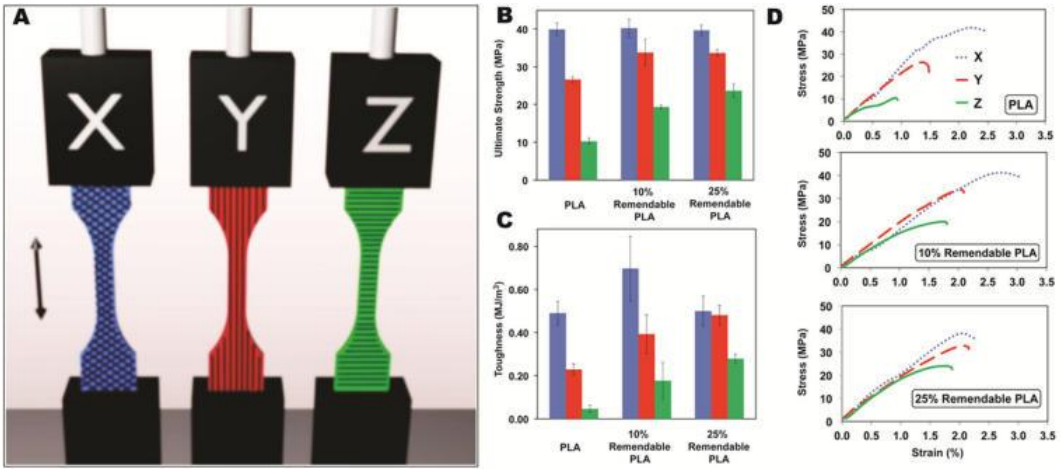

Figure 2.6: Ultimate stress and toughness of PLA printed at various printing pattern. (Image reproduced with permission from reference 31)

Post-processing heat treatment has been reported to have an impact on the improvement of tensile modulus when PLA samples were annealed at 70°C and 100°C[32]. The increase mainly comes from the secondary bonding due to formation of crystals. Viscosity of polymer melt is also essential in determining the mechanical properties of 3D printed objects. Hwang et al found that both the tensile strength and strain increased by reducing the viscosity of ABS[33]. Moreover, the nozzle is not always better with higher temperature, it should be within a specific temperature range providing optimum printing viscosity.

Surface quality of the printed objects

Another serious challenge faced by researchers and engineers is the surface quality of 3D printed objects. The high surface roughness and sometimes low accuracy of 3D printed objects are mainly due to the 'staircases' effect[21]. As shown in **Figure 2.7**, the surface accuracy of the 3D printed objects is destroyed since the objects are created by laying down materials layer-by-layer[42]. And the ideal result is that all the surface peaks are reduced. Reducing layer thickness indeed can improve resolution while also increase printing time significantly. Post-processing procedures are typically necessary to improve the smoothness of the surface. Two major methods in finish parts processing contain chemical polishing or mechanical abrasive finishing[34-38].

For instance, Pandey et al. measured the surface roughness of printed samples and built a semi-empirical model to evaluate the roughness of fabricated parts[35]. **Figure 2.8** shows the sketch that Pandey utilized to build the model. The surface roughness is estimated from the formula:

$$Ra(roughness) = 1000\frac{A1 + A2 + A3}{t/cos\theta}$$

where t is the layer thickness and y the build orientation. A_1, A_2 and A_3 are shown in the figure. A simple hot cutter machining (HCM) method was introduced. The hot cutter utilizes a hot blade to melt and cut off the surface peaks of the printed objects. This method can produce surface finishing of 87% confidence level. Barrel finishing (BF) operation can be used to reduce surface roughness of 3D printed objects as well[37]. BF involves putting the printed objects and media within a rotating barrel. By controlling the rotation speed of

the barrel, the media would abrade the surface of the printed objects to different levels. BF has no geometric limitation making it suitable for the 3D printed complex structures. Boschetto et al. carried out an experimental analysis to determine the compatibility between FDM and barrel finishing technology[37]. The significant reduction of surface roughness was observed when increasing the BF working time.

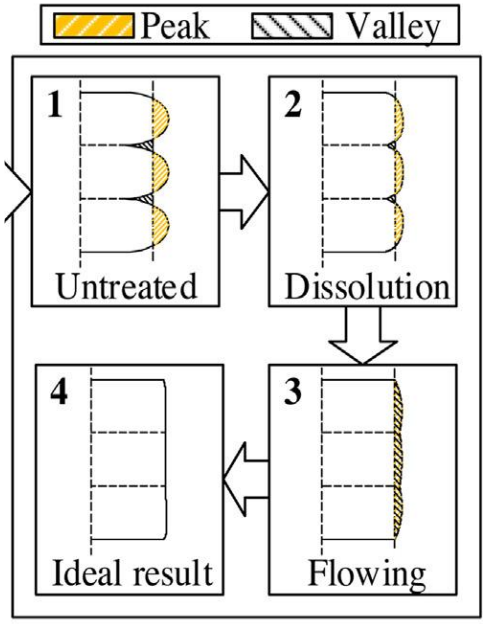

Figure 2.7: Surface polishing process of 3D printed objects. (Image reproduced with permission from reference 34)

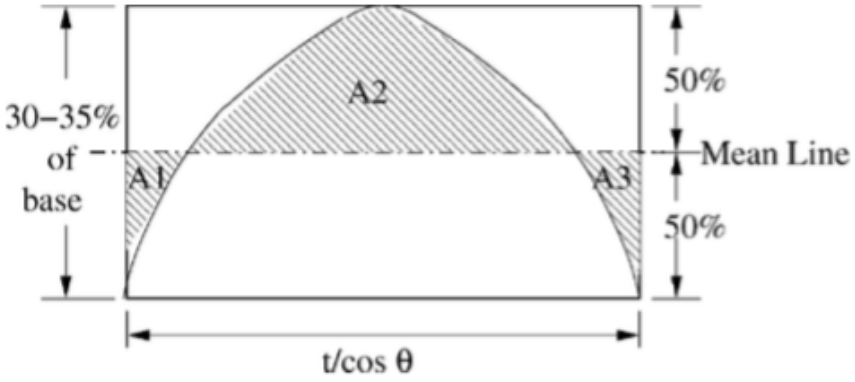

Figure 2.8: Surface profile approximation. (Image reproduced with permission from reference 35)

Utilizing chemical vapor exposure is another practical approach to improve surface finish. Singh et al. found that acetone is a promising chemical for smoothing the surface of 3D printed ABS objects[39]. They also explored the dimethyl-ketone water-based solution to reduce surface roughness for FDM prinetd ABS parts[40]. Results showed a significant improvement of surface finishing as well. Acetone vapor bath smoothing was utilized by Lalehpour et al. to increase the 3D printed sample surface quality[36]. Both the number of acetone bath cycles and the cycle duration were investigated. A digitized model was built based on a 3D microscope imaging. Cycle duration has been proved to be a more prominent factor in deciding surface roughness reduction. Surface roughness is significantly improved, and a reduction percentage value can be close to 95%.

The roughness of FDM objects was also found to be reduced when blending ABS thermoplastics with styrene ethylene butadiene styrene (SEBS) and ultra-high molecular

weight polyethylene (UHMWPE) with a ratio of 75:25:10[41]. This is due to the unique deposition morphology of the polymer blend caused by the rheological differences in comparison with ABS pure material.

2.3: Multi-Component objects fabrication

Multi-component materials have always attracted the interests of scientists and engineers as they possess properties that are not demonstrated by pure materials[42-46]. The materials can fulfill the unique requirements needed for final products. Polymer composites account for a considerable portion of multi-component materials and are vastly used. Dental filling is a resin composite which is made from ceramic and plastic compounds. General packing materials consists of multilayered structures which include plastic-aluminum-paper composites. Wood fiber embedded in high-density polyethylene is used to make milk bottles. And garden furniture usually consists of $CaCO_3$ filled polypropylene (PP). Polymer composites are popular since after mixing the polymer with reinforcing fibers or particles, the mechanical properties of the composites approach that of traditional ceramic and metals. However, the composites are significantly lighter. Several processing procedures have been introduced by researchers to obtain the desired composites.

Melt Blending

Melt processing is the most preferred processing method to fabricate polymer composites[47-49]. This approach includes heating polymer pellets into a viscous melt and dispersing reinforcing additives by shear stirring. For examples, Tanahashi et al utilized this melt-compounding based approach to introduce silica into different polymers[50]. An even distribution of particles was observed by SEM and TEM (**Figure 2.9**). It was concluded that this method has high potential to fabricate polymer composites with good performances. Dul et al. made ABS-graphene nanocomposite through the solvent–free melt compounding process[51]. They found that both the elastic modulus and dynamic modulus increased with the graphene percentage. Moreover, the addition of graphene improves the thermal stability of the composites and therefore, reduces the thermal expansion of the 3D printed parts.

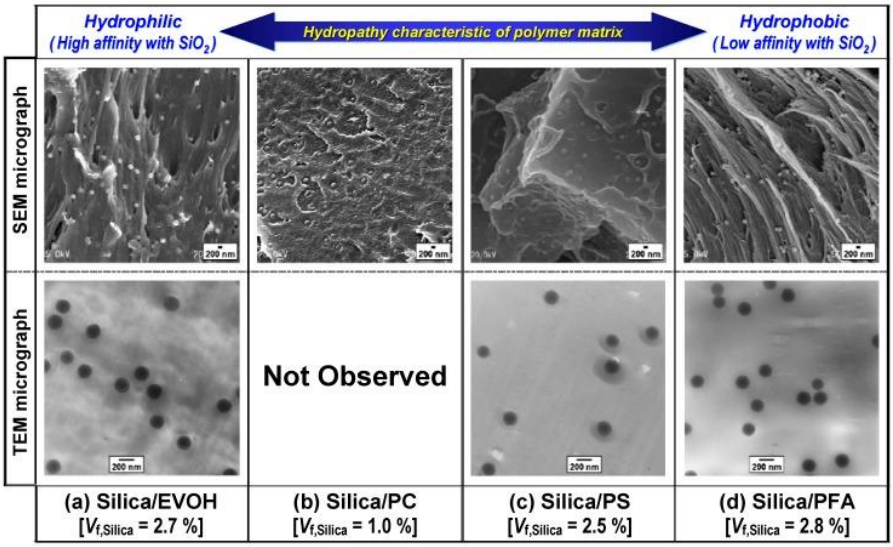

Figure 2.9: SEM and TEM images of silica particles dispersion state in the composites. (Image reproduced with permission from reference 50)

Solution compounding

Solution based mixing is also a common method to obtain inorganic powder/polymer composites[52-54]. However, it has been found that if composites are made via this approach, it is difficult to get rid of the solvent contamination. Thus, it is less preferred. The procedure includes dispersing inorganic powder in polymer solution and shear stirring to make an even distribution of inorganic powder within the solution. After evaporation of the solvent, a polymer composites film is obtained. For example, Qian et al. employed solution-evaporation method facilitated by high energy sonication for dispersion of multiwall carbon nanotube (MCNT) within toluene[55]. Polystyrene and MCNT suspensions were mixed and sonicated for 30min, and toluene evaporated to make a film with the thickness of 0.4mm. Wei et al. utilized the solution mixing method to prepare graphene-ABS composite[53]. After mixing N-Methylpyrolidone (NMP) dissolved graphene and ABS solution, the composite was precipitated by adding water into the mixture.

Mechanical mixing

Milling polymer into powder and then mixing with reinforcing additives is another approach to make polymer composites[56-58]. The advantage of this procedures is that it would not change the physical properties and thermal history of the polymer. There is no concern about contamination of the materials with solvent, ethier. For instance, Xia et al. applied this method to make polypropylene/carbon nanotubes composites[57]. The thermal and mechanical effects of CNT in PP matrix were characterized. Both physical properties

(crystallinity and glass transition temperature) and mechanical properties (Young's modulus and yield strength) are increased in comparison with the pure matrix. Cavalieri et al utilized polymer milling process with liquid CO_2 to process PP and PE polymer mixture[59].

2.3.1: Methods to make FDM composites

In regard to FDM technique, polymer composites are mainly processed by three methods: melt blending, solution casting, and in-nozzle impregnation[60-62]. The monofilament was produced utilizing melt blending and solution casting, while a multi-feed pinch and gear system is employed in the in-nozzle impregnation approach.

Melt Blending

The dual extruder system, which is based on the melt blending technique, is the most general method to fabricate polymer composites in 3D printing study[17, 63]. Both additives and thermoplastics are added into dual screw extruder. Heated polymer melts shear mix with additives at liquefier head. After granulated into pellets, polymer composites can be re-extruded into monofilament for a 3D printer. This procedure can be done several times as long as the temperature not high enough for the polymer to degrade. For instance, Torrado et al. applied a twin screw extruder when compounding ABS with functional additives[17]. Other melt blending methods involve pre-mixing multiple materials in a blender and then extruding them into a monofilament[64].

Solution mixing

Solution based mixing mainly is used when the sizes of additives are too small to be melt blended in extruder. Isakov et al. was working on creating different levels of electrical permittivity by introducing micro-ceramic particles ($BaTiO_3$) into ABS and PP polymer matrix[65]. Both thermoplastics and ceramic powder were stirred in acetone solvent. After acetone was evaporated, thin composite film was milled mechanically resulting in granulated pellets. These pellets were then melt extruded into a filament. To investigate the anisotropic dielectric properties of printed parts, a 3D printer equipped with the dual filaments feed system was used.

In-nozzle impregnation

Researchers also studied continuous fiber/polymer composites, with which either melt blending or solution casting does not work. The dual feed printer was used. Rather than feed two filaments simultaneously, one of the feed pinch gear is adjusted to feed the reinforcing fiber. Polymer filament melts in the heater band and impregnates in the fiber creating an evenly reinforced polymer/long fiber composites. Tian et al. utilized such printer to study 3D printed carbon fiber reinforced PLA composites[66]. More recently, printers equipped with more than one nozzle aligned side by side on the carriage was used to print objects containing multiple materials or colors[65, 67-68]. Multi-nozzle system printers are widely used in the bio-engineering field for scaffolds fabrication. Both Hollister et al.

and Khalil et al. used this technique to print biocompatible polymer scaffold structures[69-70].

2.3.2: Polymer composites fabricated via FDM

According to the methodology of 3D melt based printing technology, optimal glass transition temperature, optimal melting temperature and low thermal shrinkage are required for the printable materials. Thus, only a limited number of polymer thermoplastic materials can be put into usage. To expand the range of suitable materials, increase physical properties or add new properties such as electrical, thermal conductivity or biocompatibility to 3D printed objects, polymers are mixed with other polymers, fibers, metals and/or ceramic particles. Addition of inorganic fibers or ceramic, metal particles can significantly improve the mechanical properties of materials. However, several issues were reported for these composites such as phase cleavage, aggregation of particles and uneven distribution of the dispersed phases[71-73]. These problems should be addressed as monofilaments for FDM are fabricated.

Fiber reinforced polymer composites

As mentioned above, 3D printed objects have worse mechanical properties than that for objects fabricated by traditional manufacturing techniques. To increase the mechanical properties of 3D printed objects, fiber reinforced composites are most commonly employed. Continuous fiber reinforced thermoplastics are rarely explored due

to difficulty in mixture process. Li et al. built PLA composites reinforced by continuous carbon fiber by utilizing a specific FDM 3D printer which can feed long carbon fiber with PLA filament individually and mix them within the liquefier (**Figure 2.10**) [74]. The surface of the carbon fiber was modified by immerging carbon fiber within PLA solution to increase the bonding strength at PLA/carbon fiber interface. SEM images confirm an effective bonding and experimental results demonstrated the 14% and 164% improvement of both tensile strength and flexural strengths in comparison with the carbon fiber/PLA composites without the surface modification. Matsuzaki et al. produced continuous carbon fiber (CFRTP), and twisted jute fiber yarn reinforced PLA (JFRTP) composites by in-nozzle impregnation[75]. Tensile test presented in **Figure 2.11** indicates that there is a 600% and 435% increase in tensile modulus and strength comparing to pure PLA material.

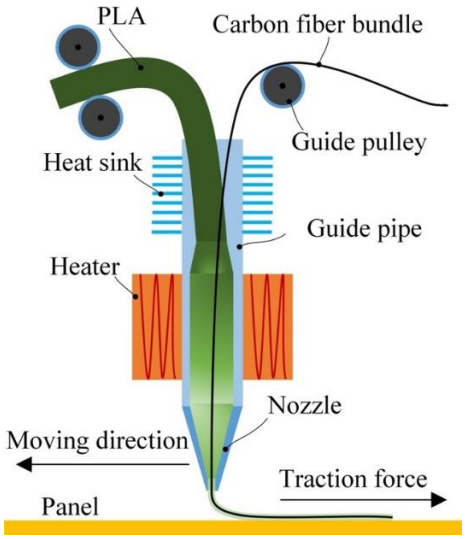

Figure 2.10: Schematic illustration of the printer to print continuous fiber with polymer. (Image reproduced with permission from reference 74)

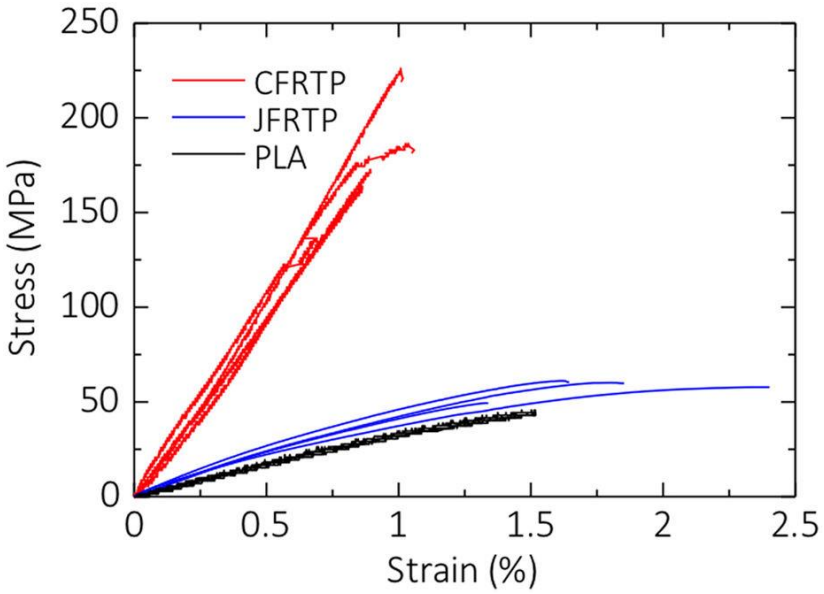

Figure 2.11: Stress-strain curves of PLA, CFRTP, and JFRTP specimens fabricated by 3D printing. (Image reproduced with permission from reference 75)

Besides continuous fibers, utilizing short fiber reinforced composites has also been reported. For instance, researchers developed a new composite system suited for FDM, which involves mixing short thermotropic liquid crystalline fibers (TLCF) with polypropylene (PP)[76]. The tensile strength of the composite is about four times higher than that of ABS. The usage of short glass fiber to strengthen ABS matrix was studied by Zhong at al.[77]. The loss of flexibility and handling ability with the fiber addition was compensated by adding plasticizer, making the composite compatible with FDM. Carneiro et al. also studied the mechanical properties of glass fiber reinforced polypropylene (PP) composite[2]. The tensile test results show a 30% and 40% increase in both Young's modulus and ultimate tensile stress, respectively. Comparison between 3D printed parts with the compression molded samples indicates that there is a comparable mechanical performance of 3D

manufactured parts when the processing parameters are optimized. Nylon fibers are also of great interests among researchers working on 3D printing. Singh et al embedded nylon fiber and Al_2O_3 powder within ABS polymer matrix[78]. As a result, mechanical characteristics, such as tensile strength and percent of elongation, were increased significantly. Natural fiber reinforced green composites were developed by Duigou et al[79]. Moisture induced self-shaping wood fibers were blended with PLA and poly (hydroxyalkanoate) (PHA) matrix using chloroform as a solvent. High porosity of the obtained materials accounts for the low mechanical properties observed. However, additive manufactured objects show a faster water-induced bending than that built using compression molding, making them promising hydromorphic objects.

Carbon-based compound, such as carbon fibers, carbon nanotubes and carbon black reinforced polymer composites have been extensively explored. Ning et al. investigated the mechanical properties of ABS improved by blending with carbon fibers of various fiber length[64]. Contents of carbon fibers in the composite was varied as well. Results show that the tensile strength and Young's modulus were increased in comparison with the pure ABS plastic, while the ductility and yield strength of the composite declined. It was also found that for longer fibers, there are better tensile properties but worse flexural properties. Besides, there is a threshold of carbon fiber contents as too many carbon fibers lead to a high porosity which significantly decreases mechanical properties of FDM parts. Halil L. et al. utilized short carbon fiber (0.2mm-0.4mm) to reinforce ABS[80]. Comparable tensile strength and modulus were found between 3D printed samples and the traditional compression molded ones. Microstructure characterization revealed that samples

fabricated by the additive manufacturing had a higher inner layer porosity but lower inter layer porosity. The highly orientated carbon fibers within the bulk lead to comparable tensile strength and modulus with the compression molded objects. However, the decrease in materials used is making 3D printed objects more favorable.

Shofner et al. studied the mechanical properties of ABS thermoplastics embedded with vapor growth nano-carbon fiber (VGCF), which is known for its excellent combination of high strength and low weight[81]. Tensile test results indicate an improvement of tensile strength for the composites with respect to ABS raw materials. However, the material changed from ductile to brittle, leading to a drastic decline in elongation. Brett G. et al utilized an epoxy-based ink having silicon carbide and carbon fiber to understand the effect of the additives on mechanical properties of 3D printed structures[82]. Nano-clay platelets and dimethyl methyl phosphonate (DMMP) were also added to tune the viscosity of the ink. Young's modulus of the obtained structures was found to be around ten times higher than those obtained by using commercial thermoplastics for 3D printing (**Figure 2.12**).

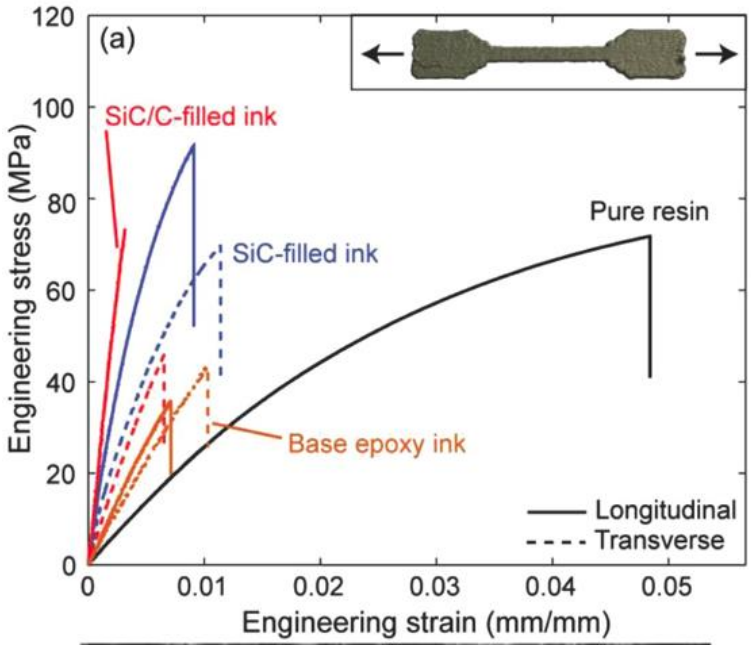

Figure 2.12: Tensile stress versus strain curves for 3D printed samples of varying composition and control samples printed from pure epoxy resin. (Image reproduced with permission from reference 82)

Polymer composites reinforced with inorganic powder

An enhancement of mechanical properties was found by researchers when inorganic powders were added to the polymer matrix. For instance, Angel et al. incorporated TiO_2 powder in ABS matrix[83]. The highest ultimate tensile strength was obtained in both horizontal and vertical directions with embedding 5% of TiO_2. However, there was an apparent decrease in ductility. Weng et al. investigated the mechanical and thermal properties of ABS/organic modified montmorillonite (OMMT) nanocomposites[5]. Tensile, flexural, thermal expansion and dynamic mechanical analysis were utilized to

characterize the composite material. The results showed that 5wt% OMMT load increased the tensile strength by 43% and decreased the linear thermal expansion ratio. Liu et al. embedded nano-titania within poly-lactide-co-glycolide (PLGA)[14]. The tensile test indicated that a well-dispersed nano-phase could improve both tensile modulus and strength of 3D printed objects.

In conclusion, creating new polymer composites is not only an effective way to increase the mechanical properties of the raw materials but also can expand the range of materials suitable for 3D printing. Carbon fiber is the most common filler blended with the polymer matrix for this purpose. It is necessary to point out that fiber reinforced polymer composites have a serious challenge. The filaments in composites tend to fracture during the monofilament extrusion. This is a result of weak bonding between the fiber reinforced phase and polymer matrix. Therefore, some special additives like binder or plasticizer should be added to reduce the fracture effect.

2.3.3: Polymer composites for FDM with unique physical properties

More recently, using nanoparticle reinforced polymer composites to enhance mechanical properties of 3D printed parts has attract significant attention. The embedded metal or ceramic nanoparticles not only can improve mechanical properties but also introduce some innovative physical properties to the polymer composites.

Thermal conductivity

The thermal conductivity of 3D printed parts was improved due to the incorporation of metal particles into polymer matrix to relieve the thermal distortion during the solidification of printed layers. Hwang et al. found an increase of thermal conductivity with increase of the iron or copper contents in ABS[33]. The better thermal transport made it possible to print objects having larger sizes. However, the increase of thermal conductivity comes along with the decrease of the tensile strength. In another example, Nikzad et al. compounded iron and copper metal particles within ABS and found a significant improvement of both thermal and mechanical properties[84]. Addition of iron and copper particles can increase the thermal conductivity of ABS matrix by one order of magnitude when the metal content exceeded a threshold of 30vol% and can overcome the thermal resistance of ABS. After blending with the metal particles, the composite materials became brittle in comparison with the ductile pure ABS materials.

In order to solve the low through-plane thermal conductivity (TPTC) of the objects fabricated, graphite flakes can be embedded inside polymer matrix. The flakes can align in the plane direction during the processing. Jia et al. made use of FDM technology to introduce graphite flakes arranged perpendicular to the plane[85]. One order of TPTC increase was found for 3D printed parts compared to that fabricated by inject molding. In another study, graphene nanoplatelets (xGnP) were incorporated in ABS[51]. Dynamic mechanical analysis indicated an improvement of elastic modulus and dynamic storage modulus with increasing of xGnP content. A decline of linear thermal expansion and creep temperature indicated a better thermal conductivity of the polymer composites, making

them potential materials for 3D printing. The thermal conductivity of iron/ nylon composites were investigated by Masood et al[15]. Two mathematical models were developed to calculate the thermal conductivity of the composites.

Electric conductivity

Polymer composites possess electricity conductivity were also fabricated using 3D printing technologies. However, these 3D printed electrical devices are mainly based on ink-jet printing or stereo lithography (SLA) technologies. Only a few of them are manufactured using FDM technique. Leigh et al. worked on embedding carbon black within the filament to be used for 3D printing[86]. Carbon black was chosen due to its stability to oxidation in comparison to copper. Polycaprolactone (PCL) was chosen as matrix material. The electrical conductivity of these composites was characterized by the lightness of a LED. The piezo-sensitive behavior has been found, leading the possibility using these materials into sensors. Dorigato et al. incorporated multi-walled carbon nanotube (MWCNT) within ABS polymer matrix by melt mixing[87]. Tensile test, electrical conductivity, and thermal diffusivity were all performed to characterize the properties of these composites. Mechanical performances of the polymer composites demonstrated increase of stiffness and stress but decrease of elongation at break. Electrical conductivity increased dramatically even with small MWCNT content. Reduction in the thermal expansion and creep temperature indicated that this composite has a better thermal conductivity. Gnanasekaran et al. studies the electrical conductivity of carbon nanotube

(CNT), graphene-based polybutylene terephthalate (PBT) composites[16]. PBT/CNT composites have a better mechanical performance and electrical conductivity than that of PBT/Graphene. Moulart et al. fabricated electromagnetic crystals and microwave devices by blending barium titanate (BT), carbon black, copper powder and carbon, steel fibers within ABS matrix[88]. The produced BT/ABS composites had a dielectric constant over 8 and loss tangents of 0.01, which satisfy the requirements for electromagnetic crystals. Carbon black/ABS and steel fiber/ABS composites were created with an electrical conductivities over 10^{-3} S/cm, allowing using these materials for electromagnetic shielding.

Piezoelectricity

Piezo-sensitive composites also synthesized through mixing $BaTiO_3$ (BT) particles with polyethylene glycol diacrylate (PEGDA)[89]. The surface of BT particles was modified by 3-trimethoxysilylpropyl methacrylate (TMSPM) molecules which can crosslink with PEGDA while exposed to laser beam. Better bonding between two phases helps to transport mechanical stress from the deformed polymer matrix to piezoelectric particles. The obtained piezoelectric property is ten times higher than that of non-surface modified BT/PEGDA composites. Isakov et al. studied the feasibility of creating dielectric sensor by FDM technique[65]. Solution casting based mixing procedure was used to blend ABS or PP polymer matrix with $BaTiO_3$, $CaTiO_3$, and $Ba_{0.64}Sr_{0.36}TiO_3$ micro-particles to create composites with different levels of permittivity. Anisotropic permittivity and microstructure of 3D printed objects were characterized. It was pointed that precise control

of the spatial permittivity offered by 3D printing has great potential in design of electromagnetic devices. Macnulty et al. embedded a wax modified lead zirconate titanate (PZT) powder within the polymer matrix which can be used to fabricate piezoelectric functional devices[90].

Bio-compatibility

Fabrication of bio-compatible polymer composites or blends is another major concentration for multi-component materials fabrication via 3D printing. For instance, Fielding et al. evaluated the effect of silica (SiO_2) and zinc oxide (ZnO) particles on the mechanical and biological properties of tricalcium phosphate (TCP) scaffolds[91]. Compressive strength demonstrated 2.5 times increase after the addition of the ceramic particles. In-vitro cells interaction studies indicated that the addition of SiO_2 and ZnO would facilitate the cells proliferation. Chen et al. evaluated the biocompatibility of a nano-composite made of polyurethane/poly (lactic acid) and graphene oxide[28]. Nanocomposites were prepared by solvent-based mixing and extruded into a filament. Addition of graphene oxide increased the mechanical properties of the materials significantly. Bio-compatibility of nanocomposites was investigated using NIH_3T_3 cells. It was found that 0.5% addition of graphene oxide is the optimum condition to support cells growth. Polycaprolactone (PCL) is a highly demanded biocompatible polymer. Haq et al. developed PCL, montmorillonite (MMT) and hydroxyapatite (HA) nanocomposites to study their mechanical properties and biocompatibility[92]. There were slight increase in tensile and

flexural properties of PCL/MMT/HA composites. The presence of apatite indicated bioactivity of this nanocomposite.

Wear-resistance

Researchers also studied some other properties of the 3D printed objects such as wear resistance. For instance, Singh et al. embedded Al_2O_3 within nylon 6 matrix to increase its wear resistance[93]. The wear resistance had been improved significantly due to the reinforcing Al_2O_3 powder. Wear and friction behavior were also investigated by Garg et al[94]. For nylon/iron/ABS composite, results showed that the composite material obtained by 3D printing was extremely wear-resistant.

In summary, various kind of polymer composites for 3D printing were studied. Organic and inorganic fibers, flakes or powders reinforced polypropylene, polyethylene, PLA and ABS were investigated to determine the effect of additives on physical properties of the 3D printed objects. The obtained results have indicated that the polymer composites can expand the range of thermoplastics materials available for 3D printing. They can also improve the mechanical properties of 3D printed parts and introduce new physical properties to the printed objects.

2.4: Conclusion

3D printing is a newly emerging technology which allows the building of complex structures based on the computer-aid design. There are four types of major techniques, including SLA, SLM, FDM and inkjet printing. Fused deposition modeling is the most commonly used 3D printing technology. However, a number of challenges such as anisotropy of physical properties, weak adhesion between printed layers, significant surface roughness and limited range materials available should be addressed to expand the applications of FDM.

2.5: Reference

1. Chua, C. K.; Leong, K. F., 3D PRINTING AND ADDITIVE MANUFACTURING Principles And Applications (The 5th edition of Rapid Prototyping: Principles and Applications) PREFACE. *3d Printing and Additive Manufacturing: Principles and Applications* **2017**, Xi-Xiv.
2. Carneiro, O. S.; Silva, A. F.; Gomes, R., Fused deposition modeling with polypropylene. *Mater Design* **2015,** *83*, 768-776.
3. Appuhamillage, G. A.; Reagan, J. C.; Khorsandi, S.; Davidson, J. R.; Voit, W.; Smaldone, R. A., 3D printed remendable polylactic acid blends with uniform mechanical strength enabled by a dynamic Diels-Alder reaction. *Polym Chem-Uk* **2017,** *8* (13), 2087-2092.
4. Kruth, J. P.; Mercelis, P.; Van Vaerenbergh, J.; Froyen, L.; Rombouts, M., Binding mechanisms in selective laser sintering and selective laser melting. *Rapid Prototyping J* **2005,** *11* (1), 26-36.
5. Weng, Z. X.; Wang, J. L.; Senthil, T.; Wu, L. X., Mechanical and thermal properties of ABS/montmorillonite nanocomposites for fused deposition modeling 3D printing. *Mater Design* **2016,** *102*, 276-283.
6. Beal, V. E.; Ahrens, C. H.; Wendhausen, P. A., The use of stereolithography rapid tools in the manufacturing of metal powder injection molding parts. *Journal of the Brazilian Society of Mechanical Sciences and Engineering* **2004,** *26* (1), 40-46.
7. Tumbleston, J. R.; Shirvanyants, D.; Ermoshkin, N.; Janusziewicz, R.; Johnson, A. R.; Kelly, D.; Chen, K.; Pinschmidt, R.; Rolland, J. P.; Ermoshkin, A.; Samulski, E. T.; DeSimone, J. M., Continuous liquid interface production of 3D objects. *Science* **2015,** *347* (6228), 1349-1352.

8. Sidambe, A., *Biocompatibility of Advanced Manufactured Titanium Implants—A Review*. 2014; Vol. 7, p 8168-8188.
9. Lin, X.; Kavalakkatt, J.; Lux-Steiner, M. C.; Ennaoui, A., Inkjet-Printed Cu2ZnSn(S, Se)4 Solar Cells. *Adv Sci (Weinh)* **2015,** *2* (6), 1500028.
10. Singh, M.; Haverinen, H. M.; Dhagat, P.; Jabbour, G. E., Inkjet Printing-Process and Its Applications. *Adv Mater* **2010,** *22* (6), 673-685.
11. Hwang, S.; Reyes, E. I.; Moon, K.-s.; Rumpf, R. C.; Kim, N. S., Thermo-mechanical Characterization of Metal/Polymer Composite Filaments and Printing Parameter Study for Fused Deposition Modeling in the 3D Printing Process. *Journal of Electronic Materials* **2014,** *44* (3), 771-777.
12. Ahn, D.; Kweon, J. H.; Kwon, S.; Song, J.; Lee, S., Representation of surface roughness in fused deposition modeling. *J Mater Process Tech* **2009,** *209* (15-16), 5593-5600.
13. Kalsoom, U.; Nesterenko, P. N.; Paull, B., Recent developments in 3D printable composite materials. *Rsc Adv* **2016,** *6* (65), 60355-60371.
14. Liu, H. N.; Webster, T. J., Enhanced biological and mechanical properties of well-dispersed nanophase ceramics in polymer composites: From 2D to 3D printed structures. *Mat Sci Eng C-Mater* **2011,** *31* (2), 77-89.
15. Masood, S. H.; Song, W. Q., Thermal characteristics of a new metal/polymer material for FDM rapid prototyping process. *Assembly Autom* **2005,** *25* (4), 309-315.
16. Gnanasekaran, K.; Heijmans, T.; van Bennekom, S.; Woldhuis, H.; Wijnia, S.; de With, G.; Friedrich, H., 3D printing of CNT- and graphene-based conductive polymer nanocomposites by fused deposition modeling. *Applied Materials Today* **2017,** *9*, 21-28.
17. Torrado, A. R.; Shemelya, C. M.; English, J. D.; Lin, Y.; Wicker, R. B.; Roberson, D. A., Characterizing the effect of additives to ABS on the mechanical property anisotropy of specimens fabricated by material extrusion 3D printing. *Additive Manufacturing* **2015,** *6*, 16-29.
18. Salentijn, G. I.; Oomen, P. E.; Grajewski, M.; Verpoorte, E., Fused Deposition Modeling 3D Printing for (Bio)analytical Device Fabrication: Procedures, Materials, and Applications. *Anal Chem* **2017,** *89* (13), 7053-7061.
19. www.stratasys.com/-/media/files/case-studies/aerospace/cs_fdm_ae_nasa.pdf.
20. Yan, Y.; Xiong, Z.; Hu, Y.; Wang, S.; Zhang, R.; Zhang, C., Layered manufacturing of tissue engineering scaffolds via multi-nozzle deposition. *Materials Letters* **2003,** *57* (18), 2623-2628.
21. Liu, L.; Yan, Y. N.; Xiong, Z.; Zhang, R. J.; Wang, X. H., A novel poly (lactic-co-glycolic acid)-collagen hybrid scaffold fabricated via multi-nozzle low-temperature deposition. *Proc Monogr Eng Wate* **2008**, 57-+.
22. Gibson, I.; Rosen, D. W.; Stucker, B., Additive Manufacturing Technologies: Rapid Prototyping to Direct Digital Manufacturing. *Additive Manufacturing Technologies: Rapid Prototyping to Direct Digital Manufacturing* **2010**, 1-459.
23. Zarek, M.; Layani, M.; Cooperstein, I.; Sachyani, E.; Cohn, D.; Magdassi, S., 3D Printing of Shape Memory Polymers for Flexible Electronic Devices. *Adv Mater* **2016,** *28* (22), 4449-+.
24. Dawoud, M.; Taha, I.; Ebeid, S. J., Mechanical behaviour of ABS: An experimental study using FDM and injection moulding techniques. *J Manuf Process* **2016,** *21*, 39-45.
25. Torres, J.; Cole, M.; Owji, A.; DeMastry, Z.; Gordon, A. P., An approach for mechanical property optimization of fused deposition modeling with polylactic acid via design of experiments. *Rapid Prototyping J* **2016,** *22* (2), 387-404.

26. Wu, W. Z.; Geng, P.; Li, G. W.; Zhao, D.; Zhang, H. B.; Zhao, J., Influence of Layer Thickness and Raster Angle on the Mechanical Properties of 3D-Printed PEEK and a Comparative Mechanical Study between PEEK and ABS. *Materials* **2015,** *8* (9), 5834-5846.
27. Ahn, S. H.; Montero, M.; Odell, D.; Roundy, S.; Wright, P. K., Anisotropic material properties of fused deposition modeling ABS. *Rapid Prototyping J* **2002,** *8* (4), 248-257.
28. Chen, Q. Y.; Mangadlao, J. D.; Wallat, J.; De Leon, A.; Pokorski, J. K.; Advincula, R. C., 3D Printing Biocompatible Polyurethane/Poly(lactic acid)/Graphene Oxide Nanocomposites: Anisotropic Properties. *Acs Appl Mater Inter* **2017,** *9* (4), 4015-4023.
29. Shaffer, S.; Yang, K. J.; Vargas, J.; Di Prima, M. A.; Voit, W., On reducing anisotropy in 3D printed polymers via ionizing radiation. *Polymer* **2014,** *55* (23), 5969-5979.
30. Ravi, A. K.; Deshpande, A.; Hsu, K. H., An in-process laser localized pre-deposition heating approach to inter-layer bond strengthening in extrusion based polymer additive manufacturing. *J Manuf Process* **2016,** *24*, 179-185.
31. Davidson, J. R.; Appuhamillage, G. A.; Thompson, C. M.; Voit, W.; Smaldone, R. A., Design Paradigm Utilizing Reversible Diels-Alder Reactions to Enhance the Mechanical Properties of 3D Printed Materials. *Acs Appl Mater Inter* **2016,** *8* (26), 16961-16966.
32. Harris, A. M.; Lee, E. C., Improving mechanical performance of injection molded PLA by controlling crystallinity. *J Appl Polym Sci* **2008,** *107* (4), 2246-2255.
33. Hwang, S.; Reyes, E. I.; Moon, K. S.; Rumpf, R. C.; Kim, N. S., Thermo-mechanical Characterization of Metal/Polymer Composite Filaments and Printing Parameter Study for Fused Deposition Modeling in the 3D Printing Process. *Journal of Electronic Materials* **2015,** *44* (3), 771-777.
34. Jin, Y. F.; Wan, Y.; Zhang, B.; Liu, Z. Q., Modeling of the chemical finishing process for polylactic acid parts in fused deposition modeling and investigation of its tensile properties. *J Mater Process Tech* **2017,** *240*, 233-239.
35. Pandey, P. M.; Reddy, N. V.; Dhande, S. G., Improvement of surface finish by staircase machining in fused deposition modeling. *J Mater Process Tech* **2003,** *132* (1-3), 323-331.
36. Lalehpour, A.; Barari, A., Post processing for Fused Deposition Modeling Parts with Acetone Vapour Bath. *Ifac Papersonline* **2016,** *49* (31), 42-48.
37. Boschetto, A.; Bottini, L., Surface improvement of fused deposition modeling parts by barrel finishing. *Rapid Prototyping J* **2015,** *21* (6), 686-696.
38. Singh, R.; Singh, M., Surface roughness improvement of cast components in vacuum moulding by intermediate barrel finishing of fused deposition modelling patterns. *P I Mech Eng E-J Pro* **2017,** *231* (2), 309-316.
39. Singh, R.; Singh, S.; Singh, I. P.; Fabbrocino, F.; Fraternali, F., Investigation for surface finish improvement of FDM parts by vapor smoothing process. *Compos Part B-Eng* **2017,** *111*, 228-234.
40. Singh, R.; Singh, S.; Singh, I. P., Effect of Hot Vapor Smoothing Process on Surface Hardness of Fused Deposition Modeling Parts. *3d Print Addit Manuf* **2016,** *3* (2), 128-133.
41. Rocha, C. R.; Perez, A. R. T.; Roberson, D. A.; Shemelya, C. M.; MacDonald, E.; Wicker, R. B., Novel ABS-based binary and ternary polymer blends for material extrusion 3D printing. *J Mater Res* **2014,** *29* (17), 1859-1866.
42. Klapdohr, S.; Moszner, N., New inorganic components for dental filling composites. *Monatsh Chem* **2005,** *136* (1), 21-45.
43. al., W. e. Multi-layer packing film. 2002.

44. A. Buasri, N. C., K. Borvornchettanuwat, N. Chantanachai and K. Thonglor, Thermal and Mechanical Properties of Modified CaCO3 PP Nanocomposites.pdf. *International Journal of Materials and Metallurgical Engineering* **2012,** *Vol:6, No:8*.
45. Niska, K. O.; Sain, M., Wood-polymer composites Introduction. *Woodhead Publ Mater* **2008**, Xv-Xv.
46. Yu, Z. Z.; Dasari, A.; Mai, Y. W., Polymer-Clay Nanocomposites - A Review of Mechanical and Physical Properties. *Processing and Properties of Nanocomposites* **2006**, 307-358.
47. Bhattacharya, M., Polymer Nanocomposites-A Comparison between Carbon Nanotubes, Graphene, and Clay as Nanofillers. *Materials (Basel)* **2016,** *9* (4).
48. Pötschke, P.; Bhattacharyya, A. R.; Janke, A.; Pegel, S.; Leonhardt, A.; Täschner, C.; Ritschel, M.; Roth, S.; Hornbostel, B.; Cech, J., Melt Mixing as Method to Disperse Carbon Nanotubes into Thermoplastic Polymers. *Fullerenes, Nanotubes and Carbon Nanostructures* **2005,** *13* (sup1), 211-224.
49. Tripathi, S. N.; Rao, G. S. S.; Mathur, A. B.; Jasra, R., Polyolefin/graphene nanocomposites: a review. *Rsc Adv* **2017,** *7* (38), 23615-23632.
50. Tanahashi, M., Development of Fabrication Methods of Filler/Polymer Nanocomposites: With Focus on Simple Melt-Compounding-Based Approach without Surface Modification of Nanofillers. *Materials* **2010,** *3* (3), 1593-1619.
51. Dul, S.; Fambri, L.; Pegoretti, A., Fused deposition modelling with ABS-graphene nanocomposites. *Compos Part a-Appl S* **2016,** *85*, 181-191.
52. Faes, M.; Valkenaers, H.; Vogeler, F.; Vleugels, J.; Ferraris, E., Extrusion-based 3D Printing of Ceramic Components. *Procedia CIRP* **2015,** *28*, 76-81.
53. Wei, X.; Li, D.; Jiang, W.; Gu, Z.; Wang, X.; Zhang, Z.; Sun, Z., 3D Printable Graphene Composite. *Sci Rep* **2015,** *5*, 11181.
54. Wu, C. T.; Fan, W.; Zhou, Y. H.; Luo, Y. X.; Gelinsky, M.; Chang, J.; Xiao, Y., 3D-printing of highly uniform CaSiO3 ceramic scaffolds: preparation, characterization and in vivo osteogenesis. *J Mater Chem* **2012,** *22* (24), 12288-12295.
55. Qian, D.; Dickey, E. C.; Andrews, R.; Rantell, T., Load transfer and deformation mechanisms in carbon nanotube-polystyrene composites. *Appl Phys Lett* **2000,** *76* (20), 2868-2870.
56. Liao, J. Z.; Tan, M. J., Mixing of carbon nanotubes (CNTs) and aluminum powder for powder metallurgy use. *Powder Technol* **2011,** *208* (1), 42-48.
57. Xia, H. S.; Wang, Q.; Li, K. S.; Hu, G. H., Preparation of polypropylene/carbon nanotube composite powder with a solid-state mechanochemical pulverization process. *J Appl Polym Sci* **2004,** *93* (1), 378-386.
58. Font, J.; Muntasell, J.; Cesari, E., Poly(butylene terephthalate) poly(ethylene terephthalate) mixtures formed by ball milling. *Mater Res Bull* **1999,** *34* (1), 157-165.
59. Cavalieri, F.; Padella, F., Development of composite materials by mechanochemical treatment of post-consumer plastic waste. *Waste Manage* **2002,** *22* (8), 913-916.
60. Castles, F.; Isakov, D.; Lui, A.; Lei, Q.; Dancer, C. E.; Wang, Y.; Janurudin, J. M.; Speller, S. C.; Grovenor, C. R.; Grant, P. S., Microwave dielectric characterisation of 3D-printed BaTiO3/ABS polymer composites. *Sci Rep* **2016,** *6*, 22714.
61. Matsuzaki, R.; Ueda, M.; Namiki, M.; Jeong, T. K.; Asahara, H.; Horiguchi, K.; Nakamura, T.; Todoroki, A.; Hirano, Y., Three-dimensional printing of continuous-fiber composites by in-nozzle impregnation. *Sci Rep* **2016,** *6*, 23058.

62. Zhang, D.; Chi, B. H.; Li, B. W.; Gao, Z. W.; Du, Y.; Guo, J. B.; Wei, J., Fabrication of highly conductive graphene flexible circuits by 3D printing. *Synthetic Met* **2016,** *217*, 79-86.
63. Okwuosa, T. C.; Pereira, B. C.; Arafat, B.; Cieszynska, M.; Isreb, A.; Alhnan, M. A., Fabricating a Shell-Core Delayed Release Tablet Using Dual FDM 3D Printing for Patient-Centred Therapy. *Pharm Res* **2017,** *34* (2), 427-437.
64. Ning, F.; Cong, W.; Qiu, J.; Wei, J.; Wang, S., Additive manufacturing of carbon fiber reinforced thermoplastic composites using fused deposition modeling. *Composites Part B: Engineering* **2015,** *80*, 369-378.
65. Isakov, D. V.; Lei, Q.; Castles, F.; Stevens, C. J.; Grovenor, C. R. M.; Grant, P. S., 3D printed anisotropic dielectric composite with meta-material features. *Mater Design* **2016,** *93*, 423-430.
66. Tian, X. Y.; Liu, T. F.; Yang, C. C.; Wang, Q. R.; Li, D. C., Interface and performance of 3D printed continuous carbon fiber reinforced PLA composites. *Compos Part a-Appl S* **2016,** *88*, 198-205.
67. Hergel, J.; Lefebvre, S., Clean color: Improving multi-filament 3D prints. *Computer Graphics Forum* **2014,** *33* (2), 469-478.
68. Mirzaee, M.; Noghanian, S.; Wiest, L.; Chang, I., Developing Flexible 3D Printed Antenna Using Conductive ABS Materials. *2015 Ieee International Symposium on Antennas and Propagation & Usnc/Ursi National Radio Science Meeting* **2015**, 1308-1309.
69. Hollister, S. J., Porous scaffold design for tissue engineering (vol 4, pg 518, 2005). *Nat Mater* **2006,** *5* (7), 590-590.
70. Khalil, S.; Nam, J.; Sun, W., Multi-nozzle deposition for construction of 3D biopolymer tissue scaffolds. *Rapid Prototyping J* **2005,** *11* (1), 9-17.
71. Czyzewski, J.; Burzynski, P.; Gawel, K.; Meisner, J., Rapid prototyping of electrically conductive components using 3D printing technology. *J Mater Process Tech* **2009,** *209* (12-13), 5281-5285.
72. Huang, C.; Jian, G. Q.; DeLisio, J. B.; Wang, H. Y.; Zachariah, M. R., Electrospray Deposition of Energetic Polymer Nanocomposites with High Mass Particle Loadings: A Prelude to 3D Printing of Rocket Motors. *Adv Eng Mater* **2015,** *17* (1), 95-101.
73. Leigh, S. J.; Purssell, C. P.; Billson, D. R.; Hutchins, D. A., Using a magnetite/thermoplastic composite in 3D printing of direct replacements for commercially available flow sensors. *Smart Mater Struct* **2014,** *23* (9).
74. Li, N. Y.; Li, Y. G.; Liu, S. T., Rapid prototyping of continuous carbon fiber reinforced polylactic acid composites by 3D printing. *J Mater Process Tech* **2016,** *238*, 218-225.
75. Matsuzaki, R.; Ueda, M.; Namiki, M.; Jeong, T. K.; Asahara, H.; Horiguchi, K.; Nakamura, T.; Todoroki, A.; Hirano, Y., Three-dimensional printing of continuous-fiber composites by in-nozzle impregnation. *Sci Rep-Uk* **2016,** *6*.
76. Gray, R. W.; Baird, D. G.; Helge Bøhn, J., Effects of processing conditions on short TLCP fiber reinforced FDM parts. *Rapid Prototyping J* **1998,** *4* (1), 14-25.
77. Zhong, W. H.; Li, F.; Zhang, Z. G.; Song, L. L.; Li, Z. M., Short fiber reinforced composites for fused deposition modeling. *Mat Sci Eng a-Struct* **2001,** *301* (2), 125-130.
78. Singh, R.; Singh, S., Development of Nylon Based FDM Filament for Rapid Tooling Application. *Journal of The Institution of Engineers (India): Series C* **2014,** *95* (2), 103-108.
79. Le Duigou, A.; Castro, M.; Bevan, R.; Martin, N., 3D printing of wood fibre biocomposites: From mechanical to actuation functionality. *Mater Design* **2016,** *96*, 106-114.

80. Tekinalp, H. L.; Kunc, V.; Velez-Garcia, G. M.; Duty, C. E.; Love, L. J.; Naskar, A. K.; Blue, C. A.; Ozcan, S., Highly oriented carbon fiber-polymer composites via additive manufacturing. *Compos Sci Technol* **2014,** *105*, 144-150.
81. M. L. Shofner, K. L., 2 F. J. Rodrı´guez-Macı´as,3 E. V. Barrera1, Nanofiber-Reinforced Polymers Prepared by FDM.pdf. *Applied Polymer Science* **2002,** *Vol. 89,* (2003), 3081–3090
82. Compton, B. G.; Lewis, J. A., 3D-Printing of Lightweight Cellular Composites. *Adv Mater* **2014,** *26* (34), 5930-+.
83. Torrado Perez, A. R.; Roberson, D. A.; Wicker, R. B., Fracture Surface Analysis of 3D-Printed Tensile Specimens of Novel ABS-Based Materials. *Journal of Failure Analysis and Prevention* **2014,** *14* (3), 343-353.
84. Nikzad, M.; Masood, S. H.; Sbarski, I., Thermo-mechanical properties of a highly filled polymeric composites for Fused Deposition Modeling. *Mater Design* **2011,** *32* (6), 3448-3456.
85. Jia, Y. C.; He, H.; Geng, Y.; Huang, B.; Peng, X. D., High through-plane thermal conductivity of polymer based product with vertical alignment of graphite flakes achieved via 3D printing. *Compos Sci Technol* **2017,** *145*, 55-61.
86. Leigh, S. J.; Bradley, R. J.; Purssell, C. P.; Billson, D. R.; Hutchins, D. A., A Simple, Low-Cost Conductive Composite Material for 3D Printing of Electronic Sensors. *Plos One* **2012,** *7* (11).
87. Dorigato, A.; Moretti, V.; Dul, S.; Unterberger, S. H.; Pegoretti, A., Electrically conductive nanocomposites for fused deposition modelling. *Synthetic Met* **2017,** *226*, 7-14.
88. Moulart, A.; Marrett, C.; Colton, J., Polymeric composites for use in electronic and microwave devices. *Polym Eng Sci* **2004,** *44* (3), 588-597.
89. Kim, K.; Zhu, W.; Qu, X.; Aaronson, C.; McCall, W. R.; Chen, S. C.; Sirbuly, D. J., 3D Optical Printing of Piezoelectric Nanoparticle - Polymer Composite Materials. *Acs Nano* **2014,** *8* (10), 9799-9806.
90. McNulty, T. F.; Mohammadi, F.; Bandyopadhyay, A.; Shanefield, D. J.; Danforth, S. C.; Safari, A., Development of a binder formulation for fused deposition of ceramics. *Rapid Prototyping J* **1998,** *4* (4), 144-150.
91. Fielding, G. A.; Bandyopadhyay, A.; Bose, S., Effects of silica and zinc oxide doping on mechanical and biological properties of 3D printed tricalcium phosphate tissue engineering scaffolds. *Dent Mater* **2012,** *28* (2), 113-122.
92. Haq, R. H. A.; Wahab, M. S.; Wahid, M. U., Fused Deposition Modeling of PCL/HA/MMT Biocompatible Polymer Nano-composites. *Adv Struct Mat* **2016,** *61*, 23-32.
93. Singh, R.; Singh, S.; Fraternali, F., Development of in-house composite wire based feed stock filaments of fused deposition modelling for wear-resistant materials and structures. *Compos Part B-Eng* **2016,** *98*, 244-249.
94. Garg, H. K.; Singh, R., Comparison of wear behavior of ABS and Nylon6-Fe powder composite parts prepared with fused deposition modelling. *J Cent South Univ* **2015,** *22* (10), 3705-3711.

CHAPTER 3

EXPERIMENTAL

3.1: Materials

Commercially available Poly (lactic acid) (PLA) and Polyethylene terephthalate glycol-modified (PETG) filaments with the diameter of 1.75mm (Builder 3D, B.V.), PLA pellets (3D850, Filabot), PETG pellets (FTG PETG+, Filabot) (Advanced Composite Materials, LLC) were utilized to fabricate polymer blends and composites. To differentiate between two PLA materials, PLA obtained as filament is designated as PLA-1 and PLA obtained as pellets is named as PLA-2. The same nomination is applied to PETG materials, PETG-1 for filaments and PETG-2 for pellets.

Chloroform (VWR International LLC.) is the solvent which was utilized to dissolve PLA and PETG for making polymer blends. Benzene (EM Science) was also used to selectively extract PLA-1 from PLA/PETG blend to determine the morphology of PETG-1 inclusions within PLA-1 matrix.

3.2: Samples Fabrication

3.2.1: Preparation of polymer blend

Polymer blend

PLA/PETG blend filaments were prepared with the following composition: 80wt%PLA-1 and 20wt%PETG-1. The purchased PLA-1 and PETG-1 filaments were

mechanically pelletized into small pieces. Dry mixing of PLA-1 and PETG-1 pellets was achieved by shaking the pellet mixture on a mechanical shaker (Lab-Line Instruments, Inc.). Then the pellets mixture was melt pelletized using Melt Flow Index (MFI) Tester (XNR-400 Melt Flow Indexer, RUIHUI Electronic Co.) two times to obtain a better dispersion of PETG-1 in PLA-1 matrix. Polymer blend pellets with proper sizes for extrusion were obtained by setting MFI tester at 215°C with a 1s cutting interval and 2.15Kg load.

3.3.2: Filament extrusion

Filament extruder (Noztek pro HT, Noztek.) was utilized to extrude filament with a diameter around 1.75mm. Extrusion temperature for PLA pellets, blends and composites were set to be 215ºC based on the physical properties characterizations of the material. A filament winder equipped with a laser sensor was used to collect the extruded filaments. **Figures 3.1** and **3.2** show the extruder and winder, respectively. The operation procedures of filaments extrusion are illustrated below:

- Press the ON/OFF button first;
- Turn on the heating band by rotating the heater switch;
- Set the extrusion temperature on the manual screen;
- Pour the pellets in the hopper and wait 15min for the whole screw chamber to heat up.

- Turn on the switches of motor screw and fan. As soon as the filament comes out of the nozzle, use a tweezer to hold it. Lead the filament passing through the guiding hole and the laser sensor;
- Fix the filament on the spool using a piece of tape;
- Turn on the winder and rotate the speed adjusting knob to tune the rolling speed in order to obtain a proper diameter.

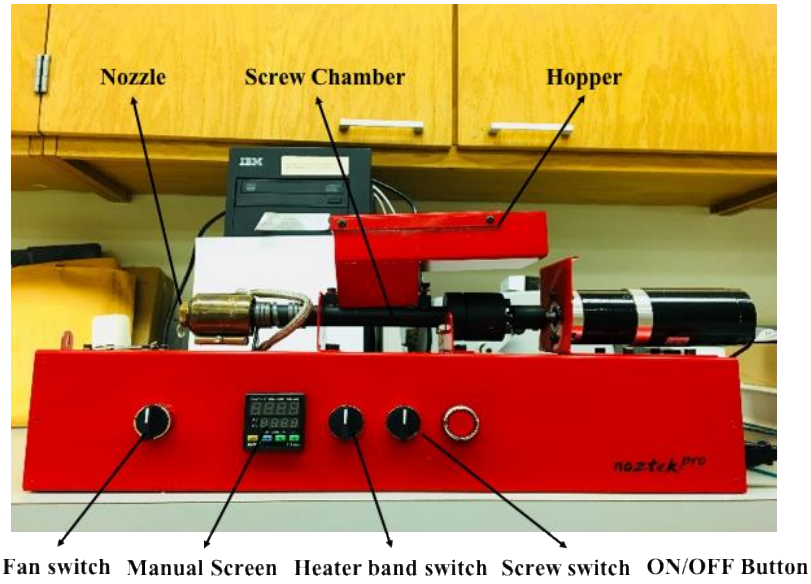

Figure 3.1: Photograph of filament extruder.

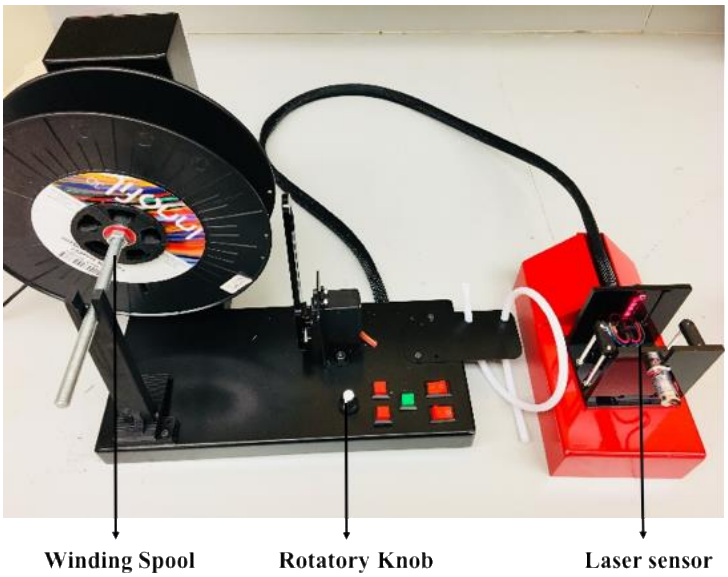

Figure 3.2: Filament winder equipped with a laser sensor.

To control the diameter of filaments more precisely, a diameter control system was designed and fabricated. **Figure 3.3** and **3.4** present the design of the diameter control system and printed objects equipped with a digital dimension indicator (Mitutoyo), which served for an in-situ diameter measurement. Two pairs of cylindrical bars are built to support the passing through filament. Another support cylinder which is located at the center of the system is the place where the diameter of the filaments can be measured. A groove was created on the surface of this cylinder to fix the position of the filaments when they pass through, making sure the digital indication measures the diameter. The readings on the digital indication screen is a relative value due to the existence of the groove. The friction between filaments and cylinders should be avoided since it would cause variation in the filaments' diameter. Thus, the surface of all these support cylinders are covered with PTFE thread seal tape. **Figure 3.5** shows a representative extruded PLA filament coil.

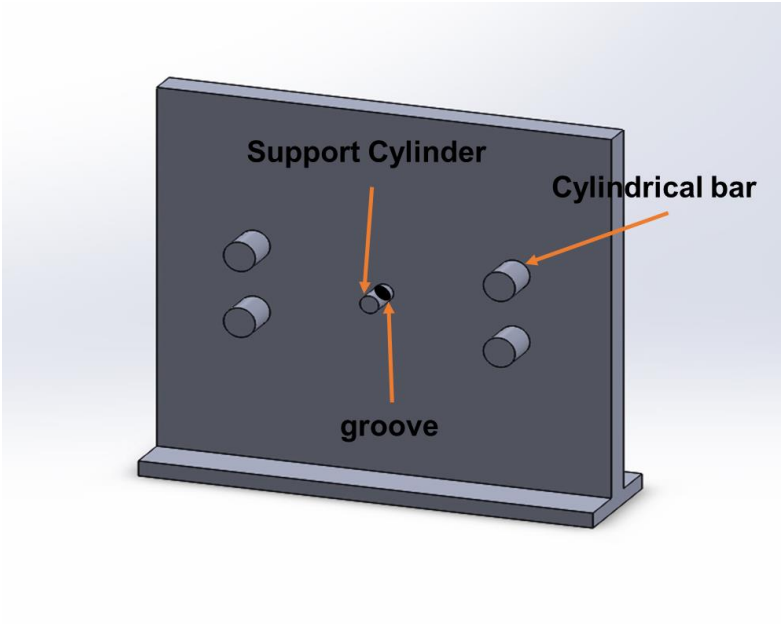

Figure 3.3: Schematic of designed diameter control system.

Figure 3.4: Filament diameter control system equipped with a digital indicator.

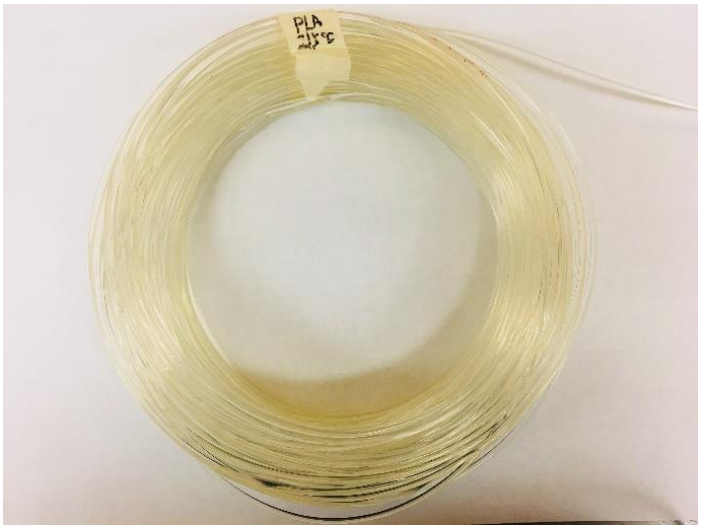

Figure 3.5: Extruded PLA filament sample.

3.3.3: 3D printing

The dual-feed 3D printer (3D printer B.V.) equipped with a 0.4mm diameter nozzle is utilized to print samples for mechanical and physical properties characterization. **Figure 3.6** shows the photograph of the printer. The printing temperature for PLA-1 and PETG-1 filaments was set to be the same as the extrusion temperature. Samples were designed in Solidworks, sliced in Slic3R and exported as g.code files. The printing parameters were pre-settled in Slic3R. Samples were designated to be printed with a layer height of 0.1mm, 100% infill density and rectilinear infill pattern. The traveling and infill speed of the nozzle are 120mm/s and 80mm/s, respectively. When the printing started, the filaments are fed through a torque pinch system to the heater band where filaments are melted pushed

through the nozzle. The nozzle head travels in the x-y plane, while platform moved downwards along the z-axis to build up 3D structures layer-by-layer.

Figure 3.6: Photograph of 3D printer.

The dual-Feed 3D printer is capable of diversifying different materials and colors while printing with only one nozzle. This unique system eliminates disadvantages of working with two nozzles. Bi-component structures were printed by feeding two filaments simultaneously. **Figure 3.7** shows the schematic illustration of the dual-feed mechanism. Bi-component structures of different compositions are obtained by tuning the feeding ratio between two filaments. A typical bi-component samples printed at 90° is shown in **Figure 3.8**. The roughness of the printed samples is estimated as the ratio between connected length and the hanging length of each layer. The average connect length is about 675±14μm

and the average unconnected length is about 36.4±3.4μm. The untouched area is only about 5%, which makes the influence of the hanging area on the mechanical properties can be neglected.

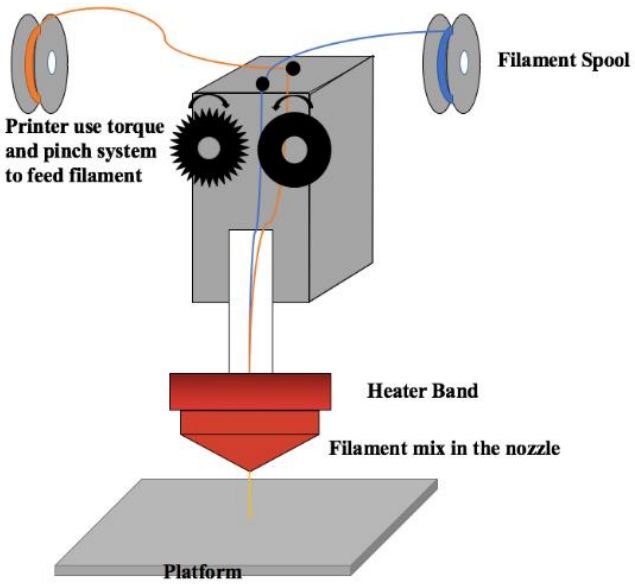

Figure 3.7: Schematic representation of dual-feed mechanism.

Figure 3.8: Morphology of samples printed at 90°.

3.3: Properties Characterization

3.3.1: Thermal Analysis

Thermogravimetric analysis (TGA)

TGA measures the weight loss of a material as a function of temperature or time under a controlled environment[1]. It is primarily used to determine the composition of the materials and to predict their thermal stability. In this work, TGA measurements were mainly used to determine the solvent presence within materials and the degradation temperatures (Td) of materials. A platinum pan was washed with methanol first and then heated to high temperature to get rid of the impurities. TGA (TGA, 2950 TA instruments) is loaded with an empty pan first. Then the furnace is closed and the weight is set to zero. The empty pan is then unloaded and re-loaded with materials. After a nitrogen purge with a flow rate of 40ml/min was run for 10min, TGA instrument was started using a heating rate of 20°C/min. The temperature range for testing PLA materials was from room temperature(25°C) to 400°C, whereas for PETG materials was up to 600°C.

Differential scanning calorimetry (DSC)

DSC determines the difference of heat flow between samples and an inert references as a function of time or temperature[2]. It can detect the main transitions of materials, such as glass transition temperature, crystallization temperature and melting temperature. In this work, DSC analysis was carried out to determine Tg, Tm and percent of crystallinity within the materials. A specimen was cut into small pieces weighting

around 3mg and then sealed in the aluminum pans. DSC (DSC, Model 2920 TA instruments) was equilibrated at 0°C first and then heated at a rate of 20°C/min under a stream of nitrogen. Temperature range for measuring PLA was 0°C-200°C, while for PETG materials was 0°C -250°C. Percentage of crystallinity was calculated by the equation shown below[3]:

$$\%\text{crystallinity} = (\Delta H_m + \Delta H_c)/\Delta H_{om} \qquad (\mathbf{3\text{-}1})$$

where, ΔH_m is the negative heat flow of the melting; ΔH_c is the positive heat flow of the crystallization; ΔH_{om} is the heat flow when melting the polymer with 100% crystallinity. For PLA materials, ΔH_{om}=93J/g[4].

3.3.2: Characterization of mechanical properties

Tensile test

Tensile tests can provide ultimate tensile stress (UTS) and strain directly by applying a tension on the samples until break. Young's modulus which describes the elastic properties of the materials can be derived from the equation[5]:

$$E = \frac{\sigma(\varepsilon)}{\varepsilon} = \frac{F/A}{\Delta L/L0} = \frac{FL0}{A\Delta L} \qquad (\mathbf{3\text{-}2})$$

where, E is the Young's modulus; σ(ε) is the tensile stress and it equals to the force exerted on samples divided by the area of cross-section perpendicular to the force; ε is

the tensile strain and it equals to the change of length (positive for elongation and negative for compression) divided by the original length of the samples.

The dog-bone samples utilized for the tensile tests were designed in Solidworks based on ASTM D638. **Figure 3.8** and **Figure 3.9** show the photograph of designed and printed dog-bone samples. The basic dimensions of dog-bone samples are shown in **Figure 3.8** as well. Tensile tests were conducted on Intron testing instrument (Model 1125). The measurements were performed under controlled environments (20°C, 65% RH). All the measurements were carried out at the strain rate of 10mm/min with a static load cell of 100kN. Three parallel samples were tested.

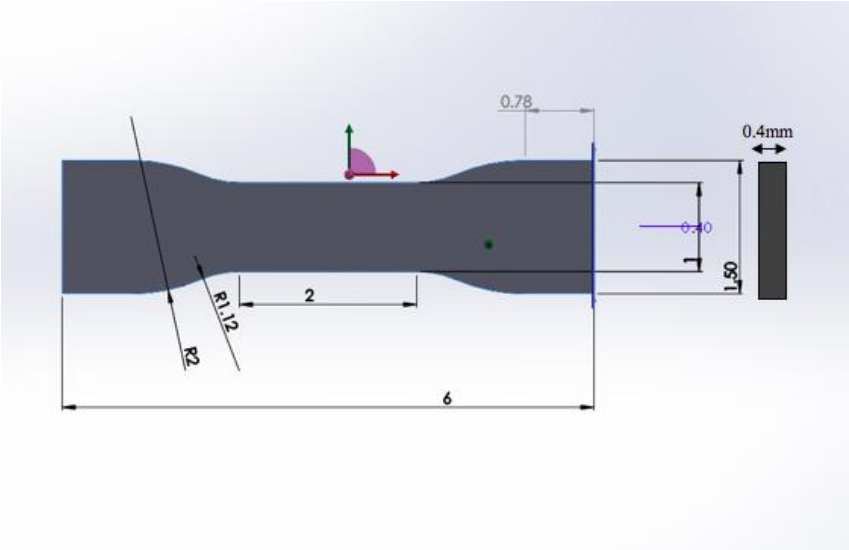

Figure 3.9: Schematic illustration of dog-bone sample.

Figure 3.10: Dog-bone samples printed from PLA filament.

Tensile tests were also performed on filaments based on ASTM D2256 method. The gauge length of filaments were set to be 10cm and the strain rate was designated as10mm/min. Four parallel samples were tested.

Dynamic mechanical analysis (DMA)

DMA measurements were used to characterize the dynamic mechanical properties of the printed samples. The samples for DMA measurements were designed in Solidworks. **Figures 3.10** and **3.11** show the designed structure and printed samples, respectively. The thickness of the samples was designed to be 0.65mm. At this thickness, the printed samples are only one layer thick. The bottom materials serve as support platform during the printing and would be removed before each measurement. After the printing, samples are cut into

a rectangular shape with a width around 0.5mm. The dimensions of the rectangular samples were measured by a digital caliper before each measurement.

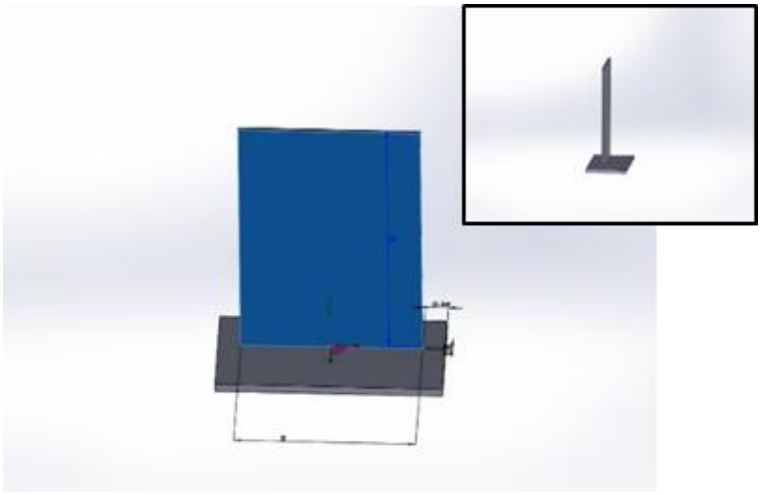

Figure 3.11: The structure of DMA samples.

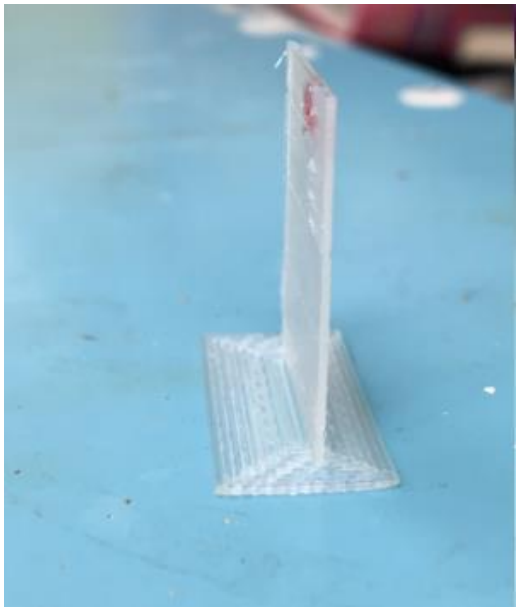

Figure 3.12: Printed PLA-1 sample for DMA measurements.

DMA measurements were performed on a DMA instrument (model Q800, TA Instruments Inc, New Castle, DE, USA) in the multi-frequency-strain mode. Samples were first cooled down to 0°C and then heated up to 100°C with a heating rate of 2°C/min. A preload of 0.001N was applied on the samples to keep them straight during the measurements. The strain oscillated at a single frequency of 5Hz and the peak amplitude was 5 μm.

3.3.3: Rheology characterization

Viscosity measurements

The viscosity of polymers was determined on ARES rheometer (TA Instruments.) equipped with a parallel-plate fixture of 25 mm diameter. All the measurements were conducted at static mode with the assistance of Dr. Ozgun from the Chemical Engineering Department, Clemson University. Temperature ramp experiments were performed in the temperature range of 210°C -250°C at the constant shear rate of $3s^{-1}$. The heating rate was set to be 2°C/min. For shear rate ramp experiments which operated at the constant temperatures, shear rate range was chosen from $0.1s^{-1}$ to $30s^{-1}$.

The shear rate of our printer can be modified by changing the moving speed of the nozzle head. We calculated the shear rate of PLA-1 polymer at different nozzle moving speed when printed at 215°C based on the equation shown below[6]:

$$\emptyset = \frac{4Q}{\pi R3} \qquad (\mathbf{3\text{-}3})$$

where, ∅ is the apparent shear rate, Q is the experimentally measured volumetric flow rate; R is the radius of the nozzle tip which is 0.23mm. We started printing the objects at different nozzle infill speed and moved the platform away to make sure the material can flow freely downward. The length of the filament coming out of nozzle was measured for every 20s. The dependence of shear rate on the nozzle head speed are summarized in the **Table 3.1** below:

Table 3.1: Dependence of shear rate on the nozzle moving speed

Nozzle head moving speed (mm/s)	Volumetric flow rate (mm/s)	Shear rate (s^{-1})
50	8.3±0.2	144.3±3.5
80	8.7±0.4	151.3±7.0
100	18.7±0.3	318.3±5.2
150	28.4±0.8	493.9±13.9

In order to get rid of the air bubbles trapped between the two parallel plates during the measurements, film-like samples were prepared by compression molding. Compression was conducted at the temperature higher than Tm of PLA materials and Tg of PETG materials, along with a pressure load of 10MPa.

Melt Flow Index

Melt Flow Index tester (XNR-400 Melt Flow Indexer, RUIHUI Electronic Co.) was also used to investigate rheological behaviors of the materials. The test method is based on ASTM D1238 and modified according to our preference. MFI measurements were performed at the temperature of 215°C with a load of 1.2kg. The cutting interval was set to be 30s. After the temperature reaches the designated value and remain constant, materials are added to the chamber. Before starting each measurement, we waited 10min for the materials to heat up and release air trapped inside.

3.3.4: Morphology observation

Dip-coating

Atomic force microscopy (AFM) was used to determine the miscibility level between PLA and PETG by observing the mixture of these two materials dip-coated on the silicon wafers from their joint solutions. PLA-1 and PETG-1 were dissolved in chloroform separately and then mixed together. The mixture was shook on the mechanical shaker for 2hrs to obtain an even dispersion. Solution mixture was then dip-coated on the silicon wafers using a dip coater (Mayer Fientechnik D-3400) with a 300mm/min withdrawal rate. Silicon wafers were first washed in DI water three times in the test tubes. Then the test tubes were put in an ultrasonic bath for 90min at 70°C. Wafers were then put into a hot "piranha" solution (3:1 concentrated sulfuric acid/ 30% hydrogen peroxide) for 2hrs. After

rinsing several times, silicon wafers were dried under a stream of dry nitrogen. After dip-coating, blend films were dried in a petri dish at room temperature.

Atomic force microscope

The morphology of dip-coated polymer blend film was observed with Dimension 3100 (Veeco Digital Instrument, Inc). AFM using tapping mode. Silicon tips with a spring constant of $50Nm^{-1}$ were used at 1Hz. AFM images were performed using software of Nanoscope version 5.31 R1.

3.3.5 Fourier-transform infrared spectroscopy Analysis

Fourier-transform infrared spectroscopy (FTIR) - Attenuated total reflection (ATR) analysis was used to identify the functional groups within materials according to the absorption or emission bands of an infrared spectrum[7]. Each functional group has a specific vibration, stretching or bending frequency, which corresponds to a particular absorption or transmission peak in infrared spectrum. A Thermo Nicolet 6700 Fourier-transform infrared spectroscopy (FTIR) spectrometer (Nicolet™ Continuum™ Infrared Microscope, Thermo Scientific TM) equipped with a transmission base plate and a "Continuum" microscope is used for the analysis of PLA/PETG blend film. Before each data collection, ATR crystal was cleaned with methanol.

3.3.6: Heat Treatment

Heat treatment (annealing) was performed in the oven (VMR international LLC) under the vacuum to prevent oxidation.

3.4: References

1. A. W. COATS, J. P. R., THERMOGRAVIMETRIC ANALYSIS_A review.pdf. *Analyst 88*.
2. Gabbott, P., *Principles and applications of thermal analysis*. Blackwell Pub.: Oxford ; Ames, Iowa, 2008; p xviii, 464 p.
3. W.J. Sichina, I. M. M., DSC as Problem Solving Tool Measurement od percent of cryatsllinity of thermoplastics.pdf.
4. Xu, R.; Xie, J.; Lei, C., Influence of melt-draw ratio on the crystalline behaviour of a polylactic acid cast film with a chi structure. *Rsc Adv* **2017,** *7* (63), 39914-39921.
5. Truesdell, C., Outline of the History of Flexible or Elastic Bodies to 1788. *J Acoust Soc Am* **1960,** *32* (12), 1647-1656.
6. Fried, J. R., *Polymer science and technology*. Third edition. ed.; Prentice Hall: Upper Saddle River, NJ, 2014; p xxiii, 663 pages.
7. Griffiths, P. R., Fourier-Transform Infrared Spectrometry. *Science* **1983,** *222* (4621), 297-302.

CHAPTER 4

FORMATION AND PROPERTIES OF PLA PRINTED OBJECTS

4.1: Introduction

This chapter is devoted to formation of PLA filaments by extrusion, identification of printing conditions for the PLA samples and characterization of the samples' physical properties. As outlined in **Chapter 3**, two types of commercially available PLA materials: PLA-1(obtained as filament) and PLA-2 (obtained as pellets) were used in the study. PLA extrusion and sample fabrication conditions were identified through the measurements of thermal properties and rheology. After the fabrication of samples, DMA and tensile tests were performed to determine their mechanical properties. The combination of DMA and tensile tests were used to obtain dynamic and static mechanical performances at different stress and strain levels. Annealing was conducted for the samples to investigate the effect of thermal treatment on the mechanical properties of the printed objects.

Comparison of the DMA results for samples printed at two different raster angles reveals anisotropy in physical properties of 3D printed objects. Physical properties were also compared between the samples printed from two different PLA materials (PLA-1 and PLA-2). It was found that physical performances of the PLA materials and samples printed from them are quite similar. Heat treatment is found to improve dynamic mechanical performances due to crystallization.

4.2: Results and Discussion

4.2.1: Processing conditions for PLA materials

Thermal Properties

Both extrusion and printing of PLA materials should be performed in a specific temperature range. First of all, extrusion temperature should be higher than the melting temperature of PLA pellets. Printing temperature also needs to be higher than Tm of PLA filament for the sake of forming a proper flow of the polymer melt. However, the formation of low viscosity liquid at higher temperatures should be avoided. At high temperatures it takes longer time for materials to solidify which would destroy the shape accuracy of both extruded filaments and printed objects.

TGA was conducted for PLA materials to determine an upper-temperature limit for processing, which in most cases is the degradation temperature of materials. DSC was utilized to identify transition temperatures for PLA materials, such as glass transition temperature, crystallization temperature, and melting temperature. All these transition temperatures are essential, since they provide a lower-temperature limit for processing PLA materials. Percent of crystallinity (%) was also calculated from DSC measurements based on **Equation 3-1** (**Chapter 3)**.

TGA thermograph of PLA-1 filament (**Figure 4.1(a))** indicates that the material begins to degrade at the temperature around 270°C. After 400°C, the polymer is fully decomposed. The weight percentage of material left is close to 0, manifesting that there are no extra additives in PLA-1. TGA thermograph of PLA-2 pellets (**Figure 4.1 (b))** shows

that degradation temperature range is 312°C-400°C. The temperature, where PLA-2 starts to decompose, is 40°C higher than that of PLA-1. This might be interpreted as the higher percentage of crystallinity within PLA-2 material or higher molecular weight of PLA pellets.

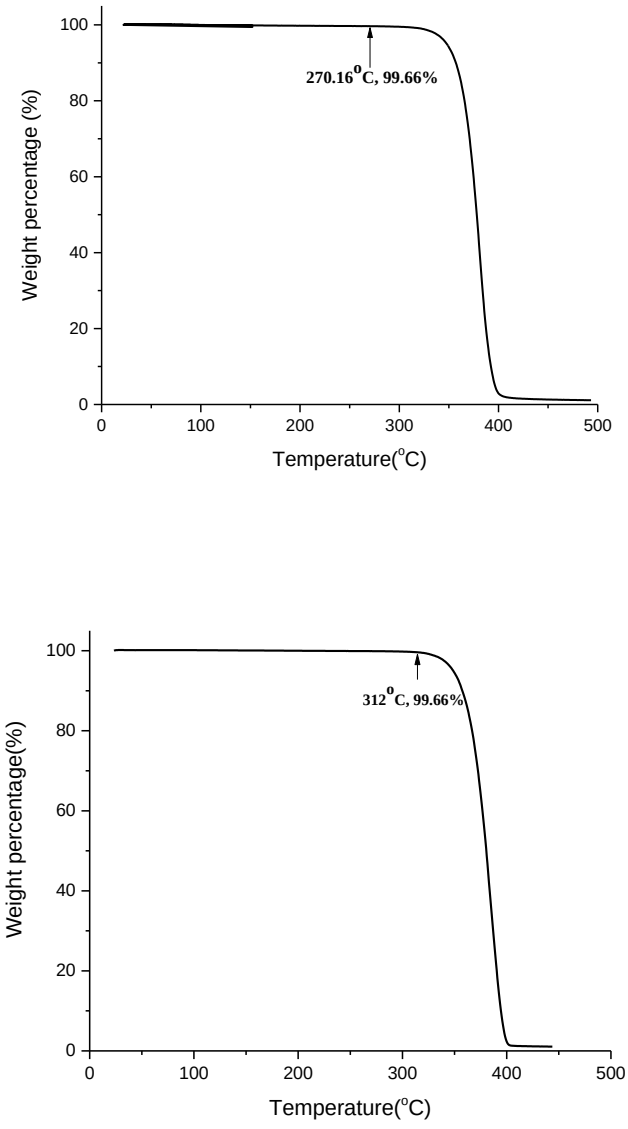

Figure 4.1: TGA thermograph. (a) PLA-1 filament. (b) PLA-2 pellets.

A glass transition temperature at ~60°C is observed on the DSC thermograph of PLA-1 filament (**Figure 4.2)**. Physical aging near Tg region is also observed[1]. Crystallization begins at about 90°C and reaches its maximum rate at 110°C. The relationship between the molecular weight of polymer and the melting temperature of the semi-crystalline polymer can be estimated from following equation[2]:

$$\frac{1}{T} - \frac{1}{Tm} = \left(\frac{R}{H}\right) * \left(\frac{\ln D}{\xi}\right) \qquad \textbf{(4-1)}$$

where, T is the observed melting point of polymer, while Tm is the melting point of polymer when it is 100% crystalline. R is the molar gas constant, H is the enthalpy of fusion for 100 % crystalline polymer, D is a correction parameter to simplify the equation, and ξ is the average length of crystallite in number of repeating units. This equation indicates that the melting point increases with the size of crystals. Therefore, the sharp melting peak in the DSC thermograph implies a narrow size distribution of crystals formed within the materials. Melting temperature of PLA-1 is around 145°C. Integration of crystallization and melting peaks gives 18.7J/g and 19.2J/g, respectively. According to **Equation 3-1** (**Chapter 3)**, the percentage of crystallinity within PLA-1 filament is about 0.5%. It can be suggested that practically no crystals are present within the filament prior any post-processing.

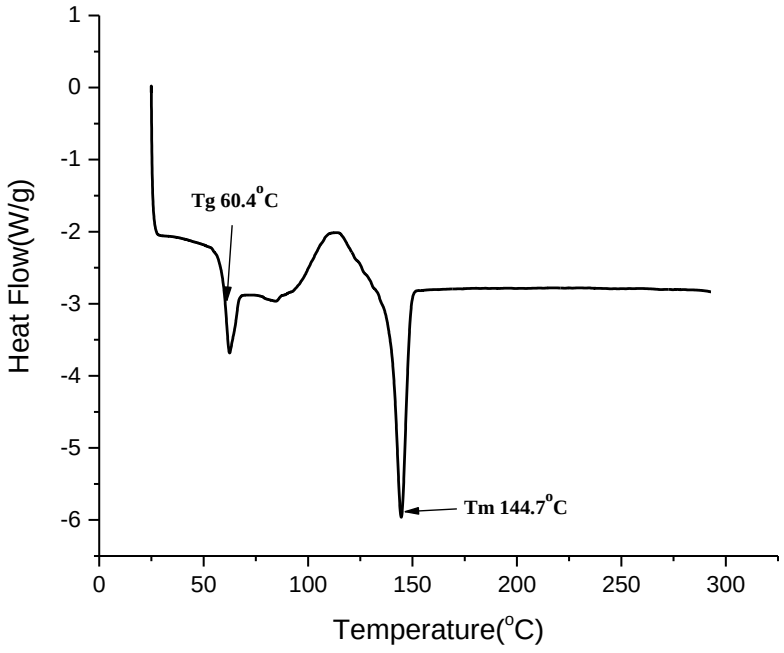

Figure 4.2: DSC thermograph of PLA-1 filament.

DSC thermograph of PLA-2 pellets (**Figure 4.3(a))** shows a glass transition at 74°C. No crystallization is found. Melting temperature of PLA-2 is 175°C. It is 30°C higher than the melting temperature of PLA-1 filament. According to TGA thermographs, there are no additives within the PLA-2 material, thus the melting temperature depression caused by impurities can be neglected. Higher Tg and Tm of PLA-2 can be a consequence of higher molecular weight of the polymer chains constituting PLA-2 materials. According to the theory of melting point depression[3]:

$$\frac{1}{\mathbf{T}f} - \frac{1}{\mathbf{T}fo} = \frac{R}{\Delta Hf}\frac{2Mo}{Mn} \qquad \textbf{(4-2)}$$

where, T_f is the melting (fusion) temperature, T_f^o is the melting point of polymers which are fully crystallized and it is about 488K for PLA[4], ΔH_f is the heat of fusion per mole of crystalline mers and is 146kJ/mol for PLA[5], Mo is the molecular weight of end mer, and Mn is the molecular weight of polymer. For both PLA materials, T_f^o, ΔH_f and Mo are the same. T_f for PLA-1 filament is 418K and for PLA-2 pellets is 448K. The calculated molecular weight ratio between two PLA materials is 1.9. Integration of melting curve gives heat of melting as 42.54J/g. Percent of crystallinity calculated from **Equation 3-1** (**Chapter 3**) is 45.8%.

DSC thermograph of filament that we extruded from PLA-2 pellets (**Figure 4.3 (b))** indicates a different thermal properties of the filament in comparison to pellets. Tg of the filament is 64°C, which is 10°C lower than that of the pellet. We associate the lower Tg with the absence of crystals in the PLA-2 filament. Therefore, polymer chains can move more freely without the constraint of crystallized parts. Melting temperature of PLA-2 crystals formed during DSC run in the filament is practically the same as in PLA-2 pellets. No change of Tm proves that there is no degradation of polymer chains during the processing. In fact, TGA thermograph of PLA-2 (**Figure 4.1(b)**) indicates that the pellets are perfectly dried. Without the presence of water, decomposition of PLA-2 during extrusion can be neglected. Area of crystallization region obtained by integration is larger than that of melting. At the end portion of crystallization curve, the slope of it decreases suddenly. Besides, there is no sharp boundary between crystallization and melting peaks. These unusual phenomena can be interpreted that the melting of crystals with smaller sizes already starts while the larger crystals are still forming.

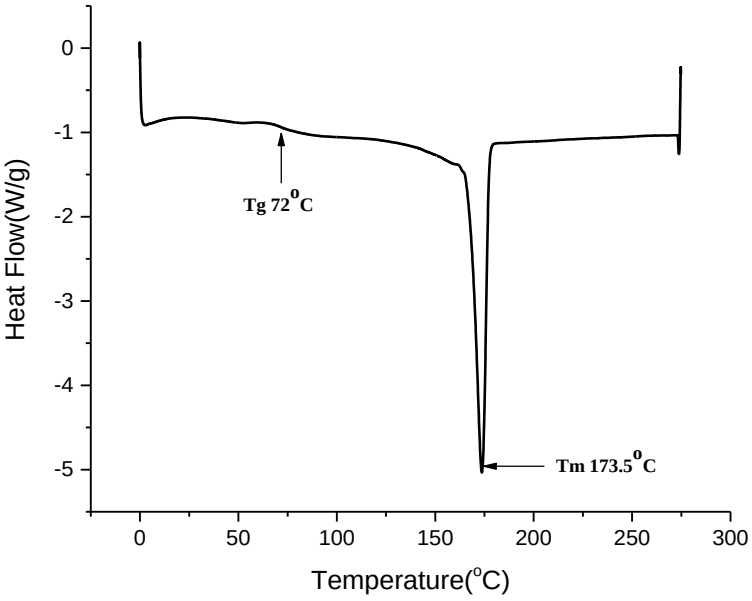

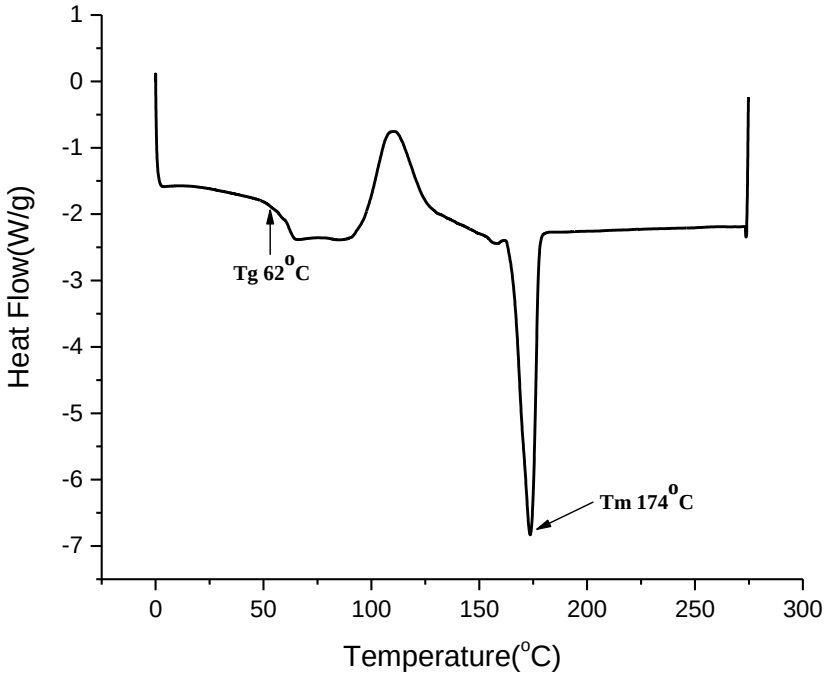

Figure 4.3: DSC thermographs. (a) PLA-2 pellets; (b) PLA-2 filament.

In conclusion, the temperature range where extrusion and printing can be conducted is 175°C-260°C, within which PLA materials are melted and there is no observed degradation. 260°C is the highest working temperature for the printer used in this work. However, this temperature range is too broad for practical processing and, therefore, additional characterization should be conducted to narrow the range down.

Rheological Behavior

We have determined the wide temperature range at which we can conduct extrusion and printing. However, a more specific processing temperature within the range also needs to be decided. This proper temperature can be found based on melt flow index and polymer melt viscosity measurements. Rheological behavior of the polymer melt is essential during the printing since it determines layers formation and bonding strength between the layers.

Viscosity measurements

Theoretically, the relationship between temperature and melt viscosity at T>Tg+100°C is described by the Arrhenius model[3]:

$$\eta = \eta r \exp[\frac{E}{R}(\frac{1}{T} - \frac{1}{Tr})] \qquad \textbf{(4-3)}$$

$$\text{or } \ln\eta = \ln\eta r + \frac{E}{R}(\frac{1}{T} - \frac{1}{Tr}) \qquad \textbf{(4-4)};$$

where, η is the viscosity at T; E is the activation energy; and η_r is the viscosity at a reference temperature Tr. Temperature dependence viscosity of PLA-1 materials (**Figure 4.4**) shows that the viscosity decreases with the rising of temperature. At the constant shear rate of $3s^{-1}$, viscosity declines from 61Pa.s at 215°C to 11Pa.s at 250°C. Linearly fitting natural logarithm of viscosity as a function of reciprocal temperature (**Figure 4.5),** a line with the formula of Y =-8.14+2640.2*X is obtained. The calculated activation energy for viscosity dependence on temperature of PLA-1 materials is about 22kJ. Therefore, temperature dependence for PLA-1 viscosity can be estimated as following:

$$\ln\eta = -8.14 + 2640.2 * \frac{1}{T} \qquad (4\text{-}5)$$

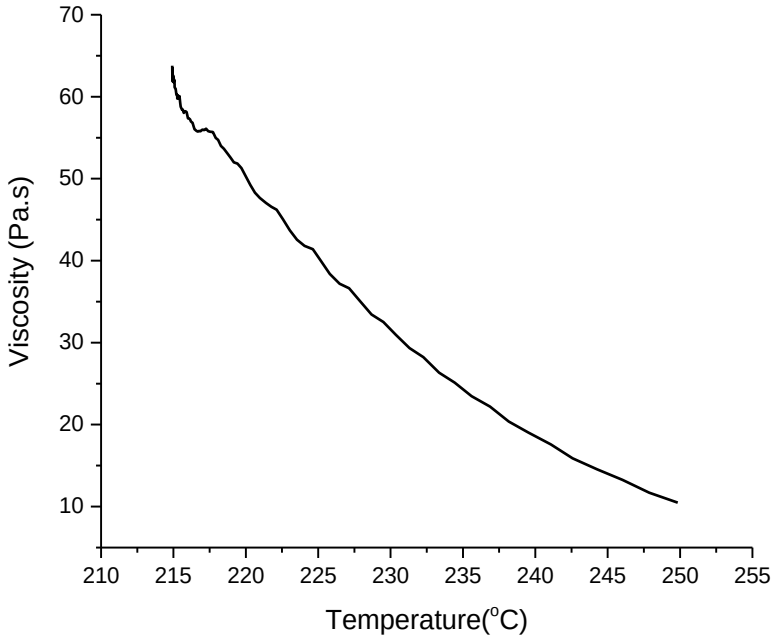

Figure 4.4: Temperature dependence for PLA-1 viscosity.

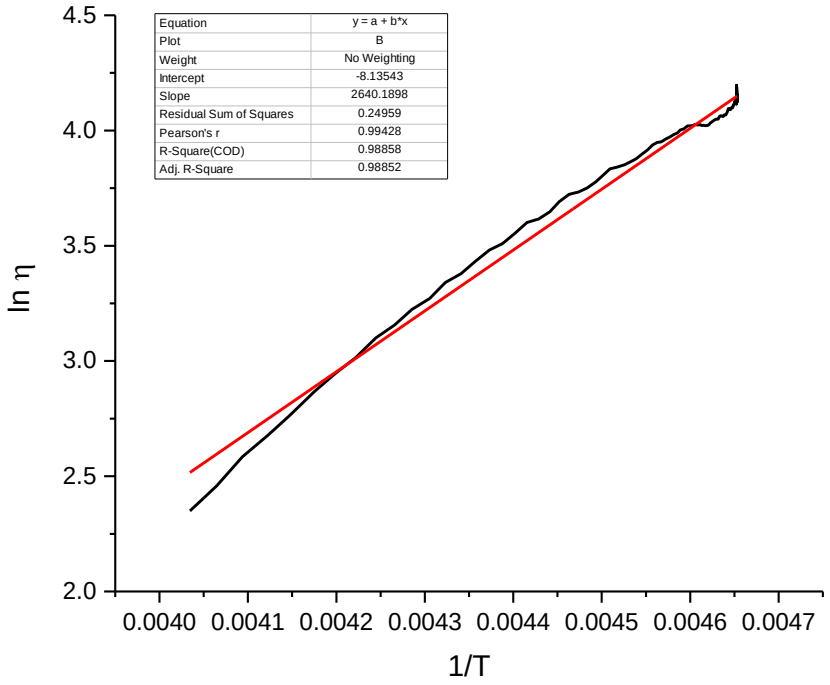

Figure 4.5: Linear fitting of lnη~1/T based on Arrhenius model.

Figure 4.6 and **Figure 4.8** show that the melt viscosity of PLA-1 material also declines with the increase of shear rate. At 215°C, the viscosity decreases from 195Pa.s at the shear rate of $0.1s^{-1}$ to 73Pa.s at the shear rate of $10s^{-1}$. At 250°C, the viscosity declines from 14.8Pa.s at the shear rate of 0.1 s^{-1} to 5.5 Pa.s at the shear rate of 10 s^{-1}. According to a well-known empirical viscosity-shear rate relationship-'power-law'[3]:

$$\eta = K_2 * \gamma^{n-1} \qquad (\mathbf{4\text{-}6})$$

$$\text{or } \log \eta = \log K_2 + (n-1) \log \gamma \qquad (\mathbf{4\text{-}7});$$

where, η is the viscosity; γ is the shear rate; n is the power-law index; and K_2 is called the 'consistency'. **Figure 4.7 and 4.9** present that linear fitting of relationship between the logarithm of viscosity and the logarithm of shear rate at the temperature of 215 ºC and 250 ºC, respectively. Both plots can be separated into three regions. The fitting lines of the three regions bring distinct effective values of K_2 and n. **Table 1** shows that the value of K_2 keeps increasing with the rising shear rate at temperature of 215ºC. While **Table 2** implies that the value of K_2 declines with the increasing shear rate at temperature of 250 ºC. Overall, the K_2 value at temperature of 215ºC is several times larger than that at 250ºC.

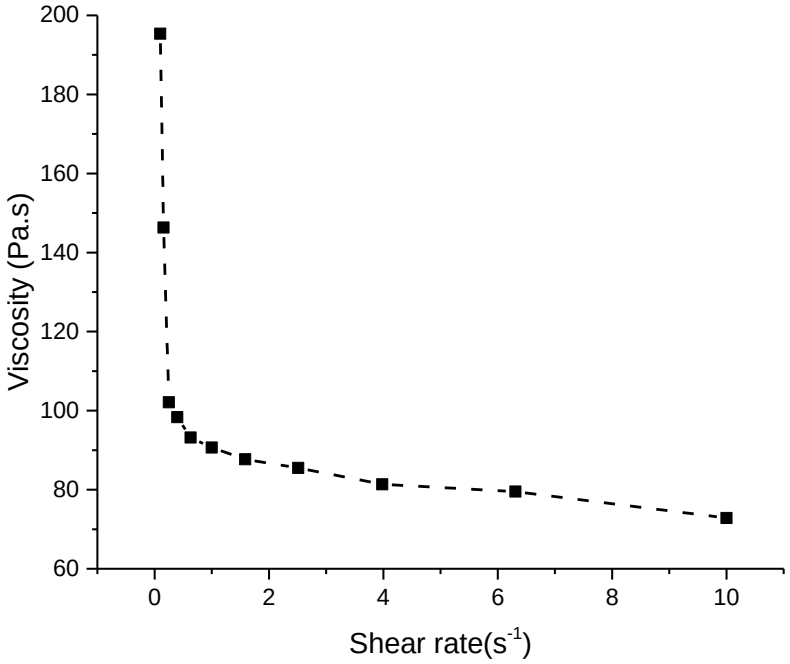

Figure 4.6: Shear rate dependence viscosity of PLA-1 at 215ºC.

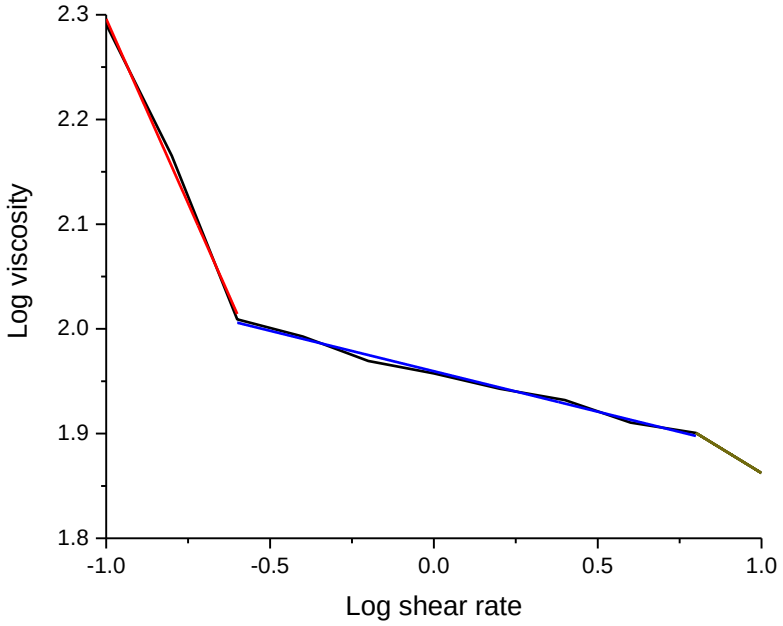

Figure 4.7: Linear fitting of Log viscosity ~ log shear rate for PLA-1 at 215ºC.

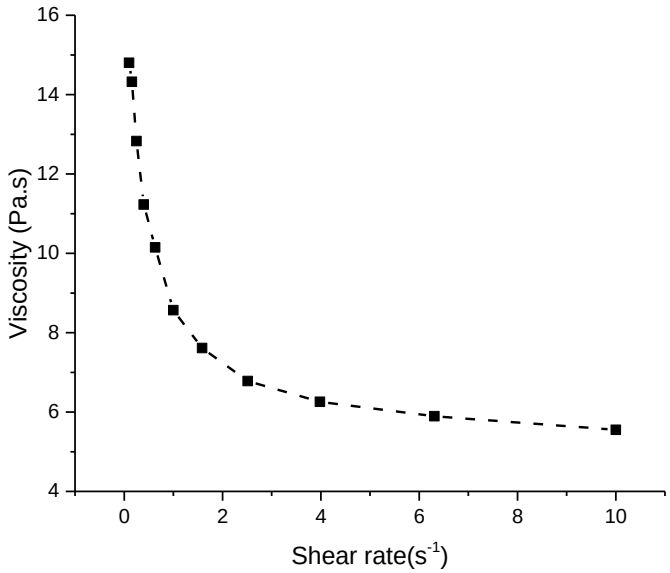

Figure 4.8: Shear rate dependence viscosity of PLA-1 at 250ºC.

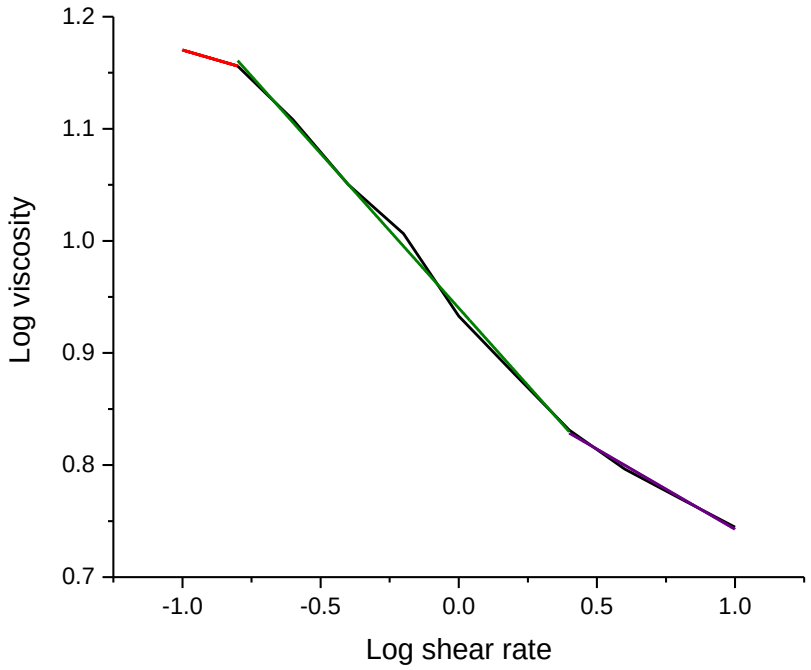

Figure 4.9: linear fitting of Log viscosity ~ log shear rate for PLA-1 at 250ºC.

Table 4.1: Fitting lines of shear rate dependence viscosity of PLA-1 materials at 215 ºC.

Shear rate regime(s^{-1})	Formula of fitting curve	Value of K_4	Value of n
0.1-0.45	Y=-0.70*x+1.60	39.05	0.50
0.45-6.44	Y=-0.08*x+1.96	91.11	0.94
6.44-10	Y=-0.19*x+2.05	113.15	0.81

Table 4.2: Fitting lines of shear rate dependence viscosity of PLA-1 materials at 250 ºC.

Shear rate regime(s^{-1})	Formula of fitting curve	Value of K_4	Value of n
0.1-0.16	Y=-0.07*x+1.10	14.56	0.95
0.16-4.5	Y=-0.48*X+0.94	8.71	0.74
4.5-10	Y=-0.14*x+0.89	7.69	0.86

The viscosity of PLA-2 materials (**Figure 4.10(a))** is several times higher than PLA-1. The viscosity of PLA-2 at constant shear rate of $3s^{-1}$ declines from 413Pa.s at the temperature of 215 ºC to 88Pa.s at the temperature of 250 ºC. Linear fitting of the natural logarithm viscosity as a function of reciprocal temperature is the red line in **Figure 4.10 (b)**. The function of the theoretical fitting line is Y = 1329*X+0.3. Based on Arrhenius model, the calculated activation energy is 11.05kJ/mol. It is about two times smaller than that of PLA-1. However, the slope of PLA-2 measured viscosity in the graph is much larger than the fitting line at high temperature regime. The viscosity of PLA-2 as a function of temperature can be estimated as:

$$\ln\eta = 1329*\frac{1}{T} +0.3 \qquad (\mathbf{4\text{-}8})$$

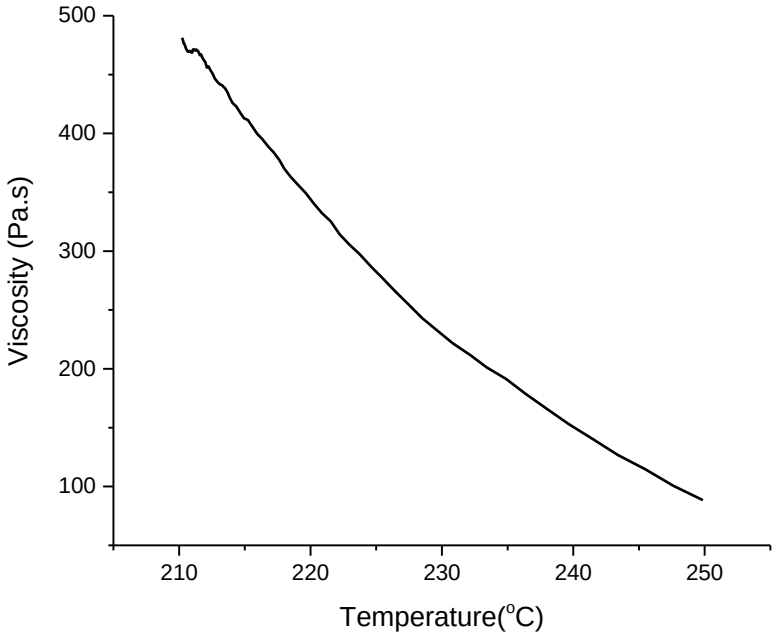

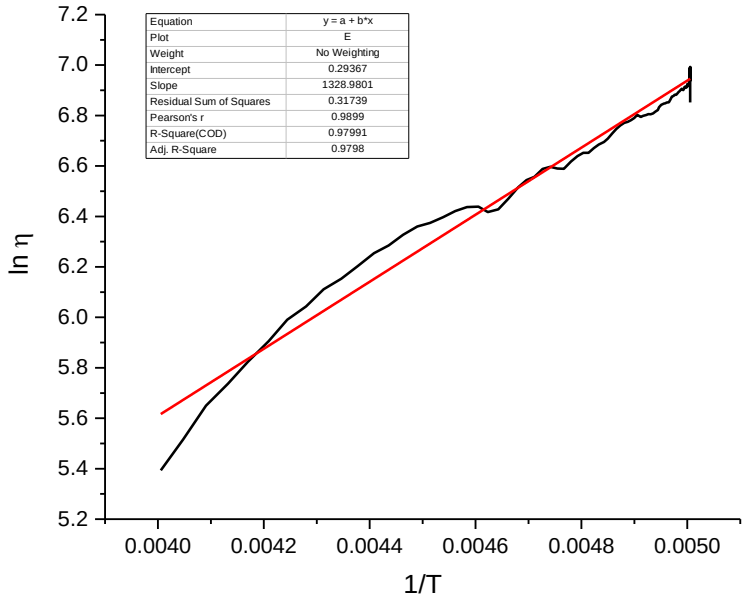

Figure 4.10: Rheological behavior of PLA-2. (a) Temperature dependence viscosity; (b) linear fitting based on Arrhenius model.

The results of shear rate ramp experiments (**Figure 4.11**) manifest that at 215 ºC, the viscosity of PLA-2 materials reduces from 145.35 Pa.s at the shear rate of $0.3s^{-1}$ to 83.5 Pa.s at the shear rate of $30s^{-1}$. Linear fitting lines of the log η~logγ curve (**Figure 4.12**) also can be divided into three regimes. **Table 3** shows that the value of K_2 decreases with the rising of shear rate. The K_2 of two PLA materials are at the same order of magnitude with the K_2 of PLA-2 materials being slightly higher.

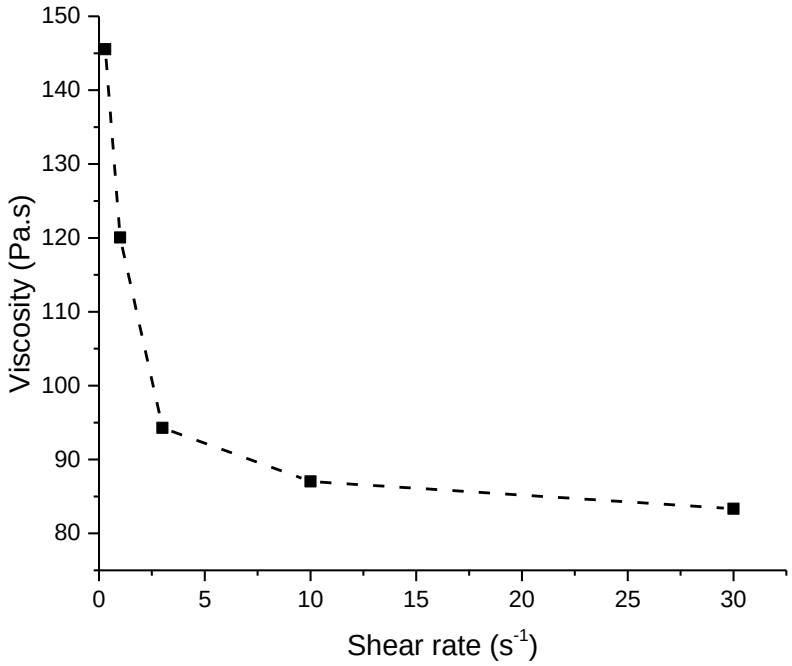

Figure 4.11: Shear rate dependence viscosity of PLA-2 at 215ºC.

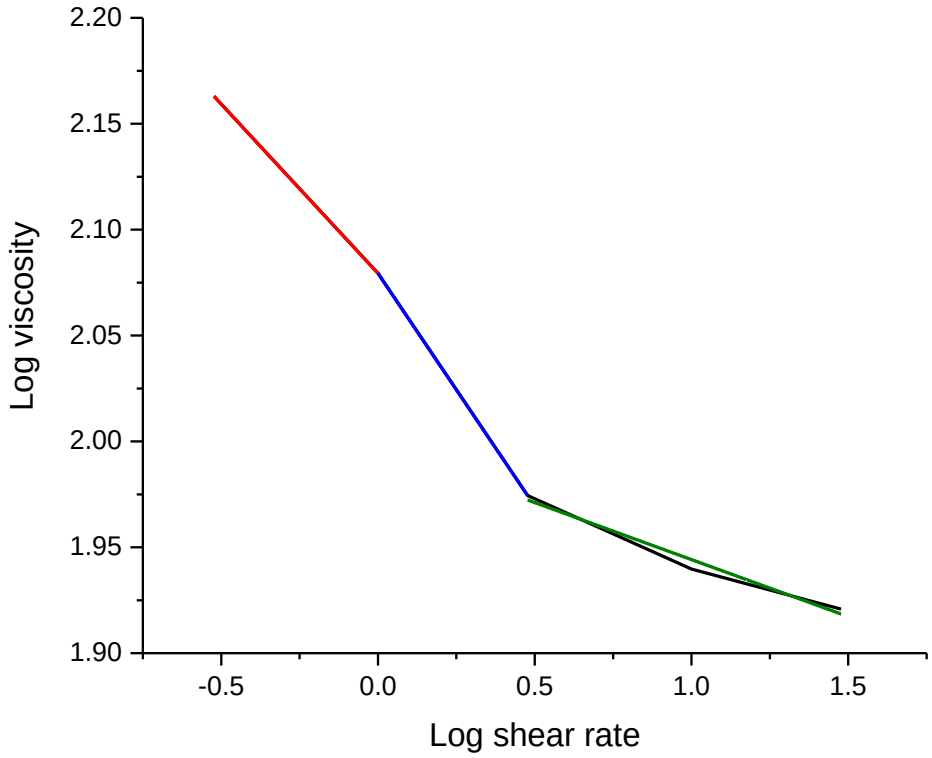

Figure 4.12: Linear fitting of Log viscosity ~ log shear rate for PLA-2 at 215ºC.

Table 4.3: Fitting lines of shear rate dependence viscosity of PLA-2 materials at 215 ºC.

Shear rate regime(s^{-1})	Formula of fitting curve	Value of K_4	Value of n
0.3-1	Y=-0.16*x+4.08	140.05	0.84
1-3	Y=-0.42*x+4.08	140.05	0.78
3-30	Y=-0.05*x+2.00	99.55	0.95

Higher molecular weight of PLA-2 materials is the reason for the higher values of viscosity. The molecular weight dependence of polymer melt viscosity is given by[3]:

$$\eta = K_H M_w^{3.4} \qquad (\mathbf{4\text{-}9})$$

where, η is the viscosity; K_H is a constant; and M_W is the weight-average molecular weight of polymers. We take the viscosity of two materials at temperature of 215 ºC, shear rate of 0.3 s^{-1} to estimate the relative molecular weight between two materials. Viscosity for PLA-1 is 100Pa.s and for PLA-2 is 145Pa.s at this temperature and shear rate. It is found that the ratio of weight-average molecular weight between two PLA materials estimated from **Equation 4-9** is about 1.2. This is lower than the ratio estimated from Tm. The reason is that **Equation 4-9** works the best for the viscosity extrapolated to zero-shear rate.

Melt Flow Index Measurements

Data in **Table 4** and **5** shows that the MFI of PLA-1 and PLA-2 materials are 10g/10min and 6g/10min, respectively. As can be anticipated, higher viscosity for PLA-2 results in lower MFI. The rheology measurements of viscosity and MFI definitely correspond to each other.

Table 4.4: Melt Flow Index of PLA-1

Material	**Sample Weight(g)**	**Average weight(g)**	**MFI(g/10min)**
PLA -1	0.3846,0.3646,0.4057,0.4439, 0.5155,0.5570,0.5709,0.5960, 0.6006	0.4948	9.9
PLA -1	0.3689,0.3890,0.2157,0.4464, 0.4751,0.5064,0.5364,0.5354, 0.5741	0.4719	9.4
PLA -1	0.3974,0.4080,0.4469,0.4359, 0.4644, 0.5435,0.6073,0.6307, 0.6551,	0.5054	10.1

Table 4.5: Melt Flow Index of PLA-2

Material	**Sample Weight(g)**	**Average Weight(g)**	**MFI (g/10min)**
PLA-2	0.4339,0.4574,0.4786,0.4908,0.4957, 0.4949,0.4907,0.4954,0.3006,0.3404, 0.3419,0.3556,0.3618,0.3734, 0.3996	0.3011	6.0
PLA-2	0.4431,0.4340,0.4387,0.4465,0.4538, 0.4609, 0.4689,0.4805,0.4911,0.3049, 0.3136,0.3435,0.3306	0.484	5.6
PLA-2	0.4854,0.4844,0.4849,0.4949,0.3037, 0.3074,0.3169,0.3434, 0.3311,0.3370, 0.3387,0.3413,0.3447,0.3479,0.3503,0.3616, 0.3870	0.3147	6.5

In conclusion, PLAs used in this work are shear thinning materials. The viscosity of two PLA materials decrease with both the temperature and the shear rate. The recommended printing temperature from the manufacturer for PLA-1 filaments is in the range of 180°C-230°C. According to literature, a suitable viscosity range for FDM manufacturing technique is 10-150Pa.s [6-7]. We experimented in this temperature range and final extrusion and printing temperature were set to be at 215°C. At this temperature we obtained consistent filaments extrusion and printing.

4.2.2: Mechanical properties of 3D printed objects

Tensile test

The tensile tests were conducted on printed dog-bone samples (**Figure 3.9 in Chapter 3**) in order to determine their static mechanical properties. The elongation during the measurements was perpendicular to the direction of printed layers. Thus, the maximum value of tensile stress would be affected by the weakest parts along this direction, which would be the layers bonding sections in most cases. The results, therefore, are to the great extent reflecting the level of bonding between the layers.

Strain-stress curves (**Figure 4.13)** of dog-bone samples fabricated from PLA-1 show pronounced strain softening. An average tensile stress at yield of 50.6MPa is obtained along with an ultimate tensile strain in the range of 20-27%. Two distinct parts can be found in the stress-strain curves, linear and nonlinear. It can be seen that the slope of strain-stress curve keep declining in the nonlinear section. At high strain, polymer chains start to

re-orientate and reduce the stress level in the samples, and therefore the effective modulus is declining. Before all polymer chains packed into an extended conformation and formed strain induced crystals, printed samples broke as a result of relatively weak adhesion between the printed layers. Variation of stress at the initial strain range of 0-5% results from alignment of structural defects. The materials along the elongation direction would align first before contributing to stress. First differentiation of strain-stress curves yield tangent modulus. **Table 6** show the Young's modulus is 370Mpa which is taken from the highest value of tangent modulus.

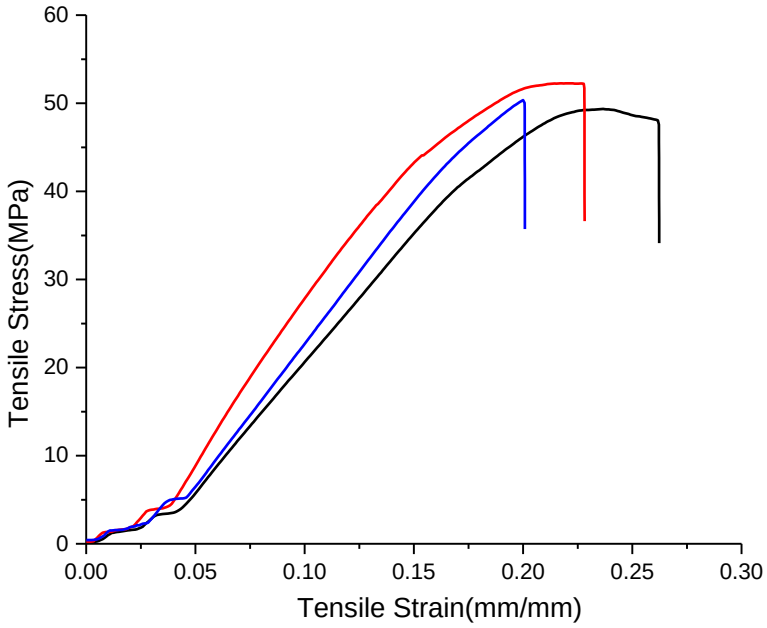

Figure 4.13: Strain-Stress curves of dog-bone samples printed from PLA-1.

Table 4.6: Young's modulus of dog-bone samples printed from PLA-1

PLA dog-bone samples	Tensile stress at yield(MPa)	Tensile strain at break (%)	Young's modulus(MPa)
1	49.5	26	433.7
2	54	22.8	344.7
3	50.4	20	331
Average	50.6±3.4	23±3	370±64

The tensile stress-strain curves (**Figure 4.14)** of dog-bone samples printed from PLA-2 materials show a significantly lower ultimate tensile stress and strain in comparison with the samples printed from PLA-1. The average tensile stress of samples printed from PLA-2 materials is about 30.8Mpa and average strain at break is 12%. There also exists an initial samples structural alignment phenomenon. Young's modulus derived from maximum tangent modulus shown in **Table 7** is 360MPa. Young's moduli of dog bone samples fabricated from these two PLA materials are quite similar.

Strain-stress curves (**Figure 4.14)** of samples printed from PLA-2 materials do not show yield points. It appears that dog-bone samples printed from PLA-2 materials break at the connecting points between the layers before the yield. The temperature of printing dog-bone samples from two PLA materials is the same. It means that, based on rheological measurements, PLA-2 materials coming out of nozzle have a higher viscosity in

comparison with PLA-1. Higher viscosity leads to a weaker adhesion between the printed layers.

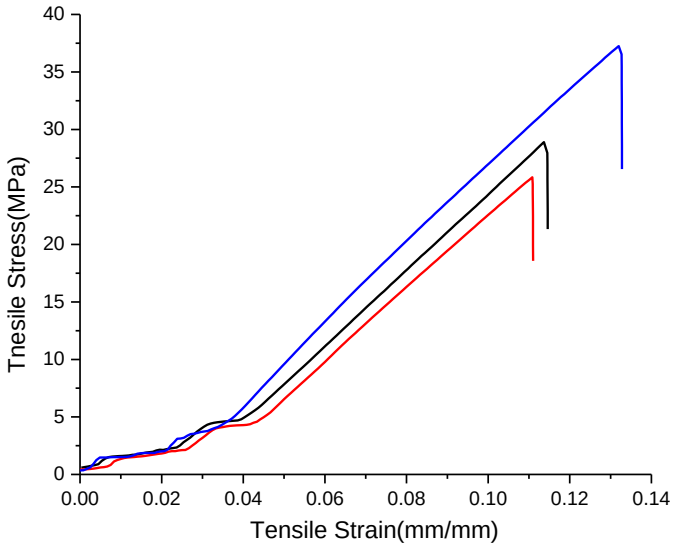

Figure 4.14: Strain-Stress curves of dog-bone samples printed from PLA-2.

Table 4.7: Young's modulus of dog-bone samples printed from PLA-2

PLA dog-bone samples	Tensile stress at yield(MPa)	Tensile strain at break (%)	Young's modulus(MPa)
1	29	11.5	344.2
2	26	11.1	343.8
3	37.3	13.5	390.8
Average	30.8±6.5	12±1.5	359±30

In order to compare the mechanical performance of printed dog-bone samples with the conventionally manufactured samples, tensile testaments were also performed on filaments. Tensile stress-strain curves of PLA-1 filaments (**Figure 4.15**) show that stress and strain at yield are 50.7MPa and 2.4%, respectively. First differentiation of tensile stress-strain curves yields an average elastic modulus of 3.7GPa (**Table 8**). The elastic modulus of PLA reported from literature which is about 3.5GPa is typically smaller than the Young's modulus we observed[8]. We associate the slightly higher modulus for produced filaments with the orientation hardening during the extrusion. Young's modulus of filaments is 10 times larger than that of printed dog-bone samples, indicating a poor bonding strength between layers of printed objects. There is an orientation hardening after yield in PLA-1 filaments tensile test plots. It results from the polymer chains oriented in the load direction. The other hardening near break is a consequence of the formation of crystals due to packing of polymer chains under stress.

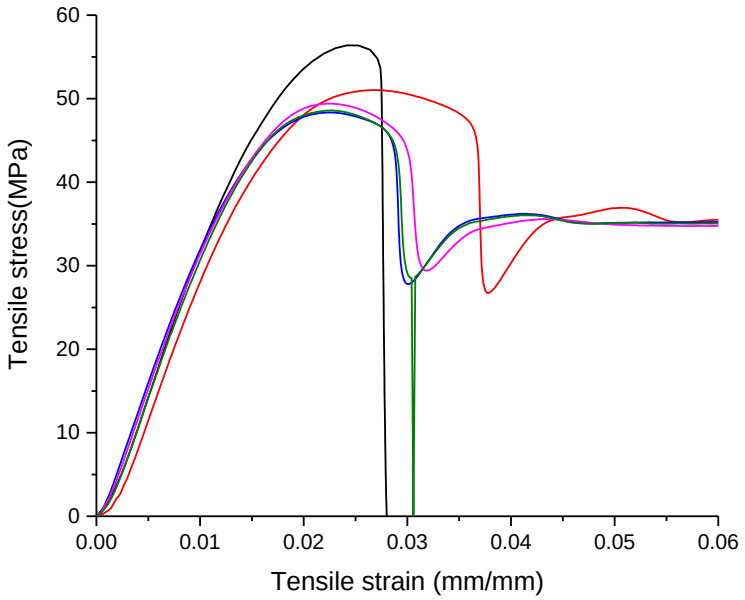

Figure 4.15: Strain-Stress curves of PLA-1 filament.

Table 4.8: Young's modulus of PLA-1 filament

PLA-1 filament	**Tensile stress at yield(MPa)**	**Tensile strain at yield (%)**	**Young's modulus(MPa)**
1	56.3	2.4	3763
2	51	2.7	3593
3	48.6	2.3	3723
4	49.4	2.2	3720
5	48.3	2.3	3692
Average	50.7±5.5	2.4±0.3	3693.4±100

Tensile tests of filaments extruded from PLA-2 pellets (**Figure 4.16**) present a similar behavior as that of PLA-1 filaments. According to **Table 9**, stress and strain at yield of PLA-2 filaments are 40.7MPa and 4.3%, respectively. It can be found that PLA-2 filaments have a lower stress and larger strain at yield compared to that of PLA-1 filaments. The calculated Young's modulus of PLA-2 filaments is also lower and is about 2GPa, which is about 5.5 times larger than that of dog-bone samples printed from PLA-2 filaments. The hardening due to the formation of crystals present in the plots of PLA-1 filaments is not seen in the plots of PLA-2 filaments.

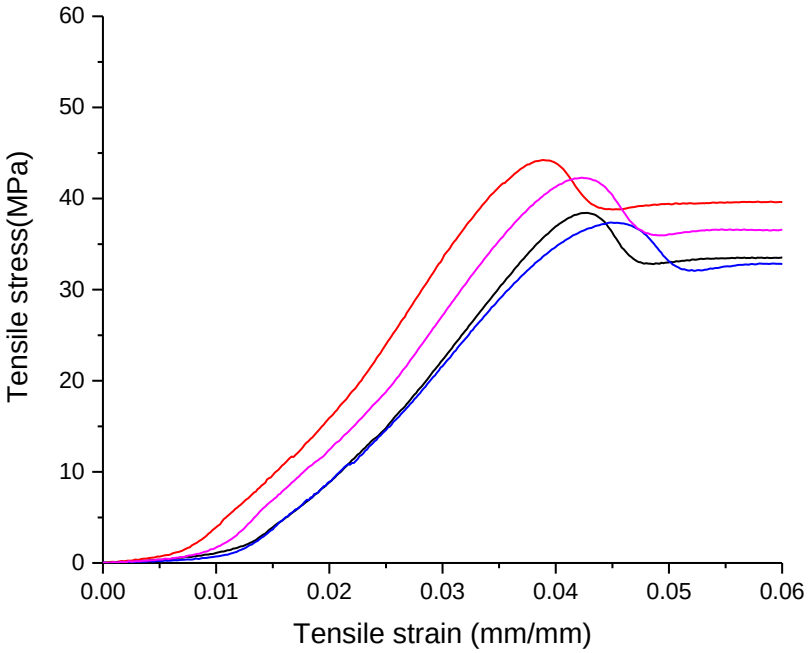

Figure 4.16: Strain-Stress curves of filament extruded from PLA-2 pellets.

Table 4.9: Young's modulus of filaments extruded from PLA-2 pellets

PLA-2 filament	Tensile stress at yield(MPa)	Tensile strain at yield (%)	Young's modulus(MPa)
1	38.4	4.3	1750.4
2	44.4	3.9	2378.4
3	37.5	4.5	1834.4
4	42.3	4.3	1910.8
Average	40.7±3.7	4.3±0.4	1968.5±410

The morphology of crack surfaces for dog-bone samples after tensile test can be used to interpret mechanical properties of printed samples. Optical microscope photography of cross section for dog-bone samples printed from two PLA materials after tensile stress are shown in **Figure 4.17.** Cross section of sample printed from PLA-1 shows a smooth and opaque surface. While a rough but transparent surface shows up for dog-bone samples printed from PLA-2. Clear plastic deformation can be seen from the crack surface of samples printed from PLA-2 materials. Opaque appearance could results from the formation of crystals beyond yield point. Since samples printed from PLA-2 do not show a yield point, the cross-sections of them are clear. Adhesion between two types of PLA flayers in the 3D printed structure is different.

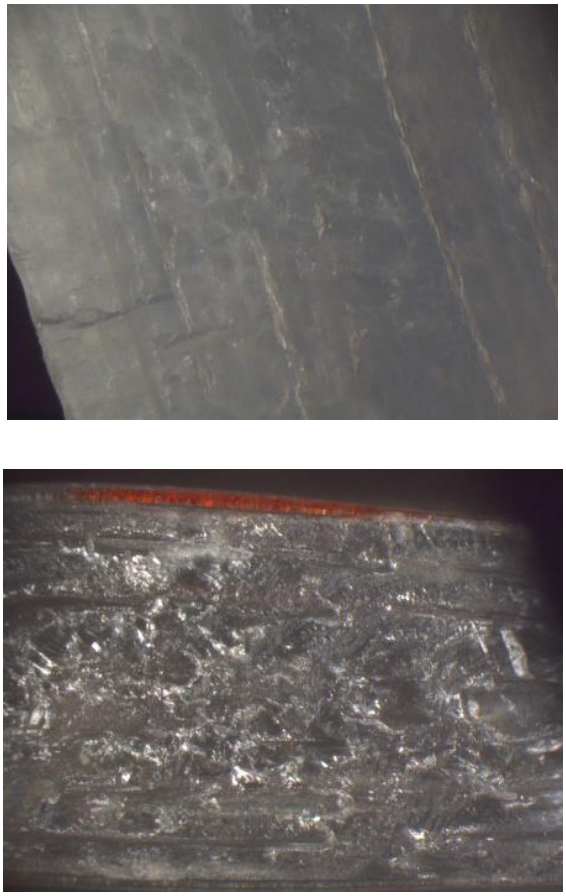

Figure 4.17: Optical microscope photograph of crack surface for samples printed from PLA-1 (up) and PLA-2 (down).

According to the literature data, PLA filaments utilized for 3D printing have Young's modulus of about 3.5 GPa[8]. Young's modulus of PLA-1 filaments has a good coherence with the data reported in the literatures while that of PLA-2 filaments is somewhat smaller. Young's modulus for dog bones printed from PLA-1 is 0.37 GPa and that for samples printed from PLA-2 is 0.36GPa. One order of magnitude smaller elastic modulus of printed samples results from weak adhesion between the layers in the printed structures.

Dynamic mechanical analysis of the 3D printed samples

Dynamic mechanical analysis is used to characterize mechanical properties of printed samples at low deformations. Also, it characterizes viscoelastic behavior of materials. The position of tan δ peaks indicates the glass transition temperature. Change of storage modulus implies an enhancement or weakening of layers adhesion. DMA results were compared between samples printed at two raster angles, two types of materials and before and after being subjected to heat treatment. Temperature range for DMA analysis was set to be 0-100°C in order to avoid significant crystallization during the measurements.

Comparison of DMA between samples printed at two raster angles

As illustrated in **Chapter 3**, samples utilized for DMA measurements are printed at two different taster angles and have the same layers packing pattern. However, the elongation direction during the measurements are different. Samples printed at raster angles of 90° were measured along the printed layers. While samples printed at 0° were measured in the direction perpendicular to the printed layers. The measurements are designated as material/90° or material/0°. The comparison of DMA results for samples printed from PLA-1 at two raster angles (**Figure 4.18, 4.19 and 4.20)** show anisotropic nature of the printed objects. In glassy region, PLA-1/0° samples have a higher storage modulus (E') than PLA-1/ 90°. At room temperature (25°C), the storage modulus of PLA-1/0° is about 2540MPa and that of PLA-1/ 90° is about 2218MPa. It gave an unexpected result. We associate this phenomenon with the possible uneven loading during DMA

measurements. It can fluctuate due to the 'staircase' effect[100]. Therefore, the PLA-1/ 90° samples might not be fully loaded. Therefore, only part of the materials contributes to storage modulus. While PLA-1/0° samples are fully loaded. Thus the storage modulus for PLA-1/90° is smaller. However, this can reflect a good adhesion between layers. Both storage moduli decline with a rise in temperature. Error bars, which derived from the standard deviation of three parallel experiments, show that variation of mechanical properties along 0° is smaller than that along 90°. In the glass transition region, dramatic storage modulus decrease occurs and the modulus drops to about 5MPa at the rubbery plateau.

PLA-1/0° samples present a relative high peak value of loss modulus and tan δ, along with a more consistent loss modulus before glass transition region. Larger tan delta at glass transition region implies a more pronounced viscoelastic behavior of the samples along this direction.

Tg of PLA-1/0° derived from the peak of tan delta is 67°C. It is slightly smaller than Tg of 69°C for PLA-1/90°. According to literature, materials would align along flow direction when coming out of nozzle due to shear effect[9]. Therefore, PLA polymer chains aligned along the deposit lines during the printing. As mentioned before, the elongation direction when measuring PLA-1/ 0º is perpendicular to the deposit lines. Less restriction of free movement for polymer chains in this direction decreases Tg. It also can be noted that the plots for the temperature dependence of tan δ have an asymmetric shape, which

related to the presence of interphases in the samples[10]. According to the thermal analysis, PLA-1 materials start to form crystals at the temperature around 100 º C.

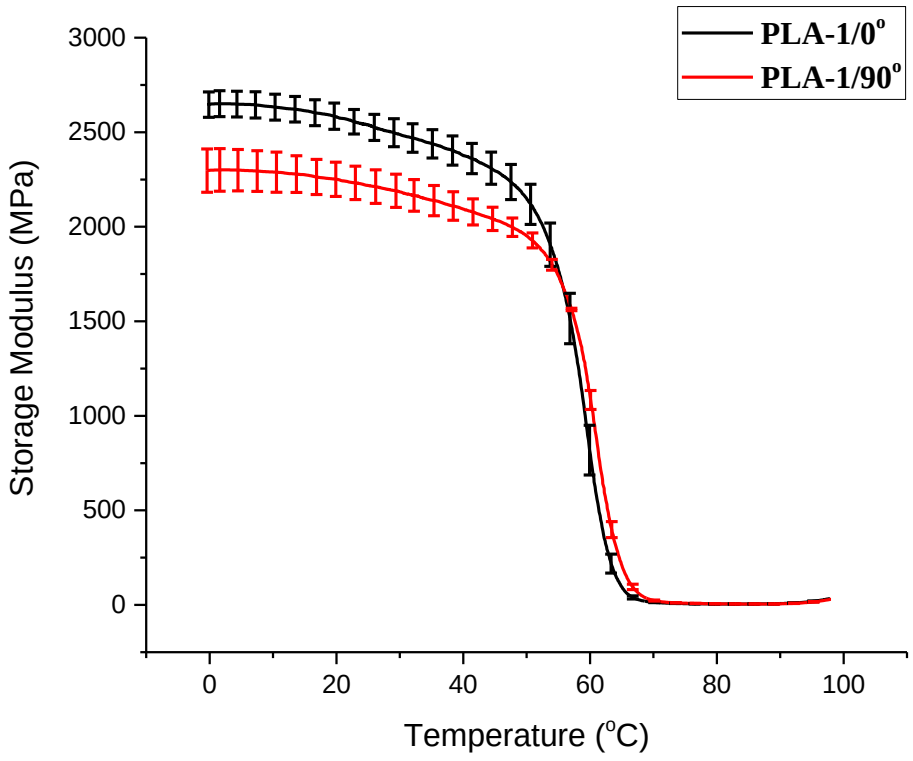

Figure 4.18: Storage modulus of PLA-1 samples printed at two raster angles.

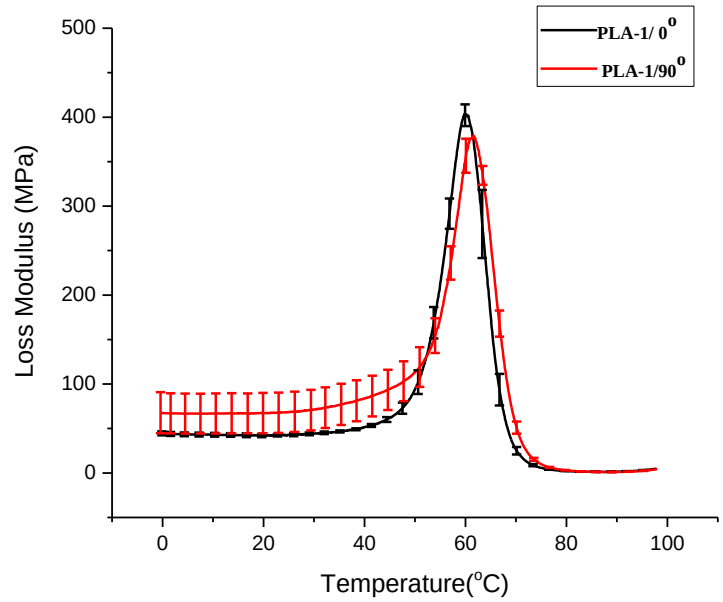

Figure 4.19: Loss modulus of PLA-1 samples printed at two raster angles.

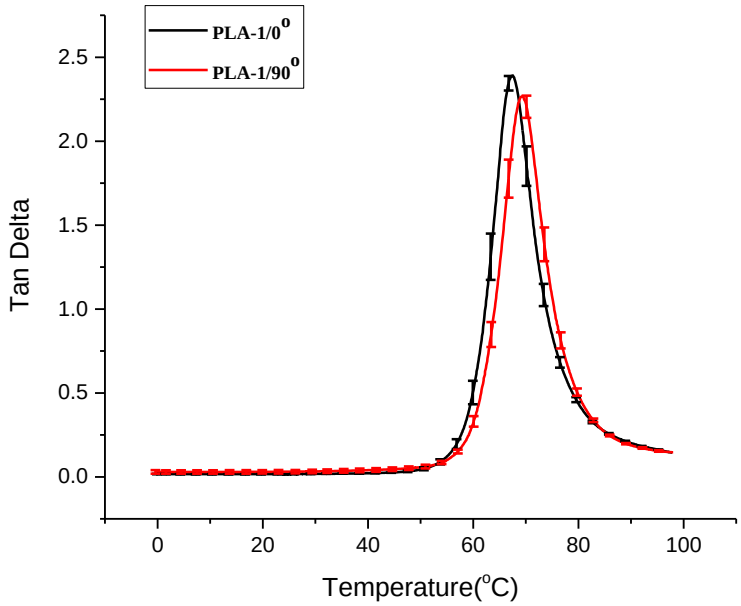

Figure 4.20: Tan delta of PLA-1 samples printed at two raster angles.

Comparison of DMA results for samples printed from PLA-2 at different raster angles (**Figure 4.21, 4.22 and 4.23**) show a very similar behavior as samples printed from PLA-1. Higher storage modulus at glassy state for PLA-2/ 0° and higher glass transition temperature for PLA-2/ 90°.

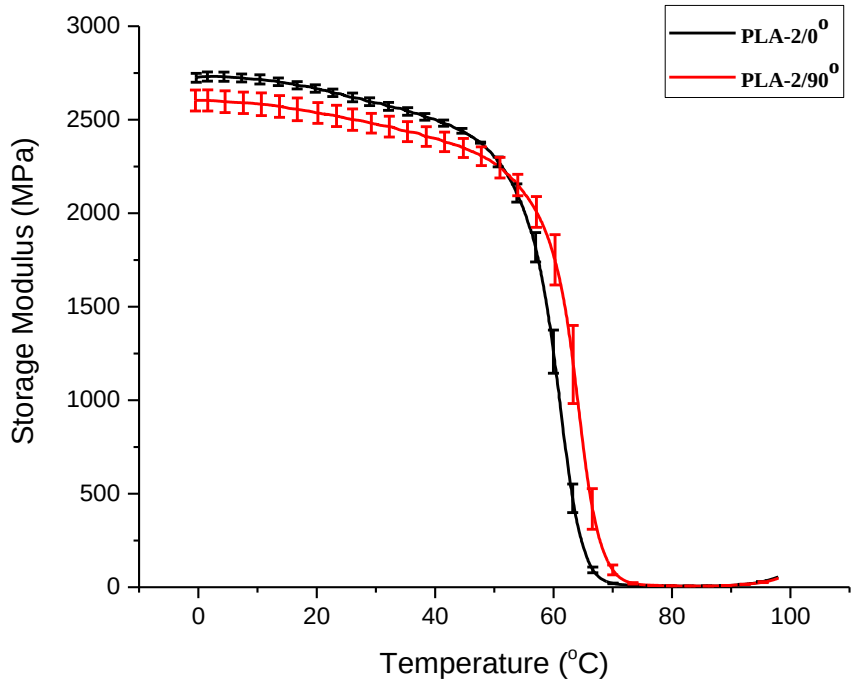

Figure 4.21: Storage modulus of PLA-2 samples printed at two raster angles.

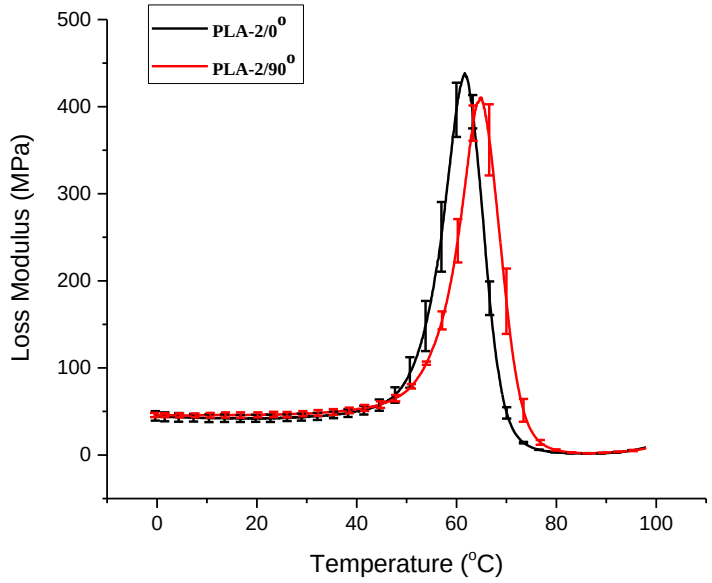

Figure 4.22: Loss modulus of PLA-2 samples printed at two raster angles.

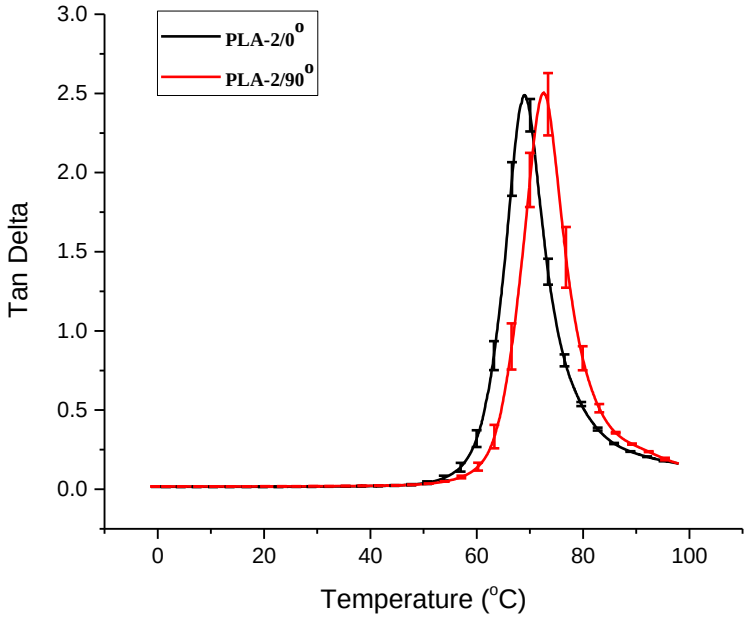

Figure 4.23: Tan delta of PLA-2 samples printed at two raster angles.

In conclusion, samples printed from two PLA materials have anisotropy in mechanical properties. Polymer chains packing regularity along deposit lines results in higher Tg for samples printed at 90°.

Comparison of DMA results for samples fabricated from PLA-1 and PLA-2

Figure 4.24, 4.25 and 4.26 show the comparison of DMA results for samples printed from two types of PLA filaments at raster angle of 0°. The plots show that PLA-2 samples possess higher storage modulus, loss modulus and tan delta relative to that of PLA-1 samples. Small error bars on the plots of PLA-2 samples imply consistent physical performances.

Glass transition temperatures derived from the peaks of tan delta are 67°C and 69°C for PLA-1 and PLA-2, respectively. Tg derived from peaks of tan delta is in most cases higher than that from DSC measurements. Tg for PLA-1 and PLA-2 from DSC analysis are 60°C and 62°C, respectively. There is a 7°C difference between Tg from peaks of tan delta and that from thermal analysis. Higher glass transition temperature of samples printed from PLA-2 has a good coherence with DSC measurements.

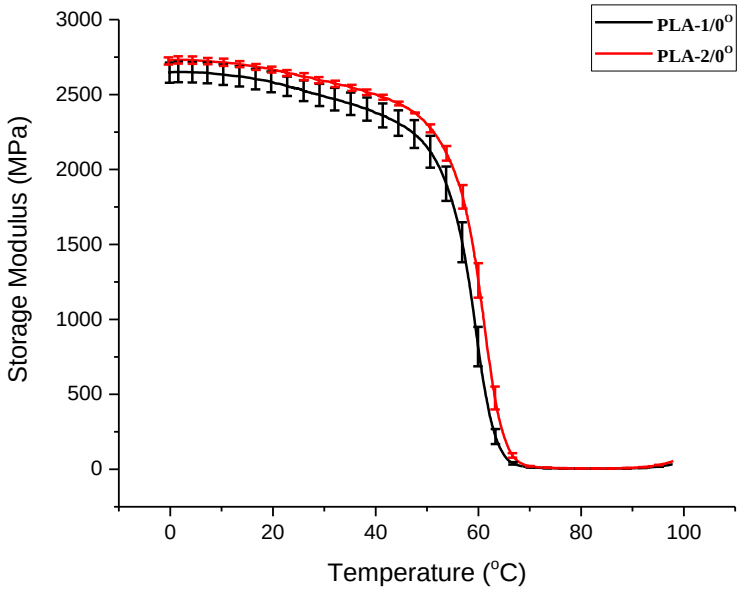

Figure 4.24: Storage modulus of samples printed at 0° from PLA-1 and PLA-2.

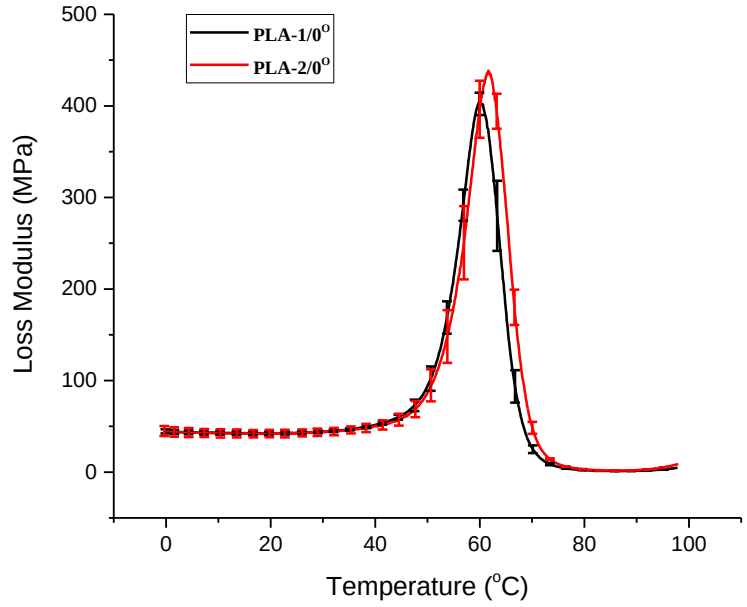

Figure 4.25: Loss modulus of samples printed at 0° from PLA-1 and PLA-2.

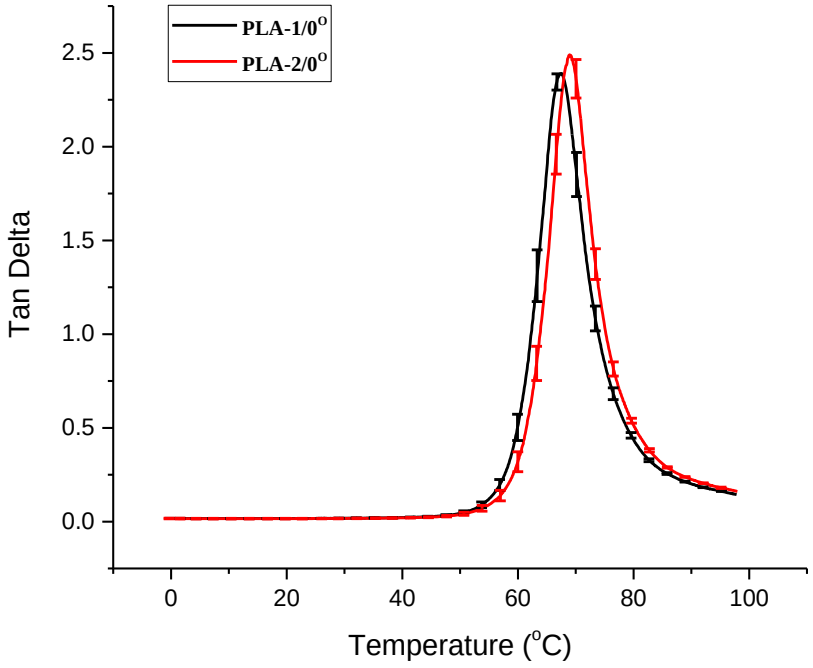

Figure 4.26: Tan delta of samples printed at 0° from PLA-1 and PLA-2.

Figure 4.27, 4.28 and 4.29 show the comparison of dynamic mechanical properties for samples printed from two PLA materials at raster angle of 90°. The plots indicate that the storage modulus, loss modulus and tan delta of samples printed from PLA-1 materials are significantly lower than that of samples printed from PLA-2. Mechanical properties along raster angles of 90° mainly come from materials' intrinsic properties. It is a result of inter-polymer chains friction, deformation of covalent bond angles and stretching of covalent bonds[11]. For the same material, the distinct mechanical properties are most likely coming from the difference of inter polymer chains friction. PLA-2 materials have a higher

molecular weight. Error bars of the curves indicate a more consistent physical properties for samples printed from PLA-2.

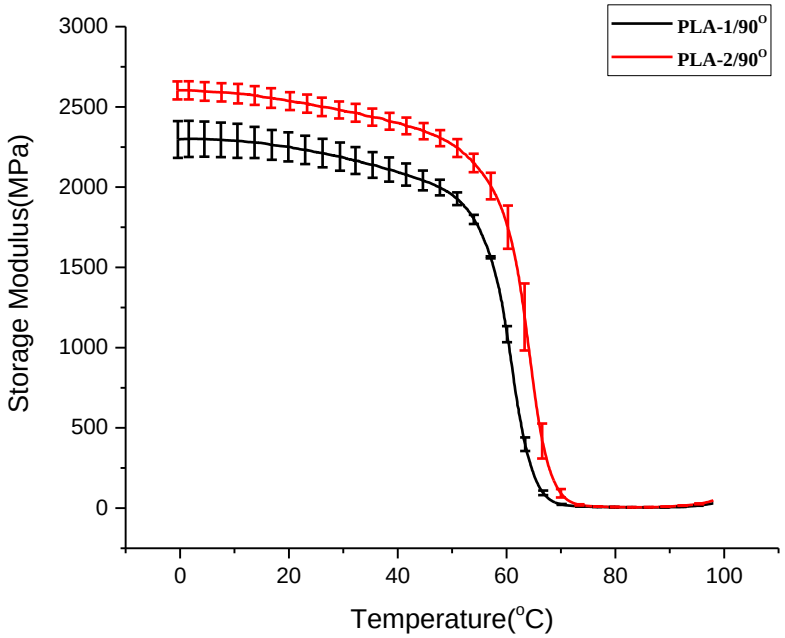

Figure 4.27: Storage modulus of samples printed at 90° from PLA-1 and PLA-2.

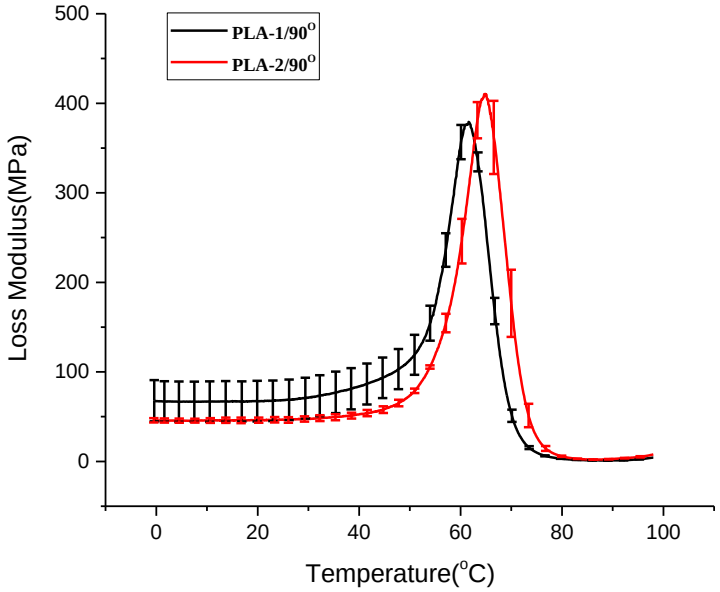

Figure 4.28: Loss modulus of samples printed at 90° from PLA-1 and PLA-2.

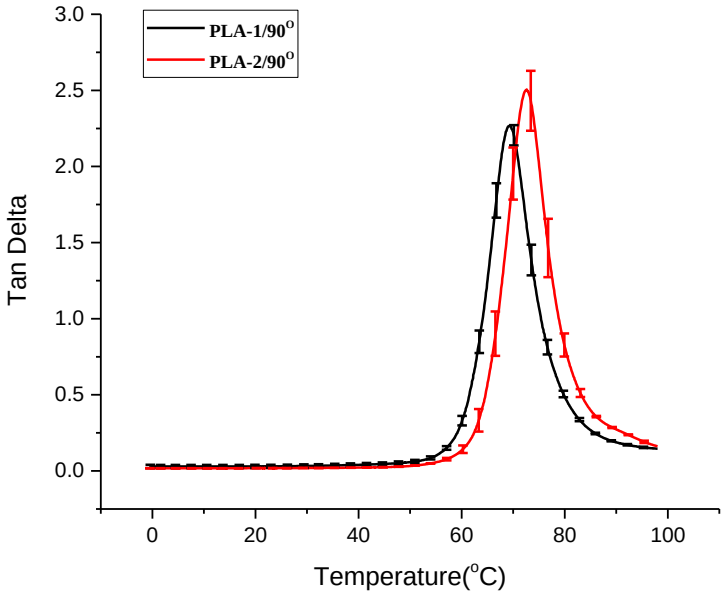

Figure 4.29: Tan delta of samples printed at 90° from PLA-1 and PLA-2.

Comparison of DMA results indicate a similar dynamic mechanical behavior between samples printed from two types of PLA materials at raster angle of 0 º. It indicates a comparable layers adhesion between samples fabricated from two different materials under the same conditions. However, DMA results between samples printed at raster angle of 90º show a much larger difference in mechanical properties. Mechanical performances are mainly determined by intrinsic properties of materials in this testing direction. The differences of physical properties that are determined by molecular weight can then be seen. However, the main goal of this project is to improve the bonding strength between layers. Therefore, these two materials are mutually replaceable for this purpose.

Heat treatment of the 3D printed samples

Heat treatment was already proven to enhance layers' adhesion for 3D printed samples[12]. **Figure 4.30(a)** presents DSC thermographs of PLA-1 material annealed at different temperatures. There are two melting peaks that appear in the graph of materials annealed at 90°C, meaning two types of crystals with distinct sizes were formed.

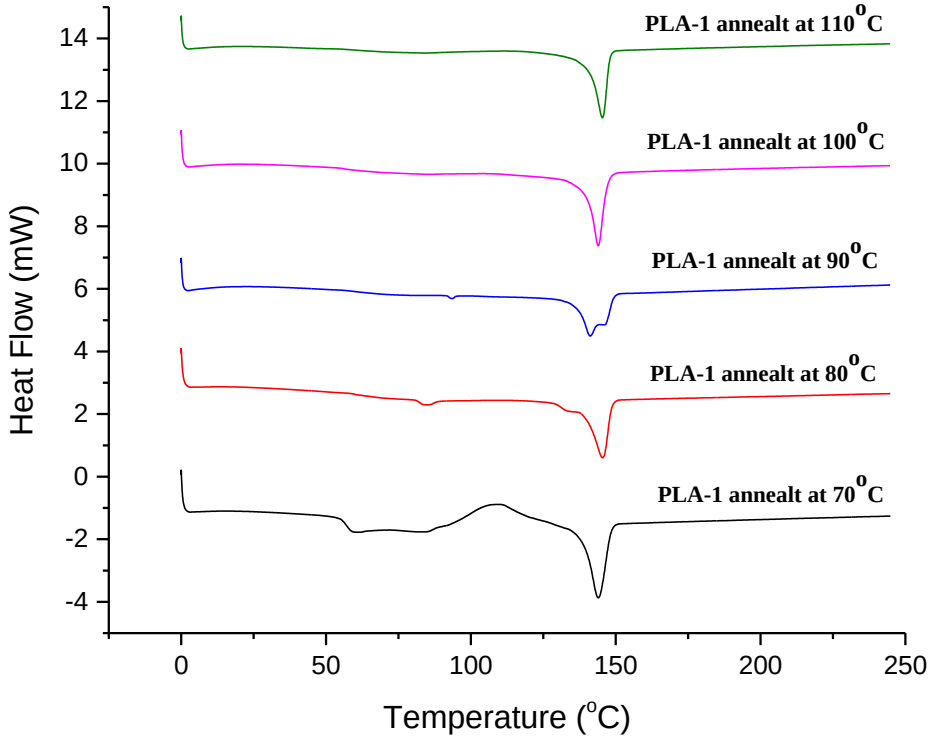

Figure 4.30: DSC thermographs of PLA-1 annealed at different temperature.

Melting temperature of samples annealed higher temperature is higher than that annealed at relative lower temperature. According to the equation derived from Hoffman's Nucleation Theory[3]:

$$Tf = Tfo\ [1 - \frac{4\sigma e}{\Delta Hf * l}] \qquad (\mathbf{4\text{-}10})$$

where, T_f is the real melting temperature of materials; T_{fo} is the ideal melting temperature for the melting of large, perfect crystals; σ_e is the fold surface interfacial free energy; and l

is the thickness of the crystal lamella. Perfect crystals are not likely to form within real polymer materials. Therefore, the actual melting temperature is always lower than the theoretical one. Higher Tm relate to the melting of larger sizes of lamella. Thus, it can be concluded that at higher annealing temperatures, larger crystals can form.

Plot (**Figure 4.31)** of percentage of crystallinity for PLA-1 materials annealed at different temperatures is obtained based on **Equation 3-1** (**Chapter 3)**. The plot shows that PLA-1 filament starts to crystallize during the heat treatment when the annealing temperature is higher than 70°C. Percent of crystallinity increases with the rise of annealing temperature. At low annealing temperature, the percent of crystallinity increases rapidly while at high annealing temperature it reaches a plateau. When annealing temperature higher than 100°C, percent of crystallinity does not change significantly. The limitation of forming total crystallinity due to the impedance of crystals on each other and the lack of nuclei for the growth. Roe, Smith, and Krigbaum pointed that during formation of crystals there would be a build-up strain within the amorphous region which limits the percent of crystals[13].

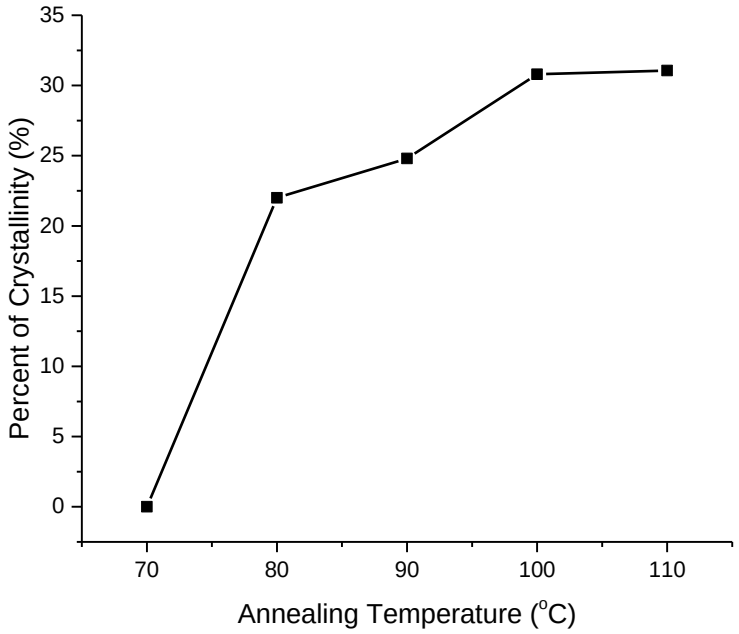

Figure 4.31: Annealing temperature dependence of percent of crystallinity for PLA-1.

Figure 4.32 presents DSC thermographs of PLA-2 materials annealed at various temperatures. No notable crystallization endotherm peak is observed after the annealing temperatures are higher than 90°C. Two distinct sizes distribution of crystals can be identified based on two melting peaks when materials are annealed below 90°C. Higher than 90°C, heat treatment leads to the formation of crystals with one size distribution. Crystallization temperature of larger crystals is about 160°C which is 50°C higher than the temperature for crystals with small sizes.

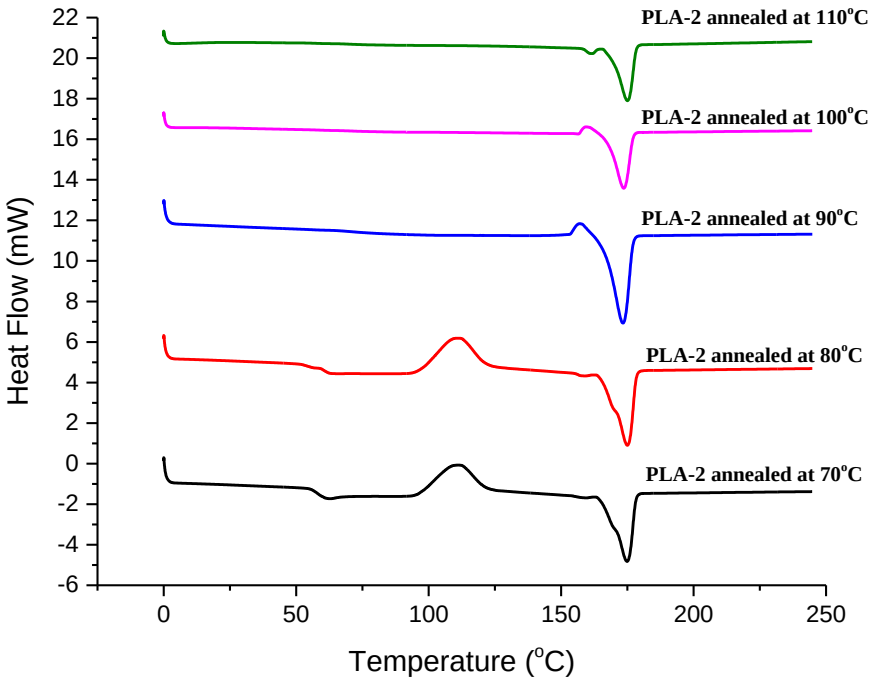

Figure 4.32: DSC thermographs of PLA-2 annealed at different temperature.

Figure 4.33 shows the calculated percent of crystallinity of PLA-2 annealed at different temperature. Significant increase of percent of crystallinity is observed when annealing temperature increased from 80°C to 90°C. Percentage of crystals within materials does not rise when annealing temperature is higher than 90°C, rather there is a slight decline. There are two possible explanations with one being inaccurate integration of exothermal and endothermal curves, and the other one could be small sizes crystals are already melted at those annealing temperatures.

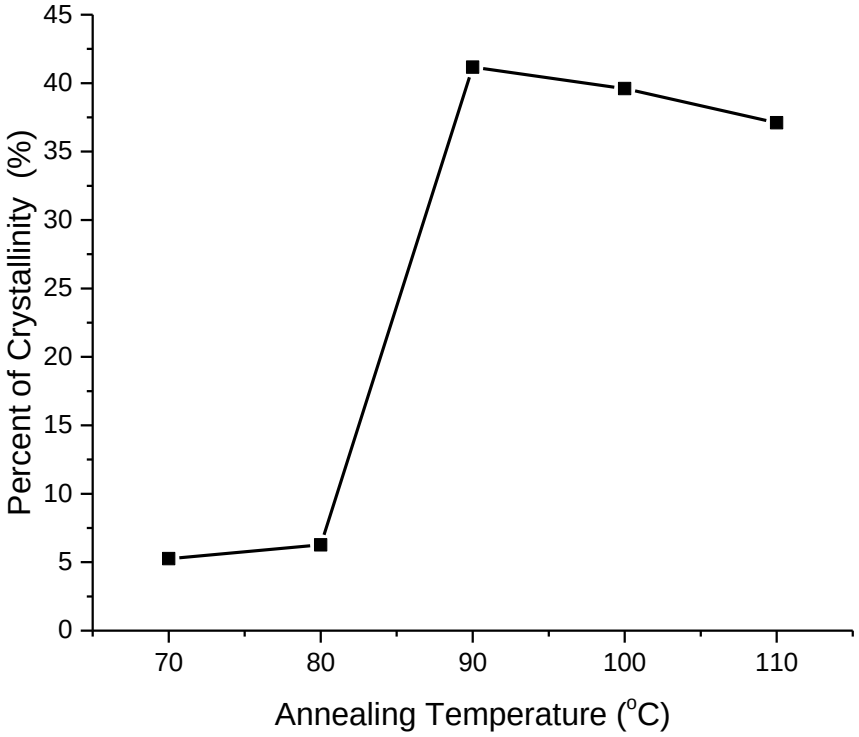

Figure 4.33: Annealing temperature dependence of percent of crystallinity for PLA-2.

Heat treatment temperature was finally decided to be at 100°C where crystallization of both materials occurs to full possible extent and melting of small crystals within PLA-2 materials can be neglected.

Dynamic mechanical analysis of 3D printed samples after heat treatment

Figure 4.34 presents the comparison of storage modulus for PLA-1 samples printed at different raster angles before and after the annealing**.** It shows that after the heat treatment, storage modulus increases for PLA-1/90° while decreases for PLA-1/0° at glassy region. Different mechanisms contribute to mechanical properties of samples tested along these two directions. As mentioned before, polymer chains pack along deposit lines after coming out of nozzle making it difficult for them to re-arrange into direction vertical to deposit lines. The formation of crystals along direction perpendicular to deposit lines can be ignored. There could be an increment of interlayers' adhesion. However, this effect is overwhelmed by the mechanical properties decreasing due to samples' shape curling. Photograph of samples before and after annealing (**Figure 4.35**) show a clear thermal warp, which is a challenge of conducting bulk thermal treatment. Therefore, there is no much improvement for samples printed at raster angles of 0°. While, intrinsic well packed polymer chains along deposit lines make the formation of crystals along 90° much easier. An increase of percent of crystallinity results in rising of storage modulus. Shape curling for samples after heat treatment accounts for larger mechanical properties variation. There exists a significant increase of storage modulus at rubbery plateau region. In the rubbery plateau region, crystallized parts contribute to storage modulus.

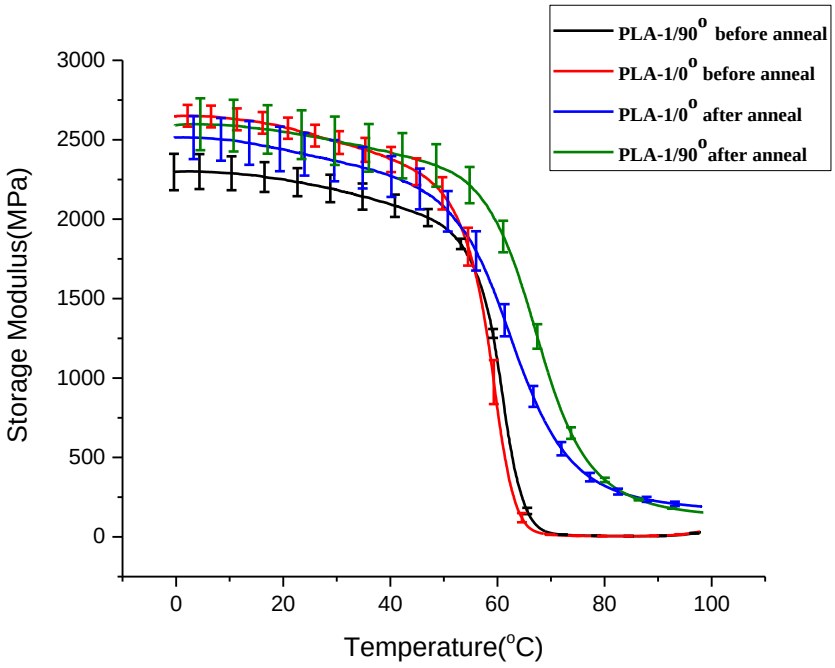

Figure 4.34: Comparison of storage modulus for PLA-1/0° and PLA-1/90º before and after heat treatment.

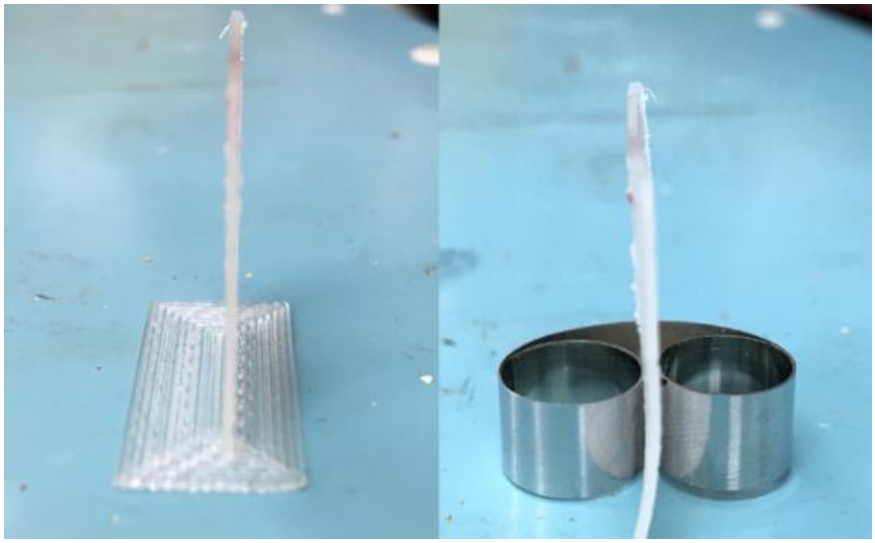

Figure 4.35: Comparison of pictures for samples between before (left) and after (right) the annealing.

Both loss modulus (**Figure 4.36**) and tan δ (**Figure 4.37**) decline drastically after heat treatment, implying an increase of elastic response of the materials. However, the width of both loss modulus and tan δ increases as the percent of crystallinity rising. The width of transition connects with network density[10]. The formation of crystals, as a format of polymer chains network, increase significantly after heat treatment, which contribute to the widening of transition peaks.

Tg derived from peaks of tan δ shows a significant increase after the annealing. Tg of PLA-1/ 0° is 62°C before the annealing and 73°C after the heat treatment. PLA-1/ 90° have the Tg of 65°C before annealing and 76°C after annealing. There is a 12°C increment of Tg for samples after conducting the thermal treatment. After annealing, more crystallized regions constrain the movement of amorphous polymer segments, leading to a higher glass transition temperature.

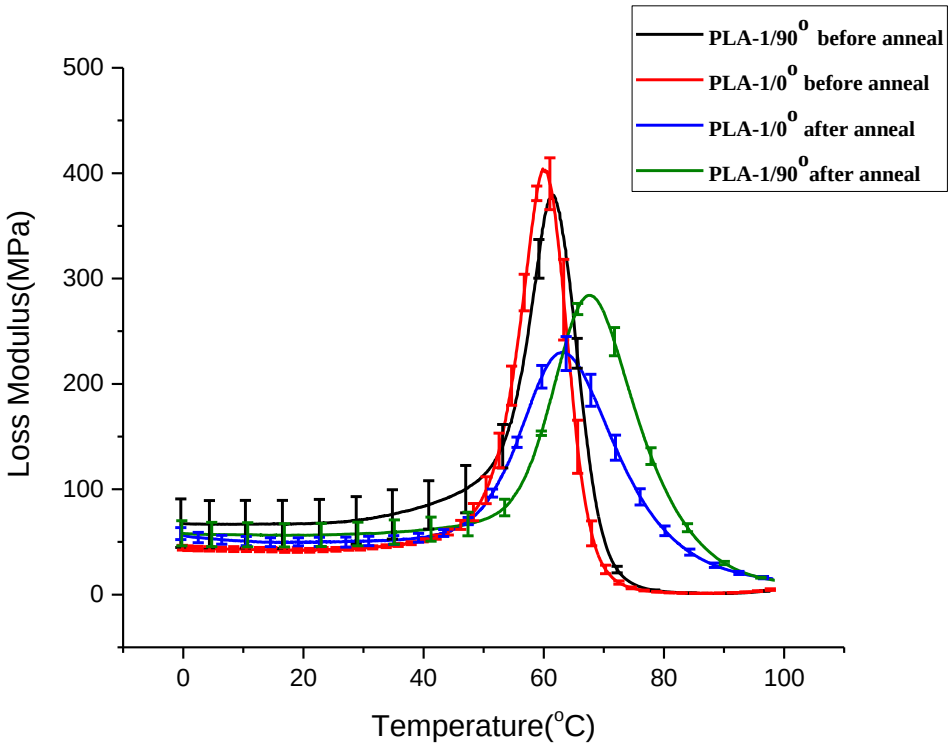

Figure 4.36: Comparison of loss modulus for PLA-1 samples printed at two raster angles before and after conducting the heat treatment.

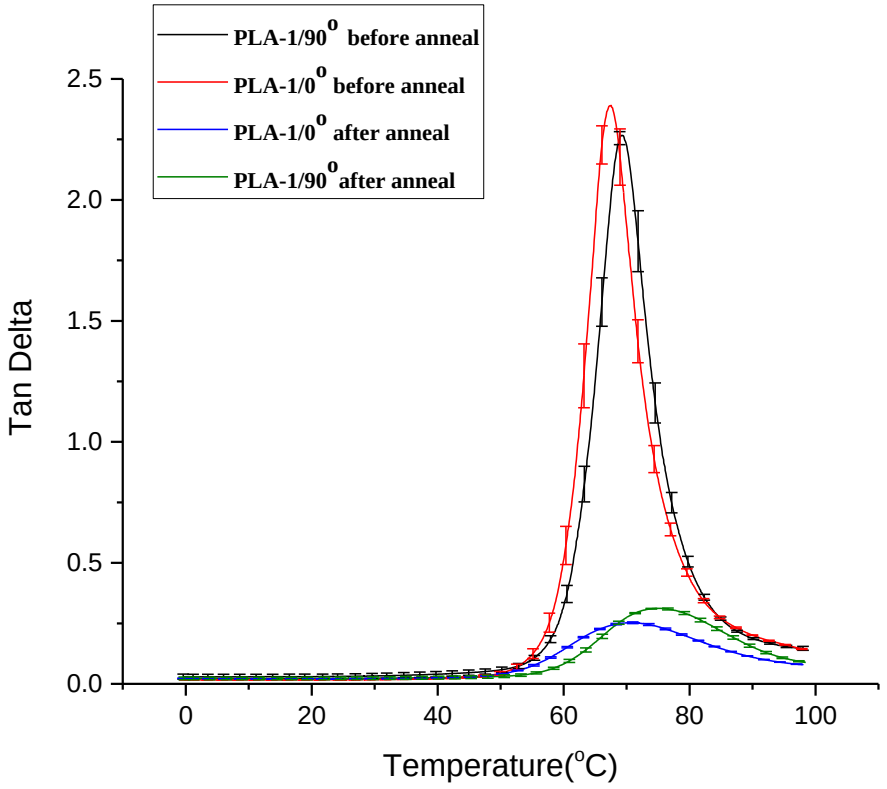

Figure 4.37: Comparison of tan delta for PLA-1 samples printed at two raster angles before and after conducting the heat treatment.

Comparison of DMA results for PLA-2/0° and PLA-2/90° samples before and after annealing (**Figure 4.38, 4.39 and 4.40**) indicate a similar trends. The only difference is the decline of storage modulus at glassy region regardless of raster angles. Larger error bars, higher glass transition temperature and greater storage modulus at rubbery plateau region can be interpreted the same as mentioned before.

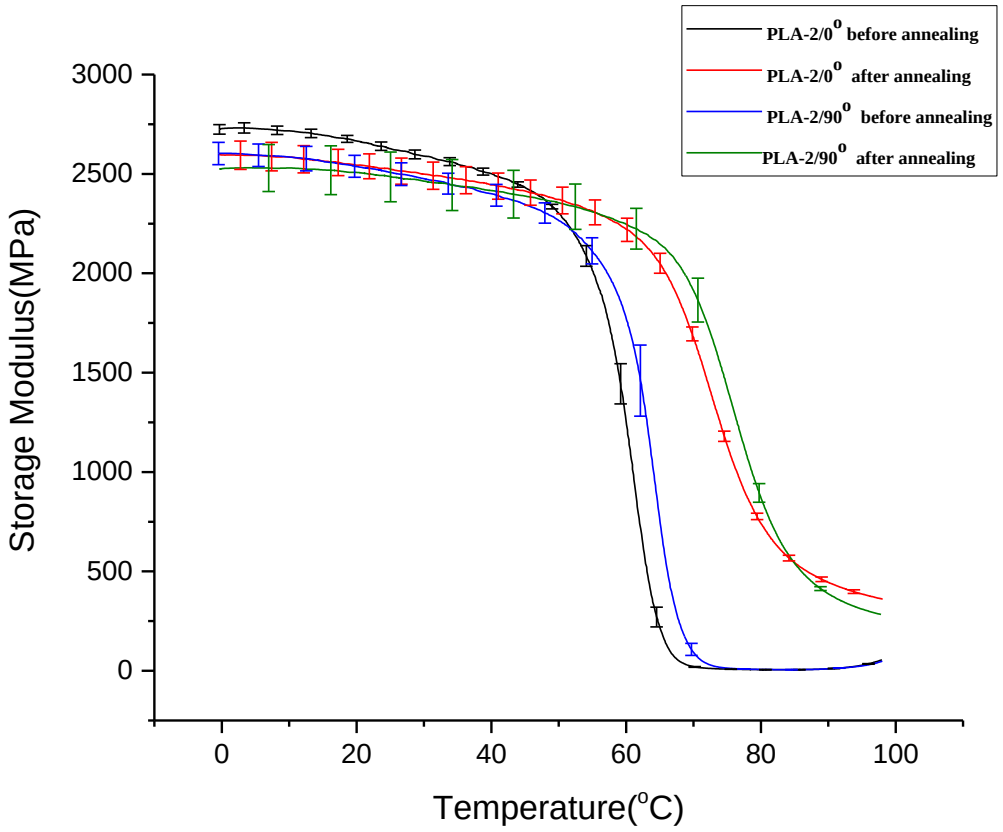

Figure 4.38: Comparison of storage modulus for PLA-2 samples printed at two raster angles before and after conducting the heat treatment.

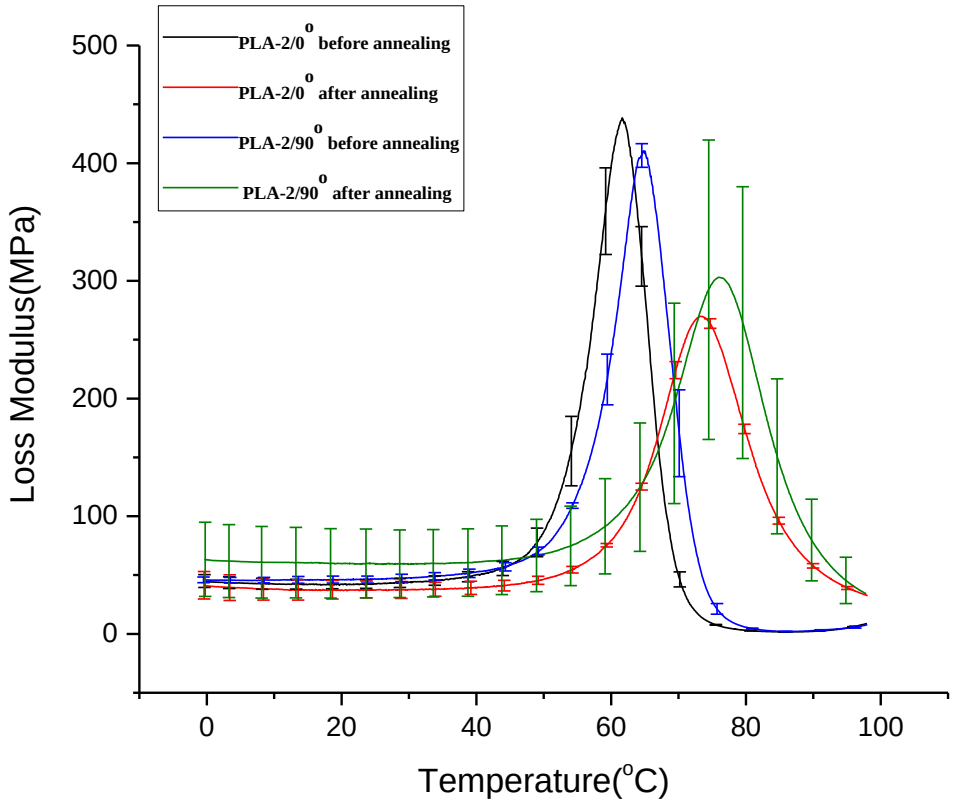

Figure 4.39: Comparison of loss modulus for PLA-2 samples printed at two raster angles before and after conducting the heat treatment.

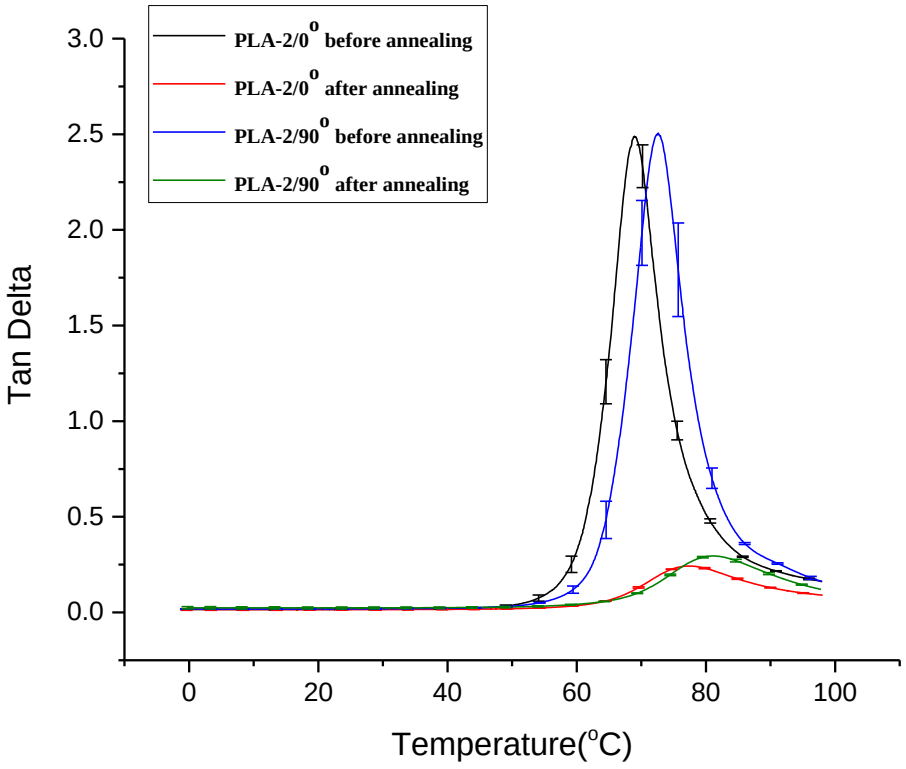

Figure 4.40: Comparison of tan delta for PLA-1 samples printed at two raster angles before and after conducting the heat treatment.

After annealing, the significant decrement of tan δ at glass transition region indicates the change in viscoelastic behaviors for samples. Tg is raised due to the restrain effects caused by the formation of crystals. Variation for mechanical properties results from thermal warp of samples shape after heat treatment.

It can be found that PLA-1 printed samples have higher Young's modulus in tensile tests but a lower storage modulus in dynamic mechanical analysis in comparison to PLA-

2 printed samples. We associate these with the small elongation in DMA measurements, which is only about 0.003 mm/mm. Distinct elongation differentiate these two characterization techniques greatly and yield inverse conclusions.

4.3: Conclusion

The following conclusions can be derived from our study of PLA materials in 3D printing:

- 3D printing conditions were successfully determined by thermal analysis and viscosity measurements. PLA is a shear thinning materials and its highest percent of crystallinity can reach 40%. Extrusion and printing temperature was decided to be at 215ºC.
- Anisotropic physical properties of PLA printed samples are not prominent before annealing. It indicates a good layers adhesion within the printed objects;
- Heat treatment causes decline in storage modulus at glassy region, however, increases storage modulus significantly at rubbery plateau. Glass transition temperature shows an obvious increase after the annealing. Samples shape warp after heat treatment increases mechanical properties variation;
- Mechanical properties of samples printed from two types of PLA filaments are quite similar.

4.4: References

1. Cangialosi, D.; Boucher, V. M.; Alegria, A.; Colmenero, J., Physical aging in polymers and polymer nanocomposites: recent results and open questions. *Soft Matter* **2013,** *9* (36), 8619-8630.
2. Flory, P. J., Thermodynamics of Crystallization in High Polymers. IV. A Theory of Crystalline States and Fusion in Polymers, Copolymers, and Their Mixtures with Diluents. *The Journal of Chemical Physics* **1949,** *17* (3), 223-240.
3. Sperling, L. H., Introduction to Physical Polymer Science, 4th Edition. *Introduction to Physical Polymer Science, 4th Edition* **2006**, 1-845.
4. Kalb, B.; Pennings, A. J., General Crystallization Behavior of Poly(L-Lactic Acid). *Polymer* **1980,** *21* (6), 607-612.
5. Celli, A.; Scandola, M., Thermal-Properties and Physical Aging of Poly(L-Lactic Acid). *Polymer* **1992,** *33* (13), 2699-2703.
6. Kamthai, S.; Magaraphan, R., Thermal and mechanical properties of polylactic acid (PLA) and bagasse carboxymethyl cellulose (CMCB) composite by adding isosorbide diesters. **2015,** *1664*, 060006.
7. Muthui, Z. W.; Kamweru, P. K.; Nderitu, F. G.; Hussein, S. A. G.; Ngumbu, R.; Njoroge, G. N., Polylactic acid (PLA) viscoelastic properties and their degradation compared with those of polyethylene. *International Journal of Physical Sciences* **2015,** *10* (21), 568-575.
8. http://2015.igem.org/wiki/images/2/24/CamJIC-Specs-Strength.pdf. (accessed 02/19/2018).
9. Agarwala, M. K.; Jamalabad, V. R.; Langrana, N. A.; Safari, A.; Whalen, P. J.; Danforth, S. C., Structural quality of parts processed by fused deposition. *Rapid Prototyping J* **1996,** *2* (4), 4-19.
10. Townsend, J.; Burtovyy, R.; Aprelev, P.; Kornev, K. G.; Luzinov, I., Enhancing Mechanical and Thermal Properties of Epoxy Nanocomposites via Alignment of Magnetized SiC Whiskers. *Acs Appl Mater Inter* **2017,** *9* (27), 22927-22940.
11. Mittal, K. L., Adhesion Measurement of Films and Coatings .1. *J Adhes Sci Technol* **1993,** *7* (8), 765-766.
12. Torres, J.; Cotelo, J.; Karl, J.; Gordon, A. P., Mechanical Property Optimization of FDM PLA in Shear with Multiple Objectives. *Jom-Us* **2015,** *67* (5), 1183-1193.

13. Roe, R. J.; Krigbaum, W. R.; Smith, K. J., Equilibrium Degrees of Crystallization Predicted for Single Pass and Folded Chain Crystallite Models. *J Chem Phys* **1961,** *35* (4), 1306-&.

CHAPTER 5

FORMATION AND PROPERTIES OF PETG PRINTED OBJECTS

5.1: Introduction

The primary purpose of the work reported in this chapter is to identify PETG 3D printing conditions and characterize mechanical properties of the printed samples. As outlined in **Chapter 3**, two types of commercially available PETG materials: PETG-1(obtained as filament) and PETG-2 (obtained as pellets) were explored in this work. Physical properties of these two materials were characterized and compared between each other. The results show that PETG-2 materials have a much higher viscosity relative to PETG-1. Excessive high viscosity makes it not suitable for the 3D printing equipment used in this work. The conditions for printing PETG-1 samples were set to be the same as that of PLA-1 since the polymers possess similar viscosity. PETG is amorphous and does not form crystals. Thus, heat treatment has no significant effect on the improvement of mechanical performances for the printed samples. In addition, annealing gives rise to a severe thermal warping of samples. It enlarges the variation of mechanical properties and suppresses the enhancement of bonding between layers results from polymer chains' diffusion.

5.2: Results and Discussions

5.2.1: Processing conditions for PETG materials

Thermal Stability

Measurements of thermal and rheological behavior were performed for PETG materials to determine their processing conditions. TGA measurements allowed the identification of the degradation temperature of PETG which set up as an upper temperature limit for processing. DSC analysis provided the glass transition temperature of PETG materials. It indicates a lower temperature limit for the extrusion and printing.

TGA thermograph (**Figure 5.1**) shows that PETG-1 filament begins to decompose at 357°C. There is no weight change at the temperature of about 100°C, indicating that no water exists in the filaments. There is carbon with a weight percentage of 15.7% left over at the end of degradation. This phenomenon is well documented for PETG in literature[1-2].

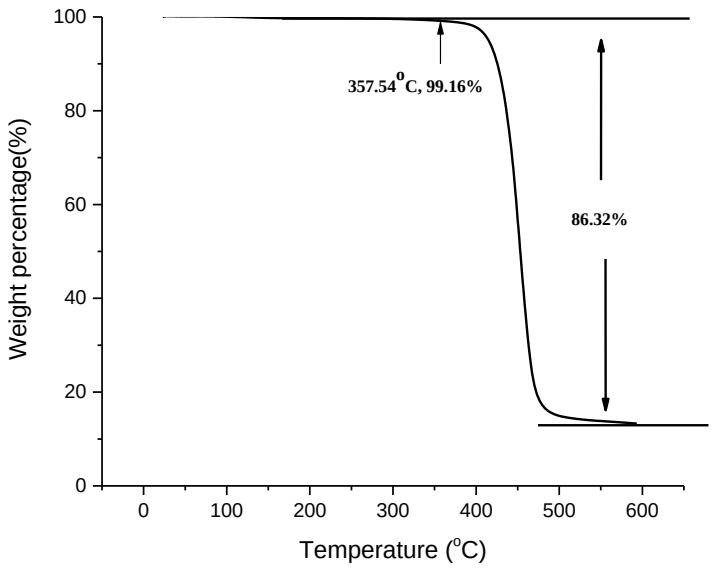

Figure 5.1: TGA thermographs of PETG-1 filament.

TGA thermograph (**Figure 5.2**) presents that the degradation of PETG-2 pellets starts at 386°C and ends at 600°C. The temperature for PETG-2 to degrade is higher than that of PETG-1. Carbon materials with a weight percentage of 7% were left over after degradation. Higher degradation temperature of PETG-2 pellets could be a consequence of higher molecular weight.

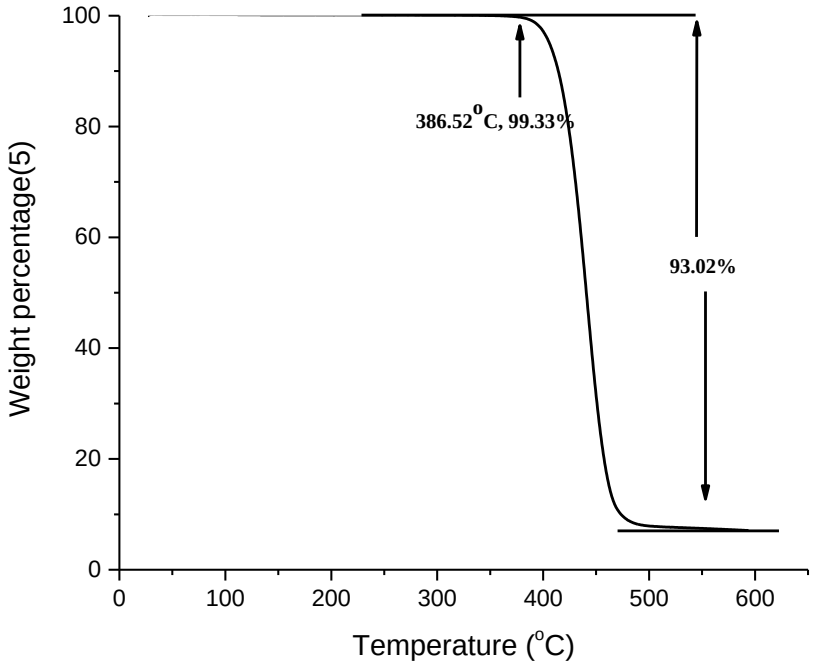

Figure 5.2: TGA thermographs of PETG -2 pellets.

DSC thermograph (**Figure 5.3**) shows that the glass transition temperature of PETG-1 filament is 72°C. A deep endothermal peak appears at the end of the glass transition. It is a sign of physical aging owing to the chain orientation, which formed during the fabrication of PETG-1 filament.

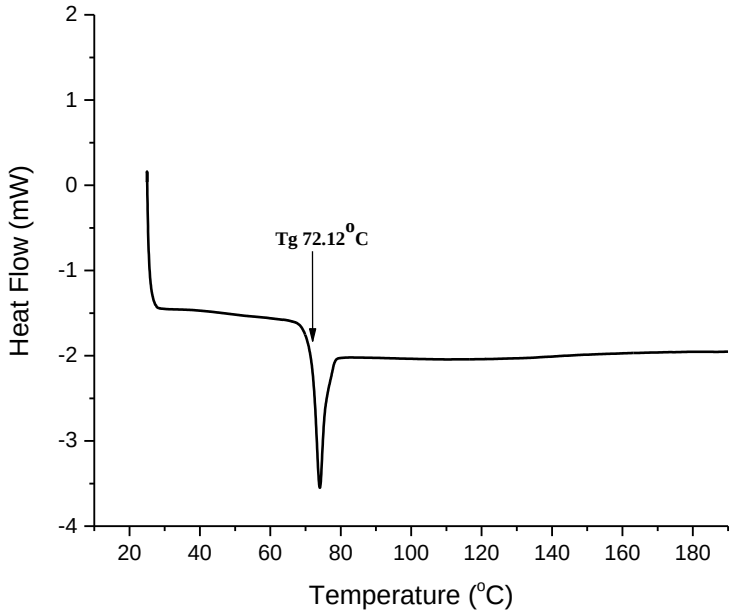

Figure 5.3: DSC thermographs of PETG-1 filament.

DSC thermograph of PETG-2 (**Figure 5.4**) indicates a glass transition temperature of 80°C. PETG-2 has a higher Tg relative to PETG-1. It could result from a larger molecular weight of PETG-2 pellets. A relatively smaller physical aging transition is presenting in PETG-2 thermograph comparing to PETG-1.

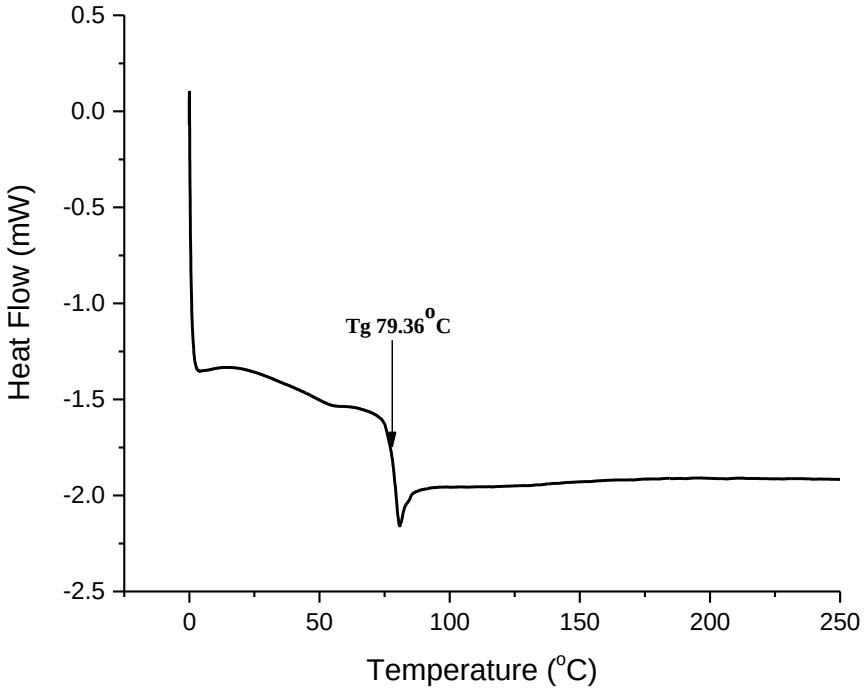

Figure 5.4: DSC thermographs of PETG -2 pellets.

According to Fox-Flory equation which describe the relationship between molecular weight Mn and glass transition temperature Tg[3]:

$$Tg = Tg,\infty - \frac{K}{Mn} \qquad \textbf{(5-1)}$$

where, Tg,∞ is the maximum glass transition temperature that can be achieved at a theoretical infinite molecular weight and K is an empirical parameter that is related to the free volume present in the polymer sample. The highest Tg,∞ reported in the literature for

PETG is 354±2K[4-6]. The ratio between molecular weight of these two PETG materials based on calculation is about 4.5.

In summary, the temperature range which can be utilized to process PETG materials is from the temperature higher than Tg which is about 80°C to the temperature lower than Td which is about 350°C. However, more characterization was conducted to narrow this range down.

Rheological Behavior

The temperature range that can be used to process PETG materials is too broad. Viscosity measurements can decrease extent of this range and help to determine specific temperatures within this range for processing PETG. Rheometer and Melt Flow Index tester were used to characterize rheological behavior of two PETG materials.

Viscosity measurements

The results of temperature ramp experiment (**Figure 5.5**) implies that the viscosity of PETG-1 declines with the rising of temperature. It decreases from 88Pa.s at 220°C to 20Pa.s at 250°C at a constant shear rate of $3s^{-1}$. Data in **Chapter 4** indicates that the viscosity of PLA-1 filaments reduces from 50Pa.s at 220°C to 11Pa.s at 250°C. The viscosity of PETG-1 is near by two times larger than that of PLA-1.

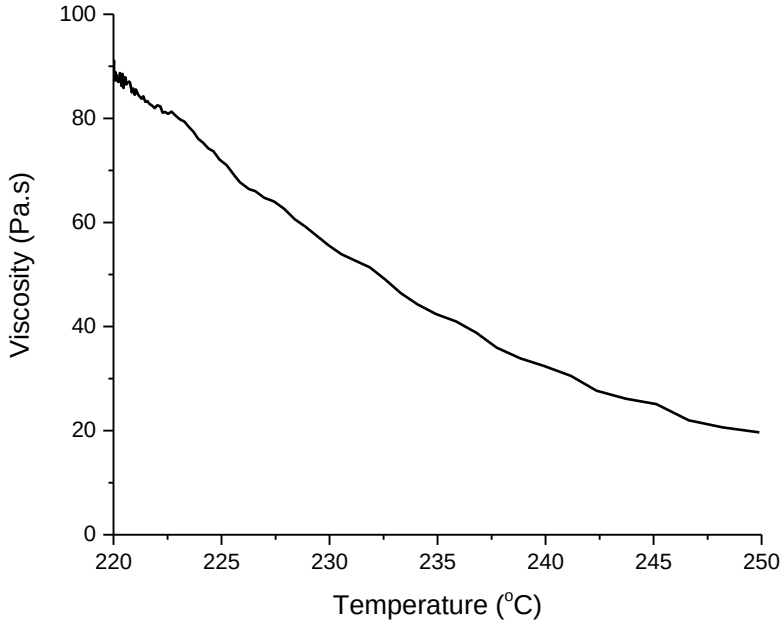

Figure 5.5: Viscosity temperature ramp measurement of PETG-1.

Figure 5.6 shows the natural logarithm of viscosity as a function of reciprocal temperature. The red line in the graph is the linear fitting of this relationship based on Arrhenius model[3] that was outlined in **Chapter 4**. The equation of the fitting line is y=-8+ 2755.05*x. The calculated activation energy for PETG-1 is 22.9kJ. Therefore, the temperature dependence of viscosity for PETG-1 can be estimated as:

$$ln\eta = -8 + 2755.05 * \frac{1}{T} \qquad (\mathbf{5\text{-}2})$$

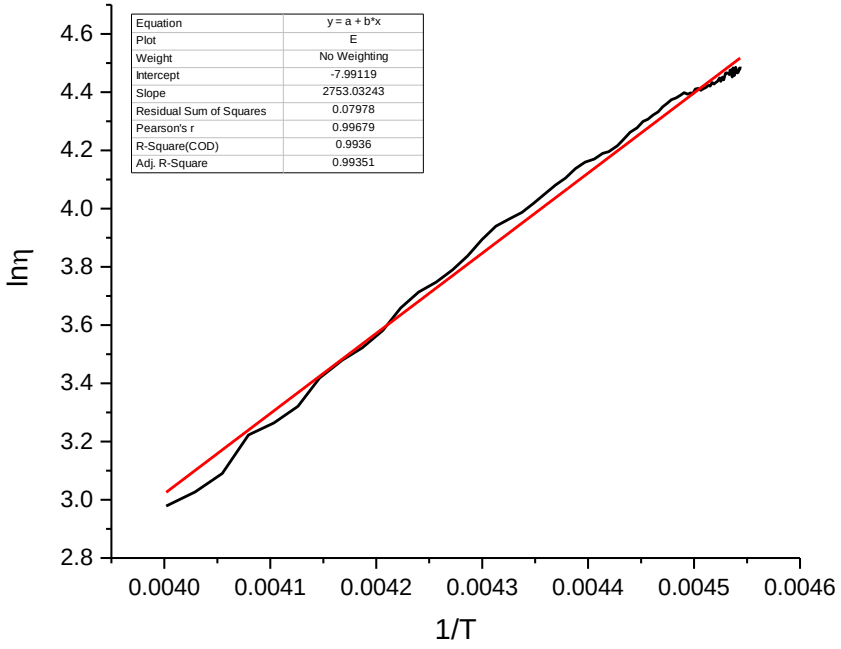

Figure 5.6: Linear fitting of temperature ramp data for PETG-1.

The temperature dependence of viscosity for PETG-2 is shown in **Figure 5.7 (a)**. The viscosity of PETG-2 materials is much higher than that of PETG-1 and also declines with the increasing of temperature at the constant shear rate of $3s^{-1}$. It reduces from 1720Pa.s at the temperature of 215°C to 556Pa.s at the temperature of 250°C. The linear fitting line of the lnη~1/T dependence is y=2621.5*x-7.5 (**Figure 5.7(b)**). Based on the Arrhenius model[3], the calculated activation energy of PETG-2 materials is 21.8kJ/mol. It is comparable with the activation energy for PETG-1 filament. However, the viscosity range which is proper for 3D printer reported in literature is 10-150Pa.s[7-9]. Even at the

highest temperature that our printer can reach, the viscosity of PETG-2 materials is still too high for the printing. Thus, PETG-2 pellets were not used in future study.

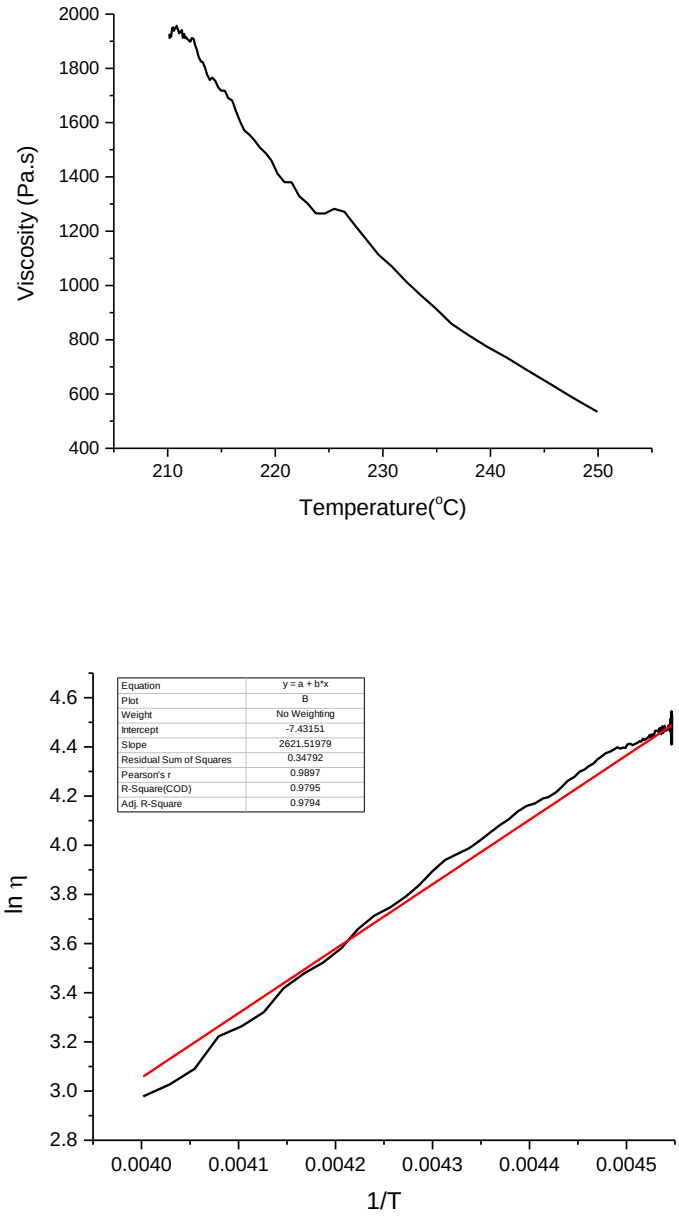

Figure 5.7: (a) Temperature ramp viscosity measurement of PETG-2; (b) linear fitting based on Arrhenius model.

Shear rate ramp experiments were performed only on PETG-1 at 215°C. The results (**Figure 5.8**) show that viscosity of PETG-1 also decreases with rising shear rate. It declines from 170Pa.s at the shear rate of $0.1s^{-1}$ to 10Pa.s at the shear rate of $10s^{-1}$. PETG-1 filaments can be considered as a shear thinning material.

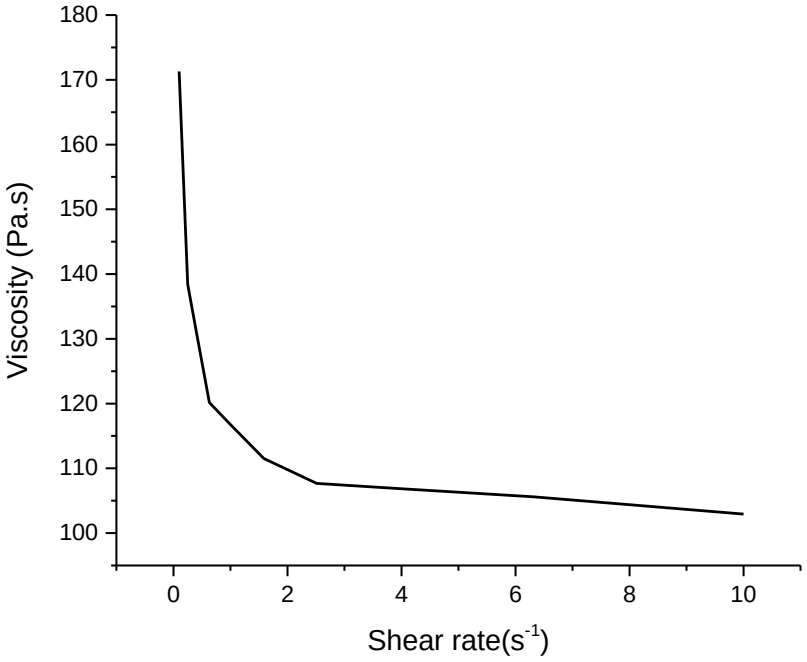

Figure 5.8: Viscosity shear rate ramp measurement of PETG-1.

According to the 'power-law'[3] presented in **Chapter 4**, linear fitting the curve of logη~logγ in **Figure 5.9** can be separated into four segments. The values of K_2 and n of PETG-1 (**Table 1**) shows a different behavior relative to that of PLA materials. K_2 of PETG-1 filaments is larger than that of PLA-1 filaments at the same testing conditions.

And the value of K_2 almost stays at the same order of magnitude at four regions. While the value of n keeps increasing along the four shear rate regimes.

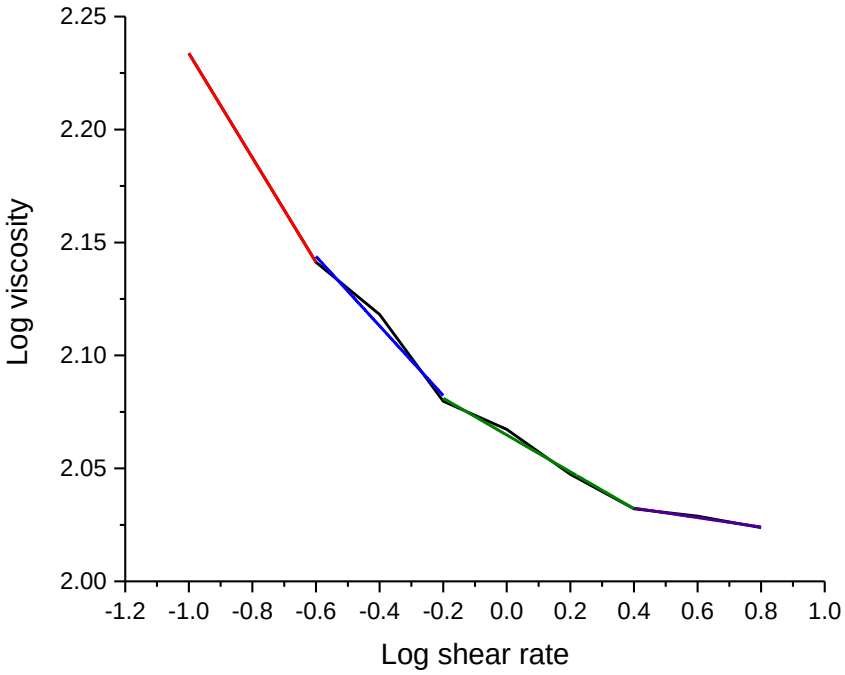

Figure 5.9: linear fitting of shear rate dependece of viscosity for PETG-1 based on 'power law'.

Table 5.1: Fitting lines of shear rate ramp viscosity of PETG-1 materials at temperature of 220 ^{o}C

Shear rate regime(s^{-1})	**Formula of fitting curve**	**Value of K_2**	**Value of n**
0.1-0.25	Y=-0.25*x+2.0259	100.6	0.77
0.25-0.6168	Y=-0.16*x+2.05	112.6	0.85
0.6168-2.5	Y=-0.08*x+2.06	116.86	0.92
2.5-10	Y=-0.02*x+2.04	109.84	0.98

Melt flow index

Data in **Table 2** and **Table 3** show that the MFI of PETG-1 and PETG-2 are 4g/10min and 1g/10min, respectively. The melt flow index results are in coherence with the viscosity measurements. Higher viscosity of PETG-2 leads to smaller MFI. Viscosity of PETG-1 materials is higher when comparing to PLA-1.

Table 5.2: Melt Flow Index of PETG-1

Material	**Sample Weight/g**	**Average Weight /g**	**MFI (g/10min)**
PETG-1	0.1805,0.1742,0.1652,0.1750,0.1871,0.1885,0.1982,0.2045,0.2075, 0.2144,0.2186,0.2257,0.2294,0.2521,0.2564,0.2560,0.2405,0.2462, 0.2540,0.2545,0.2577,0.2684,0.2755	0.2044	4.088
PETG-1	0.1785,0.1800,0.1785,0.1798,0.1819,0.1845,0.1869,0.1904,0.1928, 0.1958,0.2021,0.2049,0.2076,0.2129,0.2158,0.2179	0.1944	3.888
PETG-1	0.1960,0.1995,0.2055,0.2055,0.2074,0.2095,0.2112,0.2151,0.2149, 0.2166,0.2184,0.2201,0.2217,0.2256,0.2250,0.2266,0.2282,0.2299, 0.2515,0.2556,0.2554,0.2572	0.2155	4.266

Table 5.3: Melt Flow Index of PETG-2

Material	**Sample Weight/g**	**Average Weight/g**	**MFI (g/10min)**
PETG-2	0.0448,0.0482,0.0497,0.0499,0.0508,0.0508,0.0466,0.0517,0.0447, 0.0455,0.0516,0.0505,0.0448,0.0451,0.0508,0.0454,0.0495,0.0519, 0.0490,0.0487,0.0517,0.0497,0.0469,0.0492,0.0497,0.0488,0.0508, 0.0515,0.0502,0.0469,0.0464,0.0492,0.0494,0.0480,0.0514,0.0518, 0.0450,0.0485,0.0459,0.0479,0.0477,0.0495,0.0455,0.0516,0.0465, 0.0515,0.0451,0.0484,0.0495,0.0451	0.04856	0.9712

Rheological measurements show that the viscosity of PETG-2 is about 40 times higher than that of PETG-1. And therefore, PETG pellets were not used for further study since it is not suitable for the 3D printer. Rheological behavior of PLA and PETG-1 are

quite similar, with the viscosity of PETG-1 being slightly larger. Thus, the printing temperature of PETG-1 was also set to be 215°C.

5.2.2: Mechanical properties of 3D printed objects

Tensile Test

Tensile tests were performed on dog-bone samples described in **Figure 3.9, Chapter 3** along the direction perpendicular to the printed layers. The weakest bonding interlayers determines the ultimate tensile stress and tensile strain. It is a direct reflection of bonding strength between the layers.

Strain-stress curves (**Figure 5.10**) show that dog-bone samples fabricated from PETG-1 filaments have an average ultimate tensile stress of 48.5MPa and a tensile strain of 17%. No yield points is observed. The unstable behavior of tensile stress at the strain range of 0-5% results from the alignment of structural defects. Dog bone samples fabricated by 3D printer are not 100% infilled, therefore, there are voids inside samples structures. The material along the elongation would align first to compensate for the structural defects. After that, the diffusion of polymer chains and the distortion of covalent bonds play a leading role in affecting the stress[10].

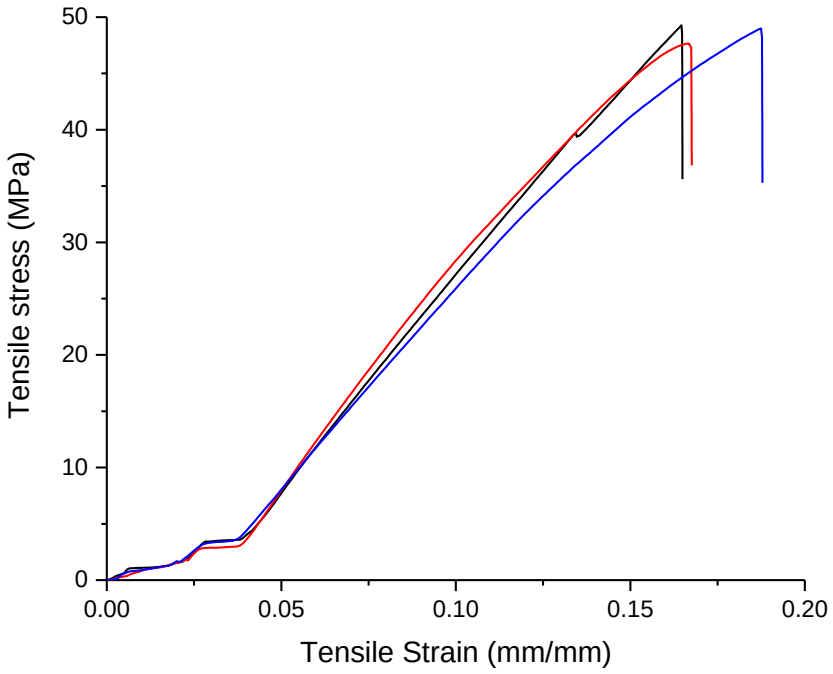

Figure 5.10: Tensile stress-strain curves of dog bones printed from PETG-1.

First derivative of tensile stress and strain yield tangent modulus. Except for the first structural alignment part, the tangent modulus keeps declining when increasing tensile strain. The re-orientating and diffusion of polymer chains along the elongation direction helps to relieve applied load and therefore, the modulus is decreasing. The largest tangent modulus is taken as Young's modulus which is about 425.5MPa (**Table 4**). It is 15% larger that Young's modulus of PLA-1. The Young's modulus of typical PETG materials is about 2.2 GPa as reported in literature[11], which is smaller than that of PLA. Relative higher mechanical performances of dog-bone samples printed from PETG-1 related to its layers

adhesion mechanism. The smaller Young's modulus of printed samples compared to conventionally manufactured objects manifests in the the worse mechanical performance nature of 3D printed structures.

Table 5.4: Young's modulus of dog-bone samples printed from PETG-1

Samples	**Ultimate Tensile stress (MPa)**	**Ultimate Tensile strain (%)**	**Young's modulus (MPa)**
1	49.5	16.6	434.4
2	47.7	16.8	458.7
5	47.9	17.1	383.5
Average	48.5±1.0	16.8±0.3	425.5±42

Dynamic Mechanical Analysis of the 3D printed samples

Samples are subjected to a series of stretching and relaxation cycles during the DMA measurements. DMA provides dynamic mechanical properties of printed samples under low deformation. DMA can also identify the viscoelastic properties of the materials. There are essential properties in determining the mechanical behaviors of printed samples. Samples printed at 0º were measured in the direction perpendicular to the printed layers during DMA analysis. Storage modulus is determined by bonding strength between layers. To investigate the anisotropic properties of 3D printed objects, samples printed at 90 º were measured in the direction parallel to the printed layers. Storage modulus is likely to be determined by the materials intrinsic properties in this case.

DMA measurements are compared between samples printed at two different raster angles. As mentioned in **Chapter 4**, samples are named as PETG-1/0° and PETG-1/90°. **Figure 5.11** shows that the storage modulus of PETG-1/0° is 2110MPA, whereas for PETG-1/90° is 1900MPa at room temperature. Storage modulus of PETG-1/0° is 11% larger than that of PETG-1/90° in the glassy region. The DMA measurements for PETG-1/90° were conducted along the printed layers, while for PETG-1/0° were performed in the direction perpendicular to the printed layers. What was expected was the storage modulus of PETG-1/90° to be higher than that of PETG-1/0°. However, the DMA results are again as in the case of PLA unexpected. We associate this fact with possibility that the samples were not fully loaded for PETG-1/90° during the measurements. The decrease of E' occurs during glass transition, leading to a much lower storage modulus at the rubbery plateau.

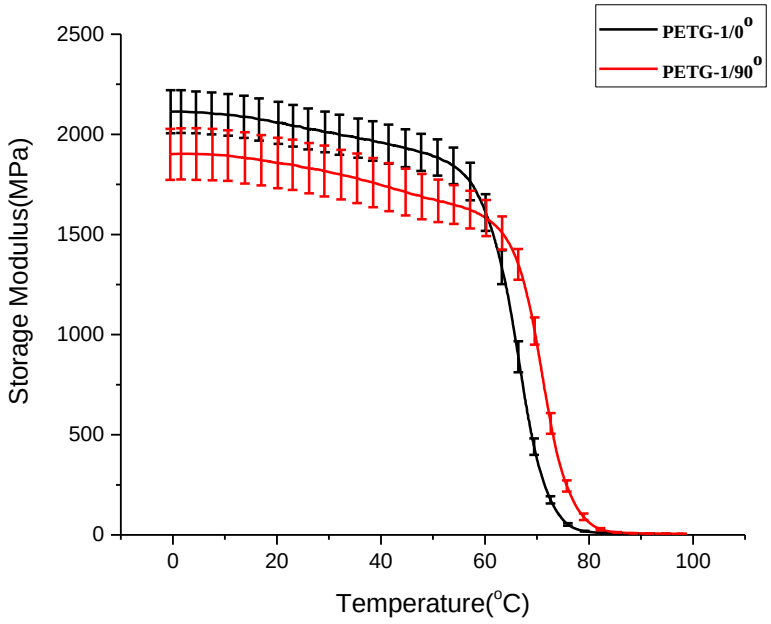

Figure 5.11: Storage modulus of PETG-1 samples printed at two raster angles.

Loss modulus (**Figure 5.12**) of PETG-1/90° shows a β-relaxation at the glassy region. β-relaxation comes from the rotation of backbone or movement of side groups[12]. Addition of glycol increases the flexibility of PET backbones and make the β-relaxation more likely to happen. This relaxation mechanism does not show in PETG-1/0°, indicating an anisotropic physical property nature of 3D printed objects. We associate the appearance of β relaxation only exists in PETG-1/90° with layer arrangement. Detailed mechanism is not yet understood.

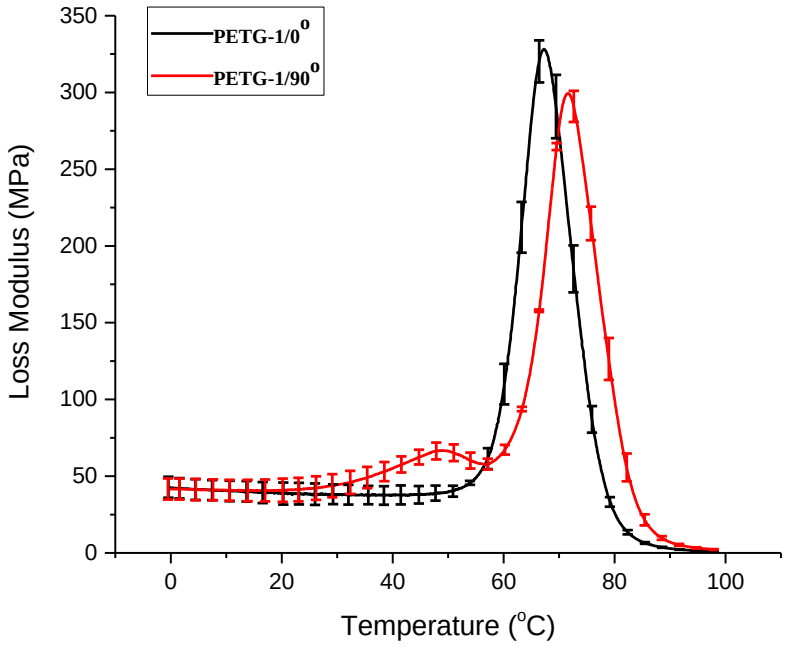

Figure 5.12: Loss modulus of PETG-1 samples printed at two raster angles.

Glass transition region starts at a higher temperature for PETG-1/90° than that for PETG-1/0°. Tg derived from the peaks of tan δ (**Figure 5.13**) are 78°C and 83°C for PETG-1/0° and PETG-1/90°, respectively. PETG-1/90° samples have well-arranged polymer chains due to the shear effect when materials flowing through the nozzle[13]. Well-packed polymer chains increase the inter-chains friction, making the free motion of polymer chains more difficult.

A more extensive peak value of tan δ for PETG-1/90° compared to PETG-1/0°, implying a more viscous behavior of PETG-1/0° in the glass transition region. The symmetry of tan δ peaks is similar for both samples. The width of tan δ peak relates to the homogeneity of chemical and/or physical network within materials[14].

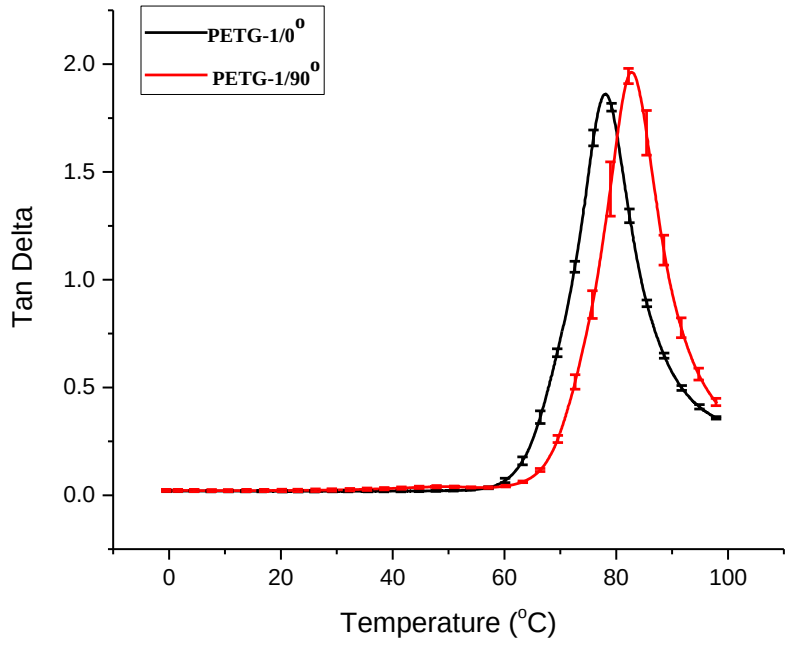

Figure 5.13: Tan Delta of PETG-1 samples printed at two raster angles.

If we compare the DMA results for PETG to the PLA-1 ones, it can be concluded that the physical properties anisotropic nature of PETG-1 samples is more prominent. It is also important that the storage modulus of samples fabricated from PETG-1 is about 20% smaller than that of samples fabricated from PLA-1. Materials' intrinsic properties and layers bonding account for storage modulus at glassy state. Young's modulus of PETG materials is about 37% smaller than that for PLA materials.

Comparison of DMA results (**Figures 5.14, 5.15** and **5.16**) for PETG-1/0° between before and after the annealing shows that average storage modulus has a small increase after the heat treatment. Both the shape and value of loss modulus and tan δ does not change much. Whereas significant variations of dynamic mechanical properties show up for PETG-1/0° samples after conducting heat treatment. The variation of physical properties increased due to the thermal warp. As shown in **Figure 5.17**, PETG-1 samples show severe bending and curling after heat treatment. It is still a significant challenge for the post-processing heat treatment.

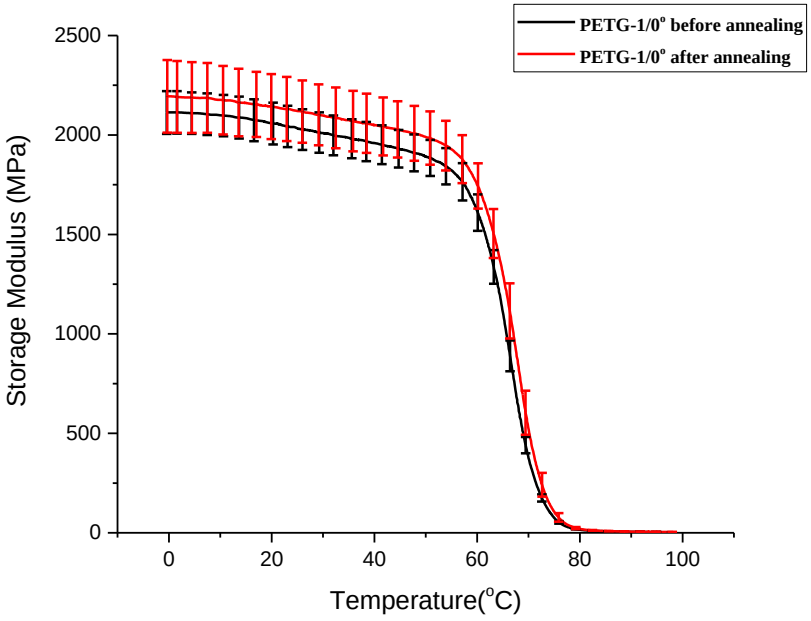

Figure 5.14: Storage modulus of PETG-1 samples tested at 0° before and after conducted annealing.

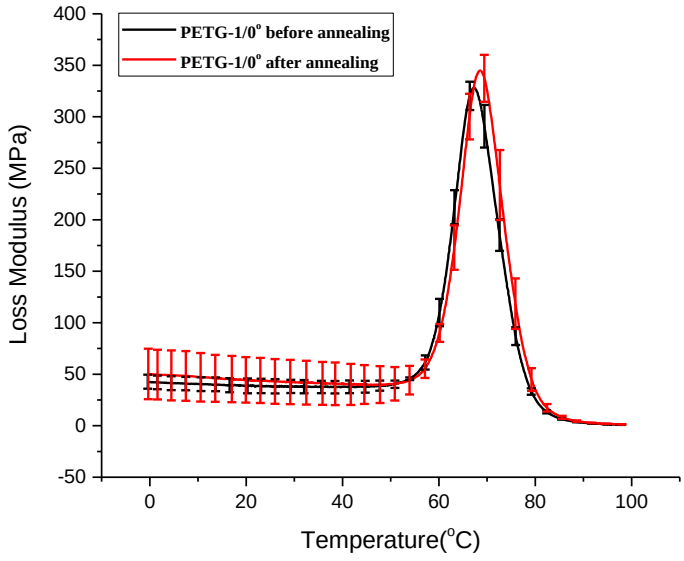

Figure 5.15: Loss modulus of PETG-1 samples tested at 0° before and after conducted annealing.

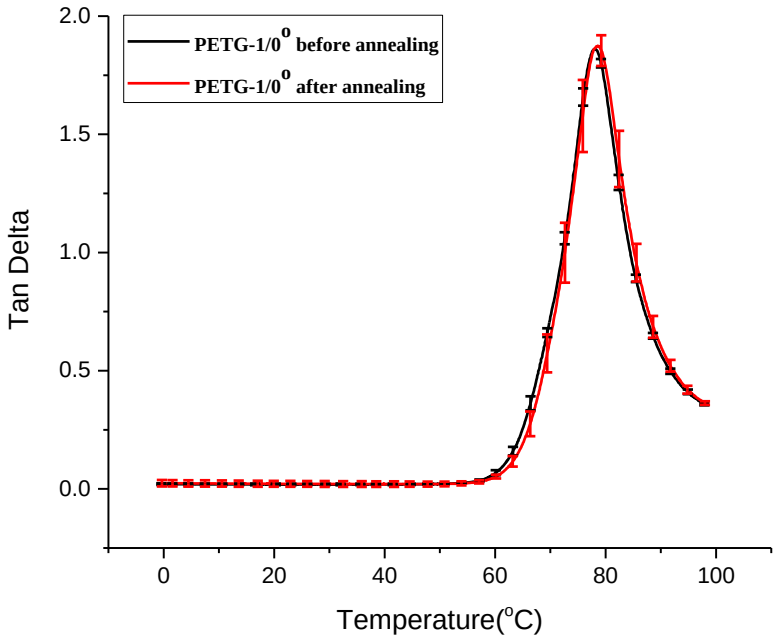

Figure 5.16: Ten delta of PETG-1 samples tested at 0° before and after conducted annealing.

Figure 5.17: Photograph of morphology of samples printed from PETG-1 before and after heat treatment.

One noticeable change in comparison (**Figure 5.18**, **5.19** and **5.20**) of PETG-1/90° is the loss of β-relaxation after annealing. β-relaxation is conventionally attributed to the highly polarized carboxyl group. The carboxyl group polar moment's hindrance effect have on the rotation of the groups around it could lead to a sudden 180° rotational jump and form a relaxation peak[5]. During the heat treatment, polymer chains release from stretched states and transfer into preferred random coil states. Hindrance effect resulting from carboxyl group polar moments weakens due to the formation of 'comfort zone' and therefore, the β-relaxation vanished.

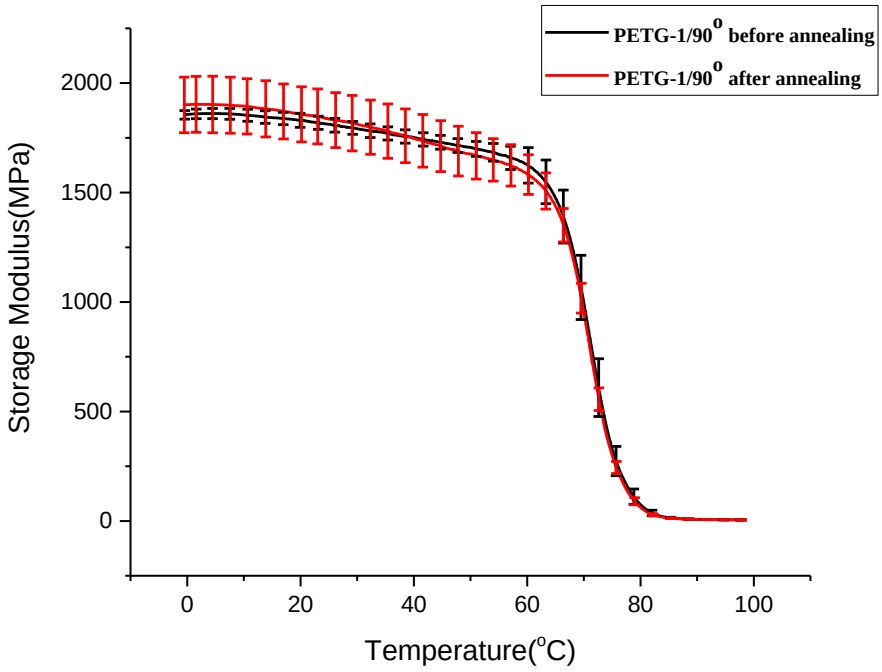

Figure 5.18: Storage Modulus of PETG-1 samples tested at 90° before and after conducted annealing.

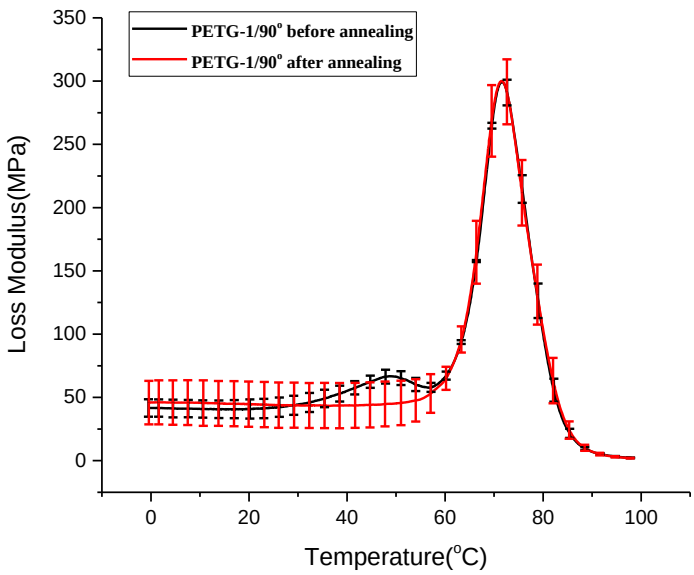

Figure 5.19: Loss Modulus of PETG-1 samples tested at 90° before and after conducted annealing.

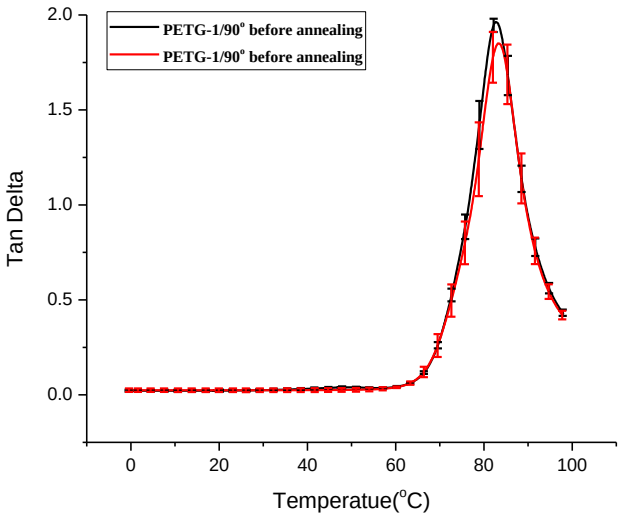

Figure 5.20: Ten delta of PETG-1 samples tested at 0° before and after conducted annealing.

In summary, the shape and position of storage modulus, loss modulus, and tan δ for PETG-1 samples stay the same after the heat treatment. The increment of physical properties' variation comes from serious thermal warping and curling as a result of the annealing.

5.3: Conclusions

Following key conclusions can be derived from experiments described above:

- PETG filaments and pellets have very different physical properties. PETG-2 pellets have a much higher viscosity, making it unsuitable for the 3D printer;
- PETG would not crystallize and therefore, there is no significant change in dynamic mechanical properties after the heat treatment. The increment of physical properties' variation results from thermal warping;
- PETG filaments have higher viscosity, smaller MFI and lower storage modulus compared to PLA. Tensile tests prove that 3D printed PETG-1 samples are more brittle in comparison to PLA-1 samples.

5.4: References

1. Shadpour, H.; Musyimi, H.; Chen, J. F.; Soper, S. A., Physiochemical properties of various polymer substrates and their effects on microchip electrophoresis performance. *J Chromatogr A* **2006,** *1111* (2), 238-251.

2. Dupaix, R. B.; Boyce, M. C., Finite strain behavior of poly(ethylene terephthalate) (PET) and poly(ethylene terephthalate)-glycol (PETG). *Polymer* **2005,** *46* (13), 4827-4838.
3. Sperling, L. H., Introduction to Physical Polymer Science, 4th Edition. *Introduction to Physical Polymer Science, 4th Edition* **2006**, 1-845.
4. Yoon, J. D.; Cha, S. W., Change of glass transition temperature of polymers containing gas. *Polymer Testing* **2001,** *20* (3), 287-293.
5. Scott, C. E.; Macosko, C. W., Morphology Development during the Initial-Stages of Polymer-Polymer Blending. *Polymer* **1995,** *36* (3), 461-470.
6. Handa, Y. P.; Wong, B.; Zhang, Z. Y.; Kumar, V. P.; Eddy, S.; Khemani, K., Some thermodynamic and kinetic properties of the system PETG-CO2, and morphological characteristics of the CO2-blown PETG foams. *Polym Eng Sci* **1999,** *39* (1), 55-61.
7. Hung, K. C.; Tseng, C. S.; Hsu, S. H., Synthesis and 3D Printing of Biodegradable Polyurethane Elastomer by a Water-Based Process for Cartilage Tissue Engineering Applications. *Adv Healthc Mater* **2014,** *3* (10), 1578-1587.
8. Weng, Z. X.; Zhou, Y.; Lin, W. X.; Senthil, T.; Wu, L. X., Structure-property relationship of nano enhanced stereolithography resin for desktop SLA 3D printer. *Compos Part a-Appl S* **2016,** *88*, 234-242.
9. Mittal, K. L., Adhesion Measurement of Films and Coatings .1. *J Adhes Sci Technol* **1993,** *7* (8), 765-766.
10. J. X. 11, M. S., ' A. HILTNER,'** and E. BAER', The ductile-to-quasi-brittle transition of particulate-filled thermoplastic polyester.pdf. *Journal of Applied Polymer Science.* **1994,** *62,255-267*
11. http://2015.igem.org/wiki/images/2/24/CamJIC-Specs-Strength.pdf. (accessed 02/19/2018).

12. Smith, G. D.; Bedrov, D., Relationship between the α- and β-relaxation processes in amorphous polymers: Insight from atomistic molecular dynamics simulations of 1,4-polybutadiene melts and blends. *Journal of Polymer Science Part B: Polymer Physics* **2007,** *45* (6), 627-643.
13. Compton, B. G.; Lewis, J. A., 3D-Printing of Lightweight Cellular Composites. *Adv Mater* **2014,** *26* (34), 5930-+.
14. Townsend, J.; Burtovyy, R.; Aprelev, P.; Kornev, K. G.; Luzinov, I., Enhancing Mechanical and Thermal Properties of Epoxy Nanocomposites via Alignment of Magnetized SiC Whiskers. *Acs Appl Mater Inter* **2017,** *9* (27), 22927-22940.

CHAPTER 6

FABRICATION AND PROPERTIES OF PRINTED BI-COMPONENT PLA/PETG STRUCTURES

6.1: Introduction

This chapter focuses on the fabrication of bi-component structures from PLA-1 and PETG-1 using the dual-feed 3D printer. Hybrid structures with various compositions were obtained by changing the feeding ratio between two filaments. The structures were printed at two different raster angles and their morphology was observed with the polarized optical microscope. We estimated the miscibility level between PLA and PETG using AFM imaging of PLA/PETG polymer blend film. AFM results showed a clear phase separation in the polymer blend film. DSC thermographs showed two glass transition temperatures which correspond to the Tg of each polymer. Therefore, the polymers are immiscible.

Heat treatment was explored to investigate the effect of annealing on the improvement of interfacial bonding strength in the bi-component structures. Also filaments from PLA/PETG blend were used in the bi-component structure fabrication to enhance the interfacial adhesion. DMA analysis was employed to characterize dynamic mechanical properties of the printed samples obtained at different processing conditions. Results show that both the heat treatment and usage of the blend filaments can improve the mechanical performances of 3D printed bi-component PLA/PETG structures.

6.2: Results and Discussions

6.2.1: Miscibility Characterization

Atomic Force Microscopy Characterization

In order to investigate the miscibility between PLA and PETG, the joint solution of these two materials was used to obtain polymer blend film. The morphology of the film was observed with AFM. A representative image of the polymer film having the composition of PLA: PETG=8:2 weight percentage (**Figure 6.1)** shows a clear pattern of phase separation. Images of the polymer blends with other compositions are presented in **Appendix 1 (Figure A1.1)**. Based on the composition, it is clear that the darker matrix is PLA-1, while the brighter dispersion phase is PETG-1. It can be concluded from the AFM results that PLA and PETG are highly immiscible.

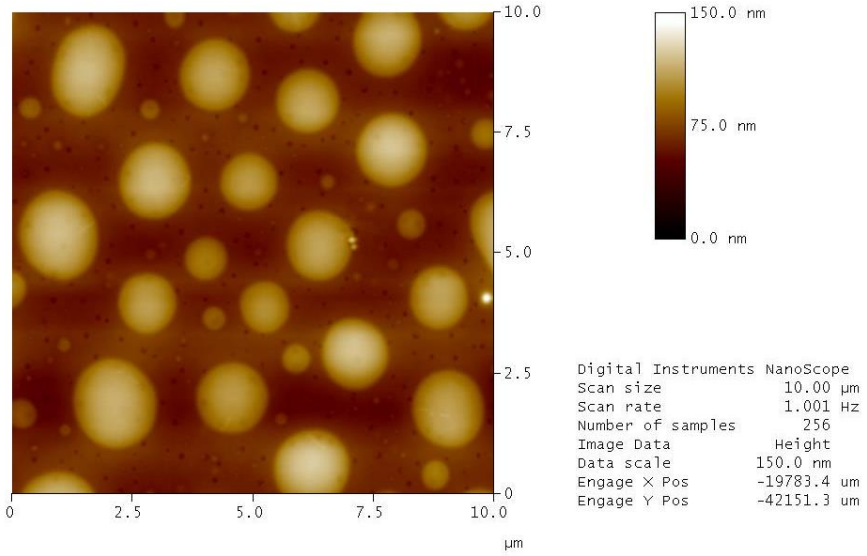

Figure 6.1: AFM photograph of PLA/PETG blend film with the compositions of PLA: PETG=8:2.

DSC Thermal Analysis

Miscible polymer blend would have only one glass transition temperature which would be located between the Tg of each polymer[1]. While, there would be two separate glass transitions shown on DSC thermographs when two polymers are immiscible. Therefore, DSC analysis to follow the polymer miscibility was conducted for PLA/PETG solution casted blend with different compositions. **Figure 6.2** shows representative DSC thermograph of the polymer blend with the composition of PLA: PETG=8:2. DSC thermographs of polymer blend with other compositions are presented in **Appendix 1 (Figure A1.2)**.

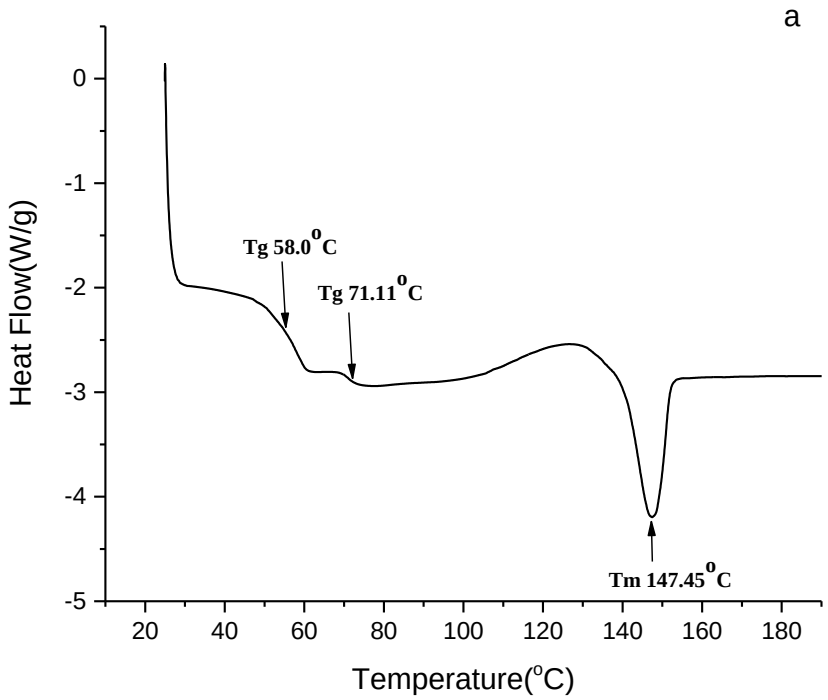

Figure 6.2: DSC thermograph of PLA/PETG blend with the composition of PLA: PETG=8:2.

DSC thermographs of the PLA/PETG blend have two separate glass transitions which are 58ºC and 71ºC. As mentioned in **Chapter 4** and **Chapter 5,** the glass transition temperatures for PLA-1 is 60ºC and for PETG-1 is 72ºC. Then it can be concluded that the two Tg shown in the DSC thermograph correspond to the glass transitions of PLA-1 and PETG-1, respectively. This result confirms PLA/PETG immiscibility. Since PETG would not crystallize, the crystallization and melting peaks result from PLA-1 material. Integration shows that the area under two curves are 4.5J/g and 6.4J/g, respectively. According to the **Equation 3-1** (**Chapter 3)**, the calculated percent of crystallinity is about 2%. There is no sharp boundary between crystallization and melting peaks which can be interpreted as the crystals with smaller sizes already melting when forming the larger crystals.

Comparison the DSC thermographs of pure PLA-1 with the one for polymer blend (**Figure 6.3**) shows that the crystallization and melting temperature are somewhat higher for the polymer blend. It appears that the presence of PETG phase is causing this increase. Crystals begin to form at higher temperature where polymer chains have more energy to overcome the barriers and pack regularly. Higher melting temperature is an indication of the formation of crystals with larger sizes.

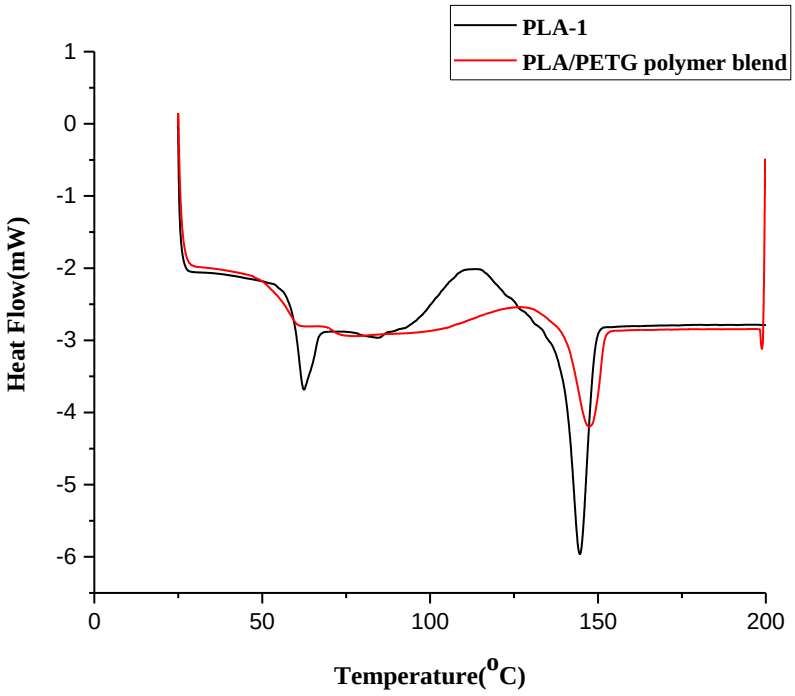

Figure 6.3: Comparison of DCS thermographs of PLLA-1 and PLA/PETG blend.

To summarize, the combination of AFM and DSC results indicate that these two materials are highly immiscible. The presence of PETG within PLA matrix can somewhat retrain PLA polymer chains from forming crystals, leading to a higher crystallization temperature.

6.2.2: Structure of the printed bi-component samples

Fourier-transform infrared spectroscopy

Bi-component structures were fabricated using the dual-feed 3D printer. As illustrated in the **Figure 6.4**, the 3D printer feeds two filaments simultaneously. We printed structures at two different raster angles, 0º and 90º. Since there are no stirring tools within the nozzle head, it is unknown whether PLA and PETG are mixed within the nozzle or form layered structures via laminar flow as shown in **Figure 6.5**. In order to identify the structures of the bi-component materials, FTIR spectra were first obtained on both sides of the samples printed at 0º. If PLA/PETG materials are well mixed in the nozzle, spectra of both sides should be close to each other and represent a combination of the spectrum for pure materials. However, if PLA and PETG formed layered structures that are only attached at the interfaces, FTIR spectra of both sides would be significantly different.

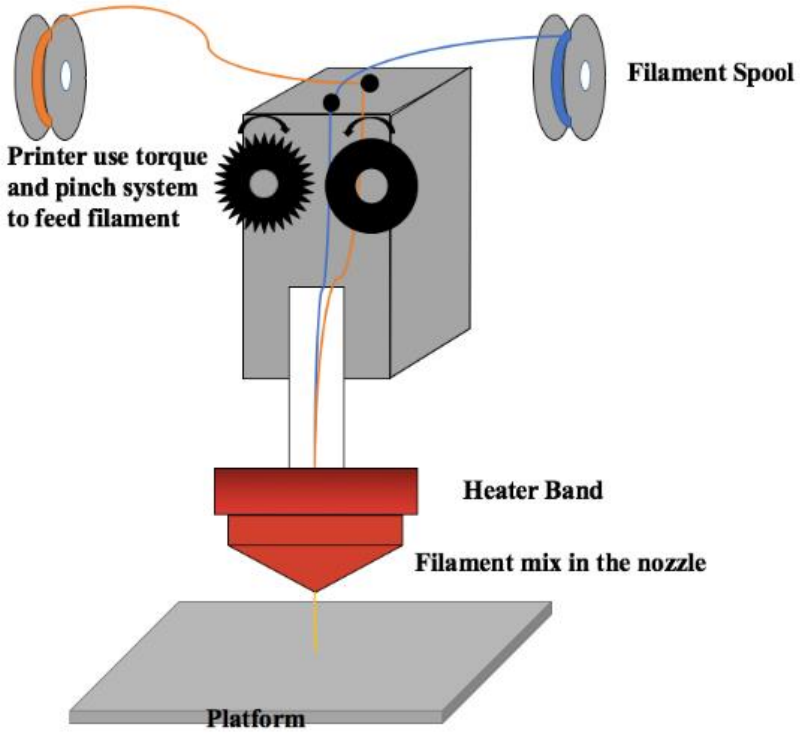

Figure 6.4: Schematic illustration of dual-feed 3D printer.

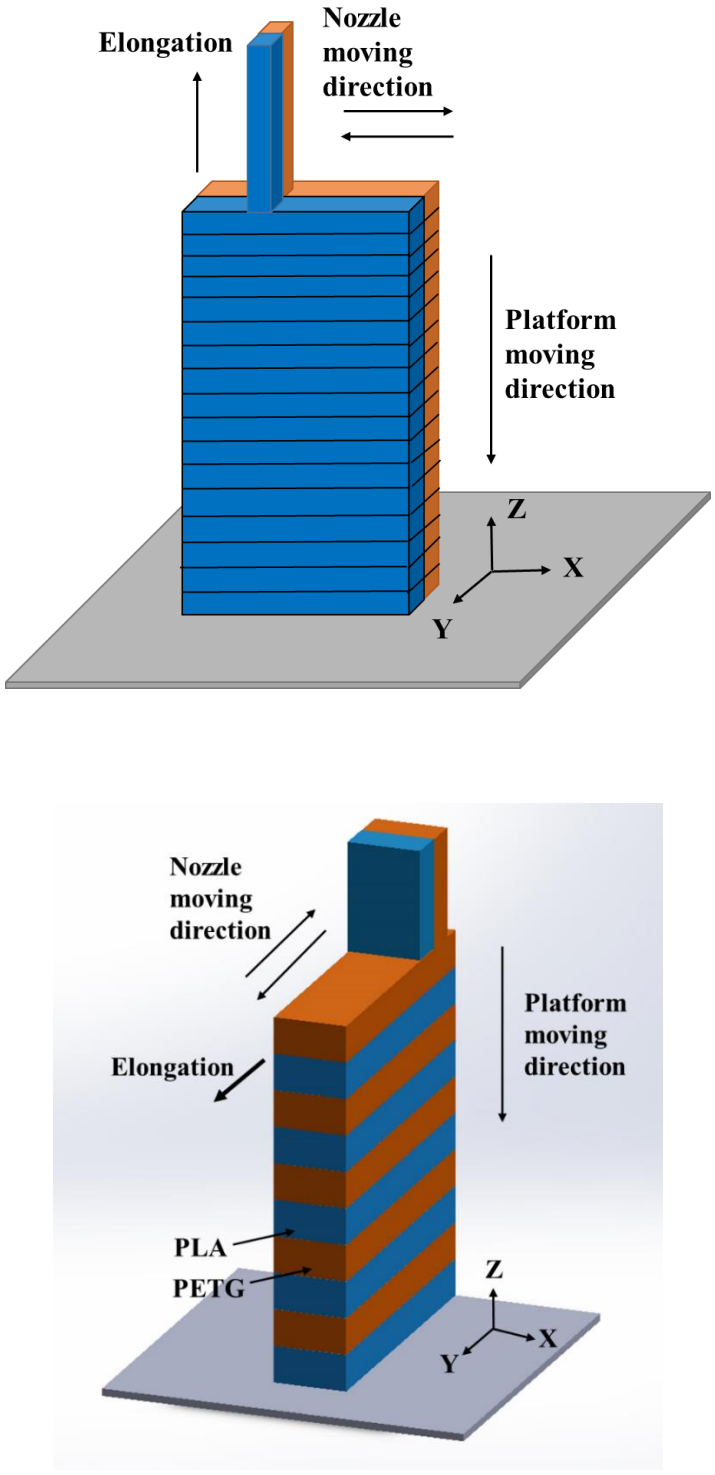

Figure 6.5: Schematic illustration of structures of samples printed at two raster angles. (a) 0°, (b) 90°.

Figure 6.6 shows a representative FTIR stack spectra for the samples printed from pure materials and solvent mixed polymer blend at 0°. FTIR stack spectra for hybrid structures with other compositions are presented in **Appendix 1** (**Figure A1.3**). For the spectrum of PLA pure material, peaks at 2965cm^{-1} originated from the alkyl C-H group stretching[2]. Peak observed at 1747cm^{-1} is due to the stretching of ester C=O group. Peaks at the wavenumber range of 1180-1080cm^{-1} result from the motion of C-C (O)-O group. In the spectrum of pure PETG, the prominent peak at wavenumber of 722 cm^{-1} comes from the C-H bending in the aromatic group. The double peaks can be seen at wavenumber around 1700 cm^{-1} in the spectrum of solvent mixed polymer blend. It is the summation of peak at 1713cm^{-1} in the spectrum of PETG and peak at 1747cm^{-1} in the spectrum of PLA. Double peaks present at the wavenumber around 750cm^{-1} is the combination of the peak at 722cm^{-1} in PETG-1 spectrum and the peak at 754cm^{-1} in PLA-1 spectrum. Spectra of both sides for the samples printed at 0° are quite different and there are no double peaks show up at wavenumbers around 1700cm^{-1} and 750cm^{-1}. The spectrum of one side practically corresponds to pure PLA while the other side corresponds to pure PETG. Therefore, it can be concluded that mixing of PLA-1 and PETG-1 in the nozzle is not significant.

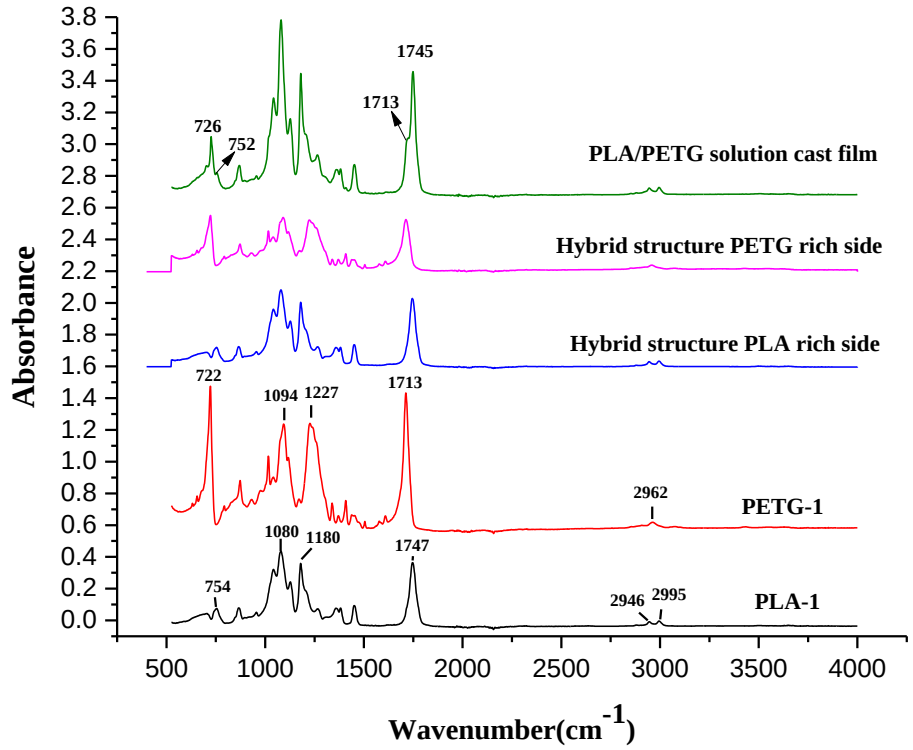

Figure 6.6: FTIR spectrum for both sides of bi-components samples.

Optical Microscopy

To further explore the structures of the printed bi-component samples, the polarized optical microscope was used to observe their cross sections. The images of the structures for all the hybrid samples are shown in **Appendix 1** (**Figure A1.4** and **Figure A1.5**). The thickness of these two layers confirms that the printed hybrid structures follow the designated composition. **Figure 6.7 (a, b)** shows the arrangement of two materials in the samples printed at two raster angles. For samples printed at 0°, PLA-1 and PETG-1 formed two thin layers and packed next to each other. While for samples printed at 90°, PLA-1 and

PETG-1 packed layer by layer along the z-axis. Schematic illustration of idealized layers packing pattern (**Figure 6.8**) for bi-component samples printed at two raster angles are close to the experimentally observed one (**Figure 6.5**).

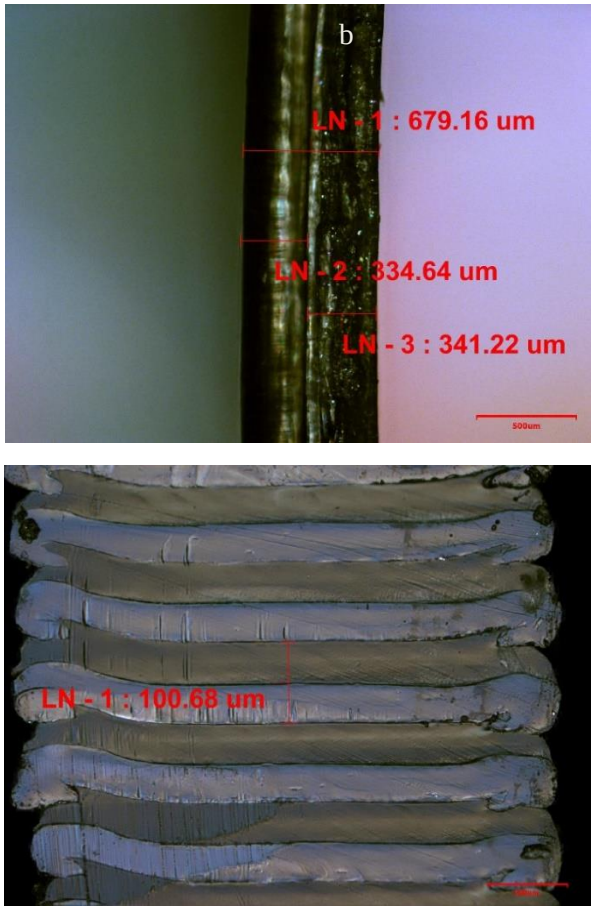

Figure 6.7: Microscope image of cross section for DMA samples with the composition of PLA: PETG=5:5 printed at two raster angles. (a) 0°, (b) 90°.

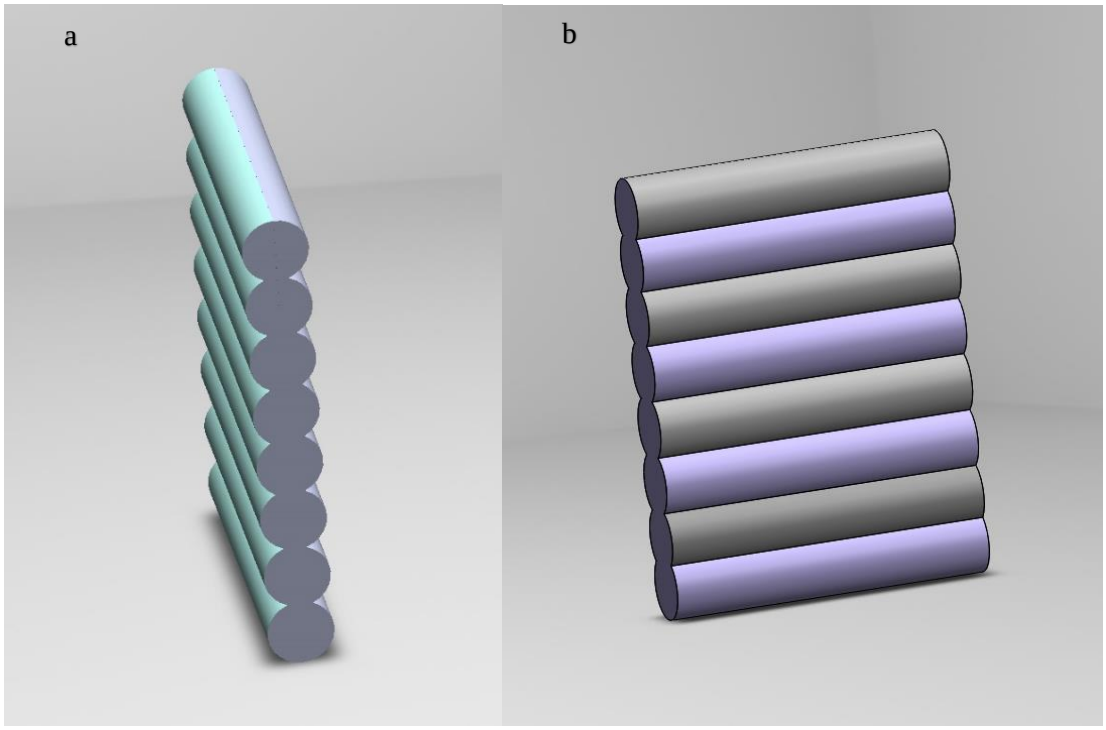

Figure 6.8: Schematic illustration of DMA samples printed at two raster angles. (a) 0°, (b) 90°.

Images obtained from the polarized microscope confirm that the dual-feed 3D printer does not mix these two materials in the nozzle. Rather it creates different conformations for the bi-component structures printed at two raster angles. Since PLA and PETG would not bond to each other at the interface due to their immiscibility, any methods utilized to improve the layers' adhesion can be straight forwardly detected.

The elongation direction in DMA analysis for samples printed at 0º was along the z-axis (**Figure 6.5 (a)**). Since, the interlayers' adhesion for samples is quite weak due to the immiscibility between PLA-1 and PETG-1, the DMA measurements could not be done

along the z-axis for 90° samples. Thus, the elongation direction for the samples printed at 90° during DMA measurements was performed along y-axis as shown in **Figure 6.5 (b)**.

6.2.3: Optimization of the annealing temperature for heat treatment

The utilization of heat treatment to increase adhesion between printed layers should be conducted at the temperature higher than Tg but lower than Tm. As illustrated in **Figure 6.9**, the temperature should be high enough to allow for the interpenetration of PLA-1 and PETG-1 polymer chains at the interface. It creates an inter-penetration zone which can enhance the interlayers bonding strength. Besides, annealing at this temperature supports the formation of crystal phase in PLA-1. Therefore, it is expected that the heat treatment can improve mechanical properties of the 3D printed objects through the inter-diffusion of polymer chains and the increase of crystallinity in PLA. However, the temperature of the heat treatment should be lower than Tm of PLA to avoid the distortion of sample shape.

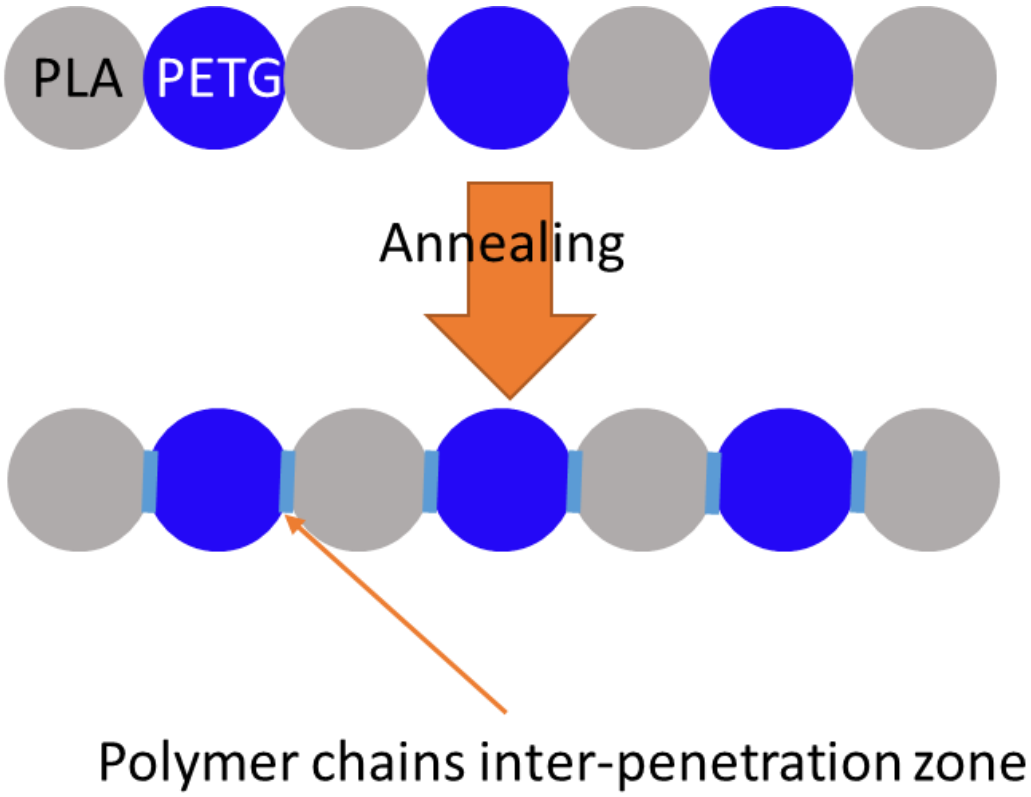

Figure 6.9: Schematic illustration of bonding strength enhancement through the heat treatment.

In order to determine the optimum temperature for the heat treatment, DMA analysis was utilized to characterize the annealing temperature dependence on mechanical properties of the bi-component samples printed at 0º. For convenience, we follow the terminology established in **Chapter 4**. For example, hybrid structures with the composition of 50vol%PLA and 50vol%PETG that printed at 0º are abbreviated as 5PLA-5PETG/0º.

DMA results of storage modulus for the 8PLA-2PETG/ 0° after the annealing at different temperatures are shown in **Figure 6.10**. It indicates that the storage modulus

increases along the whole temperature range in comparison with the hybrid samples without performing the heat treatment. And the improvement of storage modulus also rises with the annealing temperature. At room temperature (25°C), storage modulus for samples annealed at 80°C is 2031MPa and for samples annealed at 100°C is 2306MPa, while for samples before annealing is only 1777MPa. There is a 14.3% and 30% increase relative to the storage modulus for hybrid samples before the heat treatment.

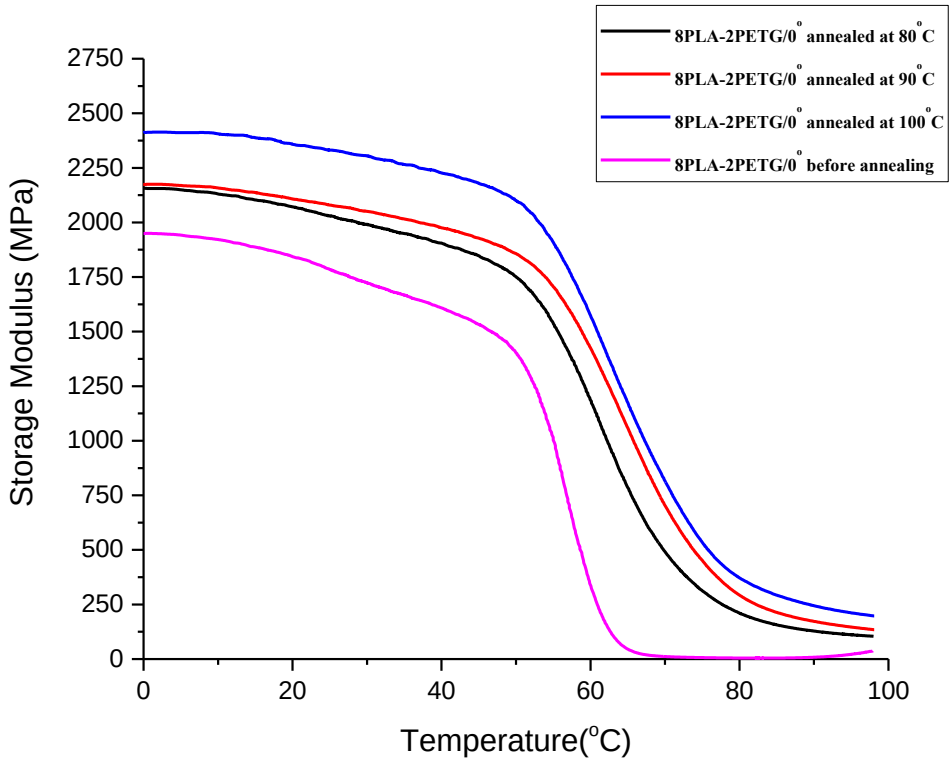

Figure 6.10: Storage modulus of bi-components samples printed at 0° after annealing at different temperature.

Interestingly, the variation of mechanical properties between parallel samples decreased with the annealing temperature (**Figure A1.6**, **Appendix 1**). The reason for this phenomenon could be the induced inter-penetration zone between PLA and PETG at interface. However, in comparison with the hybrid samples before the heat treatment, the mechanical properties variation between parallel samples increased first while then declines after the annealing. Stability of the storage modulus values for samples annealed at 100ºC is comparable to the samples before the annealing. Additionally, according to the annealing temperature dependence of percent of crystallinity reported in **Chapter 4** (**Figure 4.26**), the threshold annealing temperature to reach the maximum percent of crystallinity in PLA-1 is 100°C. Above this temperature, increasing annealing temperature can only increase the size of formed crystals. In summary, 100°C was decided to be the optimum annealing temperature.

The shift of the peaks' location in loss modulus (**Figure 6.11**) is a result of crystalline phase formation, which is restricting the motion of polymer chains within amorphous region.

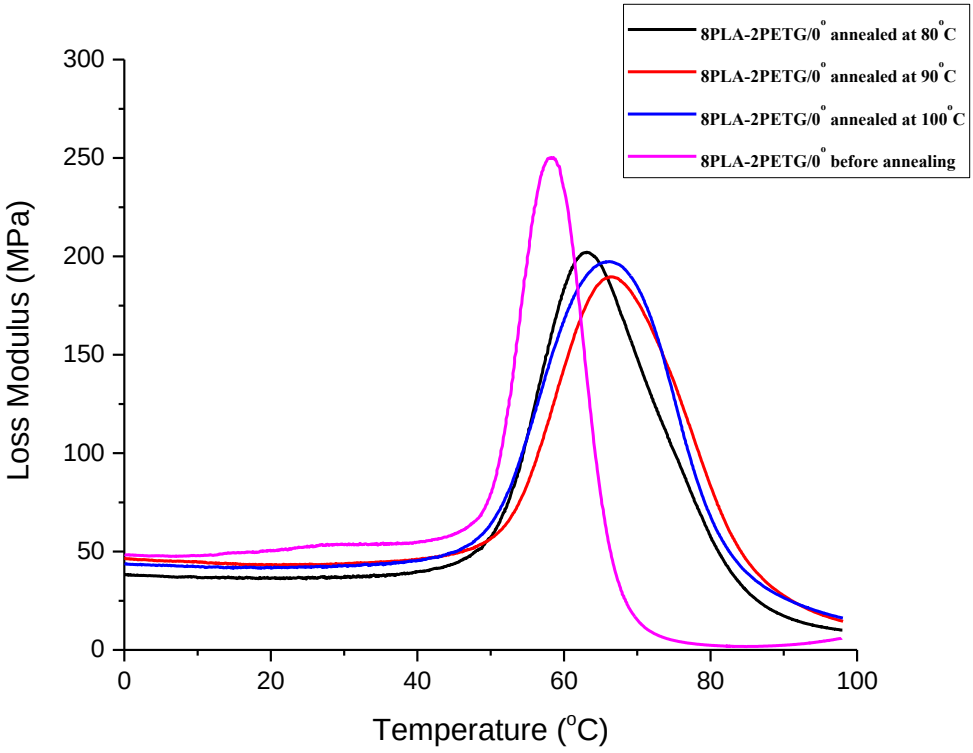

Figure 6.11: Loss modulus of bi-components samples printed at 0° after annealing at different temperature.

Glass transition temperature derived from the peaks of tan delta (**Figure 6.12**) shows an increase of Tg for annealing temperature of 90°C in comparison to 80°C and 100°C. Tg is a reflection of the outset of polymer chains movement. Higher Tg indicates that the mobility of polymer chains is more restricted. Increasing annealing temperature causes increase in the percent of crystallinity within PLA-1 materials and, therefore, the restriction effects caused by the formed crystals are more prominent. However, further increasing the annealing temperature would result in the increase of crystals sizes as well.

It is suggested that the smaller crystals are more efficient in restraining the motions of polymer chains[3]. That is why samples annealed at 90°C have a higher glass transition temperature than that annealed at 100°C.

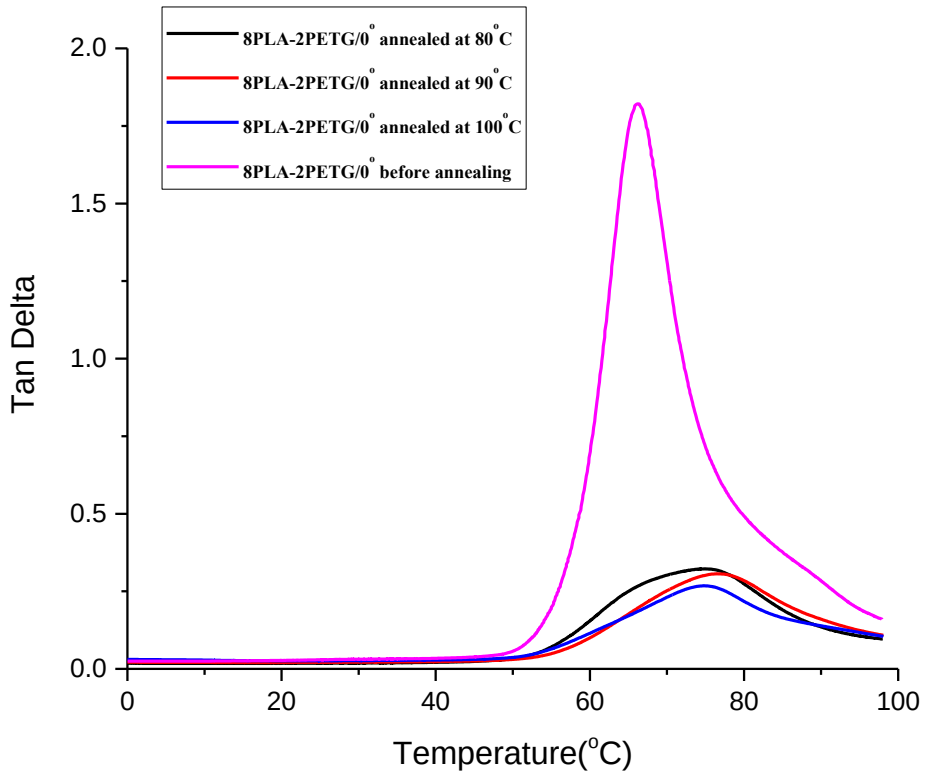

Figure 6.12: Tan Delta of bi-components samples printed at 0° after annealing at different temperature.

The value of tan delta peaks decline at higher annealing temperature due to the increase of percent of crystallinity in PLA. Additionally, in comparison with the tan delta of pure materials, tan delta for bi-component structures has a more symmetric shape. The

shape of tan delta for bi-component structures is originated from glass transition temperature of PLA-1 and PETG-1. Since peaks of tan delta for these two materials are located at different positions, the shape of tan delta for bi-component structures is distorted before the annealing. The enhancement of bonding between these two materials after annealing suppresses the two separate peaks and merges them into one.

It can be concluded that the mechanical properties of printed bi-component samples can be improved through increasing annealing temperature. Merging of tan delta peaks indicates the enhancement of adhesion between PLA-1 and PETG-1 interfaces. After combining the percent of crystallinity and the sizes of formed crystals in PLA-1, the heat treatment temperature was decided to be at 100°C to optimize the mechanical performances of the printed hybrid structures.

6.2.4: Mechanical performances improvement by heat treatment

Heat treatment has been already proven to increase mechanical properties of the 3D printed objects[4]. However, to the best of our knowledge, there is no research published devoted to the heat treatment conducted on the printed bi-component structures. DSC analysis was conducted on hybrid structure that were annealed in an oven at 100ºC for 2hrs. The DSC thermograph of 7PLA-3PETG/0º sample (**Figure 6.13**) shows two separate glass transitions which correspond to the Tg of each polymer. And there is no crystallization peaks. The two melting peaks indicate crystals with two sizes distribution were formed during the heat treatment. The area of the melting peak is about 20.4J/g. And the calculated

percent of crystallinity is about 31%. It is same as the highest percent of crystallinity that can be formed in PLA-1(**Figure 4.31**, **Chapter 4**).

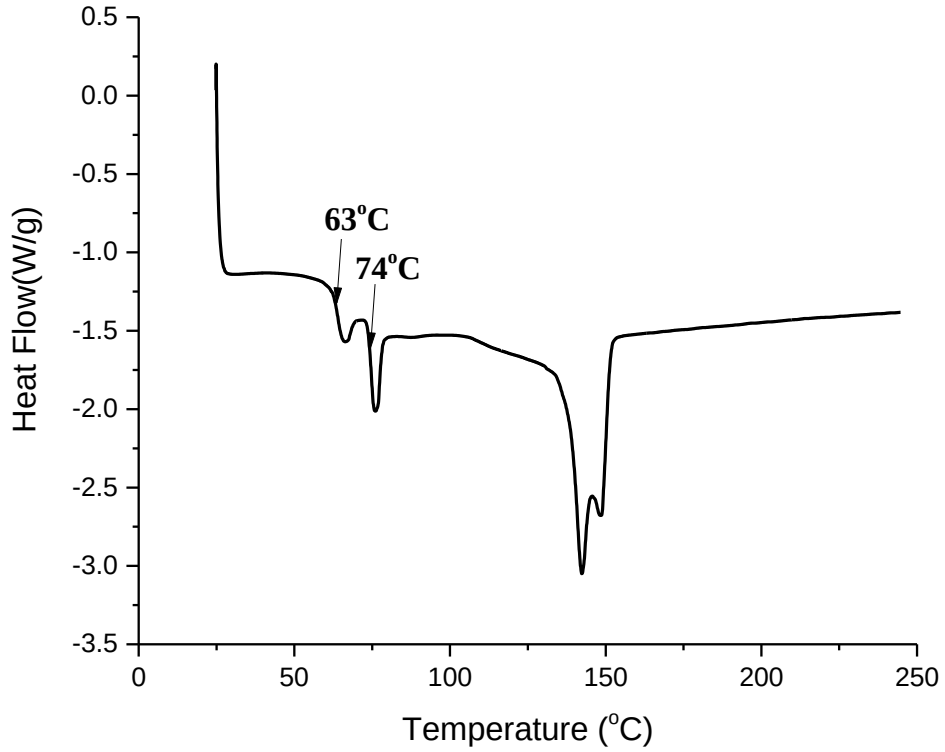

Figure 6.13: DSC thermograph of hybrid structure after the heat treatment.

Bi-component samples printed at 0°

After the DSC measurements, the mechanical performances of bi-component samples printed at two raster angles with different compositions were studied by DMA.

As mentioned above, DMA analysis was performed along the z-axis for samples printed at 0°. After the measurements, DMA results were compared among bi-component samples with different compositions between before and after the heat treatment. A representative plot of the storage modulus for 7PLA-3PETG/0° samples is shown in **Figure 6.14**. It indicates the increase of storage modulus as a result of the annealing. It is necessary to point out that the variation in mechanical properties among all the parallel samples declines significantly after the heat treatment as shown in **Appendix 1** (**Figures A1.7 - A1.11**). We suggest that the decrement of mechanical properties variation results from the consistent inter-penetration zone formed at PLA/ PETG interfaces as a result of the heat treatment.

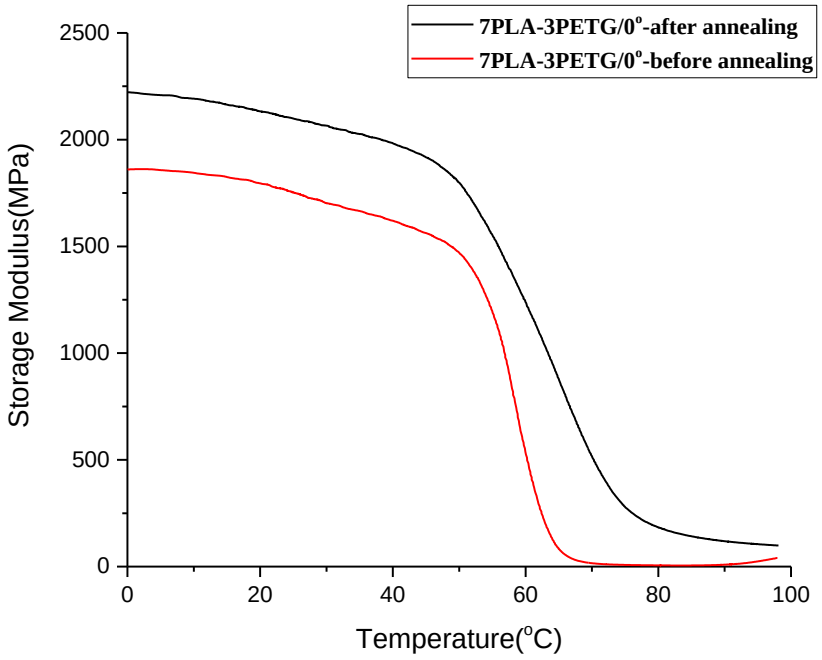

Figure 6.14: Comparison of storage modulus for samples printed 0° before and after annealing.

Double peaks that are seen in the loss modulus for samples with the percentage of PLA less than 70wt% (**Figures A1.7** and **A1.8**, **Appendix 1**) disappeared after the heat treatment. Loss of separate peaks and widen of transition region for loss modulus result from the enhancement of mechanical interaction between two immiscible polymers. Loss modulus of 7PLA-3PETG/0° (**Figure 6.15**) in rubbery plateau region decreased rapidly to MPa level before heat treatment. However, this decline of loss modulus becomes less pronounce for the annealed samples. We associate this observation with the formation of crystals within the PLA material.

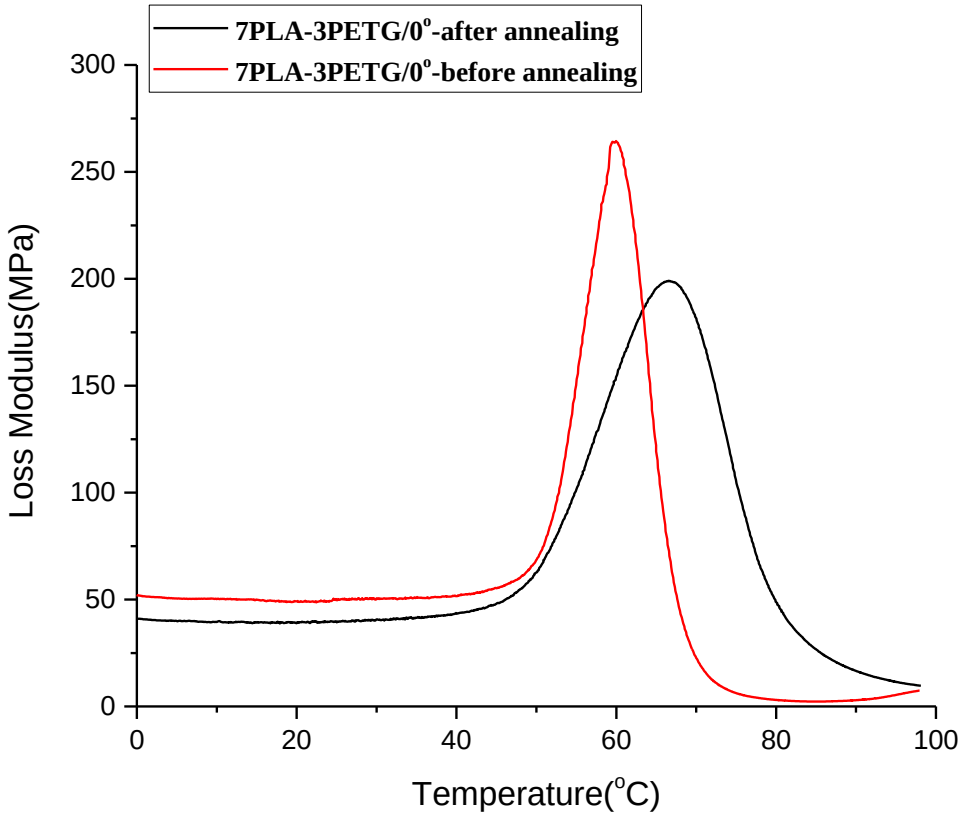

Figure 6.15: Comparison of loss modulus for samples printed 0° before and after annealing.

The value of tan delta peak for PETG is much larger than that for PLA in 5PLA-5PETG/0° samples (**Figure A1.7**). Tan delta is a reflection of viscoelasticity level of materials. PLA can form crystals after annealing, while PETG would not. Thus, the viscous portion in mechanical behavior for PETG-1 is much higher than that in PLA-1.

Tan delta for 7PLA-3PETG/0º samples (**Figure 6.16**) and samples with other compositions (**Figures A1.7 - A1.11, Appendix 1**) show two separate peaks before the annealing. The two separate peaks merged into one after the annealing and located between the peaks of PLA-1 and PETG-1. The single peak is also broader in comparison with the tan delta of hybrid samples before annealing. We suggest that as a result of the annealing process and the formation of inter-penetration zone at PLA-1/PETG-1 interface shift the peaks closer. **Fox Equation** can be used to predict the Tg of the miscible polymer blend[5-6]. It can be utilized to explain the broadening of the glass transition temperature range. First of all, the inter-penetration zone is very thin, about several nanometers, and thus, there is no enough materials for each polymer to show an apparent Tg. In addition, this zone has well distributed PLA-1 and PETG-1 polymer chains at each point. The formula of **Fox Equation** is:

$$\frac{1}{Tg} = \frac{W1}{Tg1} + \frac{W2}{Tg2} \qquad \textbf{(6-1)}$$

where, Tg_1 and Tg_2 are the glass transition temperatures of each component within the polymer blend, and W_1 and W_2 are the weight percentage of each component. Since the inter-penetration zone has a composition gradient, then the Tg has a gradient as well. As a result, a wide transition peak in tan delta formed for the hybrid samples after the annealing.

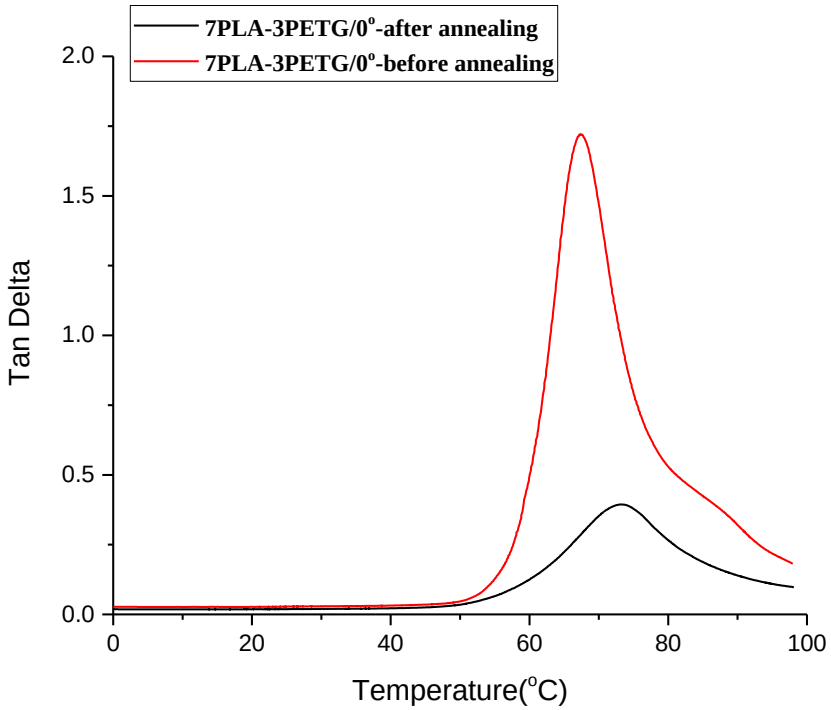

Figure 6.16: Comparison of tan delta for samples printed 0° before and after annealing.

Storage modulus of the bi-component structures with all the compositions at room temperature (25°C) and rubbery plateau (90°C) are plotted in **Figure 6.17** and **Figure 6.18,** respectively. To better understand the mechanical performances of the printed hybrid structures, **Voigt isostrain modulus model** was applied[7]. It can be used to predict the modulus for an idealized lamellar composites that assuming perfect bonding between the layers. As shown in **Figure 6.17**, the model can be utilized to calculate the modulus along the direction vertical to the layers attaching orientation.

Based on this model, strain for two lamellar is the same and force F acting on the composites equal to the sum of force acting on each lamellar.

$$F = f_{PLA} + f_{PETG} \qquad (\mathbf{6\text{-}2})$$

Force equal to stress times area, thus

$$\sigma A = \sigma_{PLA} A_{PLA} + \sigma_{PETG} A_{PETG} \qquad (\mathbf{6\text{-}3})$$

Since the PLA and PETG two lamellar have the same length, volume can be used to substitute area. Therefore, this equation can be re-written into:

$$\sigma V = \sigma_{PLA} V_{PLA} + \sigma_{PETG} V_{PETG} \qquad (\mathbf{6\text{-}4})$$

Under iso-strain condition, stress in equation (**6-3**) can be replaced by Young's Modulus. Since the basic mechanism of testing Young's modulus and Storage Modulus are the same, thus, we use Storage Modulus to replace Young's modulus and equation (**6-4**) is obtained:

$$EV = E_{PLA} V_{PLA} + E_{PETG} V_{PETG} \qquad (\mathbf{6\text{-}5})$$

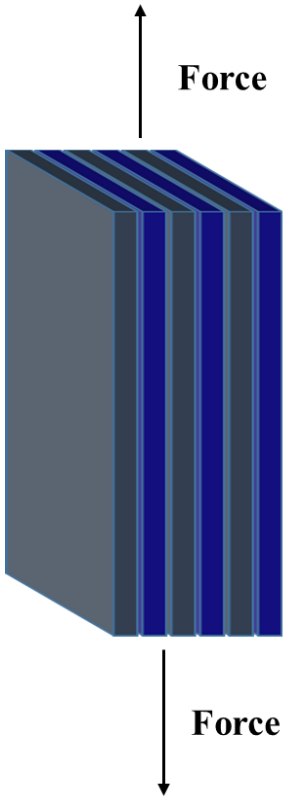

Figure 6.17: Schematic illustration of Voigt average modulus model.

The calculated ideal moduli for laminated structures are presented in **Figure 6.18** and **Figure 6.19** for the comparison. Increase of the storage modulus is apparent after the annealing for samples/0° (**Figure 6.18**). This augment has a tendency to rise with the increasing ratio of PLA within the hybrid structures. With the increase of PLA ratio within the bi-component samples, the improvement of storage modulus increases from 7% for 5PLA-5PETG/0° to 34% for 9PLA-1PETG/0°. The increase of storage modulus for the hybrid samples after the heat treatment comes from the increase of crystallinity within PLA-1 and the enhancement of bonding between PLA-1 and PETG-1. Thus, it is obvious

that the improvement of storage modulus rises with higher percentage of PLA within the hybrid structures. However, storage modulus declines after annealing for pure PLA printed samples. It can be associated with samples shape distortion after the heat treatment.

Comparison between the measured storage modulus with the theoretical ones shows that the actual storage moduli are significantly smaller than the theoretical ones before the annealing (**Figure 6.18**). While they approach the tendency of the ideal moduli after the heat treatment for hybrid structures with high PLA contents. It indicates that the layers' adhesion between PLA-1 and PETG-1 towards the ideal contact after annealing.

The significant augment of storage modulus at rubbery plateau results from the formation of crystals within PLA-1 since the crystalline phase has 3 orders of magnitude higher than rubbery phase modulus (**Figure 6.19**). At the rubbery plateau, the measured storage moduli keeps following the theoretical ones. It is a sign of good mechanical performances of the printed bi-component samples.

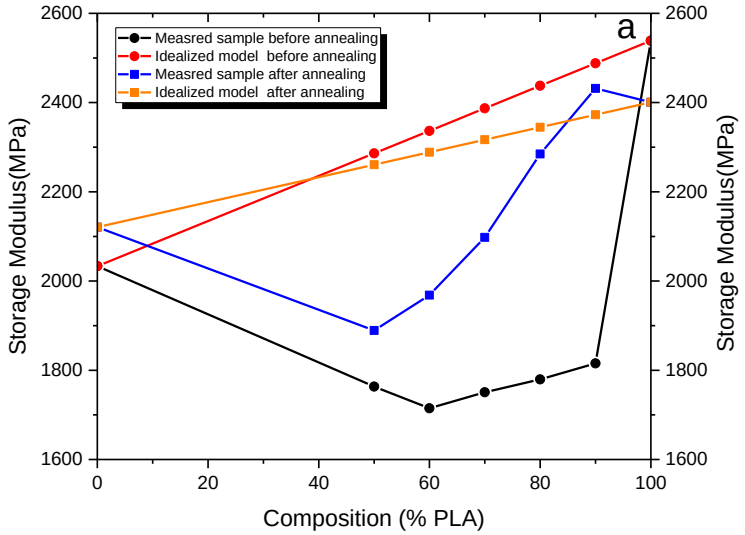

Figure 6.18: Storage modulus compare between samples printed at 0° and ideal model at room temperature (25ºC).

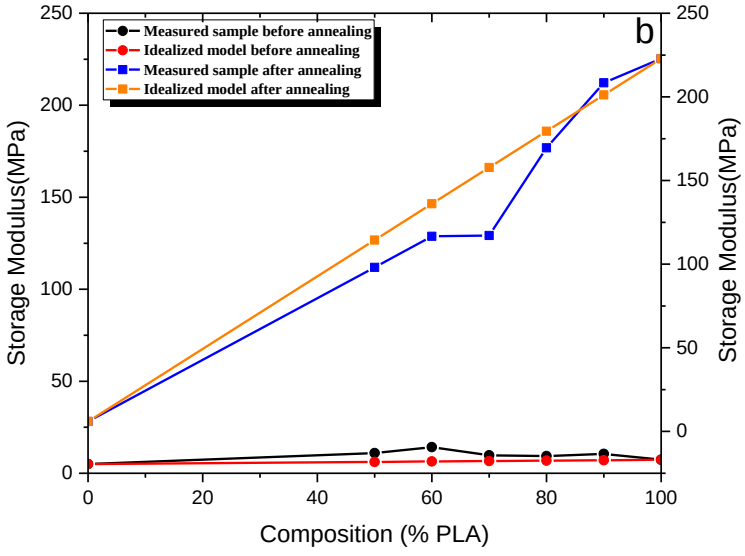

Figure 6.19: Storage modulus compare between samples printed at 0° and ideal model at rubbery plateau (90°C).

Bi-component samples printed at 90°

Due the immiscibility of PLA and PETG polymers and very low level of adhesion, DMA can only be conducted along y-axis for the samples printed at 90°. Comparison of DMA results for samples with all different compositions are presented in **Appendix** 1 (**Figures A1.12 - A1.17**). A representative comparison of storage modulus (**Figure 6.20)** for 7PLA-3PETG/90° bi-component samples between before and after annealing show the similar behaviors observed for the samples printed at 0°. Loss modulus and tan delta for 7PLA-3PETG/90° samples (**Figure 6.21** and **Figure 6.22**) have apparent double peaks which turned into one wide peak after the annealing. It relates to the formation of the inter-penetration zone during the heat treatment. Besides, the variation in all parameter values also declined after the heat treatment, meaning that the mechanical properties of printed samples became more stable (**Figure A1.12** to **Figure A1.17, Appendix 1**).

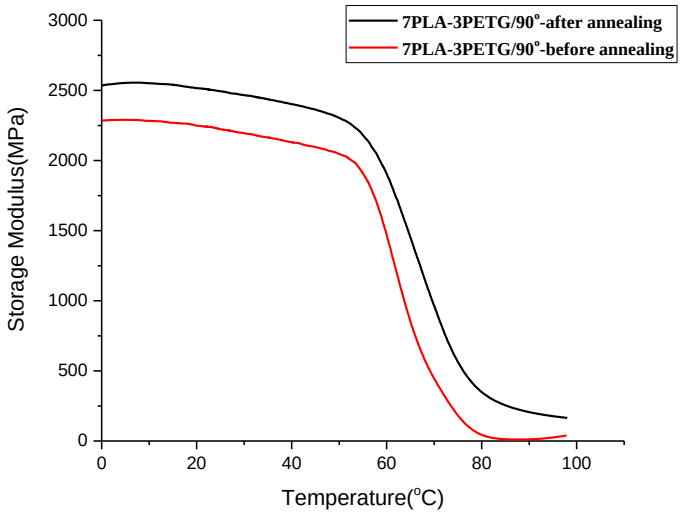

Figure 6.20: Comparison of storage modulus for samples printed 90° before and after annealing.

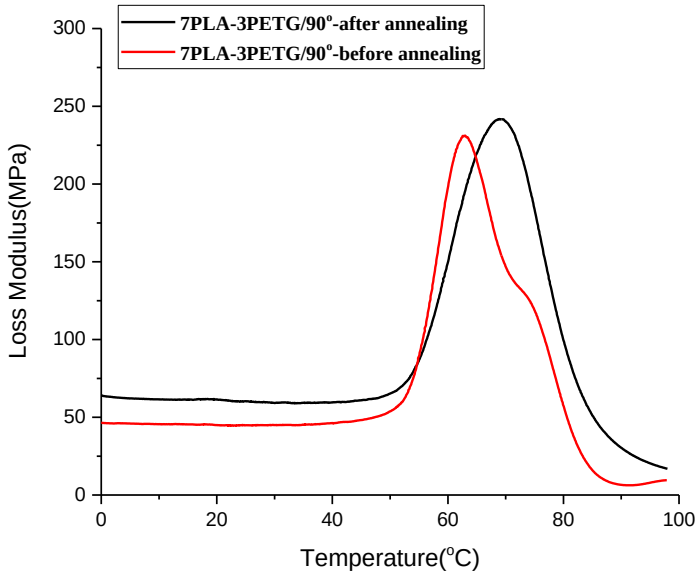

Figure 6.21: Comparison of loss modulus for samples printed 90° before and after annealing.

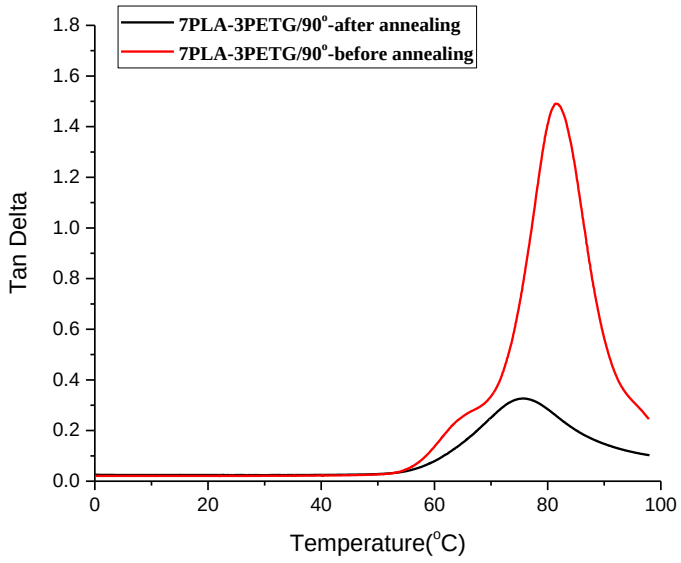

Figure 6.22: Comparison of tan delta for samples printed 90° before and after annealing.

Storage modulus dependence on composition at room temperature in **Figure 6.23** also shows an increase after annealing. However, this increase reached its maximum of 12.6% for 7PLA-3PETG/90° hybrid structures. And the augment of storage modulus for samples printed at 90° (**Figure 6.24)** is not as significant as that of samples printed at 0°. In comparison to samples printed as 0°, storage moduli of samples printed at 90° has a step growth behavior with compositions change. We associate this with the unique materials packing pattern within the bi-component structures printed at 90°.

Based on the **Voigt isostrain modulus model** mentioned before, the calculated storage modulus at the temperature of 25°C and 90°C is compared with the measured data and shown in **Figure 6.23** and **Figure 6.24** as well. It is noticeable that all the measured storage modulus is larger than the theoretical ones. This phenomenon is not well understood yet.

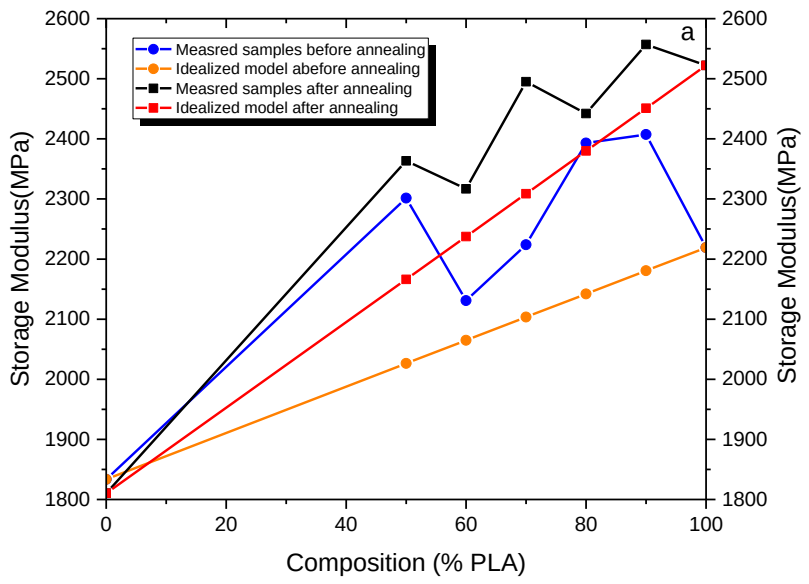

Figure 6.23: Storage modulus compare between samples printed at 90° and ideal model at 25ºC.

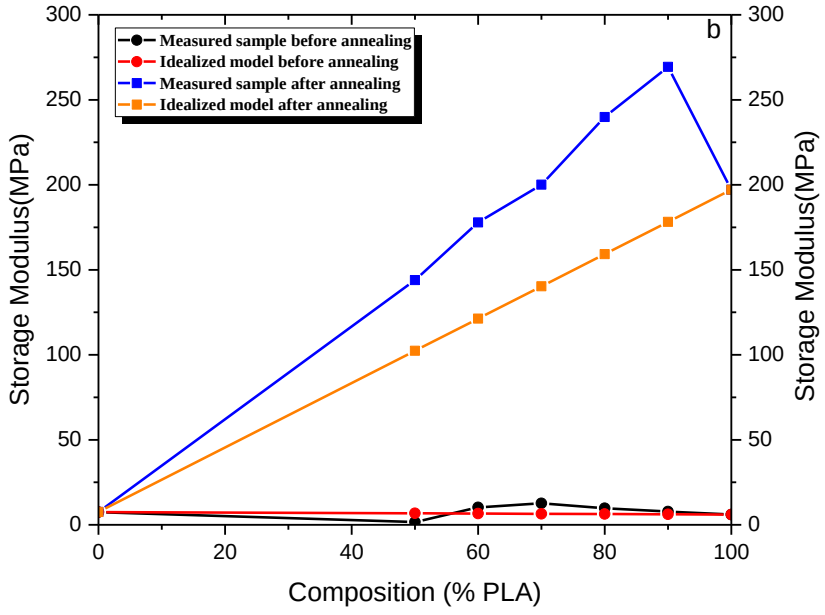

Figure 6.24: Storage modulus compare between samples printed at 90° and ideal model at 90°C.

The comparison of storage moduli for hybrid samples in **Figure 6.25** show that the storage modulus of samples printed at 90° is much larger than that of samples printed at 0° before the heat treatment. The samples printed at 90° keep this storage moduli advantage after the heat treatment. However, since annealing has more significant effect on samples printed at 0°, the difference of storage moduli for samples printed at 0° and 90° declined after the annealing. However, the comparison results suggest that hybrid structures have a better performance when printed with multiple layers.

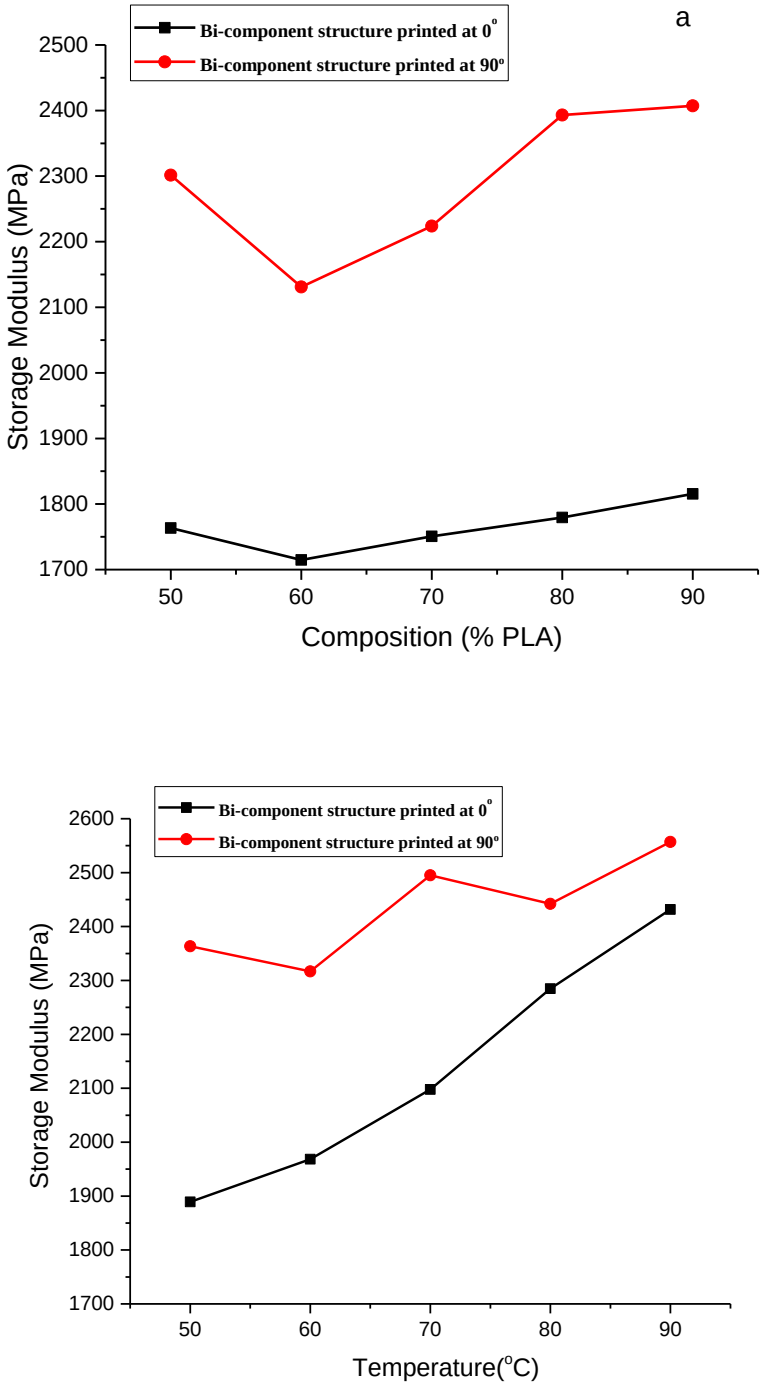

Figure 6.25: Comparison of storage moduli between hybrid samples printed at 0° and 90°. (a) Before the heat treatment. (b) After the heat treatment.

In summary, it can be concluded that the increase of mechanical performances for the printed bi-component structures after the heat treatment is a consequence of both the enhancement of layers' adhesion and the formation of crystals within PLA. The merge of separate peaks in loss modulus and tan delta indicates the significant enhancement of compatibility between PLA-1/PETG-1 interface after the annealing. It results from the formation of inter-penetration zone due to polymer chains diffusion. Besides, we note the decrease of the mechanical properties variation between the parallel samples for the printed hybrid structures after the heat treatment.

6.2.5: Mechanical performances improvement by blend filament insertion

Another approach to increase the bonding between PLA-1 and PETG-1 interfaces is to use PLA/PETG blend filament instead of the one made of pure materials. The schematic illustration of envisioned bonding strength enhancement mechanism is shown in **Figure 6.26**. The composition of the blend filament used in this work is PLA: PETG=8:2. It is possible that the PETG irregular particles in PLA matrix serve as binders at the interfaces to integrate the highly immiscible parts together.

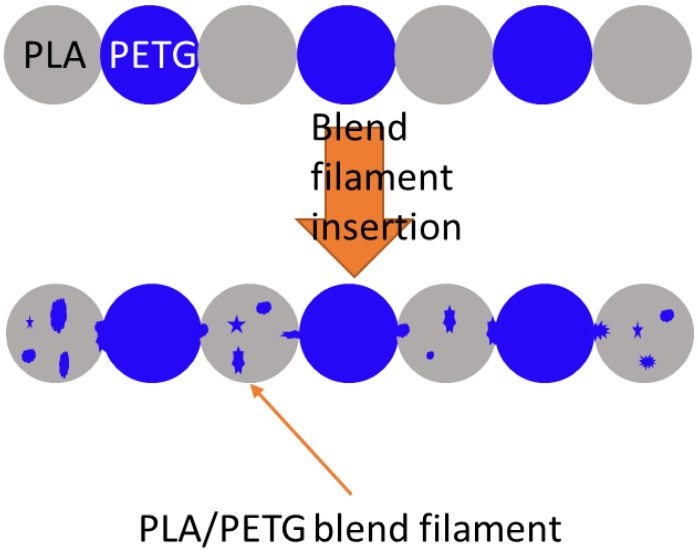

Figure 6.26: Schematic illustratio of bonding strenght enhancement though blend filaments insertion.

Optical microscope was utilized to determine the dispersion of PETG-1 within PLA-1 matrix. Cross section of the blend filaments (**Figure 6.27**) shows an opaque center along with the shinning flakes at the perimeter. Opaque core could be the crystallized PLA-1. The flakes come from the PETG-1 filament. However, it is difficult to precisely deduct that the PETG-1 materials is located at the perimeter, since it is difficult to be sure that these flakes would not diffuse during the extrusion. Thus, the conclusion that the blend filaments have a PLA-1 core and PETG-1 perimeter cannot be made. More sophisticated characterization should be applied to understand the structure of the blend filaments.

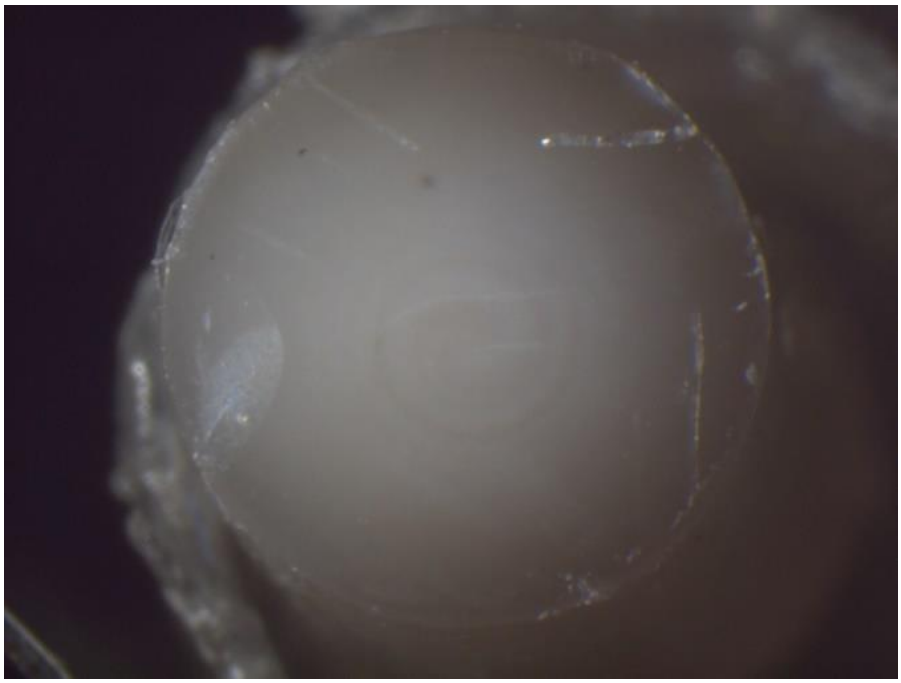

Figure 6.27: Photograph of PLA/PETG blend filament cross-section.

According to the literature, the morphology of polymer blend could be dispersed or continuous depending on the compositions and processing[8]. Based on the optical microscope photograph, one possible structure of the blend filament is that PETG-1 stays at periphery while PLA-1 stays inside, forming a core-shell structure. Due to the low percentage of PETG-1 within the blend filaments, it is unlikely for PETG-1 to form a continuous phase. Then the other morphology could be the irregular PETG-1 particles randomly dispersed within PLA-1 matrix.

Selective dissolution method was utilized to determine the morphology of PETG within the blend filament. To make it easier to identify, PETG-1 filament having black color was co-extruded with PLA-1 filament. A selective solvent benzene, which dissolves

PLA only, was utilized. Morphology of PETG-1 material inside PLA matrix, shown in **Figure 6.28**, has a needle-like appearance.

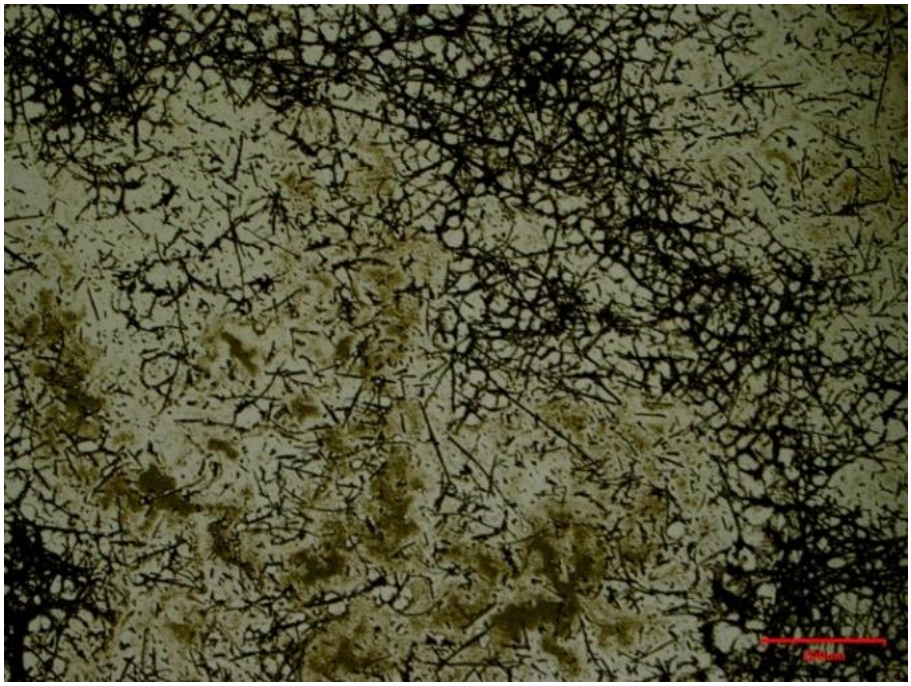

Figure 6.28: Morphology of PETG in benzene.

DMA results (**Figure 6.29)** are compared among bi-component structures printed from 6PLA-4PETG/90°, 6PLA-4(8PLA-2PETG) blend/90°, and 6(8PLA-2PETG) blend-4PETG/90°. Storage moduli at room temperature (25°C) are summarized in **Table 1**. Based on the composition of the blend filaments, we can calculate the composition of the hybrid structures. For 6PLA-4(8PLA-2PETG) blend/90° hybrid structures, it contains 92%PLA and 8% PETG. While for 6(8PLA-2PETG) blend-4PETG/90° samples, it contains 68% PETG and 32% PLA. The storage modulus for pure PLA-1 is about 2537MPa, while for

PETG-1 is about 2032MPa. It means that the storage modulus of the hybrid structures would be higher if it had larger PLA content. However, 6(8PLA-2PETG) blend-4PETG/90° samples contain lower percentage of PLA while possess a 16% higher storage modulus in comparison with 6PLA-4PETG/90° samples. It proves that PETG in the blend filaments do serve as binder that can integrate the highly immiscible parts.

PLA polymer has a lower glass transition temperature than PETG, and therefore, the Tg for 6PLA-4(8PLA-2PETG) blend/90° hybrid structure is lower due to high content of PLA within it.

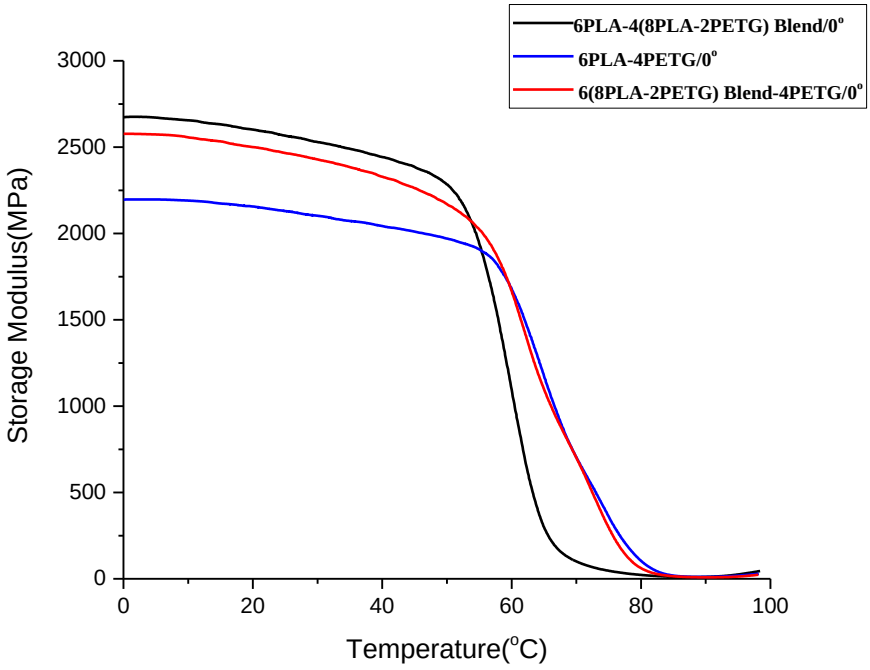

Figure 6.29: Compare Storage Modulus of all 6/4 composition.

Table 6.1: Storage modulus comparison

Materials	**E' at 25°C (Mpa)**	**Increase (%)**
6PLA-4PETG/90º	2128	
6(8PLA-2PETG)Blend-4PETG/90º	2470	16±2.6
6PLA-4(8PLA-2PETG) Blend/90º	2570	21±4.1

6.3: Conclusions

General conclusions can be draw from the conducted experiments:

- The dual-feed 3D printer can fabricate laminated hybrid structures;
- The mechanical properties of the bi-component hybrid structure increase with the annealing temperature;
- Heat treatment can improve mechanical properties and make them more consistent for the hybrid structures;
- Further improvement of the mechanical properties of the bi-component structures can be achieved by utilizing PLA/PETG blend filament.

6.4: References

1. Aubin, M.; Prudhomme, R. E., Analysis of the Glass-Transition Temperature of Miscible Polymer Blends. *Macromolecules* **1988,** *21* (10), 2945-2949.
2. Socrates, G.; Socrates, G., *Infrared and Raman characteristic group frequencies : tables and charts*. 3rd ed.; Wiley: Chichester ; New York, 2001; p xv, 347 p.
3. Murayama, T., *Dynamic mechanical analysis of polymeric material*. Elsevier Scientific Pub. Co.: Amsterdam ; New York, 1978; p viii, 231 p.
4. Torres, J.; Cotelo, J.; Karl, J.; Gordon, A. P., Mechanical Property Optimization of FDM PLA in Shear with Multiple Objectives. *Jom-Us* **2015,** *67* (5), 1183-1193.
5. Kadla, J. F.; Kubo, S., Lignin-based polymer blends: analysis of intermolecular interactions in lignin–synthetic polymer blends. *Composites Part A: Applied Science and Manufacturing* **2004,** *35* (3), 395-400.
6. Peixiang Xing, L. D., Yuxian An, and Zhiliu Feng, <Miscibility and Crystallization of Poly(b-hydroxybutyrate) andpoly p-vinylphenol Blends.pdf>. *Macromolecules* **1997,** *30, 2726-2733*.
7. Ward, I. M.; Hadley, D. W., *An introduction to the mechanical properties of solid polymers*. J. Wiley & Sons: Chichester ; New York, 1993; p xi, 334 p.
8. Scherzer, S. L.; Pavlova, E.; Esper, J. D.; Starý, Z., Phase structure, rheology and electrical conductivity of co-continuous polystyrene/polymethylmethacrylate blends filled with carbon black. *Compos Sci Technol* **2015,** *119*, 138-147.

CHAPTER 7

CONCLUSIONS

This chapter is devoted to summarize the main work reported in this thesis. The study of fabrication and characterization of PLA and PETG polymer materials based on 3D printing technique draws the major conclusions as following:

- 3D printing conditions were successfully determined by thermal analysis and viscosity measurements;
- Anisotropic mechanical properties can be observed for both PLA and PETG printed samples;
- Heat treatment can increase the storage modulus for PLA printed samples at rubbery plateau, while has little effect on the storage modulus of PETG printed samples;
- PLA and PETG samples suffer from severe shape distortion during the heat treatment processing, making the variation of the mechanical properties enlarged;
- Heat treatment can improve mechanical properties of the bi-component structures and make them more consistent;
- Further improvement of the mechanical properties of the bi-component structures was achieved by utilizing PLA/PETG blend filament.

CHAPTER 8

FUTURE WORK

Although, the work reported above established the fabrication of PLA and PETG mono-component and bi-component structures and the methodology for improving mechanical performances of the printed objects, there are still related scientific/engineering aspects that were not addressed and might be the subjects of the future work. Some of them are listed below:

- Address the samples shape distortion during the heat treatment;
- Characterize the morphology of the PLA/PETG blend filament to explain the mechanical properties improvement of the bi-component structures through the utilization of blend filament;
- Searching for new methods to improve the mechanical properties of the 3D printed objects such as the addition of reinforced phase. The preliminary work has been done and shown in **Appendix 2**.

APPENDIX 1

Fabrication and properties of printed bi-component structures

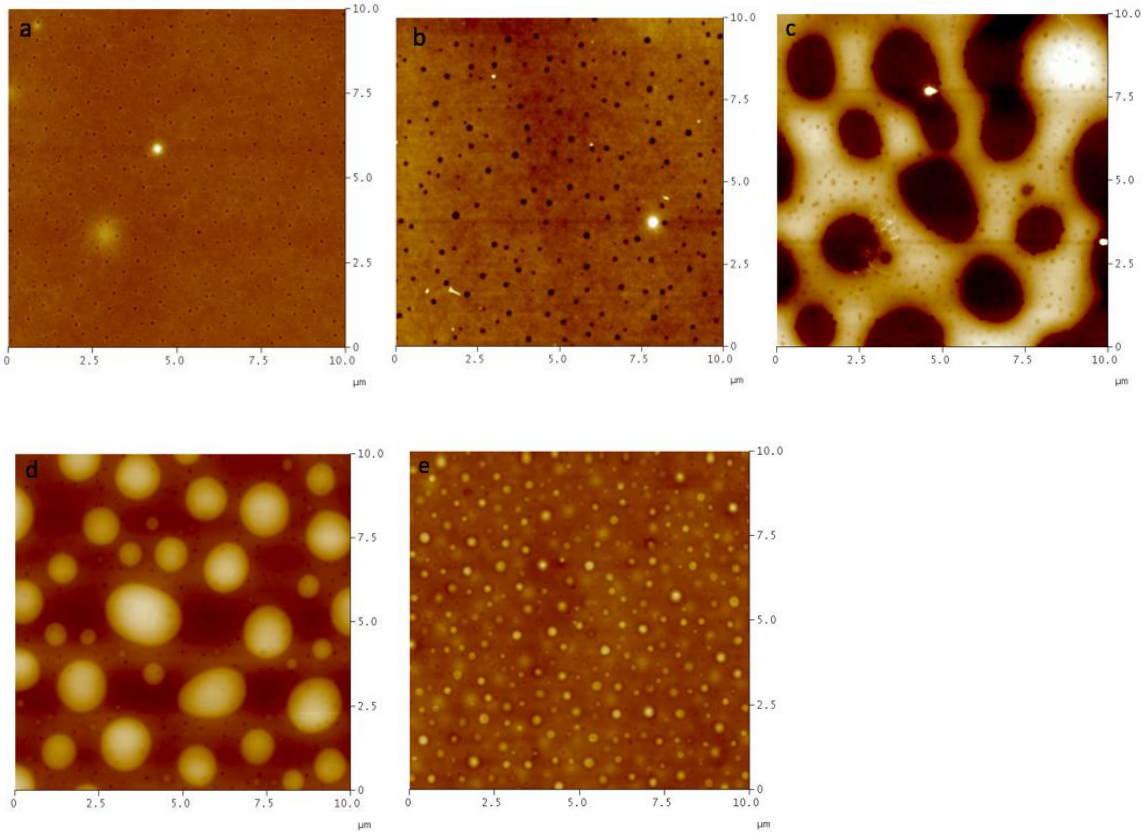

Figure A1.1: AFM morphology photo of PLA/PETG blend film with different compositions. (a) Pure PLA; (b) Pure PET; (c) PLA: PETG=2:8; (d) PLA: PETG=8:2; (e) PLA: PETG=5:5.

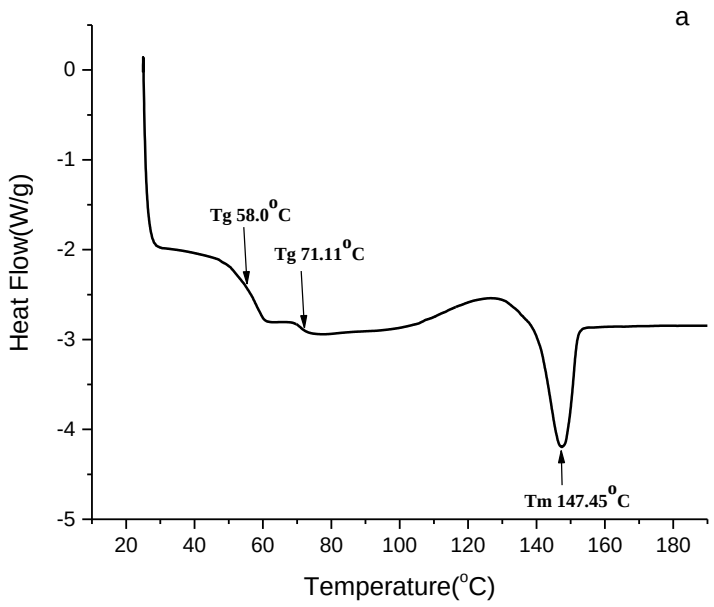

Figure A1.2: DSC thermograph of PLA/PETG blend with composition of PLA: PETG=8:2.

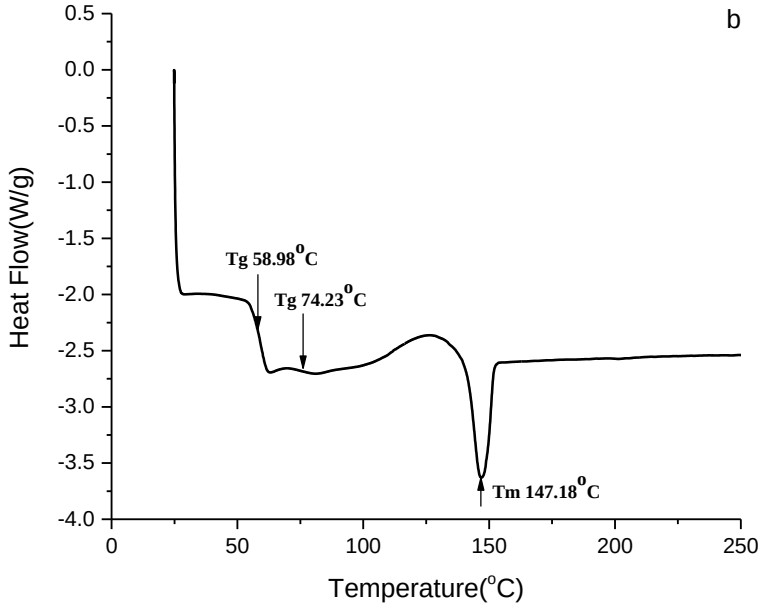

Figure A1.3: DSC thermograph of PLA/PETG blend with composition of PLA: PETG=5:5.

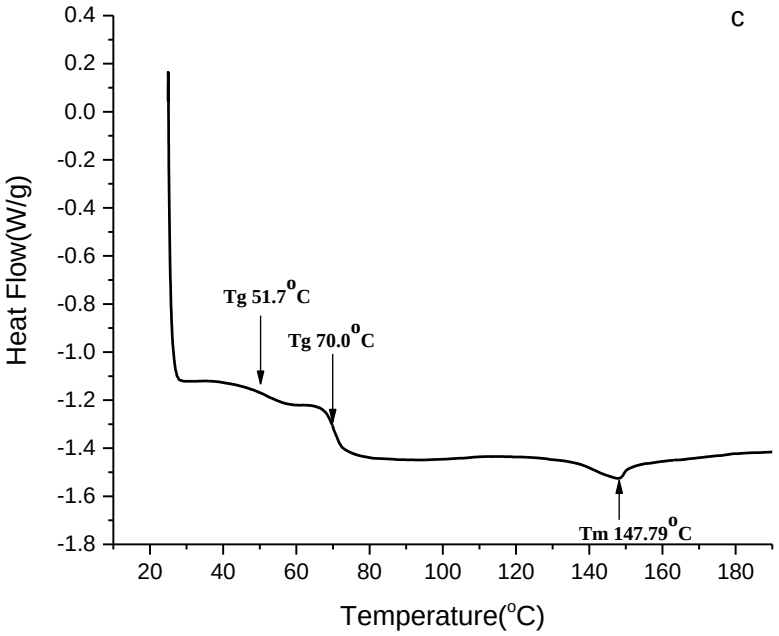

Figure A1.4: DSC thermograph of PLA/PETG blend with composition of PLA: PETG=2:8.

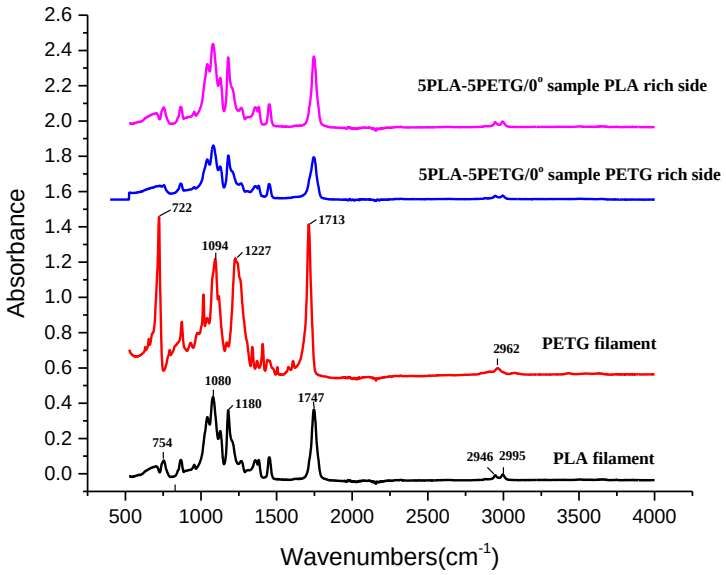

Figure A1.5: FTIR stack spectrum of blend with composition of PLA: PETG=5:5.

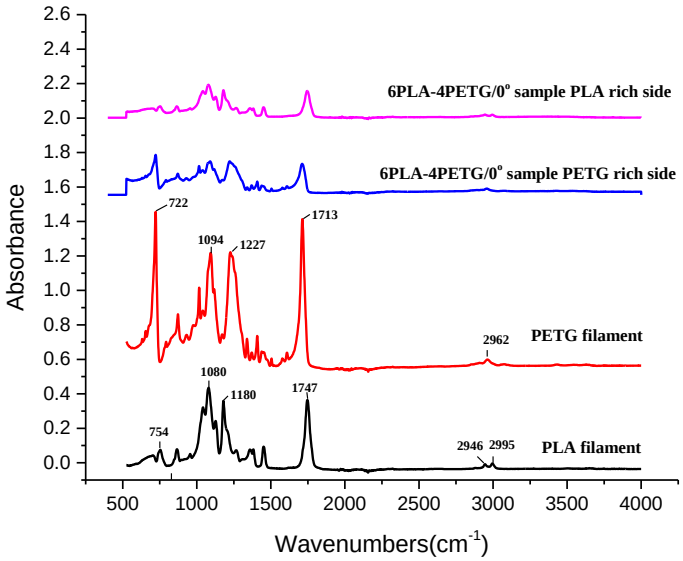

Figure A1.6: FTIR stack spectrum of blend with composition of PLA: PETG=6:4.

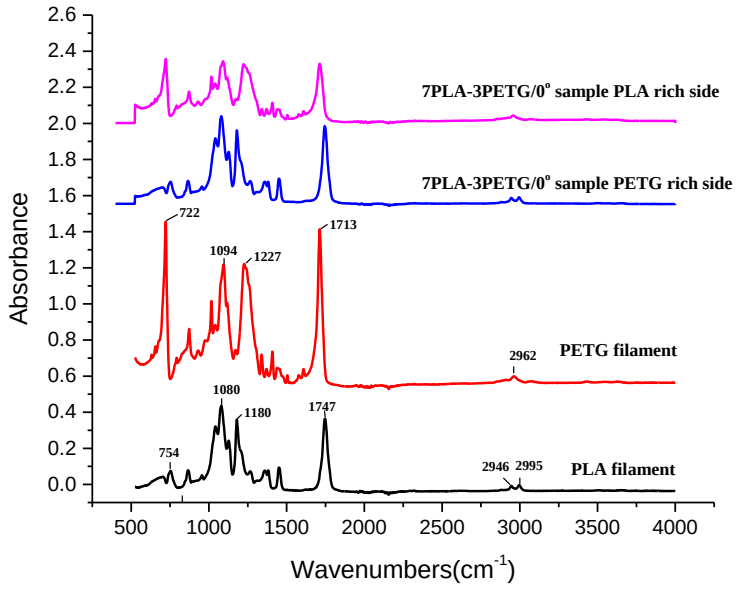

Figure A1.7: FTIR stack spectrum of blend with composition of PLA: PETG=7:3.

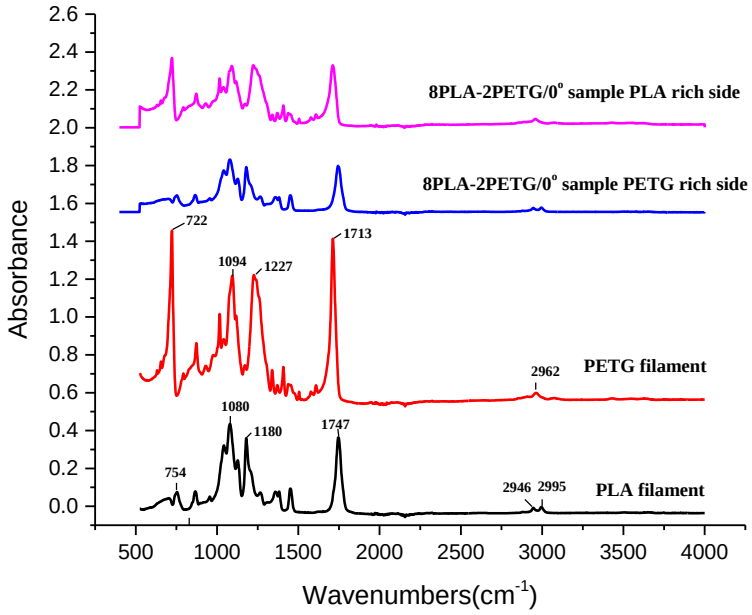

Figure A1.8: FTIR stack spectrum of blend with composition of PLA: PETG=8:2.

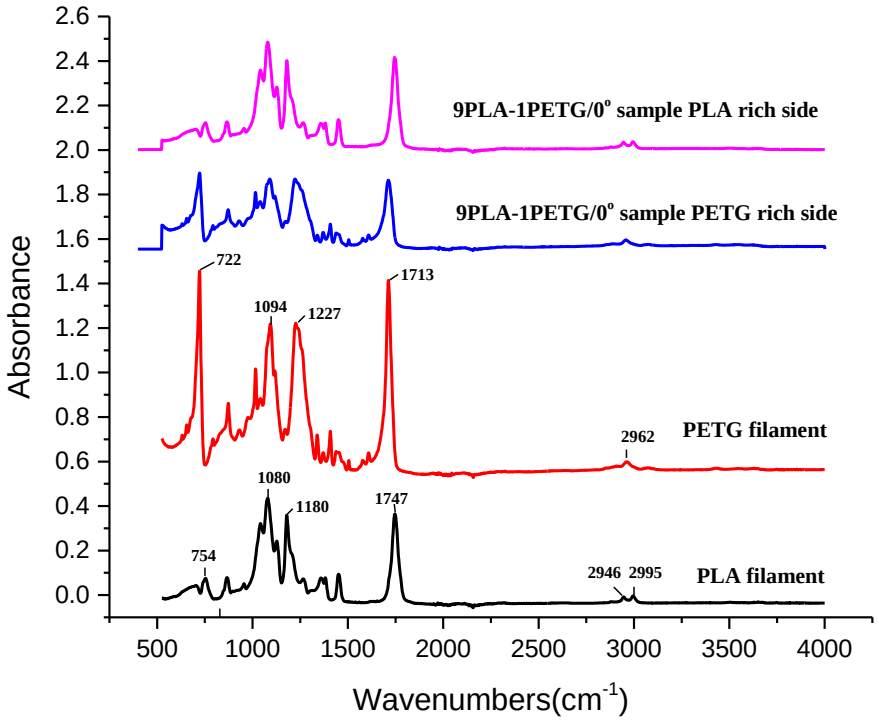

Figure A1.9: FTIR stack spectrum of blend with composition of PLA: PETG=9:1.

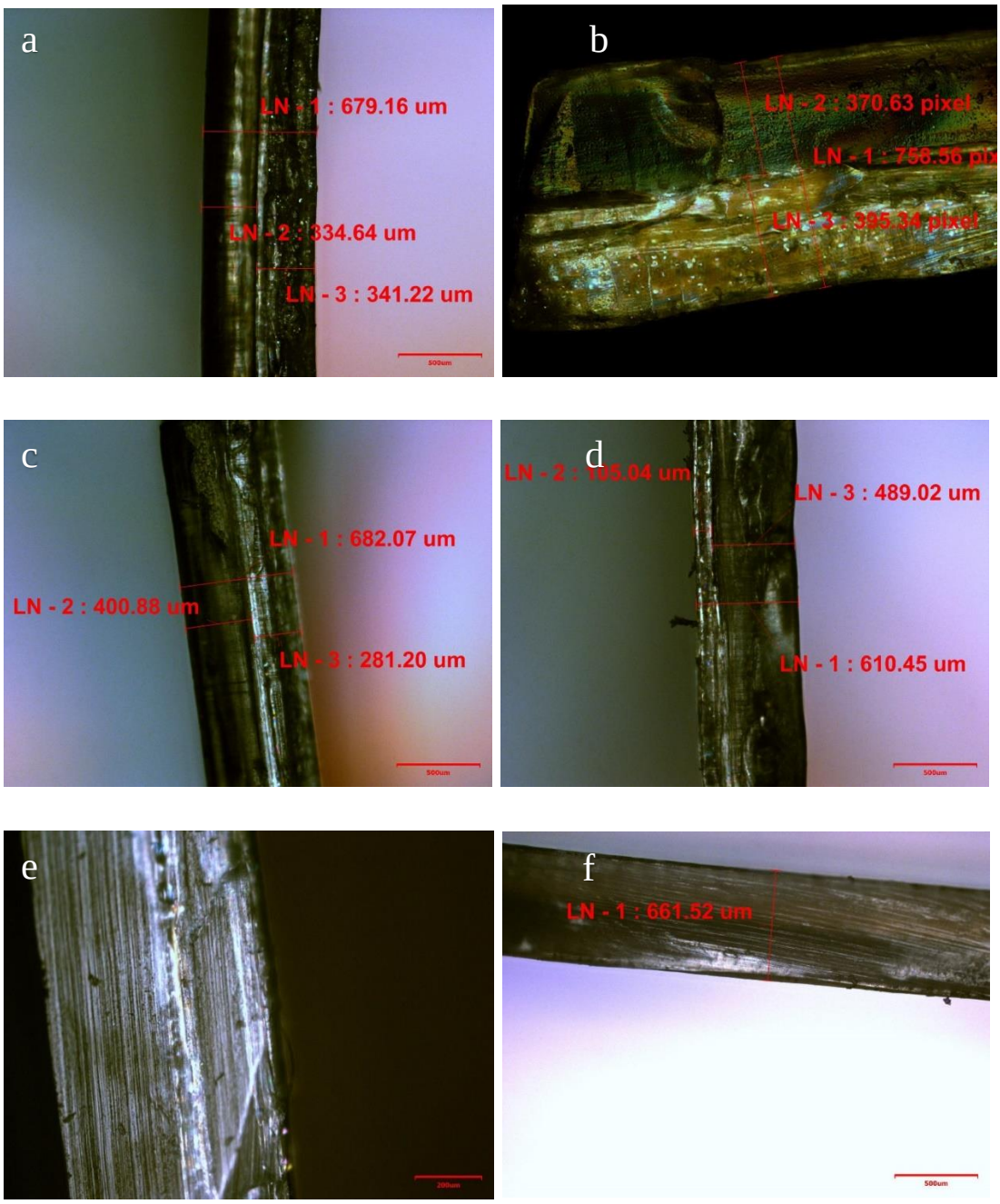

Figure A1.10: Polarized optical microscope photo for sample of various compositions. (a) PLA: PETG=5:5; (b) PLA: PETG=6:4; (c) PLA: PETG=7:3; (d) PLA: PETG=8:2; (e) PLA: PETG=9:1; (f) Pure PLA.

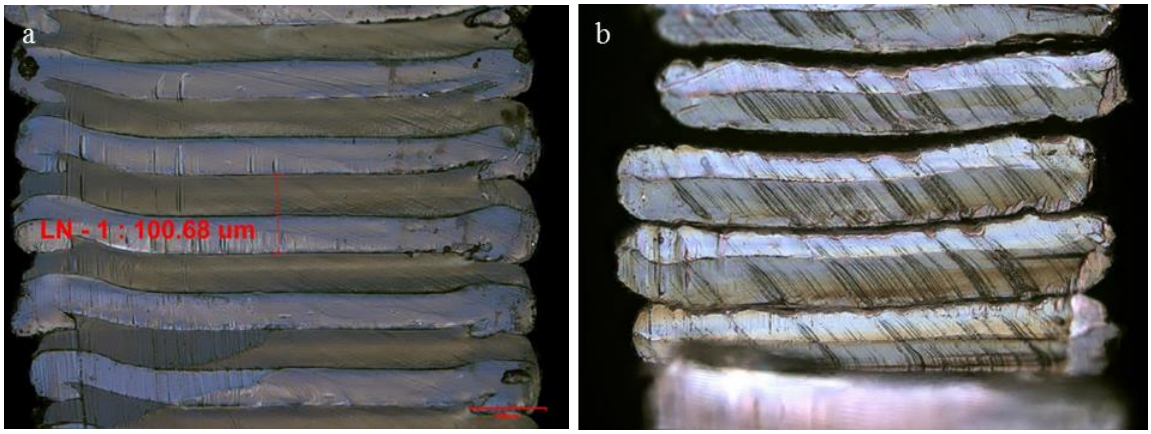

Figure A1.11: Polarized optical microscope photograph of sample printed at 90° with various composition. (a)PLA: PETG=5:5; (b) PLA: PETG=7:3.

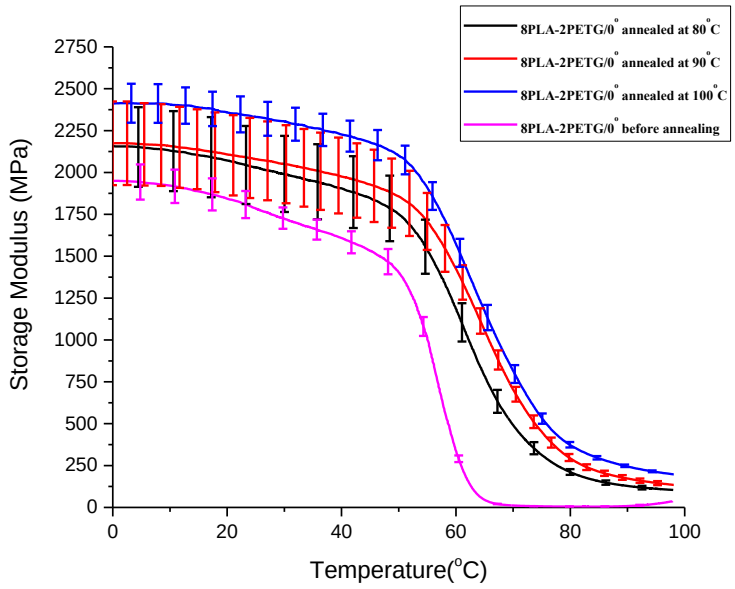

Figure A1.12: Storage modulus of 8PLA-2PETG/ 0°sampels after annealed at different temperature.

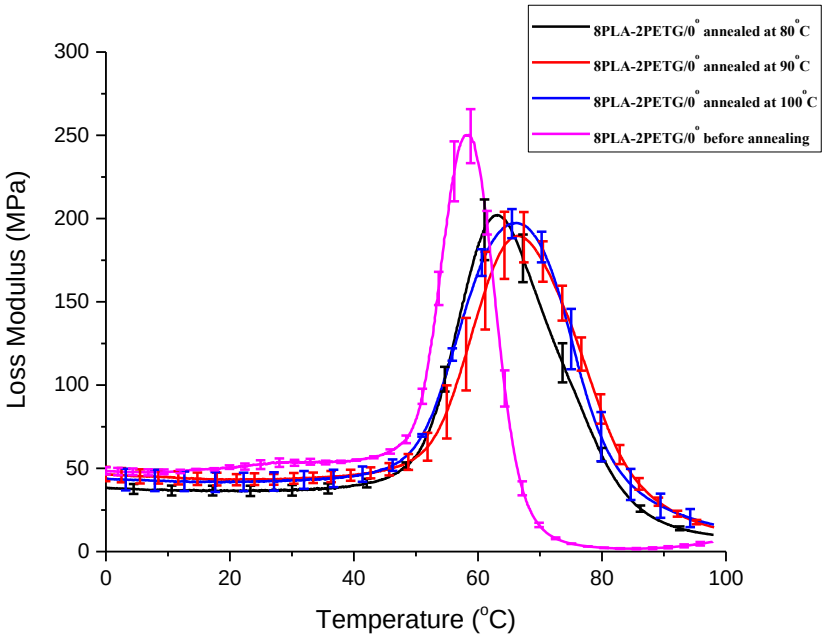

Figure A1.13: Loss modulus of 8PLA-2PETG/ 0°sampels after annealed at different temperature.

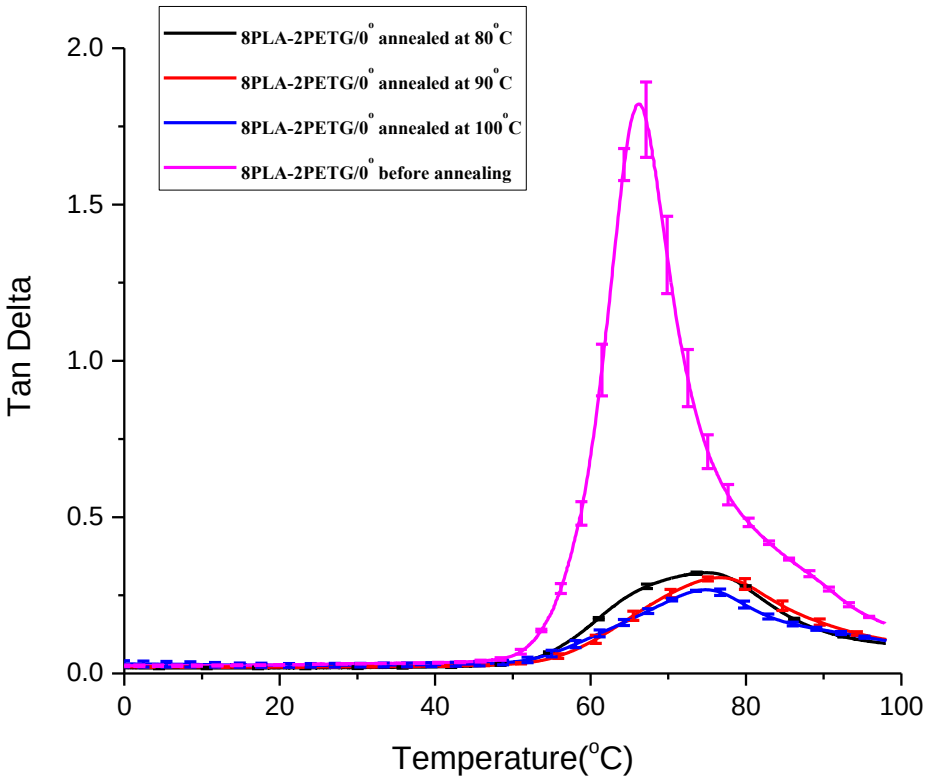

Figure A1.14: Tan delta of 8PLA-2PETG/ 0°sampels after annealed at different temperature.

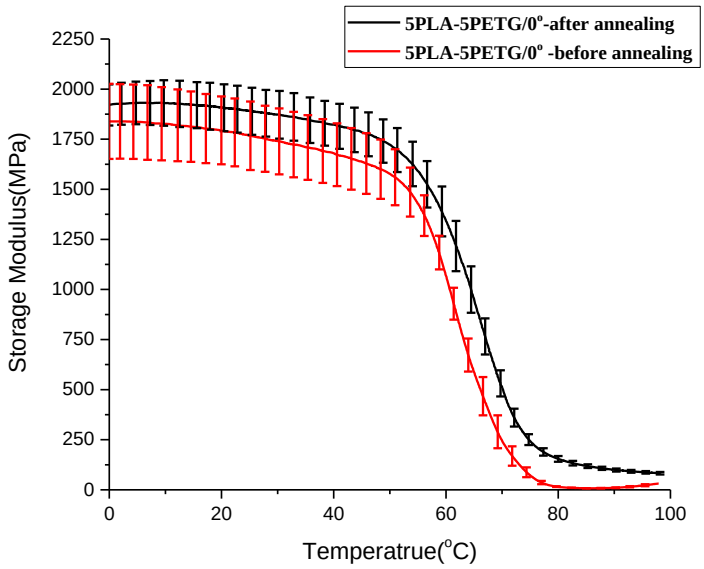

Figure A1.15: Comparison of storage modulus for 5PLA-5PETG/0° between before and after annealing.

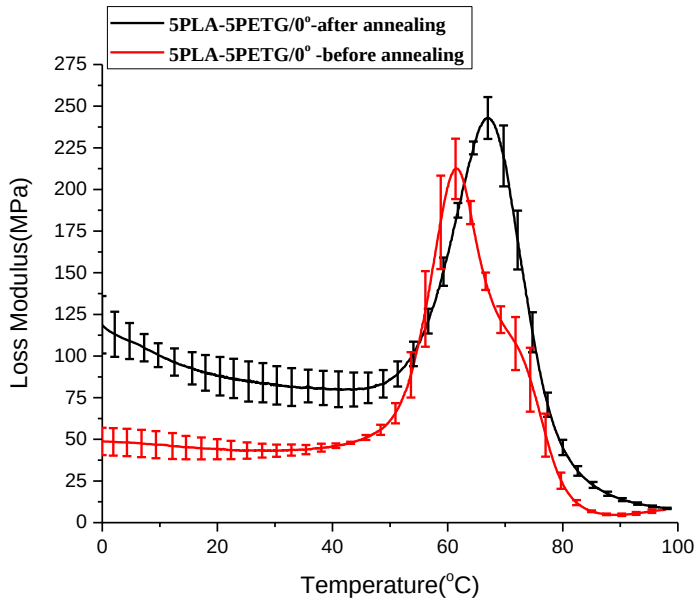

Figure A1.16: Comparison of loss modulus for 5PLA-5PETG/0° between before and after annealing.

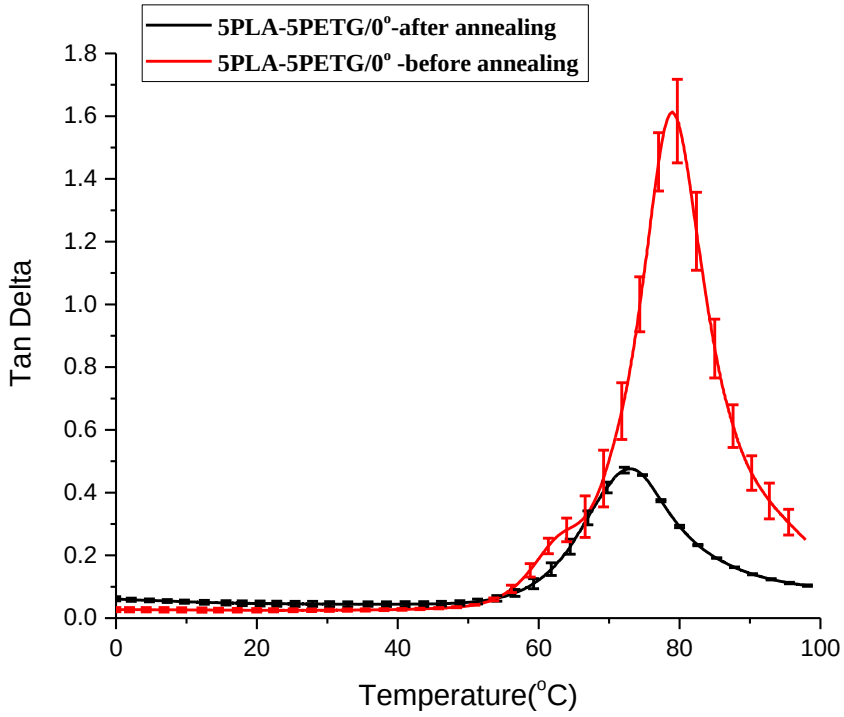

Figure A1.17: Comparison of tan delta for 5PLA-5PETG/0° between before and after annealing.

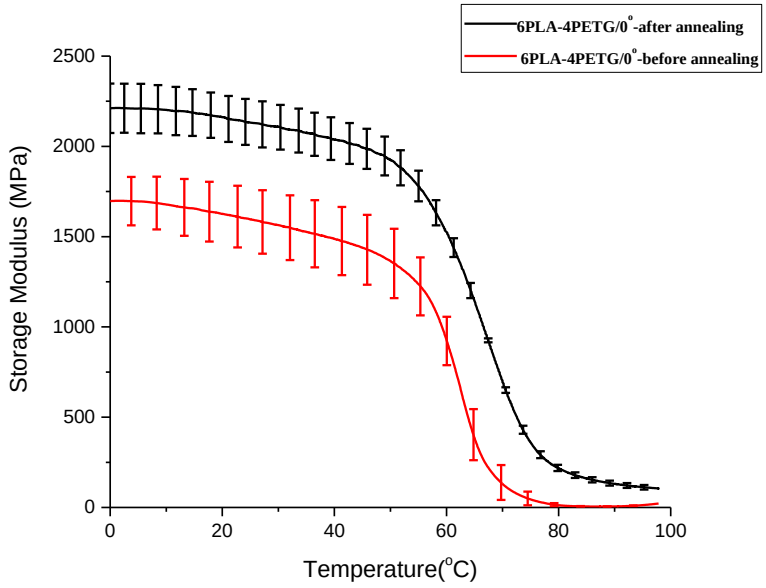

Figure A1.18: Comparison of storage modulus for 6PLA-6PETG/0° between before and after annealing.

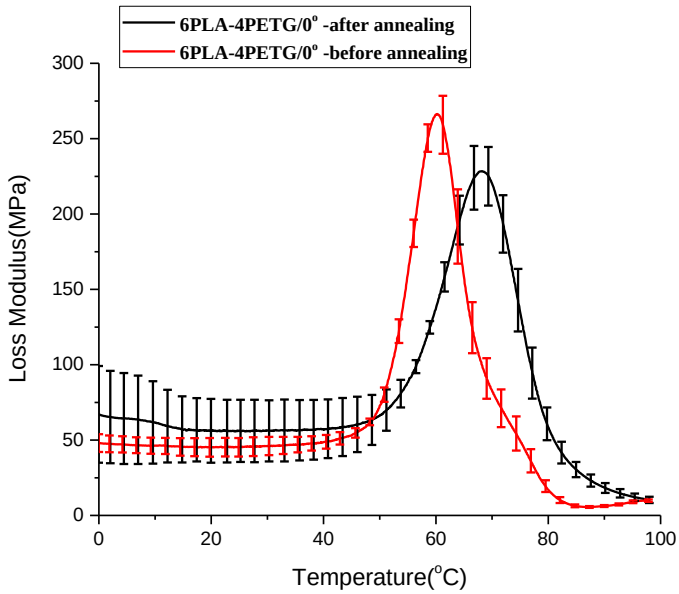

Figure A1.19: Comparison of loss modulus for 6PLA-4PETG/0° between before and after annealing.

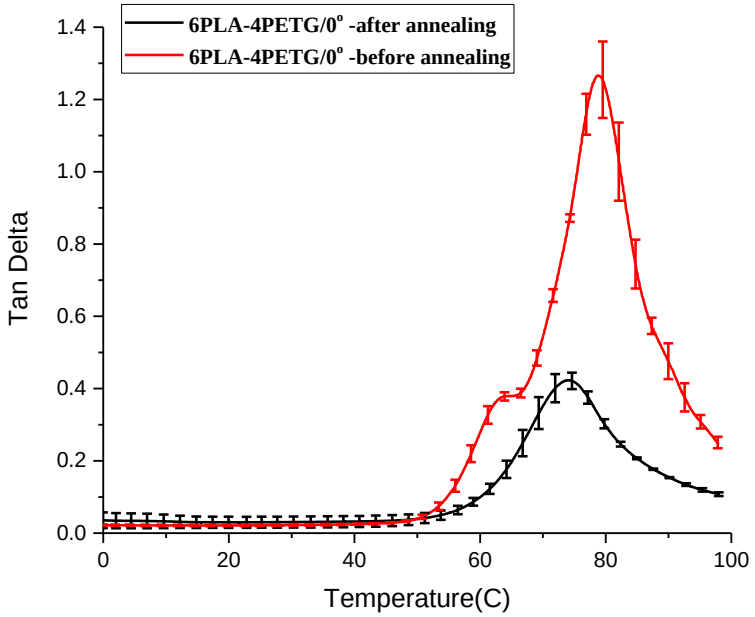

Figure A1.20: Comparison of tan delta for 6PLA-4PETG/0° between before and after annealing.

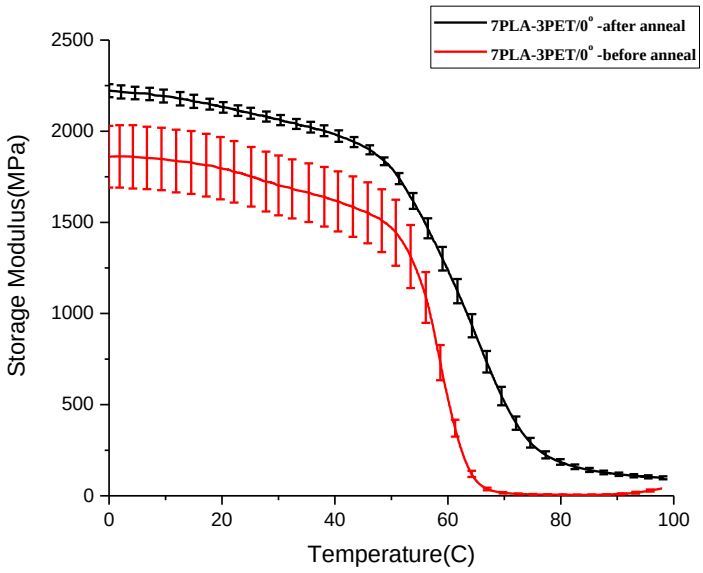

Figure A1.21: Comparison of storage modulus for 7PLA-3PETG/0° between before and after annealing.

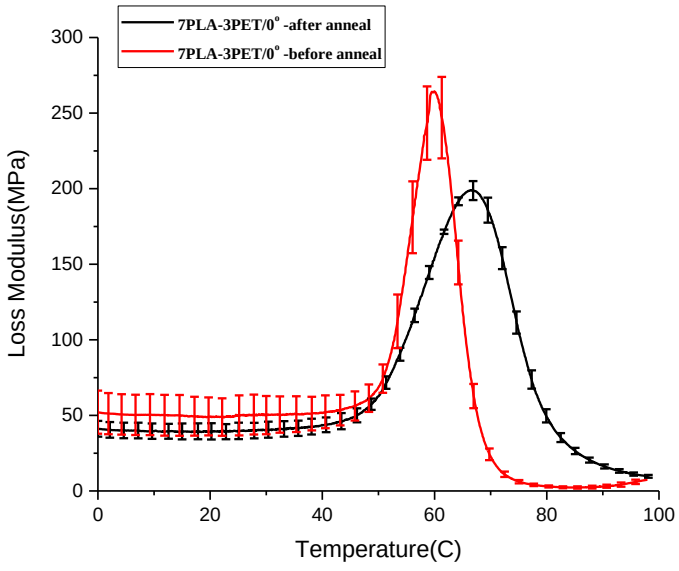

Figure A1.22: Comparison of loss modulus for 7PLA-3PETG/0° between before and after annealing.

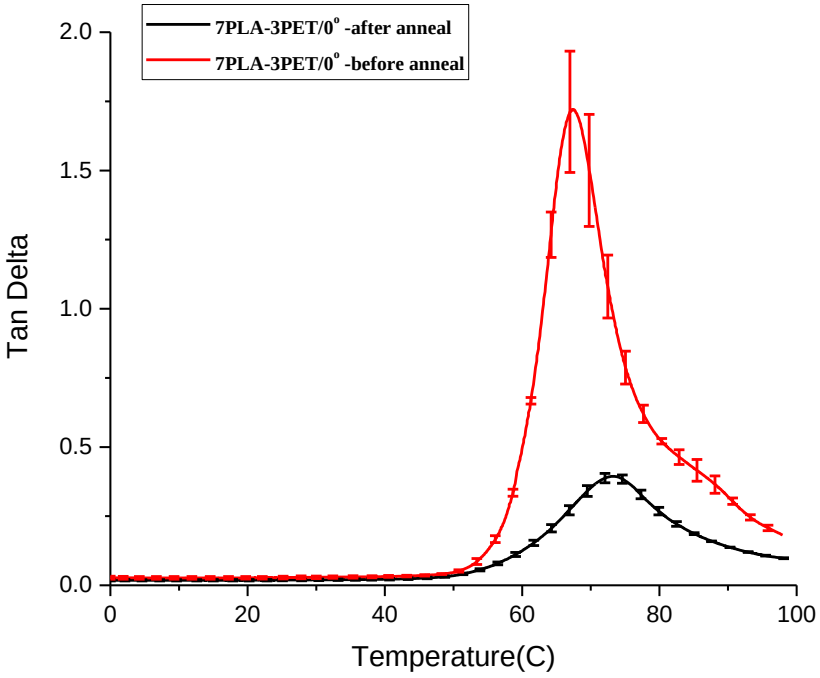

Figure A1.23: Comparison of tan delta for 7PLA-3PETG/0° between before and after annealing.

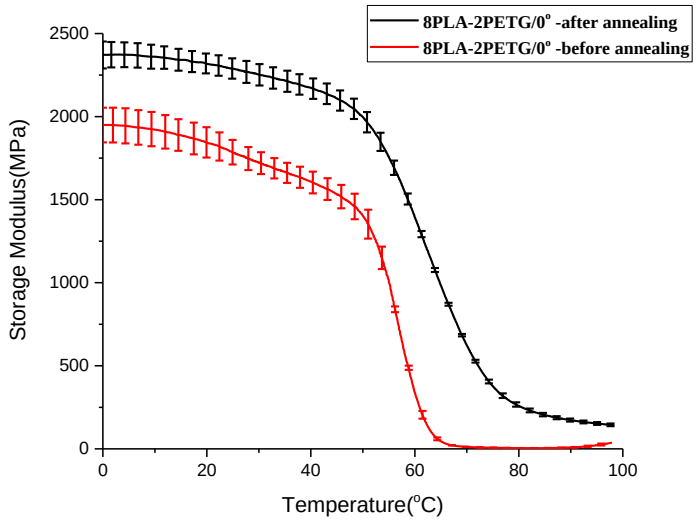

Figure A1.24: Comparison of storage modulus for 8PLA-2PETG/0° between before and after annealing.

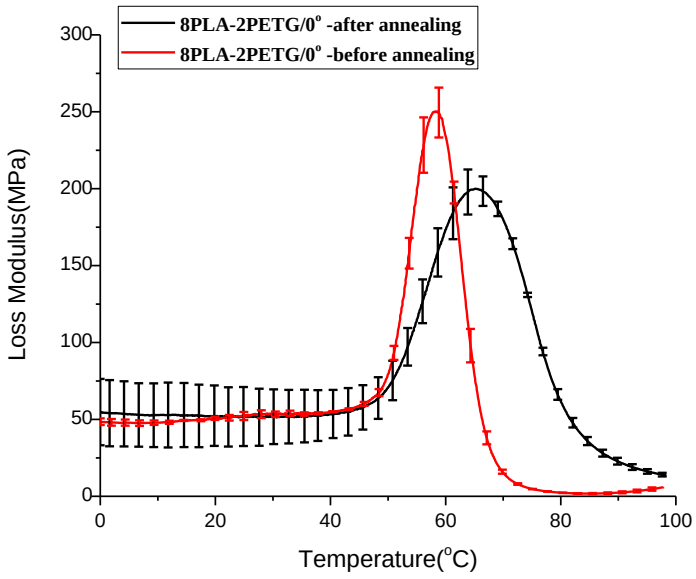

Figure A1.25: Comparison of loss modulus for 8PLA-2PETG/0° between before and after annealing.

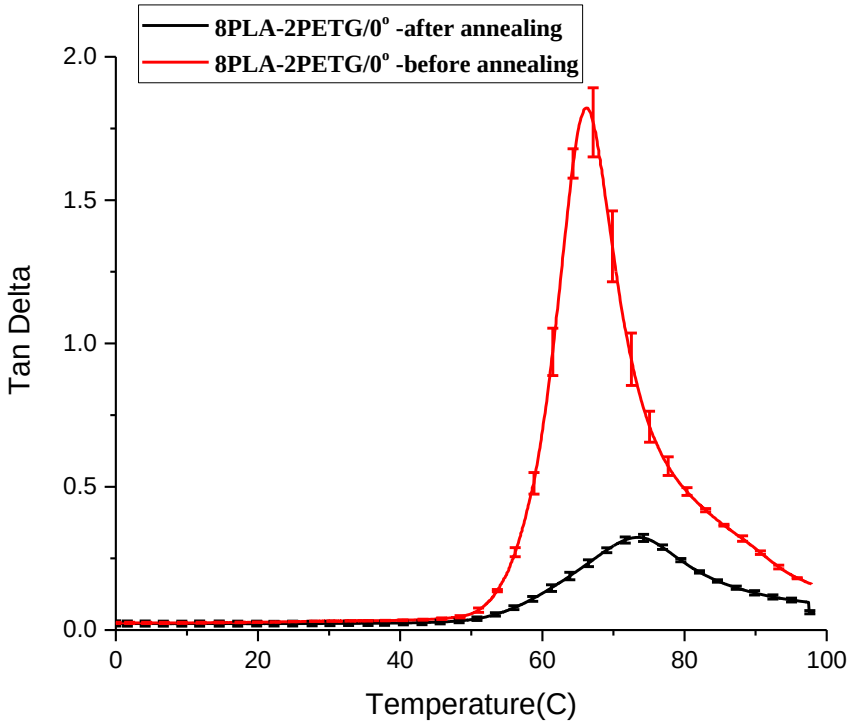

Figure A1.26: Comparison of tan delta for 8PLA-2PETG/0° between before and after annealing.

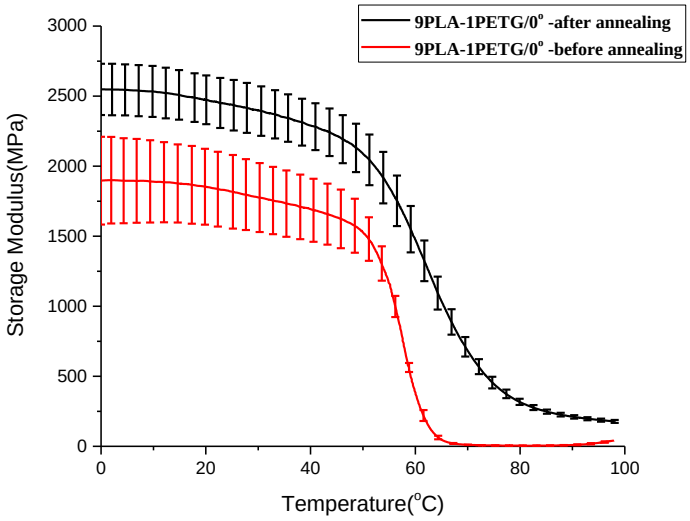

Figure A1.27: Comparison of storage modulus for 9PLA-1PETG/0° between before and after annealing.

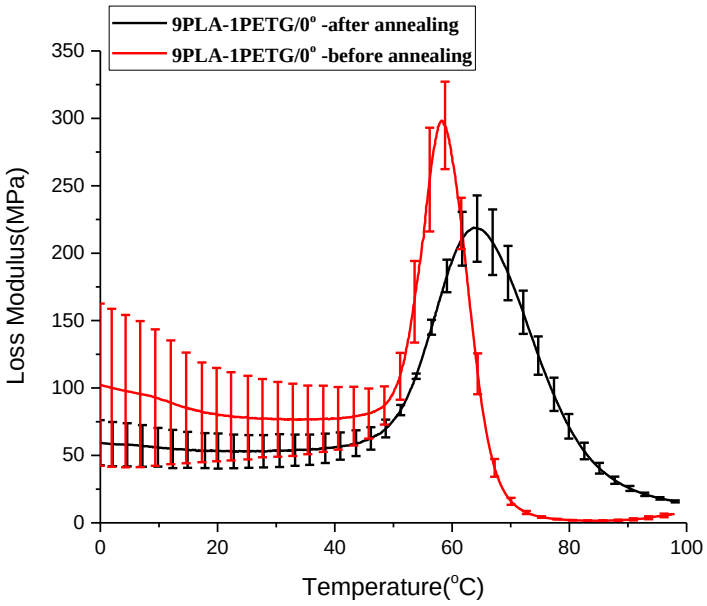

Figure A1.28: Comparison of loss modulus for 9PLA-1PETG/0° between before and after annealing.

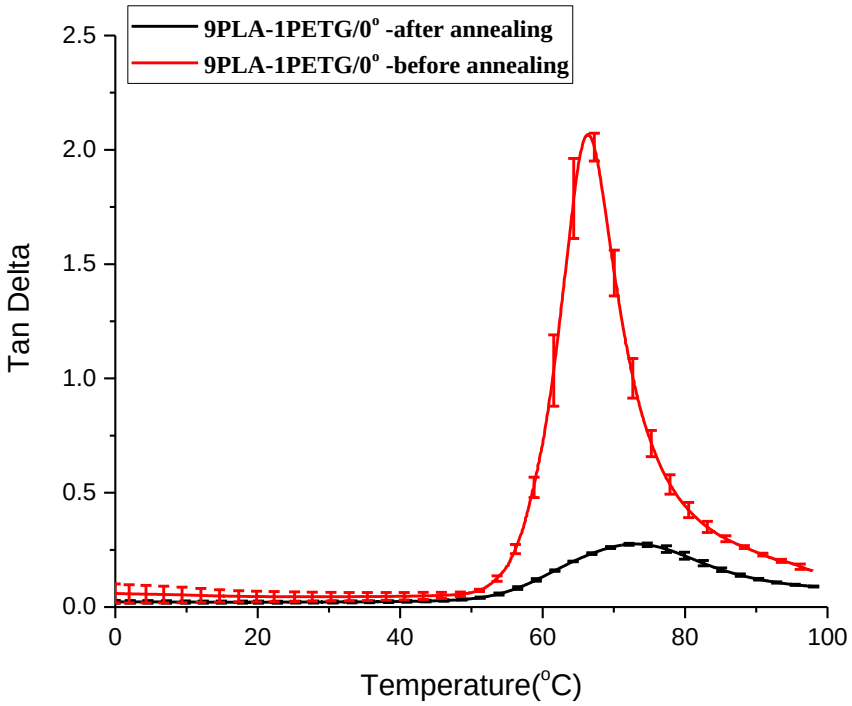

Figure A1.29: Comparison of tan delta for 9PLA-1PETG/0° between before and after annealing.

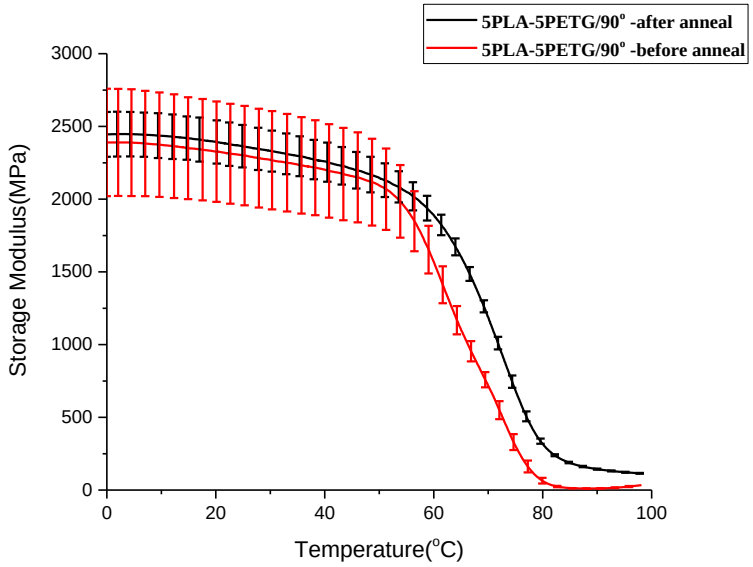

Figure A1.30: Comparison of storage modulus for 5PLA-5PETG/90° between before and after annealing.

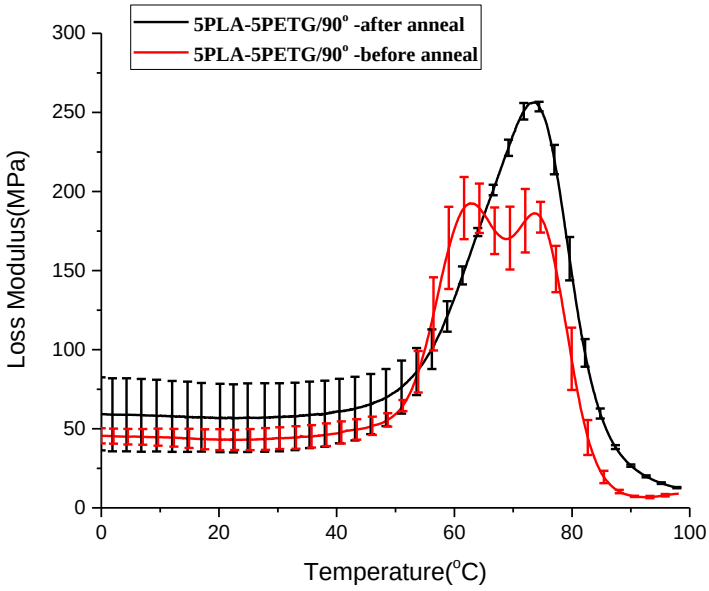

Figure A1.31: Comparison of loss modulus for 5PLA-5PETG/90° between before and after annealing.

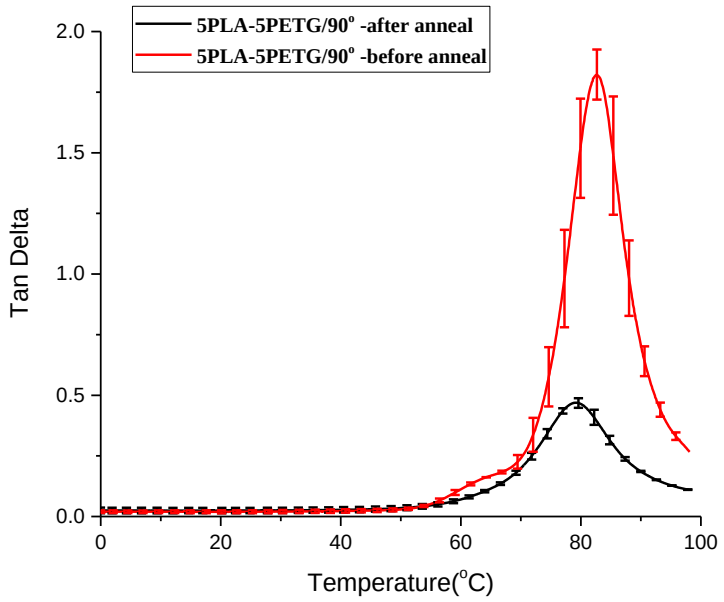

Figure A1.32: Comparison of tan delta for 5PLA-5PETG/90° between before and after annealing.

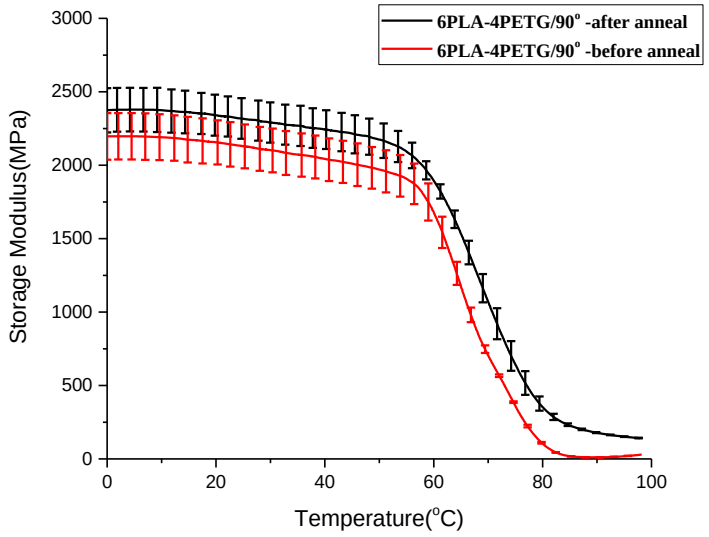

Figure A1.33: Comparison of storage modulus for 6PLA-4PETG/90° between before and after annealing.

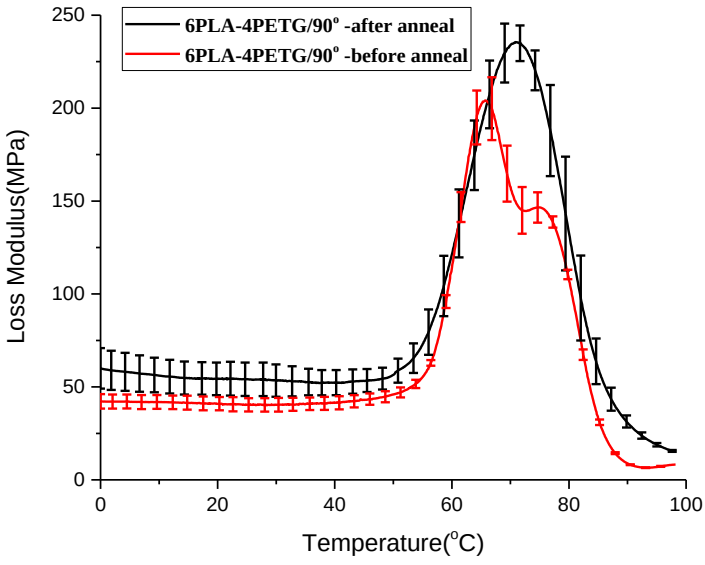

Figure A1.34: Comparison of loss modulus for 6PLA-4PETG/90° between before and after annealing.

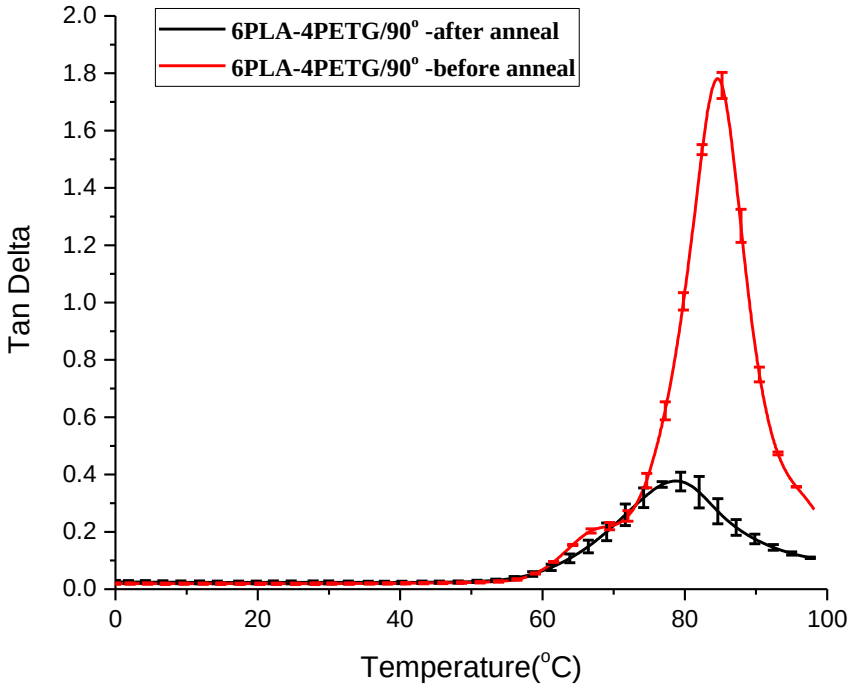

Figure A1.35: Comparison of tan delta for 6PLA-4PETG/90° between before and after annealing.

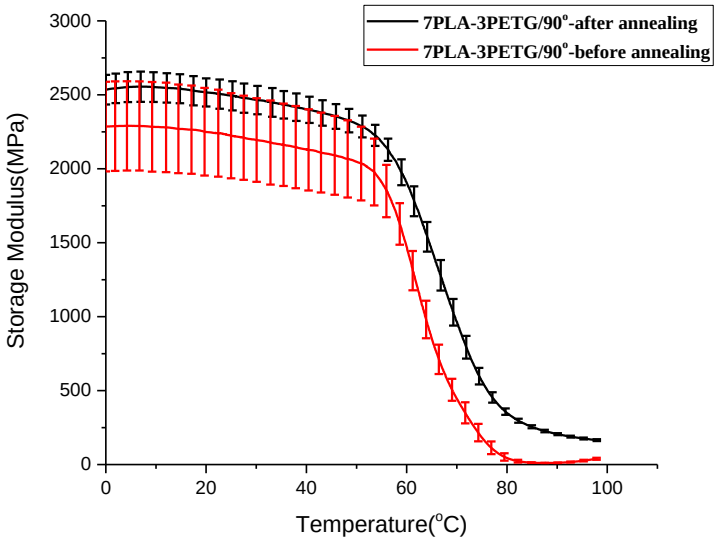

Figure A1.36: Comparison of storage modulus for 7PLA-3PETG/90° between before and after annealing.

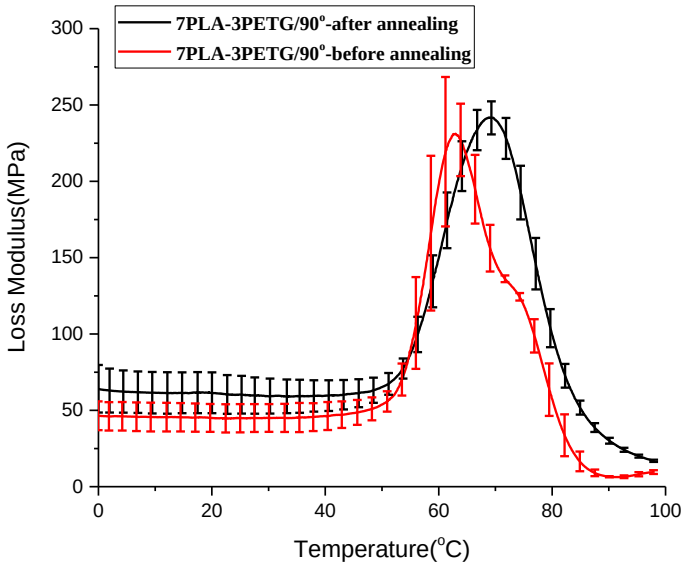

Figure A1.37: Comparison of loss modulus for 7PLA-3PETG/90° between before and after annealing.

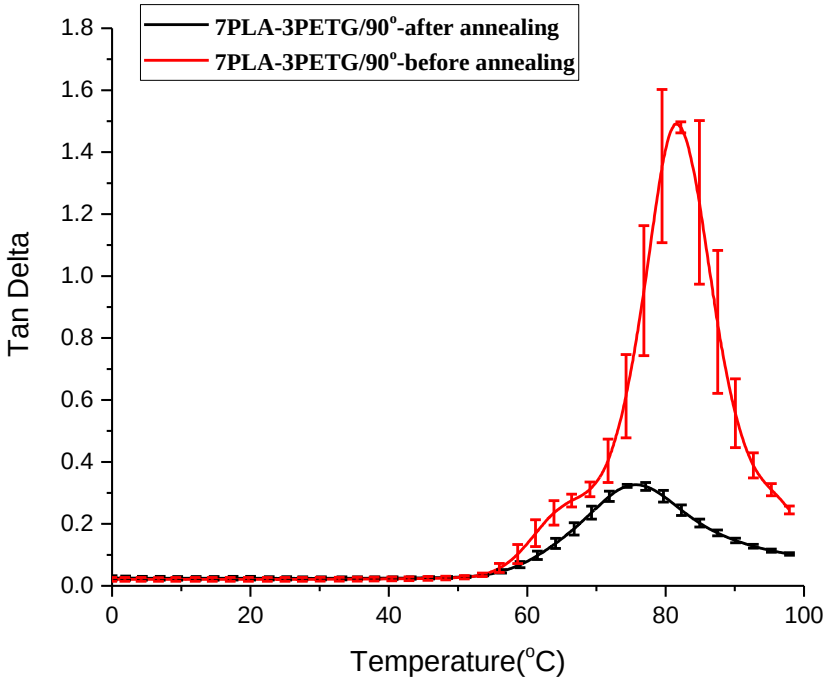

Figure A1.38: Comparison of tan delta for 7PLA-3PETG/90° between before and after annealing.

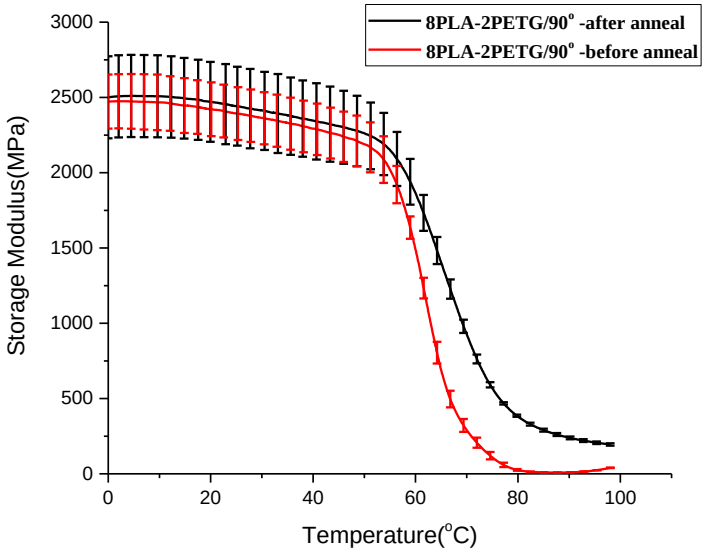

Figure A1.39: Comparison of storage modulus for 8PLA-2PETG/90° between before and after annealing.

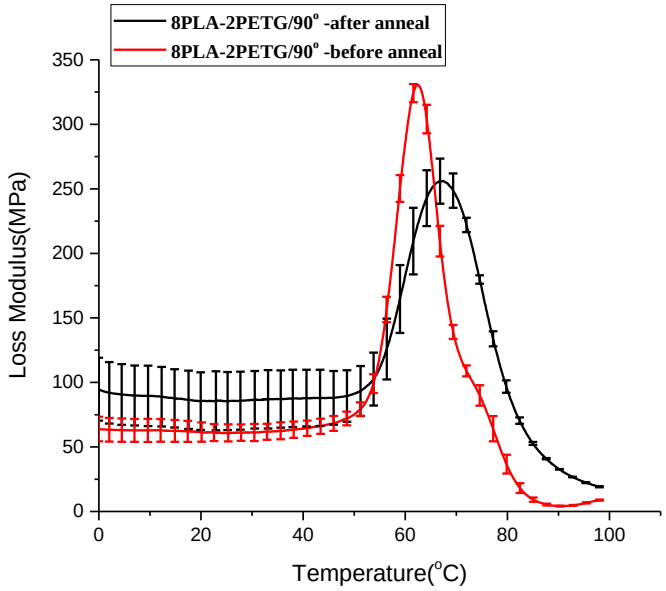

Figure A1.40: Comparison of loss modulus for 8PLA-2PETG/90° between before and after annealing.

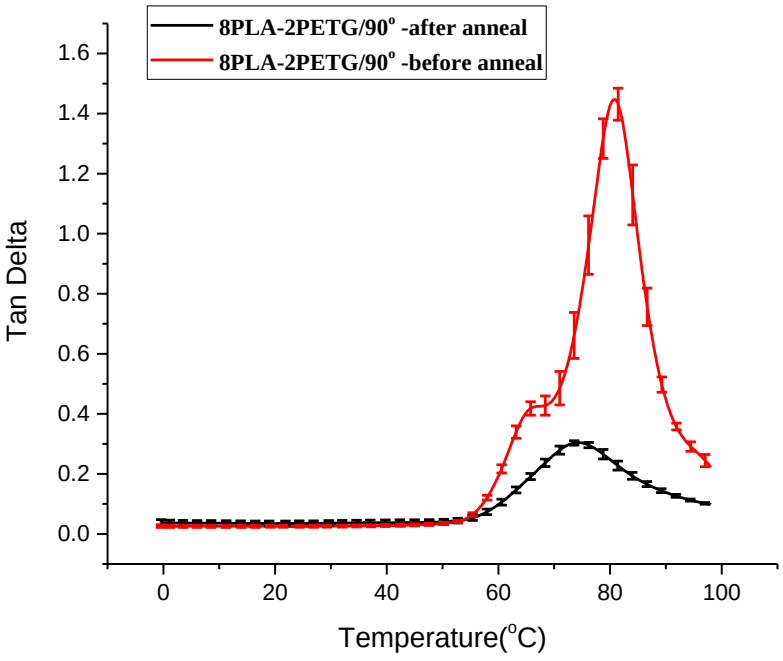

Figure A1.41: Comparison of tan delta for 8PLA-2PETG/90° between before and after annealing.

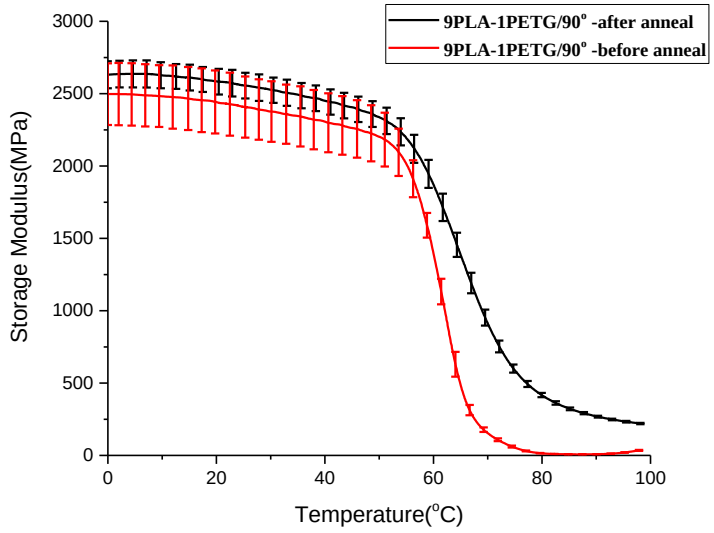

Figure A1.42: Comparison of storage modulus for 9PLA-1PETG/90° between before and after annealing.

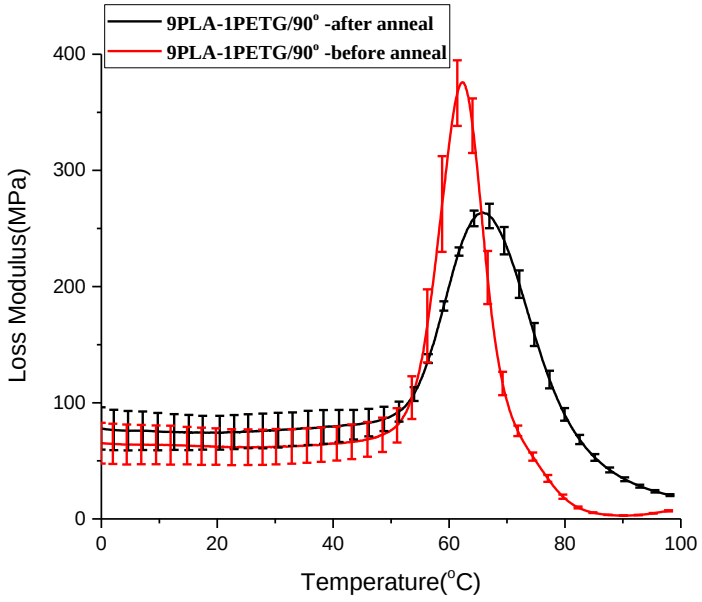

Figure A1.43: Comparison of loss modulus for 9PLA-1PETG/90° between before and after annealing.

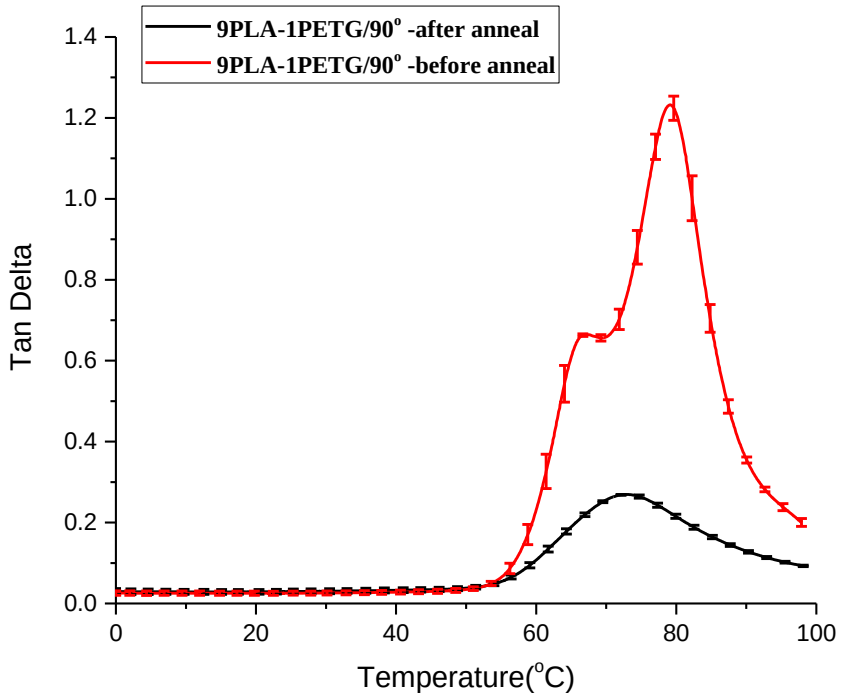

Figure A1.44: Comparison of tan delta for 9PLA-1PETG/90° between before and after annealing.

APPENDIX 2

SIC/PLA COMPOSITES INTRODUCTION

Recently, employment of microwave absorption properties of materials to improve mechanical performances of 3D printed objects has attracted great interests. For instance, carbon nanotubes were coated on the surfaces of printed layers. Microwave treatment improved the mechanical properties of 3D printed objects significantly[1]. However, carbon based materials have a lower oxidation resistances which restrict their applications[2]. In contrast, SiC is a promising microwave absorption material for 3D printing due to its high thermal and chemical stability. Addition of SiC particles within materials matrix to improve both absorbing and mechanical performances has been studied[3-5]. Whereas, there is no report about using SiC materials in 3D printing technology to improve mechanical properties of printed parts through microwave treatment. In this work, we evaluated the feasibility of utilizing SiC in PLA matrix to anneal the printed objects by microwave heating. The possible enhancement mechanism of utilizing SiC/PLA composite to weld the 3D printed objects is shown in **Figure A2.1**.

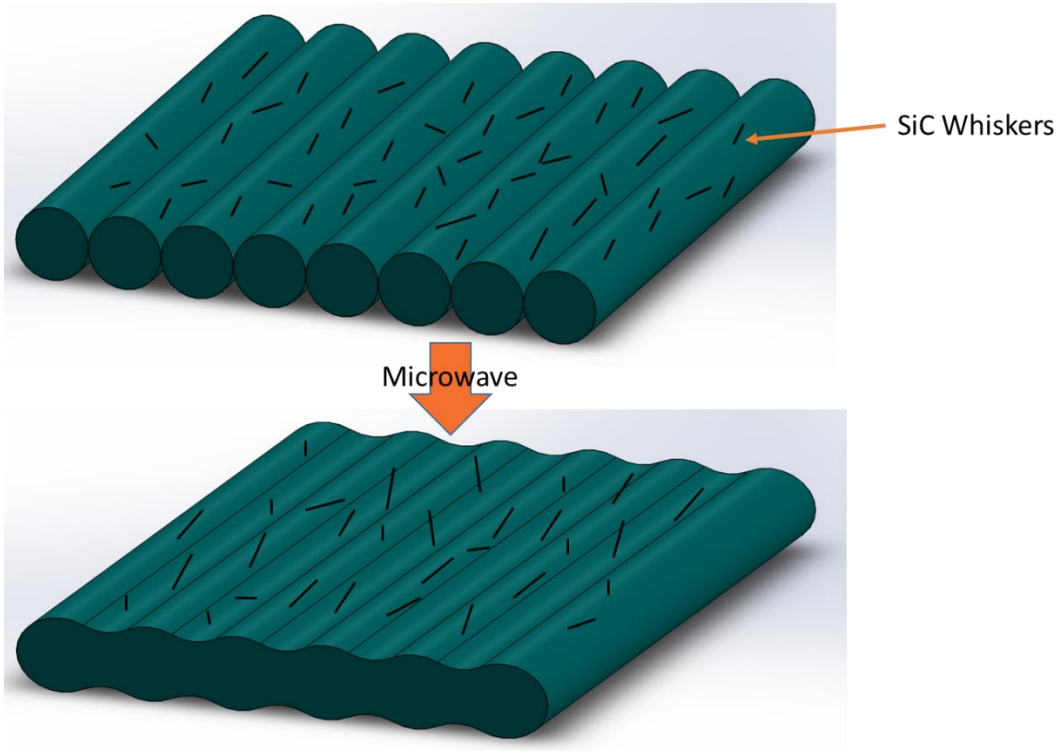

Figure A2.1: Mechanism of using SiC whiskers to weld 3D printed parts.

SiC/PLA composites preparation

Polymer composites

SiC/PLA composite with 3vol% SiC whiskers was prepared by solution casting method. PLA-2 pellets and SiC whiskers were dissolved in chloroform separately. A PLA solution was prepared using magnetic stirrer (Corning, Inc.). Two solutions were then mixed together and kept agitated for 2hrs with the purpose of forming a better dispersion of SiC whiskers and avoiding the SiC aggregation. The mixture was then casted on the aluminum foil and left under the hood overnight to evaporate the solvent. To further dry

the casted film, it was kept in the oven (VWR International LLC.) under vacuum at 70°C for several days. Level of the solvent left over was determined by TGA analysis. Composite film was then cut into small pieces and pelletized by MFI tester.

Results and Discussions

Rheological behavior

Table A2.1: Comparison of MFI for PLA-2 pellets and SiC/PLA composite

Material	**method**	**Sample Weight(g)**	**MFI(g/10min)**
PLA pellets	200C; 30s cutting interval, 1.2kg load.	0.2286,0.2293,0.2326,0.2387, 0.2450,0.2471,0.2529,0.2554, 0.2613,0.2661, 0.2705,0.2785, 0.3235,0.3382,0.3521,0.3572, 0.3629,0.3854	**4.48**
3vol% SiC-PLA	200C; 30s cutting interval, 1.2kg load.	No materials coming out	
3vol% SiC-PLA	220C; 30s cutting interval, 1.2kg load.	0.1749,0.2081,0.1831,0.2347, 0.191,0.2544,0.1872,0.2519, 0.1772,0.2555,0.1839,0.2562, 0.1937,0.1974,0.215,0.2144	**4.3**

MFI measurements indicate that the addition of SiC within PLA increase the viscosity of material.

Tensile tests

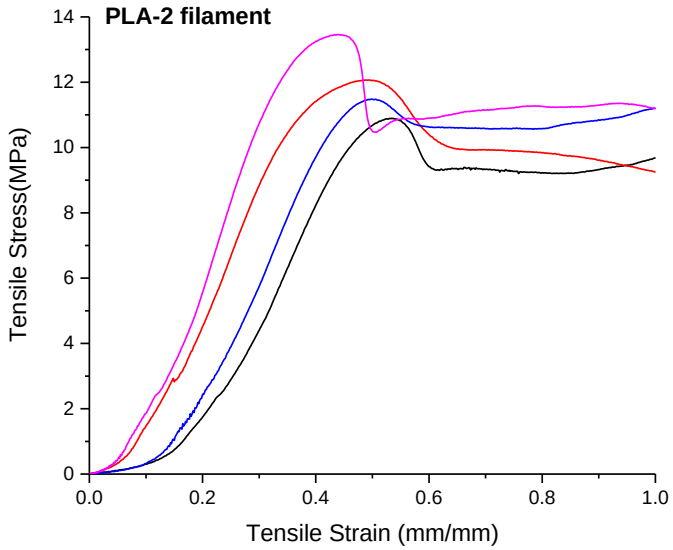

Figure A2.2: Tensile stress-strain curve for PLA-2 filament.

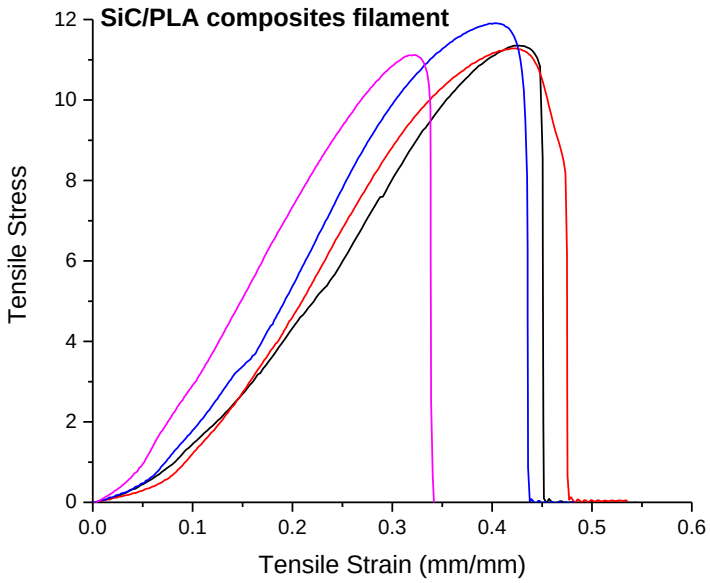

Figure A2.3: Tensile stress-strain curve for SiC/PLA composite filament.

Table A2.2: Young's modulus for PLA-2 and SiC/PLA composite filament

Material	Elongation at yield (mm/mm)	Young's Modulus (Mpa)
SiC/PLA	0.33	1287.2
PLA	0.49	1122.2

Tensile tests indicate that the addition of SiC makes the composites stiffer but also more brittle.

Thermal Analysis (DSC)

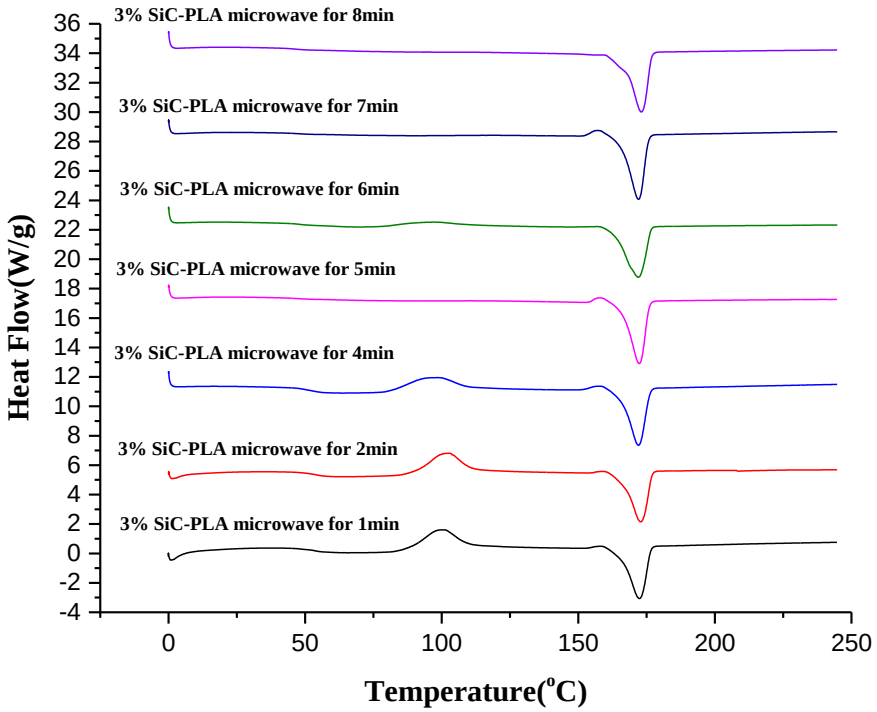

Figure A2.4: DSC thermograph of SiC/PLA composite after treatment in microwave for different time.

Table A2.3: Dependence of percent of crystallinity on microwave treatment times

Microwave treatment time (min)	Heat flow of crystallization (J/g)	Heat flow of melting (J/g)	Percent of crystallinity
1	36.67	36.74	0.08%
2	34.9	35.1	0.22%
4	21.7	37.4	16.9%
5	2	36.1	36.7%
6	12	39.4	29.5%
7	2.7	38.3	38.3%
8	0	34.3	36.9%

The DSC thermograph indicates that the PLA polymer is highly crystallized after putting the SiC/PLA composite in microwave oven for 8min. However, the thermographs of samples been microwave treated for 5min and 6min indicate that SiC whiskers are not well-dispersed within PLA matrix. The possible SiC aggregation makes some samples fully crystallized earlier than others. However, the parallel experiments show that all samples are highly crystallized after putting in microwave oven for 8min.

DMA measurements

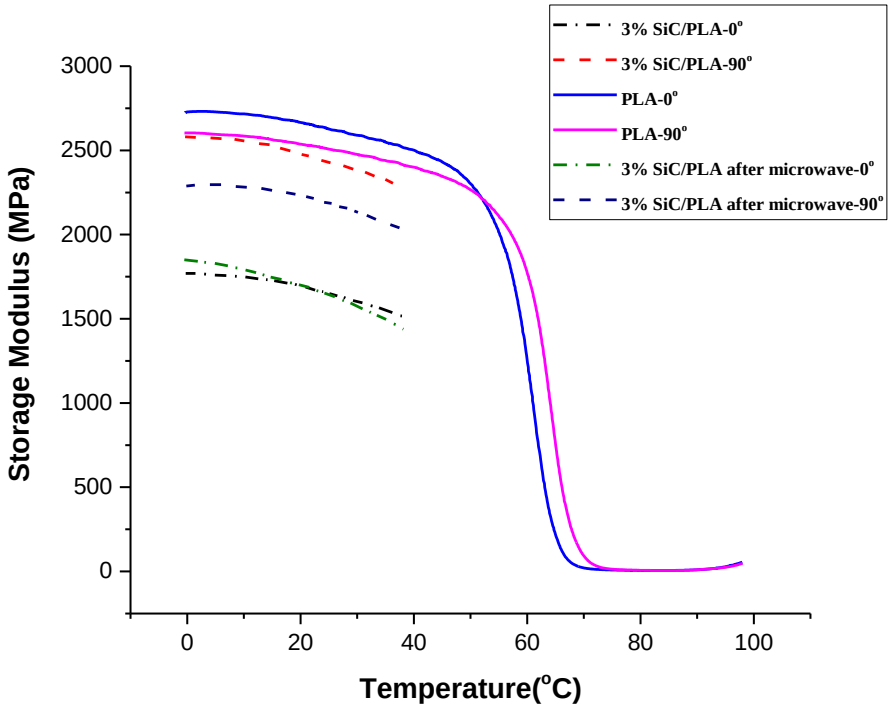

Figure A2.5: Comparison of Storage modulus of SiC/PLA and PLA-2 samples processed at different conditions.

Samples printed from SiC/PLA composites have lower storage modulus in comparison with that fabricated from pure PLA-2 filaments. The weak mechanical performances of the printed SiC/PLA samples result from the low viscosity of the composites coming out of nozzle since all the samples were printed at the same temperature.

Moreover, the storage modulus of SiC/PLA composite samples decreased after the treatment in microwave oven. We associate this unexpected result with the SiC aggregation problem. The localize concentrated SiC overheated the samples in microwave oven and decomposition of PLA was visually observed.

References

1. Sweeney, C. B.; Lackey, B. A.; Pospisil, M. J.; Achee, T. C.; Hicks, V. K.; Moran, A. G.; Teipel, B. R.; Saed, M. A.; Green, M. J., Welding of 3D-printed carbon nanotube-polymer composites by locally induced microwave heating. *Sci Adv* **2017,** *3* (6).
2. Chen, J. H.; Liu, M.; Yang, T.; Zhai, F. M.; Hou, X. M.; Chou, K. C., Improved microwave absorption performance of modified SiC in the 2-18 GHz frequency range. *Crystengcomm* **2017,** *19* (3), 519-527.
3. Wu, Q.; Li, L.; Zhang, Y. D.; Shui, W. J., Absorption and mechanical properties of SiCp/PVDF composites. *Compos Part B-Eng* **2017,** *131*, 1-7.
4. Wang, H. Y.; Zhu, D. M.; Wang, X. F.; Luo, F., Influence of silicon carbide fiber (SiCf) type on the electromagnetic microwave absorbing properties of SiCf/epoxy composites. *Compos Part a-Appl S* **2017,** *93*, 10-17.
5. Reza-E-Rabby, M.; Jeelani, S.; Rangari, V. K., Microwave processing of SiC nanoparticles infused polymer composites: Comparison of thermal and mechanical properties. *J Appl Polym Sci* **2015,** *132* (12).